UNIVERSITÉ DE STRASBOURG

ÉCOLE DOCTORALE MATHEMATIQUES, SCIENCES DE L'INFORMATION ET DE L'INGENIEUR – ED269

UMR 7357 CNRS-Unistra

THÈSE présentée par :

Yahya Zakaria

soutenue le : **31 Mai 2023**

pour obtenir le grade de : **Docteur de l'université de Strasbourg**

Discipline/ Spécialité : Science des Matériaux

Study of Thin Layers of Tin Oxide for Applications in Photovoltaic Solar Cells

THÈSE dirigée par :

M. SLAOUI Abdelilah	Directeur de Recherche, ICube, CNRS - Université de Strasbourg
M. AHZI Said	Professeur, ICube, CNRS - Université de Strasbourg

RAPPORTEURS :

Mme. BOUSQUET Angélique	Maître de Conférences HDR, Institut de Chimie de Clermont-Ferrand, Université Clermont Auvergne
M. PIERSON Jean-François	Professeur, Institut Jean Lamour, CNRS - Université de Lorraine

EXAMINATEURS :

M. COLIS Silviu	Professeur, IPCMS, CNRS - Université de Strasbourg
M. JOUIAD Mustapha	Professeur, LPMC, Université de Picardie Jules Verne
M. RUCH David	Research Team Leader, Luxembourg Institute of Science and Technology (LIST), Luxembourg

MEMBRES INVITES :

M. AISSA Brahim	Senior Scientist, Qatar Environment and Energy Research Institute, HBKU, Qatar
M. FIX Thomas	Chargé de Recherche HDR, ICube, CNRS - Université de Strasbourg

Abstract

In the last decades, solar PV has reached the technological maturity as well as high performance levels. However, the current challenge is to make solar PV more cost-effective to be more competitive with conventional sources of energy. One rational way to reduce the cost of solar PV, is through the use of cost-effective materials to reduce the manufacturing cost. Indium tin oxide (ITO) is one of the most used transparent conducting oxides in solar PV, is not a sustainable material as indium, which is the main metal, has a low earth-abundance and a very high cost. On the other hand, tin, which is the metallic element of tin oxide, is much more cost-effective and has a higher earth-abundance compared to indium.

The aim of this thesis is to conduct a detailed study of undoped tin oxide and nitrogen doped tin oxide as a transparent conducting oxide (TCO) using mainly reactive magnetron sputtering with different growth conditions and exploring the material properties with different characterisation techniques. This thesis will also assess the performance of tin oxide as electron transport layer (ETL) for perovskite solar cells.

Chapter 1 will address the state-of-the-art of undoped and doped SnO_x films in both chemical states SnO and SnO_2. Chapter 2 will present the work on undoped SnO_x synthesis and post-deposition annealing as well as material characterization related to structural, chemical, optical, and electrical properties. We will show that high conductivity is related to poor oxygen condition during the growth of SnO_x films and high optical transmittance is related to high oxidation of SnO_x films. Chapter 3 will explore the possibility to dope SnO_x with nitrogen using three nitrogen precursor gases namely, NH_3, N_2O and N_2. We will show that NH_3 treatments has etched and damaged the SnO_x, N_2O treatments have enhanced the n-type conductivity and N_2 treatments have shown the ability to convert the conductivity from n-type to p-type. Chapter 4 will present the implementation of SnO_x as electron transport layer in perovskite solar cells (PSCs) where we will show that the post-deposition annealing has improved the electrical properties of SnOx which leads to improve the performance of PSC.

Résumé

Au cours des dernières décennies, le solaire photovoltaïque a atteint une maturité technologique ainsi que des niveaux de performance élevés. Cependant, le défi actuel consiste à rendre le PV solaire plus rentable pour être plus compétitif par rapport aux sources d'énergie conventionnelles. Une manière rationnelle de réduire le coût du solaire photovoltaïque consiste à utiliser des matériaux rentables pour réduire le coût de fabrication. L'oxyde d'indium et d'étain est l'un des oxydes conducteurs transparents les plus utilisés dans le PV solaire, il n'est pas un matériau durable car l'indium, qui est le métal principal, a une faible abondance et un coût très élevé. D'autre part, l'étain, qui est l'élément métallique de l'oxyde d'étain, a une abondance de terre plus élevée que l'indium et un coût relativement faible.

L'objectif de cette thèse est de mener une étude détaillée de l'oxyde d'étain non dopé et de l'oxyde d'étain dopé à l'azote en tant qu'oxyde conducteur transparent (OCT) en utilisant principalement la pulvérisation magnétron réactive avec différentes conditions de croissance et en explorant les propriétés du matériau par différentes techniques de caractérisation. Cette thèse évaluera également les performances de l'oxyde d'étain comme couche de transport d'électrons (CTE) pour les cellules solaires à pérovskite.

Le chapitre 1 traitera de l'état de l'art des films de SnO_x non dopés et dopés dans les deux états chimiques SnO_2 et SnO. Le chapitre 2 présentera les travaux sur la synthèse de SnO_x non dopé et le recuit post-dépôt ainsi que la caractérisation des matériaux liée aux propriétés structurales, chimiques, optiques, et électriques. Nous montrons qu'une conductivité élevée est liée à une condition d'oxygène appauvrie pendant la croissance des films de SnO_x et qu'une transmission optique élevée est liée à une oxydation élevée des films de SnO_x. Le chapitre 3 explorera la possibilité de doper SnO_x avec de l'azote en utilisant trois gaz précurseurs de l'azote, à savoir NH_3, N_2O et N_2. Nous montrons que les traitements NH_3 ont gravé et endommagé les films SnO_x, les traitements N_2O des films SnO_x ont amélioré la conductivité de type n et les traitements N_2 des films SnO_x permettent de convertir la conductivité de type n en type p. Le chapitre 4 présentera la mise en œuvre de SnO_x en tant que couche de transport d'électrons dans les cellules solaires à pérovskite où nous montrons que le recuit post-dépôt a amélioré les propriétés électriques de SnO_x, ce qui conduit à améliorer les performances des cellules solaires à pérovskite.

DEDICATION

To my mother, the greatest mother in the world, to whom I owe everything in my life. To my father, fiancé, sisters, and friends.

Acknowledgements

I would like to express my acknowledgments and gratitude to my thesis director Dr. Abdelilah Slaoui, and co-director Dr. Said Ahzi for their support, motivation, professionalism, and guidance during my thesis research. I also would like to express my acknowledgement and gratitude to ICube CNRS-Unistra Team namely, Thomas Fix, Nicolas Barth, Stéphane Roques, Gérald Ferblantier, and Romain Vollondat for their respective support provided to this thesis as well as HBKU Core Labs and QEERI Teams particularly Dr. Said Mansour and Dr. Brahim Aissa.

I would also like to express my gratitude and acknowledgement to Mme. Nathalie Kostmann who provided an outstanding administrative support during the course of my PhD.

Special thanks to all family members, colleagues and friends who supported directly or indirectly this work.

Table of Contents

List of Tables

Chapter 1

Chapter 2

Chapter 3

Chapter 4

Appendix

List of Diagrams

Chapter 2

List of Figures

Introduction

Chapter 1:

Chapter 2

Chapter 3

Chapter 4

Appendix

Preface

This thesis represents the research work I conducted under the direction of Dr. Abdelilah Slaoui and Pr. Said Ahzi with the support of the research group of ICube - Materials for electronic and photovoltaic devices (MaCEPV) at University of Strasbourg from 2019 to 2023 as well as the research team at Hamad Bin Khalifa University - Core Labs and QEERI Energy Centre at Nanomaterials Laboratory.

Chapter 1 is a detailed literature review which includes around 300 references, will be converted into a review article.

The majority of my work on undoped SnO_x films in Chapter 2 has been published as open access article "Yahya Zakaria et al. - Study of wide bandgap SnO_x thin films grown by a reactive magnetron sputtering via a two-step method - Scientific Reports 12, 15294 (2022). https://doi.org/10.1038/s41598-022-19270-w" under Creative Commons Attribution 4.0 International License.

Chapter 3 is related to SnO_x film as electron transport layer was conducted in collaboration with Dr. Brahim Aissa at QEERI-HBKU. This chapter has been published as open access article "Yahya Zakaria et al. - Moderate temperature deposition of RF magnetron sputtered SnO_2-based electron transporting layer for triple cation perovskite solar cells - Scientific Reports 13, 9100 (2023). https://doi.org/10.1038/s41598-023-35651-1" under Creative Commons Attribution 4.0 International License.

Chapter 4 is based on nitrogen doped SnO_x was conducted with the support of MaCEPV team (mentioned in the acknowledgement). This chapter is based on a finalized manuscript which will be submitted for publication soon.

General Introduction

As the electric energy demand is increasing nowadays, the current fossil energy resources are not sufficient for the foreseeable future. Furthermore, despite the appealing advantages the nuclear energy, it is facing various challenges related to the materials handling, transportation, storage and disposal, its high operating cost, and the public view[1]. Adopting and implementing renewable energy, which is originated from sources that can be self-regenerated regularly to meet our energy requirements, is a viable approach to fulfil the human increasing energy need. The renewable energy includes wind energy, hydropower, and solar energy.

Solar energy is an attractive source of energy due to the highly available energy received from the sun. Renewables 2022 report by International Energy Agency reveals that the installed Solar Photovoltaics (PV) power capacity will exceed the power capacity of every other form of energy, particularly the power capacity of coal by 2027 as shown in Figure 1[2]. This increase in cumulative power capacity of solar PV is mainly due to the enhancement of cost-effectiveness that solar technologies have achieved. Like other sources of renewable energy, one of the main global objectives for research and development related to solar PV, is to reach the level of grid parity where the PV-generated power has the levelized cost of energy (LCOE) equal or less than the price of the electricity in the grid from non-renewable sources of energy such as natural gas. Most governments and energy agencies worldwide are encouraging the use of renewable energy by promoting and supporting solar energy and wind energy projects. Some countries are encouraging the use of solar energy by applying incentive plans to households to incorporate solar energy at the individual level.

---

[1] *https://www.energy.gov/ne/articles/advantages-and-challenges-nuclear-energy*

[2] *IEA (2022), Renewables 2022, IEA, Paris https://www.iea.org/reports/renewables-2022, License: CC BY 4.0*

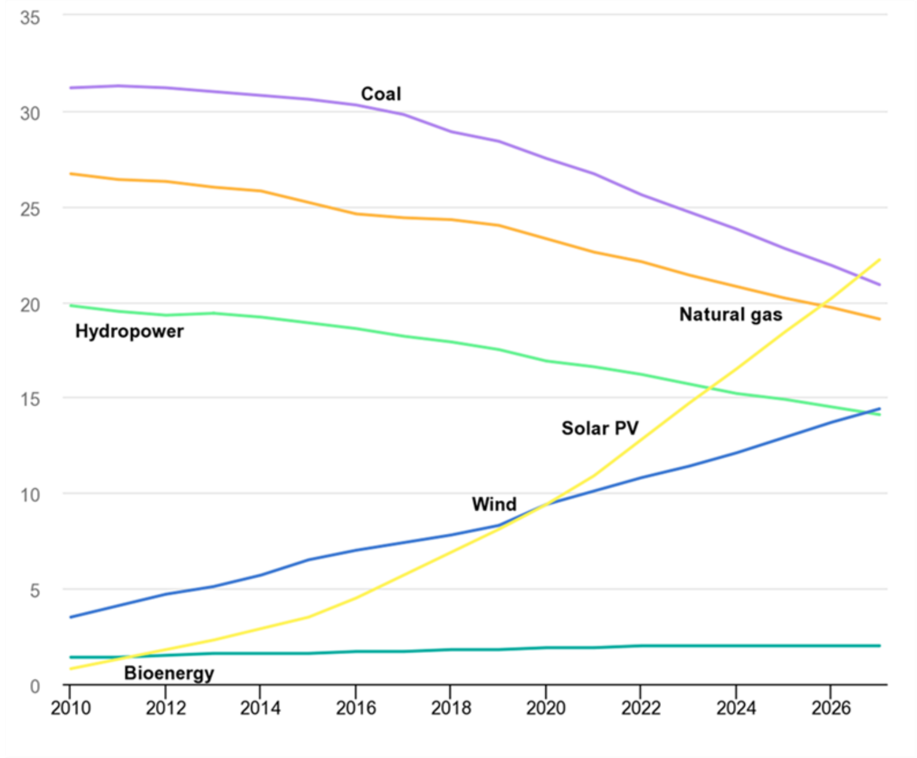

Figure 1: Projected share of cumulative power capacity by technology, 2010-2027. Reprinted (adapted) from [2]. License: CC BY 4.0.

Solar cells or photovoltaic cells, which are the essential components of solar panels, are electronic devices based on semiconducting materials that convert light into electricity directly without any intermediate mean of energy. In terms of performance, the solar cells efficiency is getting closer to the theoretical limit around 30% power conversion energy for single junction[3] using sophisticated processes. There is a need to reduce the cost of solar energy infrastructure, particularly the cost of solar panels. Increasing the efficiency is the rational way to increase the solar PV power capacity and reduce the LCOE which can encourage more investments in solar PV fabrication and implementation. Nevertheless, there is a huge potential in decreasing the fabrication cost by using low-cost abundant materials and lower the cost of deposition processes such as lowering the process temperature to reduce the energy consumption. This can also reduce the LCOE of solar PV which will make it more competitive with conventional non-renewable sources of energy as well as making solar PV more affordable to worldwide markets. Energy storage systems are very complementary to solar PV to provide electricity all the time as solar energy depends on the sun which is only available for several hours per day at most. There are different applications for solar PV as electricity source such as,

---

[3] *Shockley, W. and H.J. Queisser, Detailed Balance Limit of Efficiency of p-n Junction Solar Cells. Journal of Applied Physics, 1961. 32(3): p. 510-519.*

electricity related the power grid and there are also off grid applications whether in remote areas or in specific isolated sites.

The implementation of cost-effective and abundant elements-based materials to replace expensive and non-abundant elements-based materials in solar PV is a one of the key aspects to reduce the cost of fabrication. Furthermore, Transparent Conducting Oxides (TCO) materials are an essential part of solar cells and currently used in many optoelectronic devices, particularly in PV technologies namely, heterojunction silicon solar cells, thin films solar cells (a-Si, CdTe, CIGS, CZTS), perovskites solar cells, tandem cells. There is a constant research effort to reach this goal by implementing better cost-effective transparent conducting oxides (TCOs). Indium tin oxide (ITO), which is one of the most used TCOs in several applications related to optoelectronics, will be facing some supply challenges in the foreseeable future due to the high cost of indium as well as its limited abundance on earth crust compared to most of post-transition metallic elements. On the other hand, tin is more cost-effective and abundant element compared to indium. Tin, which is the base metallic element of tin oxide (SnO_x) materials, can reach to a high conductivity and electrical mobility by optimizing the growth conditions of SnO_x thin films.

This thesis is presenting the work on TCO materials based on tin oxide where growth conditions and materials characterisation will be analysed in depth to explore the potential possibilities to improve the optoelectronic properties of these thin films. The thesis work is presented in four chapters as well as a final conclusion and perspectives.

The first chapter of this thesis will be discussing the literature review of transparent conducting oxides (TCOs) and their respective applications. In particular, the material synthesis and properties, and the applications of In_2O_3 and ZnO thin films as TCOs will be covered in this chapter. The state-of-the-art of tin oxide (SnO_x), in both chemical states SnO_2 and SnO, will be discussed in terms of material synthesis and properties as well as their applications. The second chapter is a detailed study about deposition, thermal annealing, material characterisation, and optoelectronic performance for undoped SnO_x. The third chapter will present the work on SnO_2 as electron transport layer (ETL) for perovskite solar cells. The material characterisation of SnO_2 thin film and the performance assessment of perovskite solar cells using SnO_2 as ETL will be covered in this chapter. The fourth chapter will be focusing on the nitrogen-doped SnO_x (N-doped SnO_x) using two-step method of synthesis by magnetron sputtering and plasma assisted thermal annealing in nitrogen precursor atmosphere namely, NH_3, N_2O, and N_2. A detailed material characterisation of N-doped SnO_x is also presented in this chapter. This thesis will be completed by a general conclusion to present the overall relevant findings and by the perspectives to highlight the potential future work beyond this PhD thesis and the next-level research related to SnO_x.

Chapter 1: Literature Review on Tin Oxide (SnO_x) films

1. Literature Review on Tin Oxide (SnO_x) films

1.1. Transparent Conducting Oxides

1.1.1. Introduction

Transparent conducting oxides (TCOs) are oxide materials which have both properties of the electrical conductivity and the high optical transmittance. These two properties can be combined by TCOs as thin films on a highly transparent substrate. While the optical transparency character of materials, which allows the transmittance of the visible and near-infrared of wavelength above 380 nm, is due to the wide bandgap above 3.3 eV. In contrast, the wide bandgap of the materials above 3.3 eV would lead to a high resistivity and make the charge carriers related doping very challenging. Therefore, the transparent conducting oxide materials can be considered very unique and remarkable materials[1, 2]. The two important properties of electrical conductivity and optical transparency along with the intrinsic chemical stability of the oxides, make the TCOs essential materials for several optoelectronic applications such as solar cells, light emitting diodes, flat panel displays, touch screens[1-29].

The first widely known report about TCOs was back in 1907 by Karl Bädeker who reported a transparent and conducting film of cadmium oxide [30]. The progress in quantum mechanics in 1920s has enabled a better understanding of semiconductors mainly oxides and their doping in terms of electrical properties[31, 32]. Since then, the research interest on TCOs has increased till the 1950s when researchers could establish the first Indium Tin Oxide (ITO) which was first patented by J.M. Mochel (Corning Inc)[33]. The first academic report about ITO was published in 1954 by Rupperecht[34]. Other materials such as SnO_2 and ZnO were also explored as transparent conducting oxide materials. It is relevant to note that one of the first major advance in semiconductors was the ability to dope the amorphous silicon with substitutional pentavalent impurities such as phosphorus or trivalent impurities such as boron to form n-type or p-type conductive films, respectively, as reported by Spear and Le Comber in 1975[35].

Since the 1990s, transparent conducting oxides related properties have had a tremendous progress due to the acquired research knowledge and expertise as well as the major technological advancements which enabled much higher quality in term of material synthesis and characterization, and more powerful computational calculation. Nevertheless, most of the progress was made for n-type conductive TCOs which is due to some of the intrinsic properties of the oxide materials that will be discussed in detail later[31, 36, 37]. It is widely established that the main breakthrough in the progress of TCOs in the last three decades, was achieving the first p-type transparent conductive oxide thin films of $CuAlO_2$ as reported by Kawazoe et al. which have a polycrystalline delafossite microstructure and were prepared by laser ablation[38]. This milestone has unlocked a new wider perceptive of TCOs as well as enabling the possibility of new revolutionary applications for these materials. The other milestone for TCO materials was achieving the transparent amorphous oxide semiconductors which was first reported by Nomura et al. an amorphous Indium Gallium Zinc Oxide (a-IGZO) which was prepared at room temperature on a flexible polyethylene terephthalate substrate by pulsed laser ablation[3]. The transparent amorphous oxide semiconductors have more appealing electrical properties compared to hydrogenated amorphous silicon (a-Si:H) and amorphous chalcogenides namely, the Hall mobility which exceeded 10 $cm^2/V \cdot s$. This mobility is in the same range of the crystalline TCO materials. Moreover, it is much higher than amorphous thin film materials, namely, a-Si:H and a-chalcogenides[39, 40]. Historically, the transparent conductive oxides research was somehow focusing on materials based on In_2O_3, SnO_2 and ZnO as well as CdO[1, 2, 4, 10, 12, 13, 29, 37, 41]. Therefore, the achievement of new TCO materials using insulating earth-abundant oxides namely, $12CaO \cdot 7Al_2O_3$ and converting them to conductive oxides was also a notable breakthrough. This thin film material was achieved through thermal annealing in hydrogen atmosphere followed by ultraviolet irradiation[42]. The achievement of new TCO material Niobium doped TiO_2, which has reached a very low resistivity of 2~3 $x10^{-4}$ Ω cm, was also an important breakthrough[43]. The advantage of TiO_2 as thin film and as host material for doping is the chemical stability. This achievement has also paved the way for finding alternative materials for ITO[1, 31].

It is worth noting that the global transparent conductive films market was 4.9 billion USD in 2020 and it is expected to reach a market value of 12.9 billion USD in 2030[44]. Although Indium Tin Oxide is the widely developed TCO in the industry nowadays, there is still room for improvement in terms of optical transparency, surface electrical conductivity, material's flexibility and low cost[1-12, 23-29, 31, 45-50].

The demand on Indium, which is the main metal in ITO, has been exponentially increasing since the emerging of the ITO as an optimal TCO for many industrial applications. This demand is facing future challenges related to the low abundance of Indium metal in the earth's crust and consequently its potential price increase, or supply chain policies. While there are some research efforts focusing on Indium recycling, this new field is facing some difficulties in terms of lack of accessible and reliable data of mining activities as well as the lack of research efforts of environmental performance related to the Indium recovery. The success of this path would require efficient recycling processes and high-level international agreements between productors/consumers countries, key industrial players and the research entities which is not currently available and not possible for the foreseeable future. Thus, the research efforts and industrial sector are targeting alternatives to ITO due to the challenge of Indium, the main metal of ITO, while keeping the sheet resistances under 5 $\Omega \, \square^{-1}$ particularly for large surface display and large solid state light emitting devices[31, 50, 51].

The basic requirements for the alternative TCOs are the high electrical conductivity and the high optical transparency. Furthermore, alternative TCOs should have the advantage of low-cost production, non-toxic materials, and the ability to control the interface with the active materials. Alternative TCOs should also have the mechanical flexibility (bendability) which would systematically enable more applications[31, 50].

1.1.2. General Material Properties of Transparent Conducting Oxides

As discussed in the previous section, Transparent Conducting Oxides has gained a lot of progress in the last century, particularly in the last few decades which led to the implementation of TCOs in many applications, mainly in optoelectronics. This progress took place in many aspects, such as deep understanding of the material's properties namely, structural, electronic, optical, and electrical properties as well as improving the synthesis quality by controlling the material's defects, enhancing the crystallinity, fine-tuning the bandgap, and alloying engineering which eventually enabled the substantial improvement in TCOs design and manufacturing in optoelectronic devices.

In general, oxides, which represent an important class of solid materials, are chemical compounds formed by one oxygen atom at least and one other element at least. Furthermore, metal oxides are chemical compounds which are formed by one oxygen atom at least and one metal at least, with many metals existing naturally on earth as metal oxides. The naturally high earth abundance of metal oxides is mainly related to the stable chemical bonds between metals and to the electronegative oxygen atoms. Most of metals can be easily oxidised in presence of oxygen and form metal oxide materials. Metal oxides have largely a tendency to form ionic structure by metal oxygen metal crosslinking. They are often insoluble materials in majority of solvents. However, they can be vulnerable to acids and bases.

Technically, Transparent Conducting Oxides need to satisfy three main criteria. First, the bandgap has to be equal or above 3.1 eV and the optical transmittance has to be superior to 85% in the visible spectrum as thin film material. Secondly, the TCO need to have the ability to form degenerated doping to allow the pure oxide to transition from transparent semiconducting oxide to a metallic conductor. Finally, TCO related metal cations should a have typical electronic configuration of $(n\text{-}1)d^{10}ns^{2}np^{a}$ where n can be 4 or 5 [52, 53].

Many metal oxides have been implemented in industry, particularly in optoelectronic applications. Certain metal oxides were investigated significantly and are commonly used in various applications. Among these metal oxides, there are In_2O_3, ZnO, SnO_2, and CdO where the metal cations are In^{3+}, Zn^{2+}, Sn^{4+}, and Cd^{2+}, respectively. Nevertheless, the interest in CdO has dropped drastically due to the toxicity of Cd which is the main metallic element. In_2O_3, ZnO, and SnO_2 as TCOs are important conducting materials for optoelectronic applications as they are all considered wide bandgap as shown in Table 1 and these materials could reach resistivities as low as the order of 10^{-4} Ω·cm. Furthermore, ternary and quaternary compounds have been achieved based on these three materials, including ITO[1, 31, 37, 41, 50, 54]. Figure 1 shows possible TCO materials based on In_2O_3, SnO_2, ZnO. These materials have a very similar structural, optical, and electronic properties. Their electronic configurations of the metallic elements are $(n-1)d^{10}ns^2(np^a)$ where electrons from the *ns* orbitals interact strongly with the electrons 2*p* orbital of the oxygen as shown in Table 2. These TCO materials have close-packed structures enabling four coordinates for ZnO where the Zn elements have a coordination to four oxygen atoms while forming a corner sharing tetrahedra as well as enabling six coordinates for CdO, In_2O_3 and SnO_2 where the metallic atoms have a coordination to six oxygen atoms while forming a corner sharing octahedra. The valence band (VB) in these oxides is formed by O 2*p* energy states both bonding and non-bonding, while the conduction band is formed by the antibonding Ms-Op interactions. The energy states of the electrons n*s* related to metals and 2*p* related to oxygen contribute to the formation of the conduction band (CB) to form a three-dimension network for charge carrier transport once additional carriers fill the band [2, 12, 54-59].

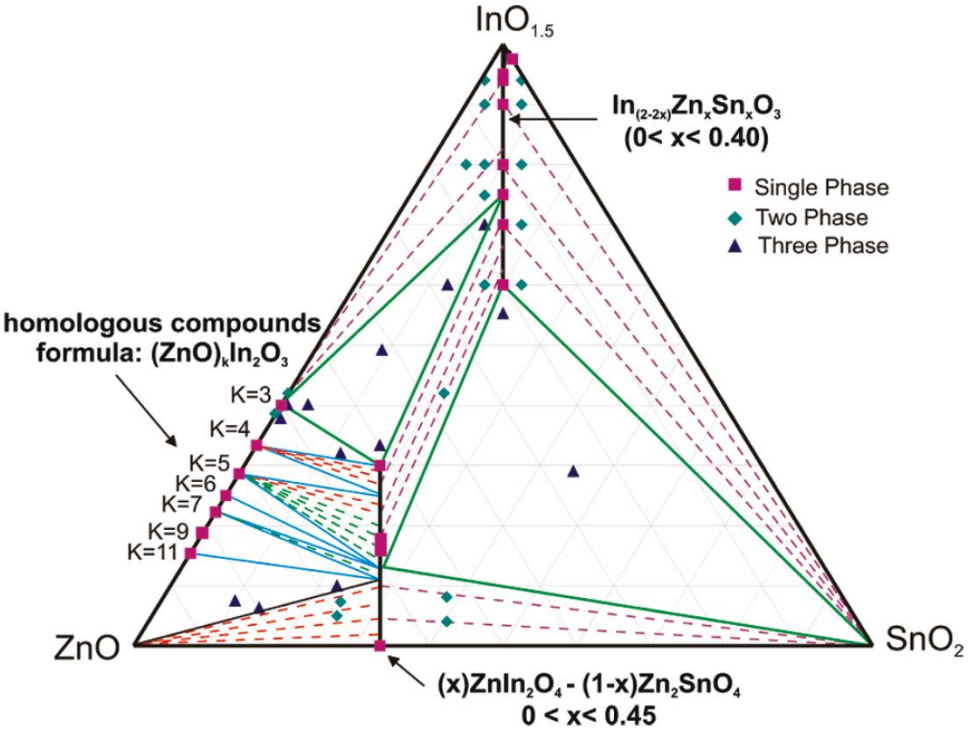

Figure 1: TCO semiconductors based on In2O3, SnO2, and ZnO. Reprinted (adapted) with permission from [53]. Copyright 2010 American Chemical Society.

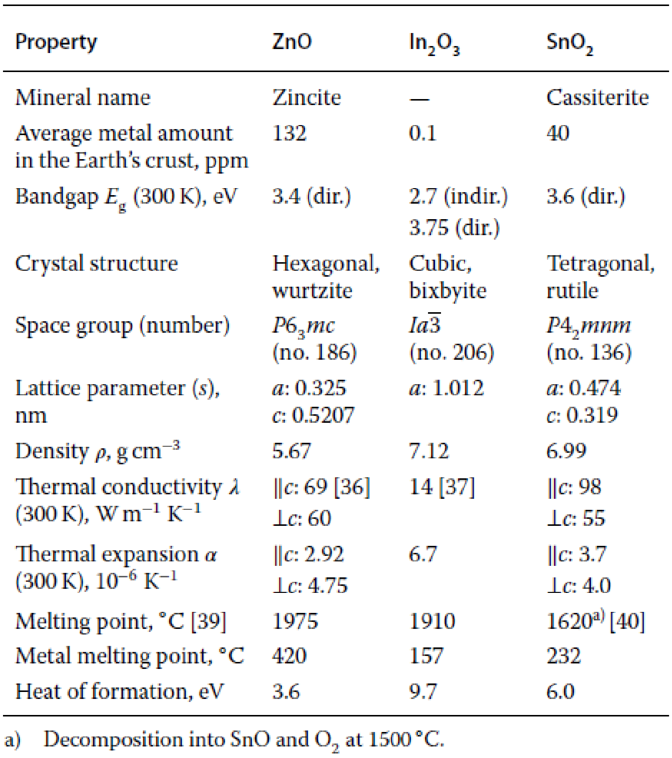

Property	ZnO	In_2O_3	SnO_2
Mineral name	Zincite	—	Cassiterite
Average metal amount in the Earth's crust, ppm	132	0.1	40
Bandgap E_g (300 K), eV	3.4 (dir.)	2.7 (indir.) 3.75 (dir.)	3.6 (dir.)
Crystal structure	Hexagonal, wurtzite	Cubic, bixbyite	Tetragonal, rutile
Space group (number)	$P6_3mc$ (no. 186)	$Ia\overline{3}$ (no. 206)	$P4_2mnm$ (no. 136)
Lattice parameter (s), nm	a: 0.325 c: 0.5207	a: 1.012	a: 0.474 c: 0.319
Density ρ, g cm^{-3}	5.67	7.12	6.99
Thermal conductivity λ (300 K), W m^{-1} K^{-1}	$\parallel c$: 69 [36] $\perp c$: 60	14 [37]	$\parallel c$: 98 $\perp c$: 55
Thermal expansion α (300 K), 10^{-6} K^{-1}	$\parallel c$: 2.92 $\perp c$: 4.75	6.7	$\parallel c$: 3.7 $\perp c$: 4.0
Melting point, °C [39]	1975	1910	1620[a)] [40]
Metal melting point, °C	420	157	232
Heat of formation, eV	3.6	9.7	6.0

a) Decomposition into SnO and O_2 at 1500 °C.

Table 1: Material properties of ZnO, In_2O_3 and SnO_2. Reprinted (adapted) with permission from [12]. Copyright 2018 John Wiley & Sons.

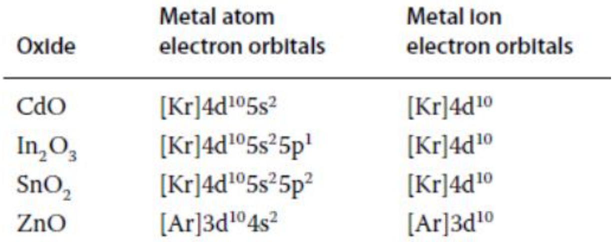

Oxide	Metal atom electron orbitals	Metal ion electron orbitals
CdO	$[Kr]4d^{10}5s^2$	$[Kr]4d^{10}$
In_2O_3	$[Kr]4d^{10}5s^25p^1$	$[Kr]4d^{10}$
SnO_2	$[Kr]4d^{10}5s^25p^2$	$[Kr]4d^{10}$
ZnO	$[Ar]3d^{10}4s^2$	$[Ar]3d^{10}$

Table 2: metal electron orbitals. Reprinted (adapted) with permission from [12]. Copyright 2018 John Wiley & Sons.

In the next section, Transparent Conducting Oxides as thin films will be discussed mainly, the most used ones namely, In_2O_3 and ZnO in terms of synthesis, crystal structure, electronic structure and their related properties as well as the possible doping and their applications. The theoretical study of electronic structure of semiconducting thin film materials is one of the most complex calculations in the scientific fields as it requires high performance supercomputing systems, and it involves solving computational chemistry studies which requires quantum chemistry methods. One of the most widely used method is density functional theory (DFT) which is a computational quantum mechanical modelling method. Therefore, computational modelling related studies are of great importance to understand, predict, and design/engineer the electronic structure of semiconducting thin film materials[60, 61]. Furthermore, a literature review of SnO_x (both SnO_2 and SnO) thin films will be presented thoroughly in a main section to cover its related synthesis techniques, crystalline structure, electronic structure as well as its potential doping to improve its optoelectronic performance as well as to convert the conductivity from p-type to n-type. In the last section of this chapters, metal oxide thin films will be discussed as an electron transport layer (ETL) for perovskite solar cells (PSC).

1.1.3. Indium Oxide

Indium oxide is a wide bandgap TCO material which was and is still heavily investigated and employed in many applications. It has very appealing optical and electrical properties as an intrinsic material as well as a doped material. It is worth noting again that the most widely used TCO material is ITO is basically an indium oxide material doped with Sn [1-12, 23-29, 31, 45-50]. There many applications for In_2O_3 based materials namely, solar cells, light emitting diodes, thin film transistors [54, 62-68]. It can be prepared as single crystal or polycrystalline thin film. In addition to ITO, there are many ternary compound semiconductors based on In_2O_3 namely, $Zn_2In_2O_5$, $Zn_3In_2O_6$, $In_4Sn_3O_{12}$, In-Sn-Zn-O as well as Zn doped Indium oxide as shown in Figure 1[24, 53].

a) Growth and structural properties

There are many synthesis techniques to grow In_2O_3 thin films which are physical deposition techniques namely, Magnetron Sputtering[54, 69], E-beam Evaporation[70], Pulsed Laser Deposition[71, 72], and Molecular Beam Epitaxy[73] as well as chemical deposition techniques namely, Atomic Layer Deposition (ALD)[74-76], Spin Coating[77], Spray Pyrolysis[78], Inkjet Printing[79, 80] and Metal Organic Chemical Vapour Deposition[81, 82].

Figure 2 is showing the widely known crystal structure of In_2O_3 which is Body-Centred Cubic denoted as bcc-In_2O_3 where the space group is $Ia\overline{3}$ (#206) and the lattice parameter a = 10.118 Å. This crystal structure can be regarded as a bixbyite structure or as a C-type rare-earth sesquioxide structure. As mentioned previously, In atoms have six coordinate to oxygen atoms where they form a corner sharing octahedra [54, 57]. There is another known phase of In_2O_3 has a rhombohedral structure denoted rh-In_2O_3 where the space group is $R\overline{3}c$ (#167) and the lattice constants are a = 5.478 Å and c = 14.51 Å[83]. Rh-In_2O_3 phase is stabilized under specific conditions particularly, high pressure condition as reported by Zhang et al[84]. While bcc-In_2O_3 phase has been extensively investigated, there is only a limited literature about the rh-In_2O_3 phase which is due mostly to the difficult synthesis conditions [83, 85].

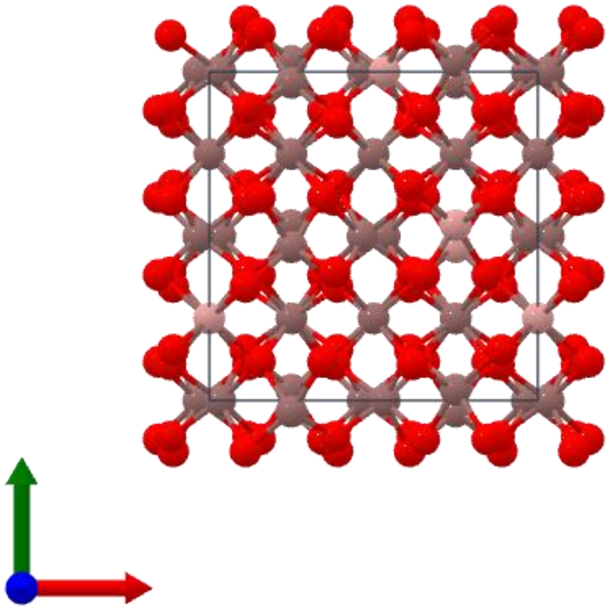

Figure 2: Crystal structure of Body-Centred Cubic In_2O_3. Reprinted (adapted) from The Materials Project [57]. License: CC BY 4.0.

b) Electronic structure

In this section, the electronic properties of In_2O_3 will be focused on the most stable and reported phase bcc-In_2O_3. Indium metal atom electron orbitals are [Kr] $4d^{10}5s^25p^1$ where the valence electrons are $5s^2$ and $5p^1$ as shown in Table 2, while oxygen atom electron orbitals are [He] $2s^22p^4$. As shown in the band structure (Figure 3(a)), the lowest conduction band is at Γ point. On the other hand, the valence band maximum is on Γ-H line while close to the Γ point. Therefore, In_2O_3 is an indirect bandgap semiconductor due to the fact that the minimum CB and the maximum VB are not on the same crystal momentum which is defined by the associate wave vector k[57]. The band structure is quite complex which is due to the different atomic orbitals' hybridization. As per the partial Density of State in figure 3(b), O 2p has the main contribution to the upper part of the valence band. However, there is also an influence on the upper part of the VB by hybridization with In 4d states. In 5s states contribute primarily to the minimum of the CB, In 5p states also contributes while increasing the k vector.

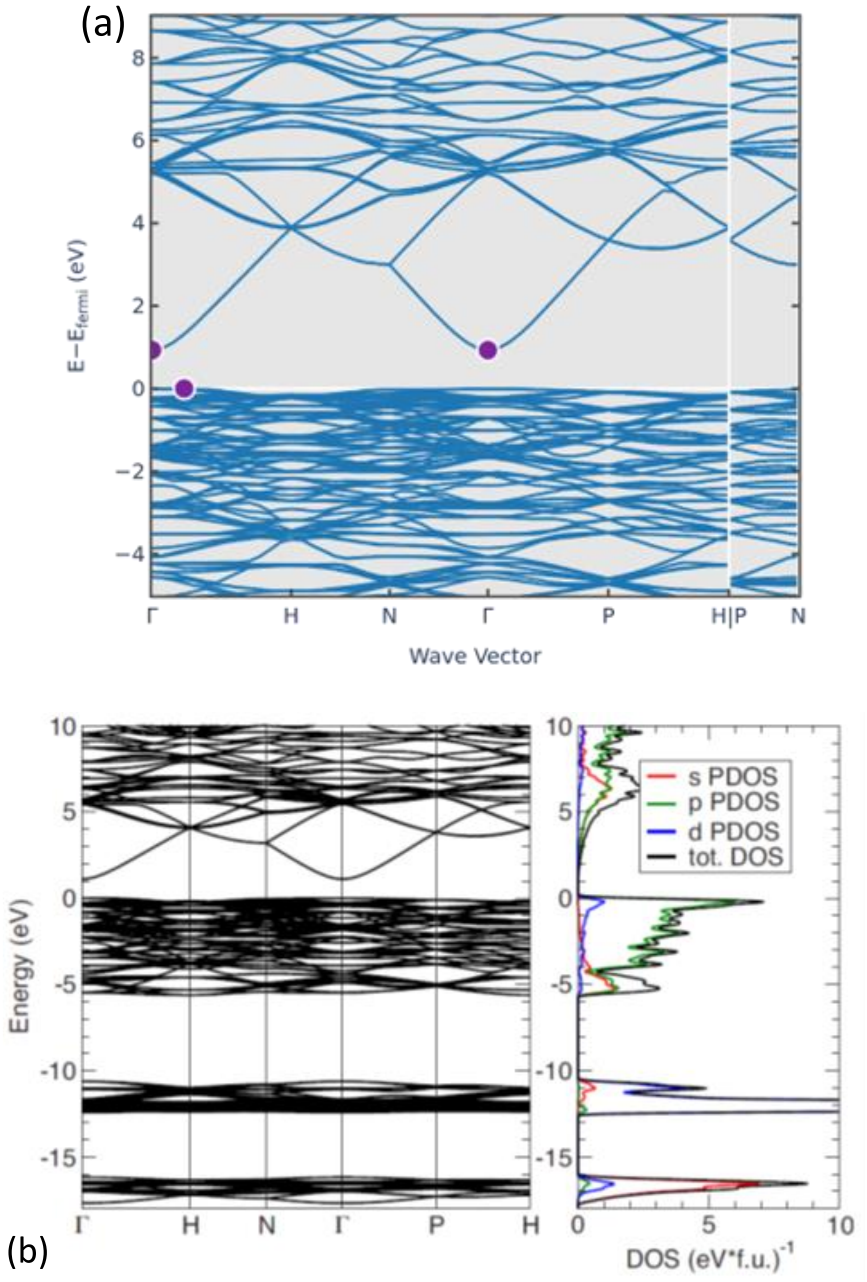

Figure 3: (a) Band structure, density of states (DOS), (b) partial DOS for bcc-In_2O_3. Calculations were performed within DFT-LDA. (a) Reprinted (adapted) from The Materials Project [57]. License: CC BY 4.0. (b) Reprinted (adapted) with permission from [86]. Copyright 2008 American Physical Society.

c) Doped Indium Oxide

It is widely reported that unintentional and/or self-doped indium oxide thin films as well as bulk crystals exhibit a moderate conductivity with n-type charge carrier concentration generally between 10^{17} and 10^{19} cm^{-3}. The origin of this significantly high charge carrier concentration, for a wide bandgap semiconducting material, is related to many point defects and unintentional doping by impurities as reported by Bierwagen. The main point defects are related to oxygen vacancies (V_o) which are established experimentally as a shallow donor. Hydrogen atoms, which tend to form interstitial defects, are also another source of shallow donors for indium oxide. This has been demonstrated both theoretically as well as experimentally [87, 88].

Although the previously mentioned unintentional and self-doping for indium oxide enable forming n-type charge carriers, the best electrical performance for indium-based materials can be achieved by a controlled doping process where the charge carrier concentration can increase drastically through various dopant, including Sn, Zr, Ti, Mo, W and F, to be used as substitutes. The doping using tin element has been the most successful and it is used widely in various industrial applications as it provides the highest electrical conductivity as well as providing a very good optical transparency. The stability of the heavily Sn-doped In_2O_3, widely known as ITO, is due to the high solubility of Sn in indium oxide which is up to about 6% atomic. These doping elements provides shallow donors within the In_2O_3 bandgap which are very close to the conductive band minimum. ITO can reach to a high charge carrier concentration of 6×10^{21} cm^{-3} and resistivities under the 10^{-4} $\Omega \cdot cm$. The high doping of Sn in In_2O_3 can enable the Fermi level to be in the conductive band. Even though, p-type doping is theoretically possible through elements from group - II, particularly Ca, Mg and Zn. Nevertheless, the p-type conductivity is still not experimentally established as the negative formation energy which compensate the V_o donors takes place and tend to drive the Fermi level above the valence band maximum [88-90].

1.1.4. Zinc Oxide

Zinc oxide is also one of the wide and direct bandgap TCO materials which has been heavily investigated and employed in many applications. It has some appealing material properties. It is known to have similar properties compared GaN[91]. It is worth to note that ZnO TCO material is not suitable to generate p-type charge carriers due to the presence of O 2p orbitals on the top of the valence band. There are many applications for ZnO based materials namely, solar cells including Perovskite Solar Cells (PSC), CuInGaSSe (CIGS) Solar cells, Organic Solar Cells and Dye Sensitized Solar Cells (DSSC) [14, 15, 92-99], light emitting diodes[100-103], gas sensors[104], thin film transistors[105]. ZnO material exhibits a great material stability. There are many ternary compound semiconductors based on ZnO namely, $Zn_2In_2O_5$, $Zn_3In_2O_6$, In-Sn-Zn-O[24] as well as Zn doped Indium oxide as shown in Figure 1.

a) Growth and structural properties

ZnO thin films can be grown using different synthesis techniques namely, magnetron sputtering[106], Chemical Vapour Deposition[107, 108] which can provide an average crystalline quality. Advanced techniques such as Molecular Beam Epitaxy[109, 110], Pulsed Laser Deposition[111] and Metal Organic Chemical Vapour Deposition[112] can provide much better crystalline quality due to higher quality of the used materials/precursors as well as the advanced control of the growth conditions.

Zinc oxide has three known crystal structures namely, hexagonal wurtzite, cubic zincblende and Rocksalt. The hexagonal wurtzite phase, which is shown in Figure 4, is the most stable thermodynamically. Zinc blende thin film is normally formed while grown on a cubic structure substrate. However, the Rocksalt phase formation requires a very high-pressure condition. The wurtzite phase has four atoms per unit cell[113], its space group is $P6_3mc$ (#186) and the lattice parameters reported experimentally using XRD are a = 3.2475 Å and c = 5.2075 Å[114]. The theoretical lattice parameters using ab initio calculations are a = 3.286 Å and c = 5.241 Å[115]. The zincblende phase has cubic crystal structure and its space group is $F\bar{4}3m$ (#216). The experimental lattice parameter is 4.463 Å determined by XRD and TEM[116] and the theoretical lattice parameters were found to be slightly higher than the experimental values. The Rocksalt phase has a cubic structure, its group space is $Fm\bar{3}m$ (#225) and the lattice parameter reported experimentally is a = 4.271 Å. The theoretical calculated lattice parameter is a = 4.30 Å[113, 117, 118].

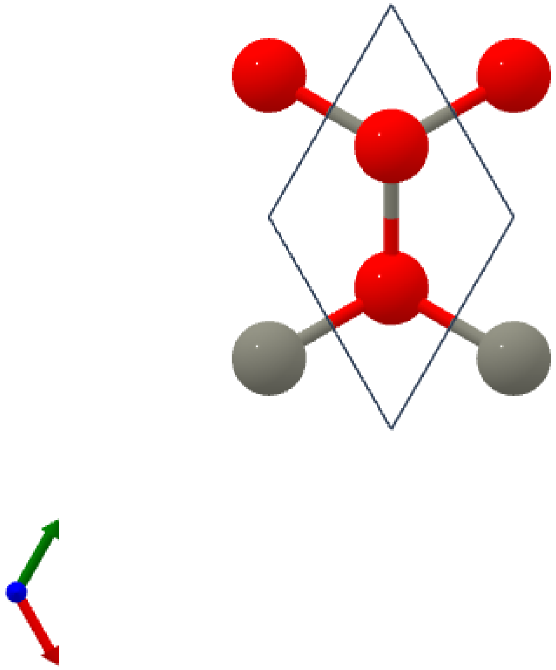

Figure 4: Crystal structure of Wurtzite ZnO. Reprinted (adapted) from The Materials Project [58]. License: CC BY 4.0.

b) Electronic structure

In this section, the electronic properties of ZnO will be focused on the most stable and reported phase which is hexagonal wurtzite. Zinc metal atom electron orbitals are [Ar] $3d^{10}4s^2$ and valence electron $4s^2$ as shown in Table 2, while oxygen atom electron orbitals are [He] $2s^22p^4$. A shown in the band structure (Figure 5(a)), similarly to In_2O_3, the lowest conduction band is at Γ point. However, the valence band maximum is on the symmetric Γ point. Therefore, ZnO is a direct bandgap semiconductor where both the minimum CB and the maximum VB are on the same crystal momentum which is defined by the associate wave vector k[58]. As per the partial Density of State in Figure 5(b), oxygen related 2p and 2s states as well as zinc related 3d states have the main contribution to the valence band. However, the upper part of the VB is mainly formed by O 2p states. The minimum of the conductive band is mainly formed by both O 2p and Zn 4s states.

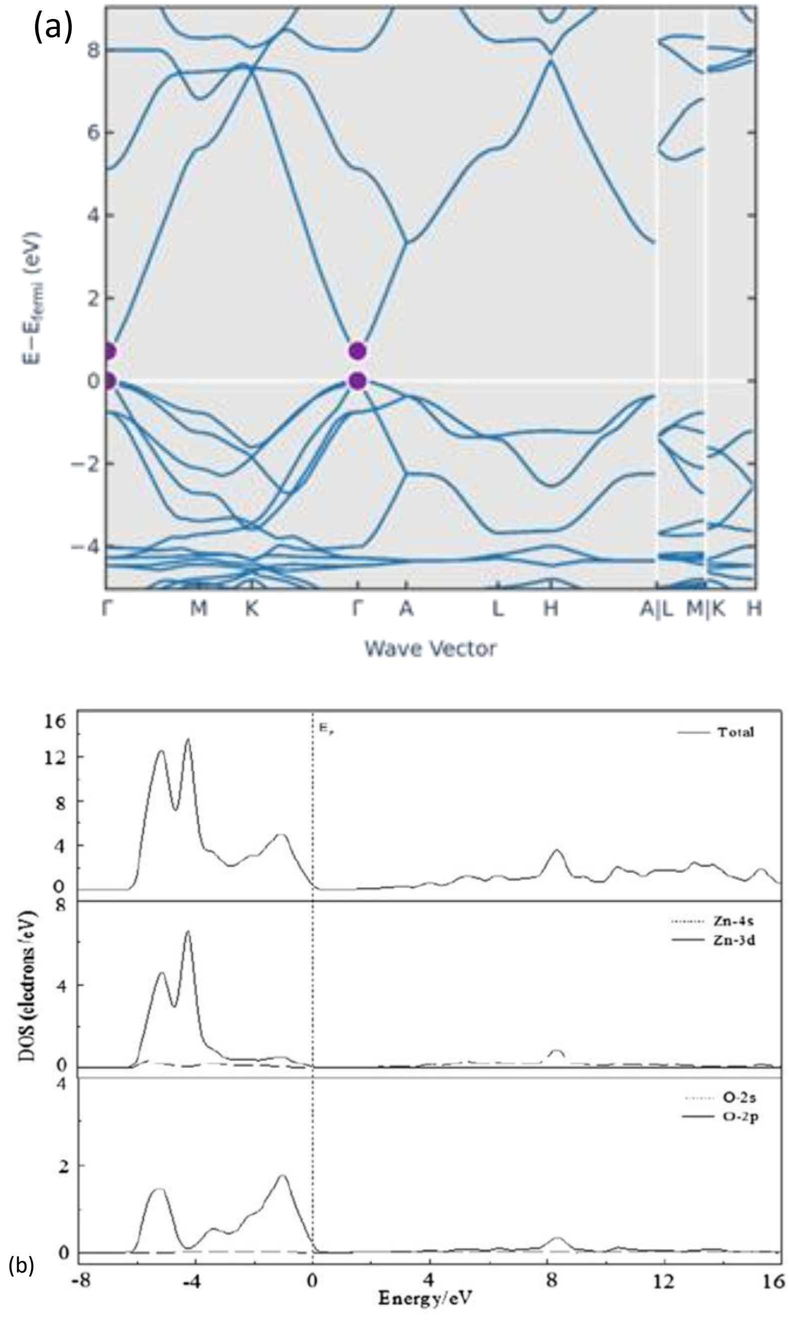

Figure 5: (a) Band structure, (b) density of states (DOS), and partial DOS for ZnO. Calculations were performed within DFT-LDA. (a) Reprinted (adapted) from The Materials Project [58]. License: CC BY 4.0. (b) Reprinted (adapted) with permission from [119]. Copyright 2012 Elsevier.

c) Doped Zinc Oxide

Zinc oxide is also widely reported to be an intrinsic n-type conductive and its charge carrier concentration, as a result of the unintentional and self doping, can reach up to 10^{19} cm^{-3}. These n-type charge carriers are present due to the formation of shallow donors. It is widely known that oxygen vacancies (V_o) mainly and zinc interstitial (Zn_i) are the source of these shallow donors[88, 120]. Nevertheless, there is still a debate around this as it is reported that the donor level formed by the oxygen vacancies is around 1 eV lower than the conductive band minimum (CBM) which is a relatively deep level. Others reported that Hydrogen impurity is the main reason for the n-type conductivity. Janotti and co-authors have reported that hydrogen is likely to form shallow donors due to its interstitial defects and/or by oxygen sites substitution[121, 122].

Even though the shallow donors formed by the presence of oxygen vacancies as well as hydrogen impurities, the n-type doping through elements, mainly group-III atoms, is highly required to assure the higher electrical performance of zinc oxide. Elements like Al, Ga and In are reported to be used as dopants to substitute Zn sites and form n-type charge carriers. Their respective donor energy levels are positioned at 51.55, 54.6, 63.2 meV from their recombination of excitons bounds which are slightly higher than the donor energy level formed by hydrogen of 46.1 meV[123]. However, the impurity band can be formed due to the heavy doping of group-III atoms which will tend to get closer to the valence band and reduce the donors' energy level. Therefore, a charge carrier concentration of 10^{21} cm^{-3} can be achieved, and the conductivity can be enhanced substantially. Zinc oxide doped with aluminium, which is widely known as AZO, was investigated extensively as a low-cost material in order to replace ITO. It has reached the acceptable performance to be used in many applications such as light emitting diodes and solar cells. Its electrical performance could reach as low as 3×10^{-4} Ω·cm as resistivity while the mobility is 20 cm^2/V·s. This best resistivity of AZO is slightly higher than the one achieved by ITO which is due to the lower mobility in AZO compared to the one in ITO[124].

1.2. Tin Oxide thin film as Transparent Conducting Oxide

Tin oxide based TCO materials have been widely investigated in different research fields, particularly in the optoelectronic ones in the last several decades. Generally, tin oxide (SnO_x) thin films, as one the metal oxide materials, are very appealing materials due to their wide bandgap from 3.3 to 4.3 eV and possibility to achieve a very low and competitive resistivity in the order of the low 10^{-4} Ω·cm. Furthermore, tin oxide is earth-abundant and non-toxic material which makes it very suitable for several applications. Tin as raw material has a much lower cost of 27.5 USD/kg compared to indium (210.6 USD/kg) which makes it very appealing for industrial application. In general tin-based materials are important materials to be applied for any global large scale terawatt solar energy supply. SnO_x has been employed in various applied fields as devices such as gas sensors, photocatalyst for water treatment, large area electronics such as flat panel displays, thin film transistors, solar cells including perovskite solar cells, light emitting diodes, transparent electrodes, anode materials, coatings, catalysis[12, 53, 88, 125-141].

Sensors related-industry demand is increasing for affordable, thermal and mechanical stable, abundant sensing materials. SnO_2 is one of the most used materials for sensing thanks to its appealing properties[142]. Undoped SnO_x as a gas sensor was reported by Martín et al.[143] to detect NO_2 with a limit of detection varying from 0.01 to 0.25 ppm and to detect CO with a limit of detection from 1 to 20 ppm. While Lei Li and co-workers have reported SnO_2 with reduced Graphene Oxide (rGO) based sensor to detect NO_2 with a detection limit down to 1 ppb[144]. There are other reports which reveal the employment of SnO_2 based materials to detect CH_4 and H_2[142, 145, 146]. Photoelectrochemical water splitting is another application for SnO_2 based materials. Li et al. have reported F-doped SnO_2 nano-cone as a light harvesting electrode[147]. Hernández and co-workers have also reported a transparent, conductive and porous F-doped SnO_2 coating for quartz sheets as an electrode for photoelectrochemical water splitting[148]. The increasingly growing optoelectronic industry leads to a high demand on semiconductors with high performance features including high carrier mobility, high optical transmittance, and its potential mechanical flexibility. Tin oxide can fulfil these criteria, as well as it has the advantage of abundant material, mechanical and chemical stability. In addition, it has a moderate temperature processing range compared to Si and other metal oxides. SnO_2 based thin film transistors (TFT), including its composite based TFT, have reached the maturity to be incorporated in the display device industry[149].

Tin oxide-based materials were explored in various application related to solar cells particularly for Perovskite Solar Cells (PSCs). This latter will be discussed in detail later in this chapter. Research efforts in thin film solar cells have explored tin oxide-based materials for the implementation of tin oxide thin film solar cells. Thomere et al. have reported fluorine-doped tin oxide as a transparent back contact for thin film solar cells of $CuGaSe_2$ absorber via two-step process and achieved the Power Conversion Efficiency (PCE) of 5.4%. It is worth noting that the relatively higher bandgap of the $CuGaSe_2$ (pure Ga) of 1.68 eV provides an appealing absorber for a tandem solar cell [150, 151]. Jiashuai Li et al. have reported Mg-doped SnO_2 as a buffer layer for Sb_2S_3-based solar cells and the best cell has reached 6.3% of PCE[152]. Jian-Min Wu and co-workers have reported a thin film GeSe-based solar cell using SnO_2 as a buffer layer with PCE of 0.51%. it was found that SnO_2 is suitable for the band alignment of this cell[153]. Ismael et al. have explored a heterojunction solar cell of Pd-doped SnO_2/porous Si/c-Si and have achieved a PCE higher than 14%[154]. It is worth noting that Indium Tin Oxide (ITO) material is widely explored in different solar cells, namely organic solar cells, polymer solar cells, dye synthetized solar cells, silicon based solar cells including polycrystalline, monocrystalline, amorphous, mono-like, and heterojunction solar cells[16, 18, 155-188].

Sn oxide-based materials has been widely investigated in Light Emitting Diodes (LEDs) to improve the device performance. Zinc doped tin oxide can improve light extraction to its high optical transmittance.

The external quantum efficiency is also a key aspect to improve the performance of the LEDs. Tin oxide based-material was also explored as a potential anode material for large area and flexible Organic Light Emitting Diodes (OLEDs). Esro and co-workers have established that Sb-doped SnO_2 at Wt.2% has provided the lowest sheet resistance and highest carrier mobility. Lee et al. have explored tin oxide nanoparticles as an interface layer sandwiched by both ITO cathode and ETL for OLED device. It was found that the incorporation of this interface layer improves the band alignment of layers and improve the electron injection in the OLED device [189-191].

There are many other applications for tin oxide-based materials where its properties were suitable to achieve the required functionalities, coating is among these other applications. Park et al. have reported a fluorine-doped tin oxide as a coating layer of stainless steel 316 plates for development of both corrosion and low contact resistant for polymer electrolyte membrane fuel cells[192]. Catalysis is another field were tin oxide-based materials are applied. Cheng et al. have reported the synthesis of a P-modified Sn/SnO_x as core/shell structure catalyst for electrochemical CO_2 reduction reaction[193].

Tin oxide can crystalize in two stoichiometric phases, namely SnO and SnO_2 which are known to be wide band gap oxide semiconductors with tetragonal litharge and rutile type structures, respectively. Tin, as an oxide, has two chemical states of Sn^{2+} for SnO phase and Sn^{4+} for the SnO_2 one. The first is known to be intrinsically p-type semiconductor while the second is n-type. SnO_2 material, which is known as tin (IV) dioxide or stannic oxide, is one of the widely known as wide bandgap TCO materials, while SnO is known as tin (II) oxide or stannous oxide[88, 127].

1.2.1. Tin(IV) oxide (SnO_2) thin film

a) Thin film growth

There are various techniques to grow SnO_2 thin film and these techniques can be categorized as physical deposition or chemical deposition. The widely used physical deposition techniques are Pulsed Laser Deposition[194, 195], E-beam Evaporator[22, 196], RF sputtering[197-202], Molecular Beam Epitaxy[203-205]. The chemical deposition techniques are Metal Organic Chemical Vapour Deposition[206, 207], Atmospheric Pressure Chemical Vapour Deposition[208], Atomic Layer Deposition[209], Sol-Gel process[210], Spin Coating[211], and Spray Pyrolysis[212, 213]. Many of the described depositions techniques above are Gaseous state – deposition techniques. Within this class, there are mainly two distinct thin film deposition process categories which are chemical vapour deposition (CVD) and physical vapour deposition (PVD). The basic principle of CVD relies on the precursor vapour which is a used for chemical reaction(s) taking place at the substrate. While PVD's basic principle relies on the condensation at the substrate of the vapour made from atoms and/or molecules. Both CVD and PVD processes form thin films onto the substrate. The other class of deposition techniques is Solution state – deposition techniques. This class includes spin coating, sol-gel, spray pyrolysis. Among all these techniques, sputtering technique is the most important technique due to its appealing features including the non-thermal ion impact induced vaporization due to the collision between the atoms at the surface of the target. The high deposition rate, the reduced space between the target and the substrate, and the high purity and vacuum deposition are interesting advantages. Furthermore, its main advantage compared to other PVD techniques is the superior adhesion and possibility to achieve uniform and higher thickness thin films. Sputtering has benefited from the technological advancements in the last decades which made it highly efficient and reliable in terms of real-time control, pumping, plasma, and automation systems. Sputtering is already used in many industrial applications, such as coatings, solar cells, and microelectronics. For metal oxides, reactive sputtering or sputtering in reactive mode is an attractive technique due to its intrinsic features of sputtering in addition to the oxygen reactive gas which allows the control of the level of the oxidation and consequentially tuning the optical and electrical properties of the thin film. Substrate temperature and O_2 partial pressure/flow rate parameters are of great importance for reactive sputtering to form metal oxides. These two parameters can have an impact on both crystalline properties and oxygen vacancies within the thin film[214-218].

b) Structural properties of SnO_2

Tin(IV) oxide or stannic oxide (SnO_2) exists naturally on earth and in mineralogy it is known as Cassiterite which is the main ore, or in other words, the main source of tin metal. It has the rutile crystal structure where the unit cell is tetragonal $P4_2/mnm$. The lattice constants are around a = b = 4.74 Å and c = 3.19 Å. There are other oxides, metal dioxides, which have also this type of crystal structure such as MnO_2, TiO_2, GeO_2, VO_2, CrO_2, and TeO_2. This crystal structure is the main structure for SnO_2 as it is very stable at ambient temperature and under atmospheric pressure. The crystal lattice where Sn has a six-fold coordination to the three-fold oxygen atom coordination is illustrated in Figure 6. The lattice positions can be represented by:

$$\mathbf{Sn : 2(a)\ 000;\ \tfrac{1}{2}\tfrac{1}{2}\tfrac{1}{2}}$$

$$\mathbf{O : 4(f) \pm (uu0;\ u + \tfrac{1}{2},\ \tfrac{1}{2} - u,\ \tfrac{1}{2})}$$

Where u is the variable parameter around 0.307 for SnO_2. Each octahedra of oxygen is attached to two adjacent ones via edge sharing in the c-axis, while it is attached to the other octahedra via corner sharing. Furthermore, there are other polymorphs of SnO_2 which were demonstrated theoretically and/or experimentally by transiting from rutile SnO_2 at a very high pressure in the order of tens of GPa, namely $CaCl_2$-type SnO_2 phase with an orthorhombic structure - Pnnm (#58) and lattice constants around a = 4.68 Å, b = 4.63 Å and c = 3.16 Å as well as α-PbO_2-type SnO_2 phase with also an orthorhombic structure - Pbcn (#60) and lattice constants around a = 4.707 Å, b = 4.710 Å and c = 5.246 Å. Furthermore, Pyrite-type SnO_2 phase has also been reported with cubic structure - Pa$\overline{3}$ (#205) and lattice constant of a = 4.888 Å and a = 5.066 Å. However, there is a significant gap between the theoretical and experimental data for pyrite-type SnO_2 [36, 219].

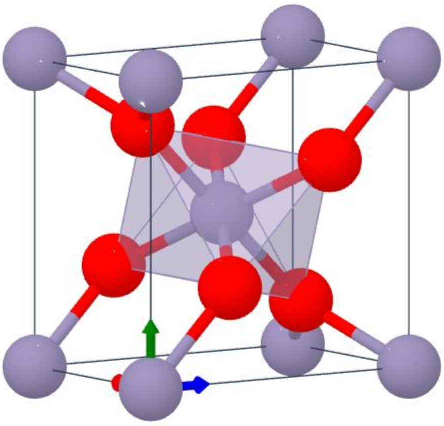

Figure 6: Crystal structure of rutile structure SnO_2. Tin atoms in purple and oxygen atoms in red. Reprinted (adapted) from The Materials Project [56]. License: CC BY 4.0.

c) Electronic structure of SnO_2

Tin(IV) oxide of rutile structure is established to be a direct wide bandgap semiconductor with a bandgap of 3.7 eV at the point Γ in the Brillouin-zone. Like In_2O_3 and ZnO which were discussed in previous sections, SnO_2 has a complex band structure as it has many valence electrons in each unit cell. In the Brillouin-zone, the band structure of SnO_2 show a high degree of symmetry. Figure 7 reveals that the conduction band in both Γ-X and Γ-M directions shows a free electron-like feature. Moreover, the minimum gap between the conduction and valence bands was found at Γ point and it is around 3.7 eV. Figure 8 reveals that O(2*s*) and Sn(4*d*) related states induce four narrow and deep bands within the valence bands and due to their dispersion, they are not considered as core states. There are twelve bands, above these narrow and deep bands, which are considered as the valence band. The lower of part of these twelve bands is dominated by hybridized O(2*p*) with Sn(5*s*) states and the upper part of these bands is dominated by O related 2p and Sn related 5*p*-4*d* orbitals. The lower part of the conduction band is dominated by antibonding Sn(5*s*)-O(2*p*) orbital while the upper part is dominated by Sn(5*p*) states [54, 61, 220, 221].

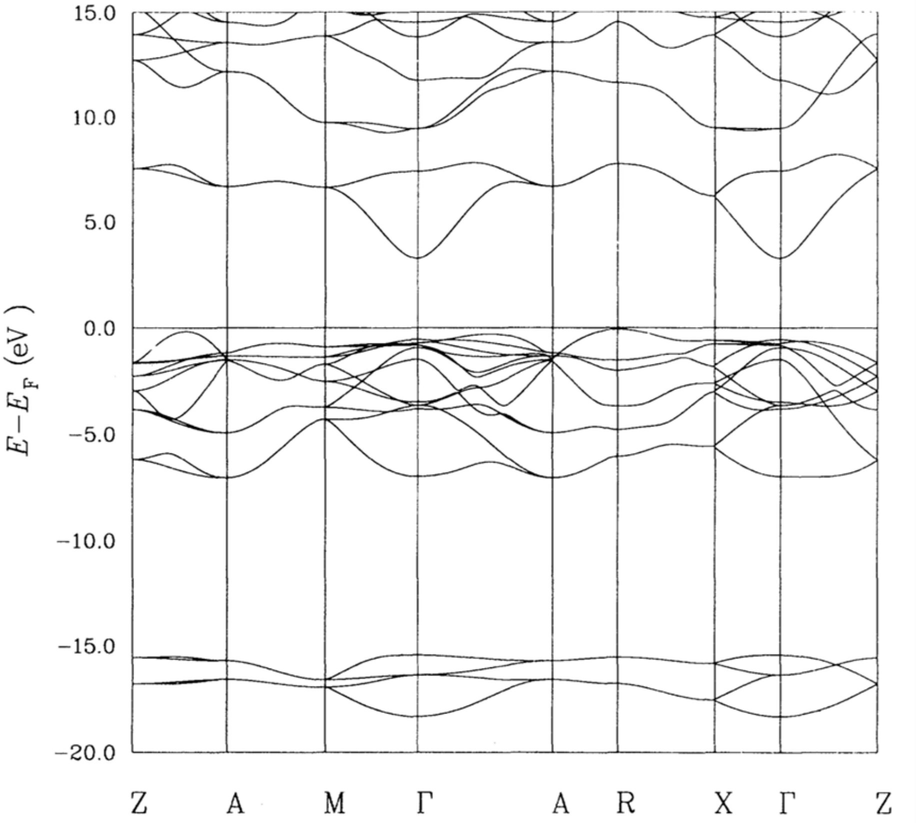

Figure 7: Band structure for rutile SnO$_2$. Reprinted (adapted) with permission from [220]. Copyright 1995 American Physical Society.

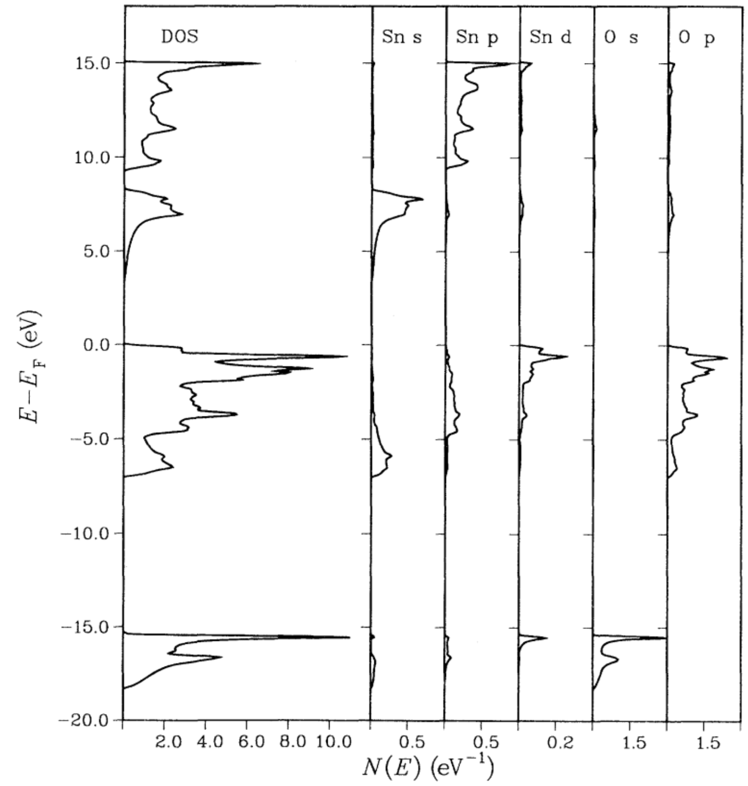

Figure 8: Density of states (DOS) of rutile SnO$_2$ along with the partial density of states (pDOS) related Sn and O. Reprinted (adapted) with permission from [220]. Copyright 1995 American Physical Society.

d) Literature of undoped SnO_2

In the literature, recent undoped SnO_x thin films reports are very limited compared to the reports related to the doped ones. This is mainly due to the attractive properties brought by the doping of SnO_x. In this section, the literature review is focusing only on the undoped tin oxide particularly, the growth conditions and the optoelectronic performance. This performance is assessed by Haacke figure of merit (FoM) equation[301] ($\phi = T^{10}/Rs$), where ϕ is figure of merit in Ω^{-1}, T is the average optical transmittance in %, and Rs is the sheet resistance in $\Omega\cdot\square^{-1}$.

Sivakumar et al. have reported the deposition of tin oxide using sol-gel spin coating technique on glass substrate where they could synthetize a polycrystalline tetragonal rutile SnO_2 with a preferred orientation of (110) and the crystallite size around 56 nm. The achieved optoelectronic properties were a high optical average transmittance greater than 85% and the electrical resistivity was around 3.3×10^{-3} Ω·cm. The optical bandgap established by Tauc plot was 3.94 eV[222]. On the other hand, using PVD technique, Tao et al. have reported SnO_2 films on glass substrate prepared by reactive magnetron sputtering using metallic Sn target while varying the substrate temperature and O_2 flow rate. They found that SnO_2 thin films have an amorphous microstructure if deposited at room temperature regardless the O_2 flow rate. However, the crystallinity improved at higher temperature (150 and 300 °C) even at low O_2 flow rate. It was also reported that the preferred crystalline orientation is also affected by O_2 flow rate. The best conductive sample with resistivity of 3.65×10^{-3} Ω·cm was found to be deposited at room temperature and its average transmittance is 81.5% in the visible range. The authors established that electrical conductivity is controlled by oxygen vacancies[223]. Soumya reported the synthesis of amorphous tin oxide thin film prepared via sol-gel spin coating technique followed by a heating process to remove the solvents at 100 °C. XRD diffraction has not shown any crystalline features which reveals the amorphous microstructure of the tin oxide thin film. The average optical transmittance in the visible region was 85% and the established optical bandgap by Tauc plot method was 3.64 eV. The calculated resistivity was around 0.12 Ω·cm and its FoM at 550 nm was 2.2×10^{-5} Ω^{-1} [224]. Yadava et al. have reported a tin oxide thin film deposition using chemical vapour deposition set-up, namely, reactive thermal evaporation of $SnCl_2$, for conducting electrode application. Structural analyses using XRD have shown that increasing the temperature has improved the crystallinity of SnO_2 and lead to different preferential orientation at each temperature. Optical analyses using UV-Visible spectroscopy (UV-Vis) have shown that the optical transmittance increases as the deposition temperature of the substrate increases from 400 to 550 °C, then this optical transmittance sharply decreases at 600 °C. The lowest electrical resistivity was reported for samples deposited at 500 and 550 °C around 0.05 Ω·cm[225]. Yadav et al. have reported a tin oxide thin film synthesis using reactive thermal evaporation of $SnCl_2$ in air atmosphere on glass substrate as a cost-effective deposition technique for good quality SnO_2. Structural analyses using XRD have shown that absence of diffraction peaks related Sn and SnO phases and that increasing the temperature has improved the crystallinity of SnO_2 and all samples show the presence of polycrystalline cassiterite tetragonal rutile structure. The average crystallite size related to peak SnO_2 (110) ranged from 20 to 32 nm. Optical analyses using UV-Vis has shown that the maximum optical transmittance is around 90% and 85% before and after heating, respectively and the transmittance increase as the temperature of the substrate, while deposition, increases from 250 to 450 °C. The sheet resistance decreases as the deposition temperature of the substrate increases from 250 to 450 °C [226]. Khallaf et al. have reported a deposition of SnO_2 using multi-dip chemical bath deposition followed by post-deposition thermal annealing at 400 °C for 1 hour. Structural analysis by XRD has shown an amorphous structure for the as-deposited tin oxide and a polycrystalline orthorhombic microstructure for the annealed SnO_2. X-ray Photoelectron Spectroscopy (XPS) results have revealed the presence of Sn(IV) and mainly oxide related O which represents SnO_2 phase. The optical bandgap for the annealed SnO_2 was reported around 4.42 eV. The electrical resistivity for the annealed SnO_2 was very high in the order of 10^3 Ω·cm which is due to the low charge carrier concentration in the order of 10^{12} cm^{-3} [227]. An older article (reported in 1981) from Muranaka et al. have described the deposition of SnO_2 by reactive Sn thermal evaporation technique along with O_2 flow. Structural analyses have shown that increasing the temperature and the O_2 pressure have formed and/or improved the crystallinity of the SnO_2. Low O_2 pressure has led to the formation of metallic Sn and SnO phases while low substrate temperature during the growth has led to an amorphous microstructure of tin oxide. Both films deposited at 3×10^{-3} and 5×10^{-3} Torr at 420 °C has reached an optical transmittance around 90% and an electrical resistivity below 5×10^{-2} Ω·cm[228]. Belayachi and co-workers reported the synthesis of polycrystalline cassiterite tetragonal tin oxide thin films on silicon substrate (oriented (100)) prepared by reactive radio-frequency magnetron sputtering at a constant O_2 flow rate and at different substrate temperatures of 100, 200, 300 and 400 °C. The best conductive sample was deposited at 100 °C with an average transmittance around 84%. It was found that the substrate temperature had a slight effect on the optical transmittance and small increase in crystallite size as substrate temperature increases. However, as the substrate temperature increases, the resistivity increases by orders of magnitude from 4.45×10^{-3} Ω·cm at 100 °C to 3.26 Ω·cm at 400 °C. The main reason for the conductivity decrease, as substrate deposition increases, is substantial decrease of mobility, while charge carrier concentration underwent a limited decrease[200].

Overall, there are a few important points to take into consideration. The first is that increasing the temperature of the substrate during the growth improves the crystalline microstructure of tin oxide thin films and the reports have revealed the polycrystalline tetragonal rutile structure of the crystalline tin oxide. Second, most of the reports reveal a relatively high average optical transmittance superior to 80% and an optical bandgap above 3.5 eV. Finally, the best electrical resistivity for these reports is around 10^{-3} Ω·cm.

e) Literature of doped SnO_2 thin film

There is a large amount of literature related to SnO_2 doping as TCO thin films which is oriented towards different applications. This literature review will focus on most of the relevant and reports of SnO_2 doping in the optoelectronic field. This section will be presented in two parts, the first will be tackling the n-type conductive doped SnO_2 thin films literature while the second will focus on the literature reporting the conversion of the n-type conductivity of SnO_2 to the p-type one.

i. N-type doping of SnO_2

As SnO_2 is widely known as an intrinsic n-type semiconducting material, most of the research efforts have been focusing on enhancing the optoelectronic properties of tin oxide by introducing doping elements and sometimes even compounds. It is worth noting that most of the literature about SnO_2 doping resulting an n-type conductivity were reporting material synthesis and deposition via chemical processes. This is mainly due to the ability to add and control doping element which the SnO_2 hosts.

Spray Pyrolysis is one of the most utilized techniques to deposit doped SnO_2 due to its process simplicity, precursor solution formulation versatility, cost-effectiveness, fast process as well as it is thermodynamical predictability[214]. Moholkar et al. have reported the deposition of fluorine doped tin oxide (FTO) thin films by spray pyrolysis on glass substrate at 475 °C using precursor solution $SnCl_4{\cdot}5H_2O$ (from 0.32 to 1.29 M) and ammonium fluoride. All FTO thin films have a polycrystalline microstructure matching with SnO_2 tetragonal structure with a preferential orientation of (200) plane. Sheet resistivity varies from 61.6 to 3.71 $\Omega{\cdot}\square^{-1}$ where the lowest value is reported for $SnCl_4$ concentration of 0.65 M. The optical transmittance at 550 nm was 87%. The best Figure of Merit (FoM), that indicates the optoelectronic performance, was $7.26 \times 10^{-2}\ \Omega^{-1}$ for FTO with $SnCl_4$ concentration of 0.81 M[229]. Singh and Basu have reported synthesis of antimony doped tin oxide (ATO) and fluorine doped tin oxide on glass slides at temperature varying from 400 to 540 °C using a modified spray pyrolysis system by spraying upwards to assure that all droplets are evaporated while reaching the surface of the substrate. The polycrystalline tetragonal Cassiterite microstructure have been determined by XRD related CuK_α diffracted pattern of the FTO films with no specific crystalline preferential orientation. Optical measurements have shown that both ATO and FTO thin films at 100 nm thickness have 95% optical transmittance in the visible region. The determined optical bandgap is 3.9 eV for ATO and 4.1 eV for FTO. Moreover, increasing the thickness has led to a reduction in optical transmittance from 95% at 100 nm to 31% at 510 nm thickness for ATO. However, the thickness effect is relatively smaller for FTO as the optical transmittance is reduced from 95% at 100 nm to 70% at 470 nm. Electrical measurements have revealed that increasing the substrate temperature from 400 to 530 °C for FTO and from 430 to 540 °C for ATO has decreased remarkably the sheet resistance of both FTO and ATO thin films. This study also has established that increasing the thin film thickness has decreased the sheet resistance while varying the thickness from 100 to approximately 600 nm for both ATO and FTO. However, the effect of the thickness is more predominant for ATO compared to FTO. This study has found that the best sheet resistance was recoded at 1.5 wt.% of NH_4F for FTO and at 3 mol % of $SbCl_3$ for ATO. The highest Figure of Merit for FTO is $24.2 \times 10^{-3}\ \Omega^{-1}$ achieved at 190 nm thickness with 1.2 wt.% of NH_4F at the growth where the $R_{sh} = 20\ \Omega\cdot\square^{-1}$ and the optical transmittance at 600 nm is 93%. The highest FoM for ATO is $7 \times 10^{-3}\ \Omega^{-1}$ achieved at 200 nm thickness with $SbCl_3$ at 3 mol%, where the $R_{sh} = 40\ \Omega\cdot\square^{-1}$ and the optical transmittance at 600 nm is 88%. As per these optoelectronic performance results, FTO have shown a better optoelectronic performance compared to ATO[213]. Babar et al. have reported antimony doped tin(IV) oxide thin film on glass substrate at 475 °C using spray pyrolysis deposition technique, Sb doping was established by adding $SbCl_3$ at 2 at.%. This concentration was determined as the optimum for high quality Sb-doped SnO_2 ($Sb:SnO_2$) thin film. The structural properties, assessed by XRD, have determined the polycrystalline tetragonal structure of the $Sb:SnO_2$ thin films without presence of any secondary phases. The optical transmittance at 550 nm was 70% and the electrical resistivity was $8.9 \times 10^{-4}\ \Omega\cdot cm$. The optoelectrical performance of these thin films were assessed via FoM and the best thin film have achieved $2.1 \times 10^{-3}\ \Omega^{-1}$ [230]. Md. Faruk Hossain et al. have assessed the impact of Sb doping on tin oxide and they reported the synthesis $Sb:SnO_2$ on glass substate at 400 °C using nebulized spray pyrolysis via $SnCl_2$ where the doping concentration varies from 0 to 8 mol.% via $SbCl_5$. The crystalline structure of undoped SnO_2 was found to be close to a standard tetragonal rutile SnO_2 structure where the lattice constants "a" and "b" are equal to 4.738 Å and "c" is equal to 3.188 Å. These values were found to be decreasing as the antimony doping increases. The average optical transmittance for the undoped SnO_2 in the visible region was 85% and it slightly decreases as the Sb doping concentration is increasing from 0 to 8%. The optical bandgap is found to be 3.7 eV for undoped SnO_2 while the $Sb:SnO_2$ increases from 3.8 to 3.9 eV as the doping increases from 2 to 8%, respectively. Electrical measurements have revealed that the resistivity decreases for SnO_2 from 16.1×10^{-4} to $6.4 \times 10^{-4}\ \Omega\cdot cm$ as the Sb doping concentration increases from 0 to 8%. This work has highlighted the importance of oxygen vacancies and interstitial Sn in the formation of charge carriers as described in the below Kroger-Vink notation.

$$O^{X}_{O} \rightarrow V^{\bullet\bullet}_{O} + 2e^{-} + \tfrac{1}{2}O_2$$

Where ($V^{\bullet\bullet}_{O}$) is a doubly ionized vacancy site with an oxygen anion leaving the SnO_2 crystal structure and two conduction electrons generated from an occupied oxygen site (O^{X}_{O}). The best optoelectrical performance assessed by FoM is found to be $1.39 \times 10^{-3}\ (\Omega/cm^2)^{-1}$ accomplished in the visible region with 2% antimony doping[231, 232]. Ramarajan et al. have reported $Sb:SnO_2$ thin films by chemical spray pyrolysis and deposited on glass substate at temperatures varying from 360 to 490 °C while keeping the antimony doping at 5 wt.%. The 0.5 M precursor solution is containing $SnCl_2.2H_2O$ and $SbCl_5$

dissolved and diluted in mixture of deionized water and ethylene glycol. ATO samples have exhibited a tetragonal polycrystalline structure without any secondary phases. Optical transmittance for ATO thin films varies from 62% to 89% and optical bandgap slightly varies from 3.73 to 3.81 eV. Electrical measurements have shown that the lowest reported resistivity for ATO thin films was 7.9 x 10^{-4} Ω·cm for ATO thin film deposited at 450 °C. The best FoM for ATO thin films was 1.25 x 10^{-2} Ω^{-1} which was also reported at 450 °C deposition temperature[233]. Ramarajan et al. also reported the deposition of Tantalum doped SnO_2 (Ta:SnO_2) on glass substrate using different doping weight percentage from 0 (undoped SnO_2) to 5 wt.% Ta:SnO_2. The precursor solution is prepared by $SnCl_2.2H_2O$ and $TaCl_5$ dissolved and diluted in mixture of deionized water and ethylene glycol. The substrate temperature was kept at 400 °C during the growth. The microstructure of all samples was found to be a polycrystalline tetragonal crystalline structure without any secondary phases. The optical transmittance at 550 nm varies from 60 to 86% and the highest value was found to be 86% for 4 wt.% Ta:SnO_2. The optical bandgap to slightly varies from 3.95 to 4.01 eV. Electrical measurements have revealed that electrical resistivity ranges from 10^{-2} to 4.36 x 10^{-4} Ω·cm, this lowest resistivity is reported for 4 wt.% Ta:SnO_2. Thus, this sample has the best achieved FoM of 4.73 x 10^{-2} Ω^{-1} [234]. Mrabet et al. have reported the deposition of lanthanum doped tin(IV) oxide (La:SnO_2) thin films on glass substrate via spray pyrolysis at 450 °C where the La doping varies from 0 to 3%. La:SnO_2 have exhibited a polycrystalline tetragonal structure and the preferred orientation for all samples is (110) plane except for La doped SnO_2 at 2% where the preferred orientation is along the (200) plane. For all La:SnO_2 thin films, including the undoped one, the mean optical transmittance is found to be varying between 0.73 and 0.81. The optical bandgap of La:SnO_2 thin films slightly varies from 3.86 to 3.88 eV. Electrical measurements have established that the sheet resistance varies drastically from 358 and 334 $\Omega\cdot\square^{-1}$ for undoped SnO_2 and 1% La:SnO_2, respectively, to 2.1 and 3 $\Omega\cdot\square^{-1}$ for 2% and 3% La:SnO_2, respectively. Therefore, the best optoelectronic performance assessed by FoM is found to be 10.6 x 10^{-2} and 10.7 x 10^{-2} Ω^{-1} for 2% and 3% La:SnO_2, respectively[235].

On the other hand, chemical vapour deposition (CVD) was also reported as a synthesis technique for SnO_2. Vishwakarma et al have reported a TCO of arsenic doped tin oxide deposited on soda glass substrate using CVD through the mixture vapour of $SnCl_2$ using O_2 as a gas carrier and $AsCl_3$ using N_2 as a gas carrier. The best electrical conductivity was reported at arsenic doping of 0.15 wt.% where the electrical resistivity has reached 1.5 x 10^{-4} Ω·cm and this resistivity increase as arsenic concertation decreases towards lower concentration and also as arsenic concentration increases towards higher concentrations. The arsenic doping concentration of 0.15 wt.% is also reported for the best mobility and charge carrier concentration. The best reported figure of merit was 16.5 x 10^{-3} Ω^{-1} observed at 700 nm for SnO_2 deposited at 400 °C [236]. Li et al. have reported ultrasonic-vibration-assisted laser annealed fluorine doped tin oxide (FTO) commercially prepared by CVD where the laser beam central wavelength at 532 nm with 1 kHz repetition rate. XRD results have revealed the polycrystalline tetragonal structure of tin oxide films without presence of any secondary phases and the crystallite size varies between 22 and 30 nm. The thickness of the films ranges from 695 and 725 nm. The average optical transmittance from 400 to 800 nm of FTO ranges from 81 to 85.5% while the sheet resistance varies from 8.8 to 9.4 $\Omega\cdot\square^{-1}$. The optoelectronic performance was assessed by figure of merit (FoM) and the best film has reached FoM of 2.32 x 10^{-2} Ω^{-1} for using 48 kHz vibrational frequency and 300 W vibration power parameters for the annealing[237]. Along with reports related to CVD synthesis, Atmospheric Pressure Chemical Vapour Deposition (APCVD) was also reported as a much more appealing synthesis technique to form SnO_2 based thin films due to its deposition upscaling ability to large area as well as the superior growth rate. For instance, Talaty et al. reported the synthesis and material's characterisation of tin(IV) oxide based thin films on glass substrate via APCVD process. One of the main studies of this report was the growth rate at different temperature. It is established that increasing the substrate temperature increases the growth rate in this technique and the best growth rate was as high as 2300 Å/min at 650 °C which is highly desired growth rates for industrial TCO applications. Structural properties revealed by XRD have found that all samples have a polycrystalline tetragonal structure for both undoped and F-doped SnO_2 (FTO) without any preferred orientation. Furthermore, Scanning Electron Microscopy (SEM) has revealed microstructural features where the SnO_2 related grain size varies for from 50 nm to 500 nm. Optical properties revealed by UV-Visible spectroscopy have shown that the optical transmittance for all samples varies from 76 to 86% from 400 to 800 nm. The fluorine doping for SnO_2 has clearly improved the optical transmittance. Furthermore, the fluorine doping for SnO_2 has also improved the electrical properties as indicated by the decrease in the sheet resistance R_{sh} from 600 to 10 $\Omega\cdot\square^{-1}$. These two improvements in optical and electrical properties have a huge impact in optoelectronic performance of SnO_2 thin film after the fluorine doping as they improved FoM from 0.4 x 10^{-3} to 16.7 x 10^{-3} Ω^{-1}. They found that their FTO sample has reached an optoelectronic performance close to the commercial FTO (American Float Glass, Pilkington NSG TEC Glass TEC 15)[208]. Tran et al. have reported a FTO thin films on glass substrate using a sol-gel dip coating method using a precursor solution made of $SnCl_4.5H_2O$ and SnF_2 (from 0 to 10 mol%) followed by post-annealing process at 500 °C for 2 hours. ATO thin films have all a polycrystalline tetragonal rutile structure. Optical transmittance at 550 nm varies from 91.7 to 89% while increasing SnF_2 concentration from 0 to 10 mol% and the optical bandgap varies between 3.66 to 3.91 eV. Electrical resistivity varies from 7 x 10^{-4} to 29 x 10^{-4} $\Omega\cdot$cm where the lowest resistivity corresponds to ATO made with SnF_2 concentration of 6 mol%. This ATO sample has also the best FoM of 2.43 x 10^{-2} Ω^{-1} [238].

Finally, the best Sb:SnO_2 thin film, as a transparent conducting oxide, was also reported by Fauzia et al. which was deposited by ultrasonic assisted spray pyrolysis on glass substates. The precursor solution was prepared by 1M $SnCl_2.H2O$ with Sb doping using $SbCl_3$ at 2 wt.% and diluted in ethanol. The structural properties revealed by XRD and the crystal structure was found to be tetragonal rutile structure. The average optical transmittance of all thin films was determined to be higher than 80% from 450 to 900 nm and all ATO samples exhibit an optical bandgap of 3.83 eV. In this research work and to the best of our knowledge, the co-authors have reported the lowest recorded electrical resistivity for ATO of 0.58×10^{-4} Ω·cm (5.8×10^{-5} Ω·cm). Thus, the achieved optoelectronic performance by FoM of 47.22×10^{-2} $(\Omega/cm^2)^{-1}$ is found to be the largest compared to the literature[239].

Reports about tin(IV) oxide doping using physical process are relatively limited compared to chemical processes. While it is very straightforward to add doping in solution precursor with every desired concentration, it is fairly more challenging to add doping elements in physical processes as it requires a long optimization process for each desired doping concentration. There is a report from Dian and co-workers about deposition of tellurium doped tin(IV) oxide ($Te:SnO_2$) thin films on glass substrate at 500 °C using pulsed laser deposition (PLD) followed by post-deposition annealing at 500 °C for 30 minutes at atmospheric pressure. All $Te:SnO_2$ thin films have a polycrystalline tetragonal structure matching with the one of SnO_2. However, the crystallinity is more predominant as the O_2 pressure increases from 1 to 150 mTorr during the growth. The post-deposition annealing has improved the crystallinity of $Te:SnO_2$ thin films. The highest optical transmittance of $Te:SnO_2$ thin films is 87% for PO_2 of 100 mTorr and the optical bandgap related to this thin film is 3.5 eV. The lowest resistivity of 4×10^{-2} Ω·cm is recorded for the as-deposited thin film as PO_2 of 100 mTorr. The highest FoM is around 1.2×10^{-5} Ω^{-1} [240].

ii. P-type doping of SnO_2

In the last two decades and upon the major achievement in metal oxide p-type conductivity, there are several reports related to theoretical studies and experimental results, showing the possibility of forming a doped SnO_2 with a p-type conductivity. Among other achievements in p-type metal oxide, this has opened a new horizon for optoelectronic devices where an all-oxide device is possible, if these p-type metal oxides can achieve the required performance for industrial applications. Nevertheless, there is still huge research and development to be done on p-type SnO_2 thin films, as well as most of p-type metal oxides, to reach the standards for such large-scale industrial applications.

To reach p-type there are two ways of doping SnO_2, the first approach is to incorporate metals with lower valence cations such as Al, Ga, and In, to substitute Sn in its SnO_2 lattice site to generate p-type charge carriers. Theoretically, this approach might be a subject to some challenges mainly due to the deep localised defect's state which can lead to pinning the Fermi level above the valence band maximum (VBM) and prevent the formation of p-type doping due to self-compensation. The second approach is to incorporate a higher anion doping element mainly nitrogen due to many advantages including similar electronegativity, ionic radius compared to oxygen. Nitrogen doping can also reduce the oxygen vacancies which are the main donor for electron charge carriers as nitrogen atoms can occupy the oxygen lattice site within the SnO_2 crystal structure. In addition, N2p-O2p hybridisation orbitals, induced by nitrogen doping, is expected to increase the valence band maximum (VBM) position. Therefore, nitrogen doping for SnO_2 is a potential doping to convert the n-type conductivity of SnO_2 to p-type[241].

There are numerous reports about theoretical studies related metallic doping of SnO_2. K. Lai et al. have reported the effect of Al doping on the electronic and optical properties of Al-doped SnO_2 along with the presence and the absence of oxygen vacancies via first-principle calculations. The co-authors have revealed that Al doping enable p-type conductivity while substituting Sn in SnO_2 and the presence of O vacancies can shift the Fermi level closer to conduction band. This can convert the conductivity back to n-type even with presence of Al doping[242]. Furthermore, there are fewer reports about experimental studies of p-type metallic doping for SnO_2. This is mainly due to the difficulty and challenges to achieve a p-type conductivity based SnO_2 via metallic doping. J. Ni et al have reported a transparent and p-type conducting Sb doped SnO_2 (Sb:SnO_2) thin films on quartz glass prepared by RF magnetron sputtering at 200°C using a pre-made target of 20 mol% Sb:SnO_2 followed by thermal annealing at different temperatures ranging 550 to 800°C. Structural properties determined by XRD have revealed that all samples have a rutile polycrystalline structure with fine grains without any secondary phases related to tin oxide or to antimony oxide. Optical measurements determined by UV-Visible spectroscopy have shown that the thermal annealing has improved the optical transmittance on the visible spectrum and that the absorption edge did not change for all samples with or without annealing. The calculated optical bandgap was around 3.6 eV. They reported that 600°C is a critical temperature for conductivity conversion from n-type to p-type, and all samples annealed above 600°C are p-type conductive. However, there is a reverse effect at higher temperatures, particularly at 750°C and above, where the hole related charge carrier concentration decreases to a very low level and eventually the Sb:SnO_2 conductivity switches back to n-type. The highest hole concentration was achieved using the thermal annealing at 700°C for 4 hours. The electrical resistivity has decreased significant after the annealing at 550°C from 9.9×10^{-2} to 2.9×10^{-3} Ω·cm, both are n-type. The electrical resistivity increases drastically at 600°C to 0.28 Ω·cm without a clear conductivity type (n/p). However, it slightly decreases to 0.25 Ω·cm as the annealing temperature increases to 650°C with a clear p-type conductivity. Then, the electrical resistivity decreases 0.17 Ω·cm at 700°C which is the highest p-type conductivity. After that, the electrical resistivity increases 0.15 Ω·cm at 750°C while keeping the p-type character. Finally, the electrical resistivity slightly decreases, and the conductivity is returned to n-type. This conversion from p-type to n-type is due to the decrease of p-type charge carriers at very high temperature. The co-authors have established a pn junction with both p-type and n-type Sb:SnO_2 thin films in a diode structure using the highest p-type charge carrier concentration. The I-V results show that an ohmic contact is achieved as revealed by the linear behaviour[243]. T. Le et al. have reported the synthesis and characterization of Zn-doped SnO_2 ($Zn:SnO_2$) deposited and annealed at different temperatures on quartz glass substrates via direct current (DC) magnetron sputtering. All the $Zn:SnO_2$ thin films have revealed a tetragonal rutile polycrystalline structure except the one deposited at room temperature and the crystallinity increases as a function of deposition temperature. Zn doping has favoured more the orientation towards (101) compared to undoped SnO_2 where the preferred orientation was on (110) plane. The average optical transmittance for $Zn:SnO_2$ thin films whether as-deposited or annealed is 84% which is very appealing for optoelectronic applications as TCO. The electrical resistivity has increased from 0.2 to 14.7 Ω·cm as the deposition temperature of $Zn:SnO_2$ increases from room temperature to 300°C. However, the resistivity decreases at higher temperatures from 14.7 to 4 Ω·cm as the deposition temperature increases from 300°C to 500°C and more importantly the conductivity has been converted from n-type to p-type at temperatures of 400°C and 500°C. It is worth noting that the thermal annealing has kept the p-type conductivity while significantly reducing the resistivity as well as that longer post-deposition annealing time increases the resistivity of the $Zn:SnO_2$ thin films. In order to confirm the p-type conductivity of $Zn:SnO_2$ thin films, a pn junction was made by $Zn:SnO_2$ on an n-type Si wafer using In as contact electrodes. I-V characteristics have confirmed the p-type character of $Zn:SnO_2$ thin film by showing an Ωic contact behaviour[244]. C.Y. Tsay et al. have also reported a p-type SnO_2 achieved by Ga doping ranging from [Ga]/[Sn]+[Ga] 0 to 20%. The Ga-doped SnO_2 ($Ga:SnO_2$) thin films have been prepared using sol-gel spin coating followed first by drying and then by thermal annealing at 520°C for 1 hour under oxygen atmosphere. The crystalline structure of $Ga:SnO_2$ is found to be polycrystalline tetragonal structure closely matching with SnO_2 rutile structure and the crystallite size decreases as the Ga doping increases. The average optical transmittance from 400 to 800 nm and is relatively high for all samples without a clear trend and it is slightly varying between 87.4% and 89.5%. The optical bandgap is also slightly varying between 3.83 eV and 3.92 eV without a clear trend. The electrical conductivity was found to be n-type for undoped and 5% $Ga:SnO_2$ and it is p-type for SnO_2 with higher Ga doping. The electrical resistivity is 0.8 Ω·cm and it slightly decreases to around 0.9 Ω·cm for Ga doping from 0 to 5% which is expected due to the charge compensation by the generated acceptors. This is clearly observed by the reduction of n-type charge carrier concentration. For 10% $Ga:SnO_2$ thin film, the electrical resistivity decreases slightly to 0.8 Ω·cm, and the conductivity becomes p-type with a relatively low charge carrier concentration. As the Ga doping for SnO_2 increases to 15%, the electrical resistivity increases as well as the p-type charge carrier concentration increases which is due to the decrease in mobility. Finally, the electrical resistivity increases significantly for 20% $Ga:SnO_2$ and the p-type charge carrier concentration decreases. It is worth noting that this decrease in p-type charge carrier concentration at high doping levels is related to the reverse effect which has been reported previously with different doping elements and it is reported previously in this section. The co-authors have confirmed the p-type conductivity of Ga:SnO_2 by achieving a pn junction made by p-type 15% Ga:SnO_2 and n-type Al:ZnO on glass substrate using In as contract electrode. P-type conductivity of Ga:SnO_2 has been confirmed by the Ωic contact behaviour in I-V characteristics[245].

On the other hand, there are several reports about nitrogen doping for SnO_2. A theoretical study by E. Albanese and co-authors have discussed the possible N doping in SnO_2. They reported possible N doping within SnO_2 whether the substitutional doping or interstitial doping, Figure 9 shows these possibilities using realistic models. This study also highlighted the effect of nitrogen doping on the electronic structure[246]. K. Watanabe et al have reported nitrogen doped SnO_2 via two steps where the first step is the deposition of SnO_2 through reactive radiofrequency (RF) magnetron sputtering under O_2/Ar (0.1) on Si wafer with SiO_2 surface, and the second step is the thermal annealing using rapid thermal process at different temperature ranging from 150 to 600°C under N_2 for 30 minutes. It was found that SnO_x annealed at 600°C have been crystallised to rutile structure from the amorphous as-deposited SnO_x and the conductivity type conversion from n-type to p-type was only enabled after post-deposition annealing at 600°C in high purity N_2 atmosphere. These results indicate that p-type SnO_2 thin film was achieved through nitrogen doping by filling oxygen lattice sites of the existing oxygen vacancies with nitrogen atoms[247]. Pan et al. have reported the synthesis of nitrogen doped SnO_2 using one step process and via reactive RF magnetron sputtering at 400°C with a mixture of O_2/N_2 atmosphere. All samples have a typical pure cassiterite phase without any secondary phases namely metallic tin, tin nitride, or tin(II) oxide. Hall effect measurements have shown that SnO_2 without N doping have a mobility between 0.21 and 6.9 $cm^2/V \cdot s$ and charge carrier concentration between 10^{18} and 10^{19} cm^{-3}. By introducing a low N_2 partial pressure (PP), the nitrogen doping was not enough to neutralize n-type charge carriers, electrons, formed by the intrinsic defects of SnO_2. Therefore, it has kept the n-type conductivity character. By introducing a higher N_2 PP, the nitrogen doping has increased and formed more, acceptors charge carrier, holes which led to conductivity type conversion from n-type to p-type. Introducing a high N_2 PP, the nitrogen doping was relatively high in SnO_2 which resulted in further decrease in resistivity, and it kept the n-type conductivity. This high N_2 PP had a reverse effect. This might be due to the formation of intrinsic compensating donors which became comparable to the generated acceptors at high level doping. In this letter, the authors have demonstrated a process toward achieving atomic nitrogen doping in SnO_2 under nitrogen different partial pressure toward achieving p-type SnO_2 films conductivity[248]. Y. Kim et al. have described his work on N-doped SnO_2 synthesis by reactive RF sputtering at 100°C and characterization on borosilicate glass substrate to probe effect of N-doping on material properties of N:SnO_2, particularly, on the electrical conductivity. The nitrogen doping was controlled by varying the N_2 flow rate during the growth from 0% for undoped SnO_2 to 40% while O_2 was fixed at 15% and the balance was Ar flow rate. XRD results show that there is no peaks related to Sn, Sn nitrides or any secondary phases which indicates nitrogen has been incorporated successfully within SnO_2 and (101) peak slightly shifted to a lower angle. This indicates that the d-spacing/interplanar spacing has slightly increases from 2.643 Å to 2.658 Å due to nitrogen doping. N-doping has improved the crystallinity of the host SnO_2. The co-authors reported that nitrogen doping has reduced the conductivity of SnO_2 which is due to the reduction in O vacancies and possible self-compensation effect by the formation of low acceptor carrier concentration. Therefore, p-type conversion was not possible[249]. X. Ding et al. have reported the electrical and optical properties of undoped SnO_2 and N-doped SnO_2 thin film deposited via reactive magnetron sputtering at 400°C. SnO_2 was deposited under a mixture of O_2/Ar of gas flow while N-doped SnO_2 was deposited under O_2/N_2. Tuning the O_2 PP as well as N_2 PP, has enabled to investigate the effect of N doping on the structural, optical and electrical properties N-doped SnO_2. Microstructure was revealed using SEM imaging and it clearly showed the presence of cracks between the SnO_x grains. These cracks became larger for N-doped SnO_2 compared to undoped SnO_2. XRD results have found that all samples have a polycrystalline rutile structure and all N-doped SnO_2 samples have also a polycrystalline rutile structure. However, there is a relatively preferred growth direction towards (101) plane. Moreover, nitrogen doping for SnO_2 thin film did not affect its crystalline structure. The average optical transmittance in the visible region has been reduced after the nitrogen doping which is due to the absorption edge redshift for each O_2 PP. The optical bandgap is low for N-doped SnO_2 ranging from 3.60 to 3.98 eV compared to undoped SnO_2 ranging from 4.02 to 4.08 eV. It is worth noting that the thickness of N-doped SnO_2 thin films is higher than the undoped SnO_2 one for each O_2 PP. N doping has improved the electrical resistivity compared to undoped SnO_2 and it is established that increasing O_2 PP has reduced the resistivity from 8.5×10^{-1} to 3.1×10^{-2} $\Omega\cdot$cm for undoped SnO_2 and from 2.8×10^{-2} to 5.9×10^{-3} $\Omega\cdot$cm for N-doped SnO_2. These optoelectronic performance results have reflected FoM where the highest value for undoped SnO_2 was 2.5×10^{-4} Ω^{-1} and the highest value for N-doped SnO_2 was 7×10^{-4} Ω^{-1}. This best FoM for N-doped SnO_2 is achieved due to the low resistivity of 5.9×10^{-3} $\Omega\cdot$cm as well as the average optical transmittance of 80% in the visible range[250]. Deposing metal oxide thin films on flexible substrates has attracted a lot of research attention in the last decades due to the potential new applications as well as the flexibility in terms of fabrication process upscaling, namely roll-to-roll. Some of these flexible substrates have a good transmittance in the visible range which makes them an essential component for ideal goal of all oxide optoelectronic devices. In this context, F. Fang et al. have demonstrated N-doped SnO_2 thin film using reactive magnetron sputtering. SnO_2:N thin film was deposited at room temperature on flexible substrate (PET) using lower process temperature. This study has explored the effect of O_2 partial pressure where $O_2:N_2$ varies from 0% to 4% on structural, electrical and optical properties of N:SnO_2 to achieve low cost, eco-friendly, higher performance flexible electronic materials. SEM imaging shows that nitrogen doping has increased the surface roughness. XRD has shown that undoped SnO_2 and N:SnO_2 thin film are amorphous which is likely due to the deposition at room temperature that is not enough to enable crystallization. However, N:SnO_2 is found to be crystalline when the substrate temperature is at 400°C. X-ray Photoelectron Spectroscopy has revealed that the tin oxide has not a perfect stoichiometry SnO_x where $x = 2$. However, the stoichiometry coefficient is 1.61, 1.68, 1.70 for the following O_2 partial pressure 0, 2, 4%, This indicate that there is a large concentration of O vacancies which makes the thin film conductive. In this report, the co-authors stated that in rich growth conditions related to both Sn and O, Interstitial nitrogen has a larger formation energy which means that nitrogen substitution is more favourable compared to interstitial. All samples of undoped SnO_2 and N:SnO_2 have revealed an average optical transmittance above 75%. However, N:SnO_2 have lower optical transmittance compared to undoped SnO_2 which is due to the optical bandgap reduction from 3.46 to 3.19 eV as the doping of nitrogen increases from 7.5 to 19.9 at.%. The electrical resistivity decreases from 2×10^{-3} to 9×10^{-4} $\Omega \cdot cm$ as the doping of nitrogen increases from 7.5 to 11 at.%, and then it increases to 0.01 $\Omega \cdot cm$ as the doping of N increases to 19.9 at.%. The best FoM for N:SnO_2 is found to be slightly above 10^{-3} Ω^{-1} [251, 252].

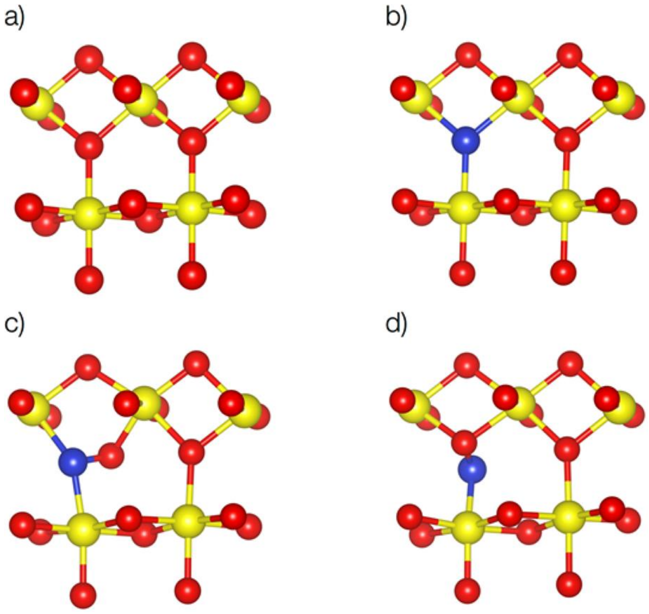

Figure 9: Structural model for: (a) undoped SnO_2, (b) substitutional (occupying O lattice site) N-doped SnO_2, and (c, d) Interstitial N-doped SnO_2 (N in blue, Sn in yellow, O in red). Reprinted (adapted) with permission from [246]. Copyright 2015 American Chemical Society.

In general, one of the main challenges for p-type doping of SnO_2 is the self-compensation where the doping related p-type charge carriers formed within the SnO_2, are compensated by the intrinsic n-type charge carriers formed by the host semiconducting material itself, SnO_2. Another challenge of N-doping of SnO_2 is the compromise between a sufficient N-doping to reach a good acceptor charge carrier concentration and a limited N-doping to avoid altering the structure of SnO_2 rutile and forming secondary phases mainly tin nitrides which can play a significant role in changing the electronic structure and overall electrical properties. There are some reports suggesting novel material designs and doping to tackle this issue. H.P. Dang et al. have suggested a secondary nitrogen doping for the Ga-doped SnO_2 material to prevent the self-compensation effect. The co-authors have reported a Ga:SnO_2 (GTO) thin film by reactive magnetron sputtering in N_2 atmosphere using Ga_2O_3-doped SnO_2 sputtering target to allow them to customize separately N-doping and Ga-doping. They prepared N-doped GTO thin films at different temperatures varying from room temperature to 500°C. All samples N-doped GTO have achieved and maintained p-type conductivity except the one deposited at room temperature, while the best p-type conductive sample was the one deposited at 400°C. This low resistivity is owed to the high p-type charge carrier concentration of 6.99×10^{19} cm^{-3} [253].

1.2.2. Tin(II) oxide (SnO) thin film

Tin(II) oxide (SnO) which is also known as stannous oxide is another form of tin oxide where the tin oxidation state is +2 and stoichiometry SnO_x is $x = 1$. Tin monoxide thin film performance has still a long way to achieve the highest required performance, particularly in electrical properties and chemical stability. Nevertheless, tin monoxide has already many applications such as sensors[254], transparent conducting oxide[255], Li ion battery[256]. However, most of the reports about SnO thin films are related to Thin Film Transistor (TFT). This is due to the pressing requirement to achieve p-type oxide thin film which can synthetised at relatively low-to-moderate temperature. The process to fabricate p-type thin film has to be scalable, and using abundant and cost-effective elements. Therefore, tin monoxide, which can fulfil all these requirements, is an attractive material to be employed in large scale industrial process. There are still some issues with chemical stability due to the oxidation towards SnO_2. In some literature, the use of a capping layer or a passivation on the top of SnO is reported as a remedy to this issue[134, 135, 257-263].

a) Thin film growth

Among the experimental literature, there are several synthesis techniques related to SnO whether through physical or chemical processes. Regarding the physical processes, the reactive magnetron sputtering has more reports compared to other synthesis techniques[254, 255, 258, 260, 263-270]. However, SnO synthesis is also reported via Pulsed Laser Deposition[135, 259, 262, 271, 272], Thermal Evaporation[257, 261, 273, 274], electron beam evaporation[134, 275-278]. In terms of chemical processes, there several reports about SnO synthesis techniques, namely Plasma Enhanced Chemical Vapour Deposition (PECVD)[279], Atomic Layer Deposition (ALD)[280], hydrothermal process[281], spray pyrolysis[282], spin coating[283].

b) Structural properties

Tin(II) oxide crystal structure at room temperature and ambient pressure is a tetragonal litharge PbO type layered structure (α-SnO) which is part of the tetragonal P4/nmm space group. This SnO structure is enabling four-coordinate geometry where the Sn elements have a coordination to four oxygen atoms in a pyramidal shape while forming a two-dimensional SnO sheet oriented towards (001) direction. In this four-coordinate geometry, each Sn^{2+} cation is bonded to four O^{2-} anions and vice-versa as shown in Figure 10. All bonds of O-Sn have a length around 2.23 Å. Sn^{2+} cations, while bonding to four O^{2-} anions, are forming a both corner-sharing and edge-sharing SnO_4 tetrahedra. There are several theoretical or experimental reports about the SnO crystal structure, where the lattice constants vary theoretically between a = b = 3.79 Å and c = 3.65 Å and a = b = 3.90 Å and c = 3.98 Å, and are experimentally around a = b = 3.80 Å and c = 3.84 Å. J.P. Allen et al. have revealed using hybrid DFT calculation that while oxygen related defects do not alter the crystal structure of SnO, instead the Sn related interstitial defects (Sn_i) induce more effect on the crystal structure by other atoms away from the Sn_i defect[284-286].

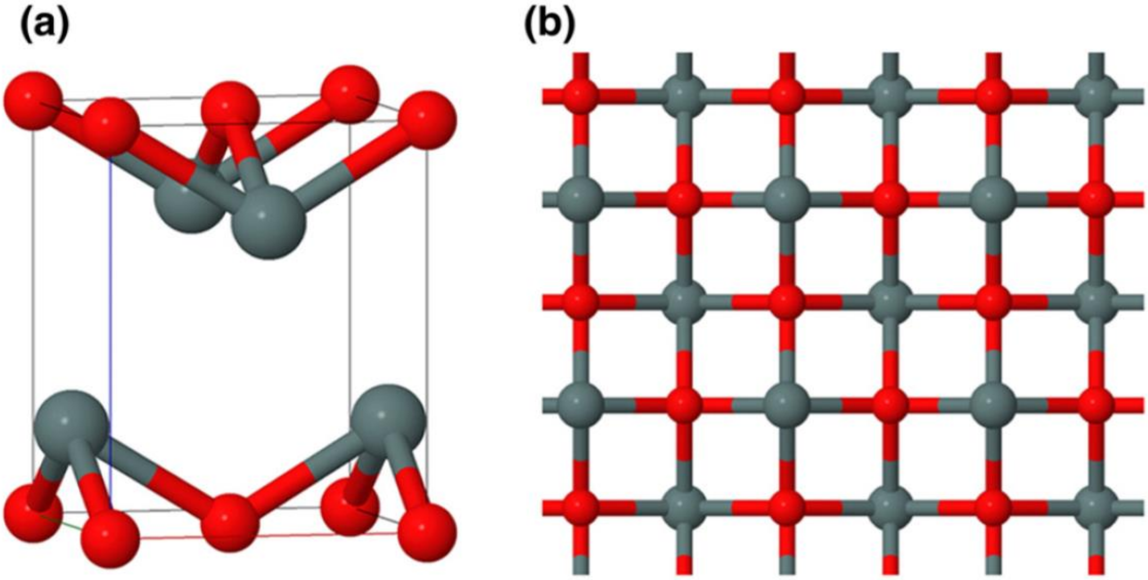

Figure 10: (a) SnO crystal structure and (b) SnO crystal structure top-view (gray spheres represent Sn and red spheres represent O). Reprinted (adapted) with permission from [285]. Copyright 2016 Elsevier.

c) Electronic structure

There are several reports about the electronic structure of SnO to describe assess the electronic bandgap as well as the contributions of electrons from Sn and O to the valence band and to the conduction band. The electronic structure shows that SnO has an indirect bandgap as the valence band maximum (VBM) and conduction band minimum (CBM) are location in a different point in the Brillouin-zone. The VBM is located at Γ point while the CBM is located at M point as shown in Figure 11. The calculated indirect bandgap of SnO 0.41 eV as reported by The Materials Project. SnO, at complete oxidation, exhibits ground state $5s^2$. The main contribution of the top of the valence band is from hybridised O2p and Sn5s. The core of the valence band is dominated by O2p and Sn5p has a lower contribution. The bottom of the valence band is dominated by Sn5s and there is a relatively smaller contribution from O2p. On the other hand, the conduction band shows a strong contribution of Sn5p orbitals with smaller O2p and Sn5s contribution as shown in the partial Density of State (pDOS) in Figure 11[284-287].

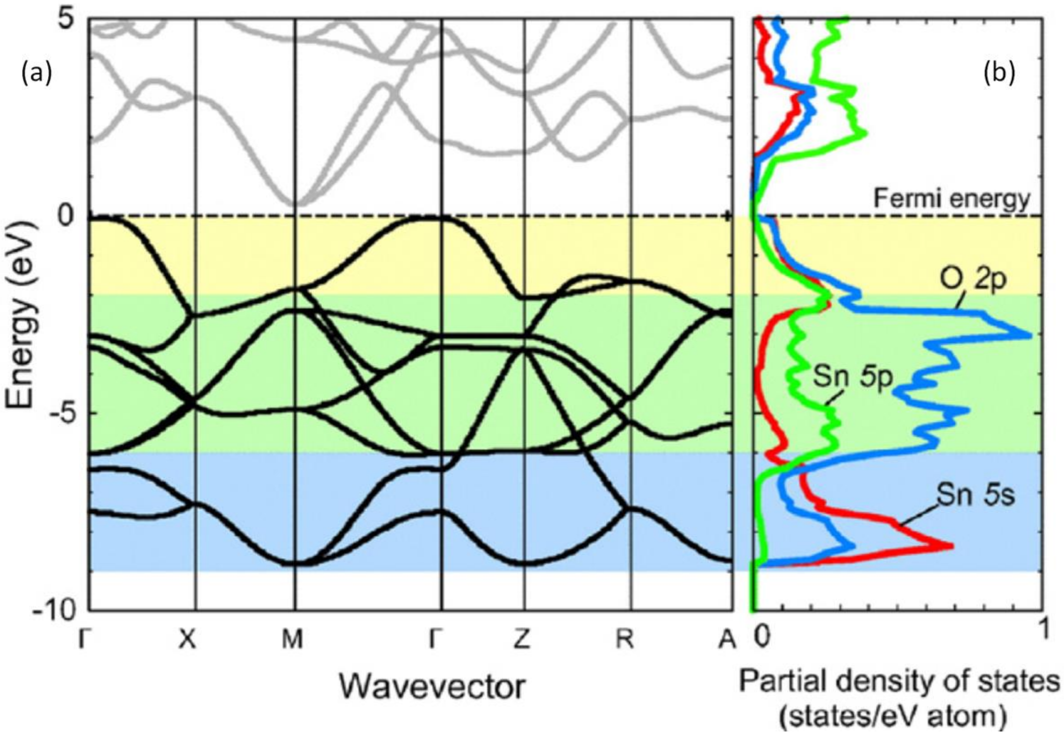

Figure 11: SnO (a) electronic band structure, (b) partial density of states. Reprinted (adapted) with permission from [285]. Copyright 2016 Elsevier.

d) Undoped SnO thin film

There is a limited number of experimental reports in terms of SnO synthesis compared to the modelling and theoretical literature as there is still a lot to explore about this material. The theoretical studies are important to investigate the electronic structure in order to understand the optical and electronic properties, particularly, the highly desired p-type conductivity which is intrinsic to the undoped SnO[286-299]. Among the experimental reports, U. Myeonghun et al. have reported the SnO synthesis by Plasma Enhanced Chemical Vapour Deposition (PECVD) at low temperature, the best SnO thin film was the one deposited at 150°C with a high field effect mobility of 4.86 $cm^2/V{\cdot}s$ with a small acceptor related charge carrier concentration. The high electrical performance, including the mobility and lower charge carrier concentration, is suggested to be due to the fine grain microstructure [279]. M. Rockele et al.

have reported the synthesis of a p-type tin oxide via thermal evaporation at room temperature on Al_2O_3 using SnO powder followed by rapid thermal annealing at 350°C under N_2 for 30 minutes. XRD results revealed that the as-deposited SnO is amorphous while the annealed SnO has secondary phases of Sn and SnO_2. The co-authors could still achieve a p-channel tin monoxide TFT via thermal evaporation[261]. H.J. Kim et al. have reported the deposition of 10 nm SnO thin film using reactive RF magnetron sputtering at room temperature. They have confirmed the p-type conductivity of SnO using TFT device[260]. J.A. Caraveo-Frescas et al. have reported a high mobility of transparent p-type of pure SnO films using reactive Direct Current (DC) magnetron sputtering at room temperature with metallic Sn target and mixture of O_2:Ar. XRD analysis shows the presence of SnO phase with a minor Sn secondary phase for low O_2 partial pressure (PP). As the O_2 PP increases a pure tetragonal SnO phase was achieved. For higher O_2 PP the SnO film can be whether amorphous or SnO_2 phase. Hall effect probe analysis shows that most of samples exhibit p-type conductivity while n-type conductivity is only found at very low O_2 PP with a low deposition pressure. The highest deposition pressure and highest O_2 PP has enabled a high resistive tin oxide film. The summary of the sputtering conditions is shown in table 3. It is worth noting that highest mobility and the highest conductivity are achieved at 9% O_2 PP and 1.8 mTorr. The sample which exhibits the highest mobility/conductivity is not a pure SnO phase as it has a minor presence of metallic β-Sn[258].

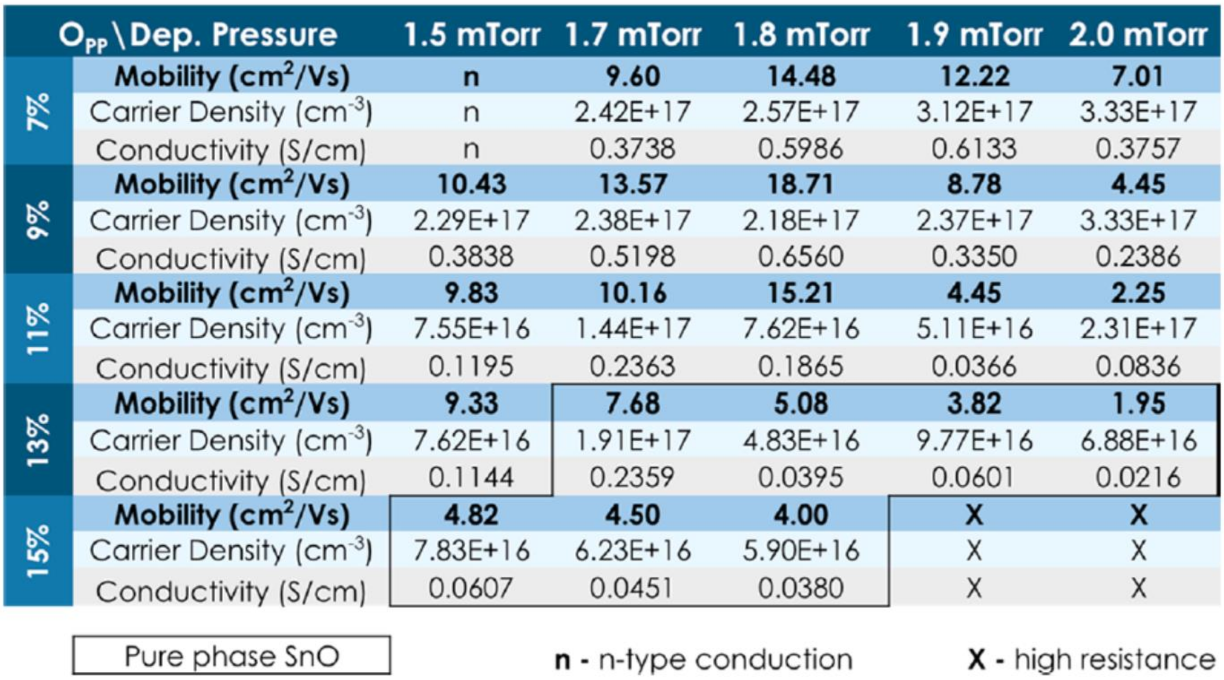

O_{PP}\Dep. Pressure		1.5 mTorr	1.7 mTorr	1.8 mTorr	1.9 mTorr	2.0 mTorr
7%	**Mobility (cm^2/Vs)**	**n**	**9.60**	**14.48**	**12.22**	**7.01**
	Carrier Density (cm^{-3})	n	2.42E+17	2.57E+17	3.12E+17	3.33E+17
	Conductivity (S/cm)	n	0.3738	0.5986	0.6133	0.3757
9%	**Mobility (cm^2/Vs)**	**10.43**	**13.57**	**18.71**	**8.78**	**4.45**
	Carrier Density (cm^{-3})	2.29E+17	2.38E+17	2.18E+17	2.37E+17	3.33E+17
	Conductivity (S/cm)	0.3838	0.5198	0.6560	0.3350	0.2386
11%	**Mobility (cm^2/Vs)**	**9.83**	**10.16**	**15.21**	**4.45**	**2.25**
	Carrier Density (cm^{-3})	7.55E+16	1.44E+17	7.62E+16	5.11E+16	2.31E+17
	Conductivity (S/cm)	0.1195	0.2363	0.1865	0.0366	0.0836
13%	**Mobility (cm^2/Vs)**	**9.33**	**7.68**	**5.08**	**3.82**	**1.95**
	Carrier Density (cm^{-3})	7.62E+16	1.91E+17	4.83E+16	9.77E+16	6.88E+16
	Conductivity (S/cm)	0.1144	0.2359	0.0395	0.0601	0.0216
15%	**Mobility (cm^2/Vs)**	**4.82**	**4.50**	**4.00**	**X**	**X**
	Carrier Density (cm^{-3})	7.83E+16	6.23E+16	5.90E+16	X	X
	Conductivity (S/cm)	0.0607	0.0451	0.0380	X	X

Pure phase SnO

n - n-type conduction

X - high resistance

Table 3: Hall mobility, charge carrier concentration and electrical conductivity for room temperature reactive DC magnetron sputtered SnO thin films (the reported results are average of 3 for each sample). Reprinted (adapted) with permission from [258]. Copyright 2013 American Chemical Society.

E. Eqbal and E.I. Anila have reported the synthesis and characterization of tin monoxide as transparent conducting oxide using spray pyrolysis by preparing two precursor solutions of 0.1 M and 0.25 M out of $SnCl_2.H_2O$ in water in addition to some drops concentrated HCl. The spray pyrolysis was conducted at 350°C substrate temperature. XRD analysis revealed the presence of orthorhombic crystal structure for the prepared SnO thin films with a minor presence of SnO_2 phase. The optical transmittance of SnO was found to be 82% with a wide bandgap of 3.58 eV for precursor solution of 0.1 M and 30% for 0.25 M. Hall effect probe analysis has established that both thin films exhibit p-type conductivity, and the resistivity is 0.059 Ω·cm for 0.25 M precursor solution compared to 0.12 Ω·cm 0.1 M. Both samples have the charge carrier concertation around 7×10^{18} cm^{-3}. However, the mobility is 17.1 $cm^2/V{\cdot}s$ for 0.25 M precursor solution compared to 7.8 $cm^2/V{\cdot}s$ 0.1 M. This report shows that p-type conductivity can be achieved in SnO even with presence of secondary phase namely, Sn and SnO_2[282].

e) SnO thin film doping

There are only few experimental reports about SnO doped thin films which is likely due to the complexity to achieve high purity undoped SnO. Among these reports, N-doped SnO was reported by Y. Kim et al. via reactive RF magnetron sputtering with metallic Sn target and mixture of $Ar/O_2/N_2$ at 300°C on borosilicate substrates. Structural properties by XRD have revealed the presence of a polycrystalline SnO phase with preferred growth on (101) direction and the absence of any secondary phase related to metallic Sn, other tin oxides or tin nitrides. However, it is noticed that the nitrogen doping has decreased the crystallinity of SnO thin films. Scanning Electron Microscopy (SEM) imaging has revealed the microstructural properties and it showed that nitrogen doping has made the thin film grain more regular and the film more much dense. Hall effect probe analysis has revealed the electrical properties and that generating Sn-N bonds has increased the resistivity. The nitrogen doping of SnO has generated donors and contributed significantly increasing the resistivity due to self-compensation. The mobility is improved by nitrogen doping of SnO due to the increase of the density and the regular microstructure of the thin film. Vacuum annealing has increased the resistivity of both nitrogen doped and undoped SnO. UV-Visible spectroscopy has determined the optical properties and it revealed that the optical bandgap decreased due to the defects formation by nitrogen doping which formed new states within the bandgap. The bandgap decreased from 2.43 eV for undoped SnO to 2.17 eV N doped SnO. Vacuum annealing has slightly improved the optical transmittance[267]. G. Dai et al. have reported ball and sheet-like Cr-doped SnO synthetised via hydrothermal process. XRD results have shown that all samples are all closely matching to the polycrystalline tetragonal of SnO without presence of secondary phases. The optical bandgap is slightly changing between 3.1 to 3.3 eV. It was established that Cr atoms have been incorporated as substitutional to Sn (Cr_{Sn}) and as interstitial (Cr_i)[281]. H. Hosono et al. have reported the synthesis of tin monoxide thin film doped with antimony (Sb:SnO) using Pulsed Laser Deposition (PLD) with doping level from 0 to 10 at.% (Sb/Sb+Sn) on Yttria-stabilised

ZrO_2 single crystal (001) substrates at temperatures ranging from 300°C to 600°C. It is worth noting that the substrate selection took into consideration the lattice parameter matching with SnO. The best film was achieved at substrate temperature of 550°C and it was determined that increasing Sb doping decreases the crystallinity of SnO. They revealed that 5 at.% Sb:SnO was not enough to switch the p-type conductivity to n-type due to the large concentration of acceptors[272].

1.3. Summary

Metal oxides are interesting materials due to their unique ability to combine both high electrical conductivity and high optical transmittance with a wide bandgap. SnO_x has shown to be an excellent material that allows tuning its structural, optical and electrical properties. Literature review has shown the possibility to form tin oxide thin films with both conductivity n-type and p-type. N-type conductive SnO_2 thin film is well established material and reached the maturity as TCO in various applications. Nevertheless, p-type SnO_x based material whether intrinsic tin monoxide SnO or doped SnO_2 to form a stable p-type thin film is still an interesting topic of research and development with a potential prospect for improvement. Achieving a high quality and stability p-type tin oxide based material will be an important step toward all oxide devices such as thin film transistors[300]. In the next chapter, the tuning of tin oxide based thin films will be explored to achieved both conductivity types via magnetron sputtering which is vacuum-based technique. This technique can assure a high quality and reproducibility SnO_x thin films. Furthermore, the post-deposition thermal annealing will be investigated to explore the possibility of tuning the structural properties which can lead to customized optical and electrical properties.

References

1. Hosono, H., Transparent Oxide Semiconductors: Fundamentals and Recent Progress, in Transparent Electronics. 2010. p. 31-59.

2. Medvedeva, J.E., Combining Optical Transparency with Electrical Conductivity: Challenges and Prospects, in Transparent Electronics. 2010. p. 1-29.

3. Nomura, K., et al., Room-temperature fabrication of transparent flexible thin-film transistors using amorphous oxide semiconductors. Nature, 2004. 432(7016): p. 488-492.

4. Hosono, H., 68.3: Invited Paper: Transparent Amorphous Oxide Semiconductors for High Performance TFT. SID Symposium Digest of Technical Papers, 2007. 38(1): p. 1830-1833.

5. Kamiya, T. and H. Hosono, Material characteristics and applications of transparent amorphous oxide semiconductors. NPG Asia Materials, 2010. 2(1): p. 15-22.

6. Park, J.S., et al., Review of recent developments in amorphous oxide semiconductor thin-film transistor devices. Thin Solid Films, 2012. 520(6): p. 1679-1693.

7. Nathan, A., et al., Transparent Oxide Semiconductors for Advanced Display Applications. Information Display, 2013. 29(1): p. 6-11.

8. Nathan, A., et al., Amorphous Oxide Semiconductor TFTs for Displays and Imaging. Journal of Display Technology, 2014. 10(11): p. 917-927.

9. Lee, S., et al., Transparent Semiconducting Oxide Technology for Touch Free Interactive Flexible Displays. Proceedings of the IEEE, 2015. 103(4): p. 644-664.

10. Fujiwara, H. and S. Fujimoto, Transparent Conductive Oxide Materials, in Spectroscopic Ellipsometry for Photovoltaics: Volume 1: Fundamental Principles and Solar Cell Characterization, H. Fujiwara and R.W. Collins, Editors. 2018, Springer International Publishing: Cham. p. 523-563.

11. Jang, J., et al., Thin-Film Optical Devices Based on Transparent Conducting Oxides: Physical Mechanisms and Applications. Crystals, 2019. 9(4): p. 192.

12. Levy, D. and E. Castellón, Transparent Conductive Materials. 2019, Newark: John Wiley & Sons, Incorporated.

13. Afre, R.A., et al., Transparent Conducting Oxide Films for Various Applications: A Review. REVIEWS ON ADVANCED MATERIALS SCIENCE, 2018. 53(1): p. 79-89.

14. Cui, X., et al., Enhanced Heterojunction Interface Quality To Achieve 9.3% Efficient Cd-Free Cu2ZnSnS4 Solar Cells Using Atomic Layer Deposition ZnSnO Buffer Layer. Chemistry of Materials, 2018. 30(21): p. 7860-7871.

15. Zhang, T., et al., Atomic layer deposited ZnxNi1−xO: A thermally stable hole selective contact for silicon solar cells. Applied Physics Letters, 2018. 113(26): p. 262102.

16. Aïssa, B., et al., Impact of the oxygen content on the optoelectronic properties of the indium-tin-oxide based transparent electrodes for silicon heterojunction solar cells. AIP Conference Proceedings, 2019. 2147(1): p. 030001.

17. Aïssa, B., et al. Development of N-Type Amorphous and Microcrystalline Hydrogenated Silicon-Oxides (SiOx:H) and Investigation of their Impact as Window Layers on Silicon Heterojunction Solar Cells Device. in 2019 IEEE 46th Photovoltaic Specialists Conference (PVSC). 2019.

18. Aïssa, B., et al. Impact of the Oxygen Flow during the Magnetron Sputtering Deposition on the Indium Tin Oxide thin films for Silicon Heterojunction Solar Cell. in 2019 IEEE 46th Photovoltaic Specialists Conference (PVSC). 2019.

19. Zhang, T., et al. Atomic Layer Deposited AlxNiyO as Hole Selective Contact for Silicon Solar Cells. in 2019 IEEE 46th Photovoltaic Specialists Conference (PVSC). 2019.

20. Hossain, M.A., et al., Doped Nickel Oxide Carrier-Selective Contact for Silicon Solar Cells. IEEE Journal of Photovoltaics, 2021. 11(5): p. 1176-1187.

21. Tong, J., et al., Impact of Pregrown SiOx on the Carrier Selectivity and Thermal Stability of Molybdenum-Oxide-Passivated Contact for Si Solar Cells. ACS Applied Materials & Interfaces, 2021. 13(30): p. 36426-36435.

22. Hossain, M.I., et al., E-beam evaporated hydrophobic metal oxide thin films as carrier transport materials for large scale perovskite solar cells. Materials Technology, 2022. 37(4): p. 248-259.

23. Habis, C., J. Zaraket, and M. Aillerie, Transparent Conductive Oxides. Part I. General Review of Structural, Electrical and Optical Properties of TCOs Related to the Growth Techniques, Materials and Dopants. Defect and Diffusion Forum, 2022. 417: p. 243-256.

24. Nakata, M., C. Zhao, and J. Kanicki, DC sputtered amorphous In–Sn–Zn–O thin-film transistors: Electrical properties and stability. Solid-State Electronics, 2016. 116: p. 22-29.

25. Riedl, T., Transparent OLED Displays, in Transparent Electronics. 2010. p. 299-323.

26. Huang, J., et al., Transparent Solar Cells Based on Organic Polymers, in Transparent Electronics. 2010. p. 343-372.

27. Ito, M., Application of Transparent Amorphous Oxide Thin Film Transistors to Electronic Paper, in Transparent Electronics. 2010. p. 213-229.

28. Fortunato, E., et al., Oxide Semiconductors: From Materials to Devices, in Transparent Electronics. 2010. p. 141-183.

29. Coutts, T.J., et al., Chapter 4 A Review of NREL Research into Transparent Conducting Oxides, in Materials Challenges: Inorganic Photovoltaic Solar Energy. 2015, The Royal Society of Chemistry. p. 89-134.

30. Bädeker, K., Über die elektrische Leitfähigkeit und die thermoelektrische Kraft einiger Schwermetallverbindungen. Annalen der Physik, 1907. 327(4): p. 749-766.

31. Ellmer, K., Past achievements and future challenges in the development of optically transparent electrodes. Nature Photonics, 2012. 6(12): p. 809-817.

32. Wagner, C., Fehlordnungserscheinungen in kristallisierten polaren Verbindungen als Grundlage für Elektronen- und Ionen-Leitung. Zeitschrift für Elektrochemie und angewandte physikalische Chemie, 1933. 39(7b): p. 543-545.

33. Mochel, J.M., Electrically conducting coatings on glass and other ceramic bodies. 1951, Google Patents.

34. Rupprecht, G., Untersuchungen der elektrischen und lichtelektrischen Leitfähigkeit dünner Indiumoxydschichten. Zeitschrift für Physik, 1954. 139(5): p. 504-517.

35. Spear, W.E. and P.G. Le Comber, Substitutional doping of amorphous silicon. Solid State Communications, 1975. 17(9): p. 1193-1196.

36. Ginley, D.S., H. Hosono, and D.C. Paine, Handbook of Transparent Conductors. 2010: Springer US.

37. Edwards, P.P., et al., Basic materials physics of transparent conducting oxides. Dalton Transactions, 2004(19): p. 2995-3002.

38. Kawazoe, H., et al., P-type electrical conduction in transparent thin films of CuAlO2. Nature, 1997. 389(6654): p. 939-942.

39. Hosono, H., M. Yasukawa, and H. Kawazoe, Novel oxide amorphous semiconductors: transparent conducting amorphous oxides. Journal of Non-Crystalline Solids, 1996. 203: p. 334-344.

40. Hosono, H., Ionic amorphous oxide semiconductors: Material design, carrier transport, and device application. Journal of Non-Crystalline Solids, 2006. 352(9): p. 851-858.

41. Minami, T., Transparent conducting oxide semiconductors for transparent electrodes. Semiconductor Science and Technology, 2005. 20(4): p. S35-S44.

42. Hayashi, K., et al., Light-induced conversion of an insulating refractory oxide into a persistent electronic conductor. Nature, 2002. 419(6906): p. 462-465.

43. Furubayashi, Y., et al., A transparent metal: Nb-doped anatase TiO2. Applied Physics Letters, 2005. 86(25): p. 252101.

44. N n Kundan , V.K., Transparent Conductive Films Market by Material (Indium Tin Oxide (ITO) on Glass, Indium Tin Oxide (ITO) on PET, Silver Nanowire, Carbon Nanotubes, Conductive Polymers, Others), by Application (Smartphones, Notebooks, Tablet, PC, Wearable Devices, Others): Global Opportunity Analysis and Industry Forecast, 2020-2030. 2022.

45. Afre, R.A., et al., Transparent Conducting Oxide Films for Various Applications: A Review. 2018. 53(1): p. 79-89.

46. Brotherton, S.D., Transparent Amorphous Oxide Semiconductor TFTs, in Introduction to Thin Film Transistors: Physics and Technology of TFTs, S.D. Brotherton, Editor. 2013, Springer International Publishing: Heidelberg. p. 301-338.

47. Carcia, P.F., Application of Transparent Oxide Semiconductors for Flexible Electronics, in Transparent Electronics. 2010. p. 265-297.

48. Bright, C.I., Deposition and Performance Challenges of Transparent Conductive Oxides on Plastic Substrates, in Transparent Electronics. 2010. p. 103-140.

49. Zhang, T., et al., Flexible inorganic oxide thin-film electronics enabled by advanced strategies. Journal of Semiconductors, 2020. 41(4): p. 041602.

50. Kumar, A. and C. Zhou, The Race To Replace Tin-Doped Indium Oxide: Which Material Will Win? ACS Nano, 2010. 4(1): p. 11-14.

51. Leaf-nosed bat, in Encyclopædia Britannica. 2009, Encyclopædia Britannica Online.

52. Hamberg, I. and C.G. Granqvist, Evaporated Sn-doped In2O3 films: Basic optical properties and applications to energy-efficient windows. Journal of Applied Physics, 1986. 60(11): p. R123-R160.

53. Hoel, C.A., et al., Transparent Conducting Oxides in the ZnO-In2O3-SnO2 System. Chemistry of Materials, 2010. 22(12): p. 3569-3579.

54. Spencer, J.A., et al., A review of band structure and material properties of transparent conducting and semiconducting oxides: Ga2O3, Al2O3, In2O3, ZnO, SnO2, CdO, NiO, CuO, and Sc2O3. Applied Physics Reviews, 2022. 9(1): p. 011315.

55. The Materials, P., Materials Data on CdO by Materials Project. 2020: United States.

56. The Materials, P., Materials Data on SnO2 by Materials Project. 2020: United States.

57. The Materials, P., Materials Data on In2O3 by Materials Project. 2020: United States.

58. The Materials, P., Materials Data on ZnO by Materials Project. 2020: United States.

59. Mazumder, J.T., R. Mayengbam, and S. Tripathy, Theoretical investigation on structural, electronic, optical and elastic properties of TiO2, SnO2, ZrO2 and HfO2 using SCAN meta-GGA functional: a DFT study. Materials Chemistry and Physics, 2020. 254: p. 123474.

60. Kamiya, T. and H. Hosono, Electronic Structures and Device Applications of Transparent Oxide Semiconductors: What Is the Real Merit of Oxide Semiconductors? International Journal of Applied Ceramic Technology, 2005. 2(4): p. 285-294.

61. Yu, P.Y. and M. Cardona, Electronic Band Structures, in Fundamentals of Semiconductors: Physics and Materials Properties, P.Y. Yu and M. Cardona, Editors. 2010, Springer Berlin Heidelberg: Berlin, Heidelberg. p. 17-106.

62. J., M. and S. L., Efficient sprayed In2O3:Sn n-type silicon heterojunction solar cell. Appl. Phys. Lett., 1977. 31: p. 459.

63. T., K., F. H., and K. M., High-mobility hydrogen-doped In2O3 transparent conductive oxide for a-Si:H/c-Si heterojunction solar cells. Sol. Energy Mater. Sol. Cells, 2009. 93: p. 851.

64. R., S., et al., Optimization of growth of In2O3 nano-spheres thin films by electrodeposition for dye-sensitized solar cells. J. Alloys Compd., 2009. 479: p. 840.

65. Y., M., et al., A new transparent conductive thin film In2O3: Mo. Thin Solid Films, 2001. 394: p. 218.

66. S., L.J., K. Y.-J., and C. W.-S., Inkjet-printed In2O3 thin-film transistor below 200c. ACS Appl. Mater. Interfaces, 2013. 5: p. 11578.

67. Z., Y., et al., Annealing effects of In2O3 thin films on electrical properties and application in thin film transistors. Thin Solid Films, 2011. 519: p. 3254.

68. K., N.P., et al., High performance In2O3 thin film transistors using chemically derived aluminum oxide dielectric. Appl. Phys. Lett., 2013. 103: p. 33518.

69. Z., Q., L. R., and M. D., Thickness dependence of In2O3:Sn film growth. Thin Solid Films, 2004. 466: p. 250.

70. Michel, J., et al., Processing Strategies for High-Performance Schottky Contacts on n-Type Oxide Semiconductors: Insights from In2O3. ACS Applied Materials & Interfaces, 2019. 11(30): p. 27073-27087.

71. E., T., E. J., and S. J., Pulsed laser deposition of oriented In2O3 on (001) InAs, MgO, and yttria-stabilized zirconia. Appl. Phys. Lett., 1993. 62: p. 2332.

72. R., G., et al., Opto-electrical properties of Ti-doped In2O3 thin films grown by pulsed laser deposition. Appl. Surf. Sci., 2007. 253: p. 9422.

73. N., T., et al., Deposition of heteroepitaxial In2O3 thin films by molecular beam epitaxy. Jpn. J. Appl. Phys., Part 1, 1998. 37: p. 6524.

74. D.-J., L., et al., Self-limiting film growth of transparent conducting In2O3 by atomic layer deposition using trimethylindium and water vapor. J. Phys. Chem. C, 2011. 115: p. 15384.

75. O., N., et al., Thin films of In2O3 by atomic layer deposition using In(acac)(3). Thin Solid Films, 2009. 517: p. 6320.

76. K., R.R., et al., Low temperature atomic layer deposition of crystalline In2O3 films. J. Phys. Chem. C, 2015. 119: p. 11786.

77. W.-Y., C., et al., Spin-coated indium oxide thin film on alumina and silicon substrates and their gas sensing properties. Sens. Actuators B, 2000. 65: p. 312.

78. J., P.J., et al., Spray pyrolysis growth and material properties of In2O3 films. J. Cryst. Growth, 2002. 240: p. 142.

79. Leppäniemi, J., et al., In2O3 Thin-Film Transistors via Inkjet Printing for Depletion-Load NMOS Inverters. IEEE Electron Device Letters, 2016. 37: p. 1-1.

80. Jouin, J., et al., Ink-Jet Printing of In2O3/ZnO Two-Dimensional Structures from Solution. Journal of the American Ceramic Society, 2011. 94: p. 2834-2840.

81. L., K., et al., Characterization of single-crystalline In2O3 films deposited on y-stabilized ZrO2 (1 0 0) substrates by MOCVD. Appl. Surf. Sci., 2010. 257: p. 518.

82. X., D., et al., Epitaxial growth and characterization of high quality In2O3 films on a-plane sapphire substrates by MOCVD. Vacuum, 2019. 167: p. 1.

83. Y., W.C., et al., Phase stabilization and phonon properties of single crystalline rhombohedral indium oxide. Cryst. Growth Design, 2008. 8: p. 1257.

84. K., Z., et al., Domain matching epitaxial growth of In2O3 thin films on α-Al2O3 (0001. Cryst. Growth Design, 2012. 12: p. 1000.

85. Y., W.C., et al., Phase selective growth and properties of rhombohedral and cubic indium oxide. Appl. Phys. Lett., 2006. 89: p. 011904.

86. Fuchs, F. and F. Bechstedt, Indium-oxide polymorphs from first principles: Quasiparticle electronic states. Physical Review B, 2008. 77(15): p. 155107.

87. Bierwagen, O., Indium oxide—a transparent, wide-band gap semiconductor for (opto)electronic applications. Semiconductor Science and Technology, 2015. 30(2): p. 024001.

88. He, H., 2 - Metal oxide semiconductors and conductors, in Solution Processed Metal Oxide Thin Films for Electronic Applications, Z. Cui and G. Korotcenkov, Editors. 2020, Elsevier. p. 7-30.

89. Lany, S. and A. Zunger, Dopability, Intrinsic Conductivity, and Nonstoichiometry of Transparent Conducting Oxides. Physical Review Letters, 2007. 98(4): p. 045501.

90. Bierwagen, O. and J.S. Speck, Plasma-assisted molecular beam epitaxy of Sn-doped In2O3: Sn incorporation, structural changes, doping limits, and compensation. physica status solidi (a), 2014. 211(1): p. 48-53.

91. V., K., et al., Zinc oxide–Analogue of GaN with new perspective possibilities. Cryst. Res. Technol., 2004. 39: p. 980.

92. S., L.K., et al., Nanowire-quantum-dot solar cells and the influence of nanowire length on the charge collection efficiency. Appl. Phys. Lett., 2009. 95: p. 193103.

93. Ramanathan, K., et al., Properties of 19.2% efficiency ZnO/CdS/CuInGaSe2 thin-film solar cells. Progress in Photovoltaics: Research and Applications, 2003. 11(4): p. 225-230.

94. Hagiwara, Y., T. Nakada, and A. Kunioka, Improved Jsc in CIGS thin film solar cells using a transparent conducting ZnO:B window layer. Solar Energy Materials and Solar Cells, 2001. 67(1): p. 267-271.

95. Lee, Y.-J., et al., ZnO Nanostructures as Efficient Antireflection Layers in Solar Cells. Nano Letters, 2008. 8(5): p. 1501-1505.

96. Zhang, P., et al., Perovskite Solar Cells with ZnO Electron-Transporting Materials. Advanced Materials, 2018. 30(3): p. 1703737.

97. Kidowaki, H., T. Oku, and T. Akiyama, Fabrication and characterization of CuO/ZnO solar cells. Journal of Physics: Conference Series, 2012. 352(1): p. 012022.

98. Huang, J., Z. Yin, and Q. Zheng, Applications of ZnO in organic and hybrid solar cells. Energy & Environmental Science, 2011. 4(10): p. 3861-3877.

99. Zhang, Q., et al., ZnO Nanostructures for Dye-Sensitized Solar Cells. Advanced Materials, 2009. 21(41): p. 4087-4108.

100. Xu, W.Z., et al., ZnO light-emitting diode grown by plasma-assisted metal organic chemical vapor deposition. Applied Physics Letters, 2006. 88(17): p. 173506.

101. Kim, D.C., et al., Fabrication of the hybrid ZnO LED structure grown on p-type GaN by metal organic chemical vapor deposition. Physica B: Condensed Matter, 2007. 401-402: p. 386-390.

102. Lim, J.-H., et al., UV Electroluminescence Emission from ZnO Light-Emitting Diodes Grown by High-Temperature Radiofrequency Sputtering. Advanced Materials, 2006. 18(20): p. 2720-2724.

103. Hwang, D.-K., et al., p-ZnO/n-GaN heterostructure ZnO light-emitting diodes. Applied Physics Letters, 2005. 86(22): p. 222101.

104. S., R. and B. S., Improved zinc oxide film for gas sensor applications. Bull. Mater. Sci., 2002. 25: p. 513.

105. M., M.A., et al., Zinc oxide thin film transistors with schottky source barriers. Solid-State Electron., 2012. 76: p. 104.

106. A., H., et al., Heteroepitaxial growth of ZnO films on diamond (111) plane by magnetron sputtering. Appl. Phys. Lett., 1994. 65: p. 2556.

107. M., P., et al., Optical and structural investigation of ZnO thin films prepared by chemical vapor deposition (CVD. Thin Solid Films, 2002. 403: p. 485.

108. S., T., L. C., and L. K., Chemical vapor deposition of ZnO epitaxial films on sapphire. Appl. Phys. Lett., 1980. 36: p. 318.

109. Y., C., et al., Plasma assisted molecular beam epitaxy of ZnO on c-plane sapphire: Growth and characterization. J. Appl. Phys., 1998. 84: p. 3912.

110. K., I., et al., Improvement of electrical properties in ZnO thin films grown by radical source (RS)-MBE. Phys. Status Solidi (a), 2000. 180: p. 287.

111. A., O. and T. A., Pulsed laser deposition of thin films and superlattices based on ZnO. Semicond. Sci. Technol., 2005. 20: p. S1.

112. Y., L., et al., Ultraviolet detectors based on epitaxial ZnO films grown by MOCVD. J. Electron. Mater., 2000. 29: p. 69.

113. Ü., Ö., et al., A comprehensive review of ZnO materials and devices. J. Appl. Phys., 2005. 98: p. 041301.

114. L., G. and O.J. S., The high-pressure phase of zincite. J. Synchrotron Radiat., 1995. 2: p. 233.

115. M., C., N. Y., and D. R., Full piezoelectric tensors of wurtzite and zinc blende ZnO and ZnS by first-principles calculations. J. Phys. Chem. Solids, 2003. 64: p. 2183.

116. A., A.A., et al., Growth and characterization of hypothetical zinc-blende ZnO films on GaAs (001) substrates with ZnS buffer layers. Appl. Phys. Lett., 2000. 76: p. 550.

117. J., J. and H. A., Hartree-Fock study of phase changes in ZnO at high pressure. Phys. Rev. B, 1993. 48: p. 7903.

118. H., K., et al., Lattice dynamics and hyperfine interactions in ZnO and znse at high external pressures. Phys. Rev. B, 1996. 53: p. 11425.

119. Liu, Y., et al., First-principles study of the effect of heavy Ni doping on the electronic structure and absorption spectrum of wurtzite ZnO. Physica B: Condensed Matter, 2012. 407(13): p. 2359-2364.

120. Kim, D.-H., G.-W. Lee, and Y.-C. Kim, Interaction of zinc interstitial with oxygen vacancy in zinc oxide: An origin of n-type doping. Solid State Communications, 2012. 152(18): p. 1711-1714.

121. Janotti, A. and C.G. Van de Walle, Hydrogen multicentre bonds. Nature Materials, 2007. 6(1): p. 44-47.

122. Janotti, A. and C.G. Van de Walle, Native point defects in ZnO. Physical Review B, 2007. 76(16): p. 165202.

123. Meyer, B.K., et al., Bound exciton and donor–acceptor pair recombinations in ZnO. physica status solidi (b), 2004. 241(2): p. 231-260.

124. T-Thienprasert, J., et al., Compensation in Al-Doped ZnO by Al-Related Acceptor Complexes: Synchrotron X-Ray Absorption Spectroscopy and Theory. Physical Review Letters, 2013. 110(5): p. 055502.

125. Dalapati, G.K., et al., Tin oxide for optoelectronic, photovoltaic and energy storage devices: a review. Journal of Materials Chemistry A, 2021. 9(31): p. 16621-16684.

126. Jarzebski, Z.M. and J.P. Morton, Physical Properties of SnO2 Materials: III . Optical Properties. Journal of The Electrochemical Society, 1976. 123(10): p. 333C-346C.

127. Zakaria, Y., et al., Study of wide bandgap SnOx thin films grown by a reactive magnetron sputtering via a two-step method. Scientific Reports, 2022. 12(1): p. 15294.

128. Altinkaya, C., et al., Tin Oxide Electron-Selective Layers for Efficient, Stable, and Scalable Perovskite Solar Cells. Advanced Materials, 2021. 33(15): p. 2005504.

129. Ginley, D., M.A. Green, and R. Collins, Solar Energy Conversion Toward 1 Terawatt. MRS Bulletin, 2008. 33(4): p. 355-364.

130. Jiang, Q., X. Zhang, and J. You, SnO2: A Wonderful Electron Transport Layer for Perovskite Solar Cells. Small, 2018. 14(31): p. 1801154.

131. Fukai, Y., et al., Highly efficient dye-sensitized SnO2 solar cells having sufficient electron diffusion length. Electrochemistry Communications, 2007. 9(7): p. 1439-1443.

132. Calderer, J., et al., Synthesis and characterisation of metal suboxides for gas sensors. Microelectronics Reliability, 2000. 40(4): p. 807-810.

133. Coles, G.S.V., G. Williams, and B. Smith, The effect of oxygen partial pressure on the response of tin (IV) oxide based gas sensors. Journal of Physics D: Applied Physics, 1991. 24(4): p. 633-641.

134. Liang, L.Y., et al., Phase and Optical Characterizations of Annealed SnO Thin Films and Their p-Type TFT Application. Journal of The Electrochemical Society, 2010. 157(6): p. H598.

135. Ogo, Y., et al., p-channel thin-film transistor using p-type oxide semiconductor, SnO. Applied Physics Letters, 2008. 93(3): p. 032113.

136. Isono, T., et al., Highly conductive SnO2 thin films for flat-panel displays. Journal of the Society for Information Display, 2007. 15(2): p. 161-166.

137. Odani, A., et al., Development and testing of nanomaterials for rechargeable lithium batteries. Journal of Power Sources, 2003. 119-121: p. 517-521.

138. Han, Z., et al., Solvothermal preparation and morphological evolution of stannous oxide powders. Materials Letters, 2001. 48(2): p. 99-103.

139. Liu, A., M. Zhu, and B. Dai, A novel high-performance SnO2 catalyst for oxidative desulfurization under mild conditions. Applied Catalysis A: General, 2019. 583: p. 117134.

140. Zakaria, Y., et al., Moderate Temperature deposition of RF magnetron sputtered SnO2-based electron transporting layer for triple cation perovskite solar cells 2023.

141. Daily Metal Price: Free Metal Price Tables and Charts. Accessed on 15 Feb 2023.

142. Sharma, A., et al., Review—Recent Advances in Tin Oxide Nanomaterials as Electrochemical/Chemiresistive Sensors. Journal of The Electrochemical Society, 2021. 168(2): p. 027505.

143. Martín, M.A., et al., Study of the interferences of NO2 and CO in solid state commercial sensors. Sensors and Actuators B: Chemical, 1999. 58(1): p. 469-473.

144. Li, L., et al., Three-Dimensional Mesoporous Graphene Aerogel-Supported SnO2 Nanocrystals for High-Performance NO2 Gas Sensing at Low Temperature. Analytical Chemistry, 2015. 87(3): p. 1638-1645.

145. Korotchenkov, G.S., S.V. Dmitriev, and V.I. Brynzari, Processes development for low cost and low power consuming SnO2 thin film gas sensors (TFGS). Sensors and Actuators B: Chemical, 1999. 54(3): p. 202-209.

146. Navazani, S., et al., Facile synthesis of a SnO2@rGO nanohybrid and optimization of its methane-sensing parameters. Talanta, 2018. 181: p. 422-430.

147. Li, J., et al., A three-dimensional hexagonal fluorine-doped tin oxide nanocone array: a superior light harvesting electrode for high performance photoelectrochemical water splitting. Energy & Environmental Science, 2014. 7(11): p. 3651-3658.

148. Hernández, S., et al., New Transparent Laser-Drilled Fluorine-doped Tin Oxide covered Quartz Electrodes for Photo-Electrochemical Water Splitting. Electrochimica Acta, 2014. 131: p. 184-194.

149. Jenifer, K., et al., A Review on the Recent Advancements in Tin Oxide-Based Thin-Film Transistors for Large-Area Electronics. Journal of Electronic Materials, 2020. 49(12): p. 7098-7111.

150. Thomere, A., et al., 2-step process for 5.4% CuGaSe2 solar cell using fluorine doped tin oxide transparent back contacts. Progress in Photovoltaics: Research and Applications, 2022. n/a(n/a): p. 1–12.

151. Bremner, S.P., M.Y. Levy, and C.B. Honsberg, Analysis of tandem solar cell efficiencies under AM1.5G spectrum using a rapid flux calculation method. Progress in Photovoltaics: Research and Applications, 2008. 16(3): p. 225-233.

152. Li, J., et al., Manipulating the morphology of CdS/Sb2S3 heterojunction using a Mg-doped tin oxide buffer layer for highly efficient solar cells. Journal of Energy Chemistry, 2022. 66: p. 374-381.

153. Wu, J.-M., et al., Stable GeSe thin-film solar cells employing non-toxic SnO2 as buffer layer. Rare Metals, 2022. 41(9): p. 2992-2997.

154. Ismail, R.A. and A.M. Abdul Majeed, Preparation and investigation of nanostructured SnO2:Pd/ porous silicon/c-Si heterostructure solar cell. Journal of Solid State Electrochemistry, 2021. 25(3): p. 1039-1048.

155. Kim, H.-J., et al., Direct laser patterning of transparent ITO–Ag–ITO multilayer anodes for organic solar cells. Applied Surface Science, 2015. 328: p. 215-221.

156. Cheng, Y.-T., et al., Improvement of organic solar cells by flexible substrate and ITO surface treatments. Applied Surface Science, 2010. 256(24): p. 7606-7611.

157. Choi, K.-H., et al., Ag nanowire-embedded ITO films as a near-infrared transparent and flexible anode for flexible organic solar cells. Solar Energy Materials and Solar Cells, 2013. 110: p. 147-153.

158. Zhou, Y., et al., Inverted organic solar cells with ITO electrodes modified with an ultrathin Al2O3 buffer layer deposited by atomic layer deposition. Journal of Materials Chemistry, 2010. 20(29): p. 6189-6194.

159. Hu, T., et al., Effect of UV–ozone treatment on ITO and post-annealing on the performance of organic solar cells. Synthetic Metals, 2009. 159(7): p. 754-756.

160. Taha, H., et al., Sol-gel derived ITO-based bi-layer and tri-layer thin film coatings for organic solar cells applications. Applied Surface Science, 2020. 530: p. 147164.

161. Fang, M., C. Zhang, and Q. Chen, Tuning the ITO work function by capacitively coupled plasma and its application in inverted organic solar cells. Applied Surface Science, 2016. 385: p. 28-33.

162. Yu, S., et al., Improved chemical stability of ITO transparent anodes with a SnO2 buffer layer for organic solar cells. Solar Energy Materials and Solar Cells, 2016. 144: p. 652-656.

163. Lei, T., et al., 13.5% flexible organic solar cells achieved by robust composite ITO/PEDOT:PSS electrodes. Materials Today Energy, 2019. 14: p. 100334.

164. Knesting, K.M., et al., ITO Interface Modifiers Can Improve VOC in Polymer Solar Cells and Suppress Surface Recombination. The Journal of Physical Chemistry Letters, 2013. 4(23): p. 4038-4044.

165. Jiang, C.Y., et al., Low work function metal modified ITO as cathode for inverted polymer solar cells. Solar Energy Materials and Solar Cells, 2010. 94(10): p. 1618-1621.

166. Tan, Z.a., et al., High-Performance Inverted Polymer Solar Cells with Solution-Processed Titanium Chelate as Electron-Collecting Layer on ITO Electrode. Advanced Materials, 2012. 24(11): p. 1476-1481.

167. Tan, Z.a., et al., Solution-processed vanadium oxide as a hole collection layer on an ITO electrode for high-performance polymer solar cells. Physical Chemistry Chemical Physics, 2012. 14(42): p. 14589-14595.

168. Sun, J., et al., High Efficiency and High Voc Inverted Polymer Solar Cells Based on a Low-Lying HOMO Polycarbazole Donor and a Hydrophilic Polycarbazole Interlayer on ITO Cathode. The Journal of Physical Chemistry C, 2012. 116(27): p. 14188-14198.

169. Lei, H., et al., Performance enhancement of polymer solar cells with high work function CuS modified ITO as anodes. Organic Electronics, 2015. 22: p. 173-179.

170. Morvillo, P., et al., Influence of annealing treatments on solution-processed ZnO film deposited on ITO substrate as electron transport layer for inverted polymer solar cells. Solar Energy Materials and Solar Cells, 2015. 141: p. 210-217.

171. Shikoh, A.S., et al., Optimization of ITO glass/TiO2 based DSSC photo-anodes through electrophoretic deposition and sintering techniques. Ceramics International, 2017. 43(13): p. 10540-10545.

172. Diantoro, M., et al., Performance of Pterocarpus Indicus Willd Leaf Extract as Natural Dye TiO2-Dye/ITO DSSC. Materials Today: Proceedings, 2019. 17: p. 1268-1276.

173. Mazalan, M., et al. Development of dye-sensitized solar cell (DSSC) using patterned indium tin oxide (ITO) glass: fabrication and testing of DSSC. in 2013 IEEE Conference on Clean Energy and Technology (CEAT). 2013.

174. Dhamodharan, P., et al., Al-doped ZnO thin films grown onto ITO substrates as photoanode in dye sensitized solar cell. Solar Energy, 2017. 141: p. 127-144.

175. Hino, T., Y. Ogawa, and N. Kuramoto, Preparation of functionalized and non-functionalized fullerene thin films on ITO glasses and the application to a counter electrode in a dye-sensitized solar cell. Carbon, 2006. 44(5): p. 880-887.

176. Yengantiwar, A., et al., Growth of aligned ZnO nanorods array on ITO for dye sensitized solar cell. Current Applied Physics, 2011. 11(1, Supplement): p. S113-S116.

177. Dhamodharan, P., et al., Preparation and characterization of spray deposited Sn-doped ZnO thin films onto ITO subtracts as photoanode in dye sensitized solar cell. Journal of Materials Science: Materials in Electronics, 2015. 26(7): p. 4830-4839.

178. Lee, A.R., et al., Study of Double Layer Indium Tin Oxide in Silicon Hetero-Junction Solar Cells. Journal of Nanoscience and Nanotechnology, 2020. 20(1): p. 161-167.

179. Zahid, M.A., et al., Utilization of CaF2/ITO Double-Layer Anti-Reflective Coating for Increasing the Efficiency in Rear Emitter SHJ Solar Cells. Crystal Research and Technology, 2022. 57(8): p. 2100233.

180. Luderer, C., et al., Influence of TCO and a-Si:H Doping on SHJ Contact Resistivity. IEEE Journal of Photovoltaics, 2021. 11(2): p. 329-336.

181. Herasimenka, S.Y., et al., ITO/SiOx:H stacks for silicon heterojunction solar cells. Solar Energy Materials and Solar Cells, 2016. 158: p. 98-101.

182. Cruz, A., et al., Influence of Silicon Layers on the Growth of ITO and AZO in Silicon Heterojunction Solar Cells. IEEE Journal of Photovoltaics, 2020. 10(2): p. 703-709.

183. Du, G., et al., Surface Passivation of ITO on Heterojunction Solar Cells with Enhanced Cell Performance and Module Reliability. ECS Journal of Solid State Science and Technology, 2021. 10(3): p. 035008.

184. Li, S., et al., Comparison of ITO, In2O3:Zn and In2O3:H transparent conductive oxides as front electrodes for silicon heterojunction solar cell applications. Vacuum, 2017. 145: p. 262-267.

185. Lee, D., A. Lee, and H.D. Kim, IZO/ITO Double-Layered Transparent Conductive Oxide for Silicon Heterojunction Solar Cells. IEEE Access, 2022. 10: p. 77170-77175.

186. Donercark, E., et al. Enhanced Passivation Properties of a-Si:H and Reactive ITO Sputtering for SHJ Solar Cells. in 2020 47th IEEE Photovoltaic Specialists Conference (PVSC). 2020.

187. Chebotareva, A.B., et al., Bifacial silicon heterojunction solar cells with advanced Ag-free multi-wire metallization attached to ITO layers using new transparent conductive PAEK copolymers. Solar Energy, 2019. 193: p. 828-836.

188. Zahid, M.A., et al., Improved optical and electrical properties for heterojunction solar cell using Al2O3/ITO double-layer anti-reflective coating. Results in Physics, 2021. 28: p. 104640.

189. Kim, D.-H.K., Gi-Yong Transparent Conducting Zinc-Tin-Oxide Layer for Application to Blue Light Emitting-diode. Proceedings of the Korean Vacuum Society Conference, 2014. 2014.02a: p. 346.2-346.2.

190. Esro, M., et al., Solution processed SnO2:Sb transparent conductive oxide as an alternative to indium tin oxide for applications in organic light emitting diodes. Journal of Materials Chemistry C, 2016. 4(16): p. 3563-3570.

191. Lee, H., et al., Improved Efficiency of Inverted Organic Light-Emitting Diodes Using Tin Dioxide Nanoparticles as an Electron Injection Layer. ACS Applied Materials & Interfaces, 2013. 5(6): p. 1977-1981.

192. Hun Park, J., et al., Effect of deposition temperature on the formation of the corrosion-protective SnOx:F coating layer on SUS 316 bipolar plates for PEMFC. Physica Scripta, 2010. 2010(T139): p. 014020.

193. Cheng, C., et al., Amorphous Sn(HPO4)2-derived phosphorus-modified Sn/SnOx core/shell catalyst for efficient CO2 electroreduction to formate. Journal of Energy Chemistry, 2023.

194. R., K., et al., Effects of deposition temperature on the structural and morphological properties of SnO2 films fabricated by pulsed laser deposition. Opt. Laser Technol., 2009. 41: p. 89.

195. S., Y., et al., Transparent conducting Sb-doped SnO2 thin films grown by pulsed laser deposition. J. Non-Crystall. Solids, 2012. 358: p. 3137.

196. Jiang, J.C., K. Lian, and E.I. Meletis, Influence of oxygen plasma treatment on the microstructure of SnOx thin films. Thin Solid Films, 2002. 411(2): p. 203-210.

197. H., E., N. T., and E. J., The electrical and optical properties of the ZnO-SnO2 thin films prepared by rf magnetron sputtering. Phys. Status Solidi (a), 1992. 129: p. 181.

198. A., A., et al., Study of topological morphology and optical properties of SnO2 thin films deposited by rf sputtering technique. J. Lumin., 2015. 158: p. 165.

199. S., H. and A. M., Effects of temperature and rf power sputtering on electrical and optical properties of SnO2. Appl. Energy, 2000. 65: p. 19.

200. Belayachi, W., et al., SnO2 Films Elaborated by Radio Frequency Magnetron Sputtering as Potential Transparent Conducting Oxides Alternative for Organic Solar Cells. ACS Applied Energy Materials, 2022. 5(1): p. 170-177.

201. Kim, C., S. Kim, and S.E. Kim, Transparent SnOx thin films fabricated by radio frequency reactive sputtering with a SnO/Sn composite target. Thin Solid Films, 2017. 634: p. 175-180.

202. Wu, Q.-H., et al., Nano-particle thin films of tin oxides. Materials Letters, 2007. 61(17): p. 3679-3684.

203. M., B., B.J. M., and D. U., Pure and cobalt-doped SnO2 (101) films grown by molecular beam epitaxy on Al2O3. Thin Solid Films, 2005. 484: p. 132.

204. M., T., W. M., and S. J., Plasma-assisted molecular beam epitaxy of SnO2 on TiO2. J. Cryst. Growth, 2008. 310: p. 4256.

205. T., W., et al., Molecular beam epitaxy growth of SnO2 using a tin chemical precursor. J. Vac. Sci. Technol. A, 2015. 33: p. 020606.

206. R., D., et al., Metal organic precursor effect on the properties of SnO2 thin films deposited by MOCVD technique for electrochemical applications. Surf. Coat. Technol., 2015. 271: p. 234.

207. Z., Z., et al., Structure and photoluminescence properties of epitaxial SnO2 films grown on α-Al2O3 (0 1 2) by MOCVD. J. Lumin., 2011. 131: p. 88.

208. Talaty, N.N., et al., Characterization of Tin(IV) Oxide Thin Films Prepared by Atmospheric Pressure Chemical Vapor Deposition of cis-[SnCl4{OC(H)OC2H5}2]. Zeitschrift für anorganische und allgemeine Chemie, 2009. 635(1): p. 53-63.

209. V., A., et al., Atomic layer deposited (ALD) SnO2 anodes with exceptional cycleability for Li-ion batteries. Nano Energy, 2013. 2: p. 720.

210. Marikkannan, M., et al., A novel synthesis of tin oxide thin films by the sol-gel process for optoelectronic applications. AIP Advances, 2015. 5(2): p. 027122.

211. F., G., et al., Luminescence of SnO2 thin films prepared by spin-coating method. J. Cryst. Growth, 2004. 262: p. 182.

212. T., S., et al., Electrical, structural and optical properties of SnO2 thin films prepared by spray pyrolysis. J. Non-Cryst. Solids, 2006. 352: p. 209.

213. Singh, S.K. and S. Basu, Characterisation of conducting SnO2layers deposited by modified spray pyrolysis technique. Materials Chemistry and Physics, 1988. 20(4): p. 381-396.

214. Olayinka Oluwatosin, A., et al., Overview of thin film deposition techniques. AIMS Materials Science, 2019. 6(2): p. 174-199.

215. Seshan, K., Handbook of Thin Film Deposition Techniques Principles, Methods, Equipment and Applications, Second Editon. 2002: p. 72.

216. Ulf Seyfert, U.H., Götz Teschner, Johannes Strümpfel, 40 Years of Industrial Magnetron Sputtering in Europe. SVC Bulletin Fall 2015, 2015: p. 22.

217. Tudose, I.V., et al., Chapter 2 - Chemical and physical methods for multifunctional nanostructured interface fabrication, in Functional Nanostructured Interfaces for Environmental and Biomedical Applications, V. Dinca and M.P. Suchea, Editors. 2019, Elsevier. p. 15-26.

218. Oke, J.A. and T.-C. Jen, Atomic layer deposition and other thin film deposition techniques: from principles to film properties. Journal of Materials Research and Technology, 2022. 21: p. 2481-2514.

219. Spencer, J.A., et al., A review of band structure and material properties of transparent conducting and semiconducting oxides: Ga2O3, Al2O3, In2O3, ZnO, SnO2, CdO, NiO, CuO, and Sc2O3

Vesta 3 for three-dimensional visualization of crystal, volumetric and morphology data. Applied Physics Reviews, 2022. 9(1): p. 011315.

220. Mishra, K.C., K.H. Johnson, and P.C. Schmidt, Electronic structure of antimony-doped tin oxide. Physical Review B, 1995. 51(20): p. 13972-13976.

221. Miglio, A., et al., Computed electronic and optical properties of SnO2 under compressive stress. Optical Materials, 2014. 38: p. 161-166.

222. Sivakumar, P., et al., Influence of Ga doping on structural, optical and electrical properties of transparent conducting SnO2 thin films. Optik, 2021. 226: p. 165859.

223. Tao, Y., et al., The structural, electrical, and optical properties of SnO2 films prepared by reactive magnetron sputtering: Influence of substrate temperature and O2 flow rate. Materials Chemistry and Physics, 2020. 250: p. 123129.

224. Soumya, S.S., Highly transparent amorphous tin oxide thin films by sol-gel spin coating technique. AIP Conference Proceedings, 2021. 2369(1): p. 020002.

225. Yadava, Y.P., et al., Preparation and characterization of transparent conducting tin oxide thin film electrodes by chemical vapour deposition from reactive thermal evaporation of SnCl2. Materials Chemistry and Physics, 1997. 48(3): p. 263-267.

226. Yadav, J.B., et al., Studies on undoped SnO2 thin film deposited by chemical reactive evaporation method. Materials Science and Engineering: B, 2007. 139(1): p. 69-73.

227. Khallaf, H., et al., Chemical bath deposition of SnO2 and Cd2SnO4 thin films. Applied Surface Science, 2012. 258(16): p. 6069-6074.

228. Muranaka, S., Y. Bando, and T. Takada, Preparation by reactive deposition and some physical properties of amorphous tin oxide films and crystalline SnO2 films. Thin Solid Films, 1981. 86(1): p. 11-19.

229. Moholkar, A.V., et al., Effect of concentration of SnCl4 on sprayed fluorine doped tin oxide thin films. Journal of Alloys and Compounds, 2008. 455(1): p. 440-446.

230. Babar, A.R., et al., Physical properties of sprayed antimony doped tin oxide thin films: The role of thickness. Journal of Semiconductors, 2011. 32(5): p. 053001.

231. Hossain, M.F., et al., Transparent conducting SnO2 thin films synthesized by nebulized spray pyrolysis technique: Impact of Sb doping on the different physical properties. Materials Science in Semiconductor Processing, 2021. 121: p. 105346.

232. Kykyneshi, R., J. Zeng, and D.P. Cann, Transparent Conducting Oxides Based on Tin Oxide, in Handbook of Transparent Conductors, D.S. Ginley, Editor. 2011, Springer US: Boston, MA. p. 171-191.

233. Ramarajan, R., et al., Substrate Temperature Dependent Physical Properties of Spray Deposited Antimony-Doped SnO2 Thin Films. Thin Solid Films, 2020. 704: p. 137988.

234. Ramarajan, R., et al., Boltzmann conductivity approach for charge transport in spray-deposited transparent Ta-doped SnO2 thin films. Journal of Alloys and Compounds, 2022. 897: p. 163159.

235. Mrabet, C., et al., Improvement of the optoelectronic properties of tin oxide transparent conductive thin films through lanthanum doping. Journal of Alloys and Compounds, 2016. 666: p. 392-405.

236. Vishwakarma, S.R., J.P. Upadhyay, and H.C. Prasad, Physical properties of arsenic-doped tin oxide thin films. Thin Solid Films, 1989. 176(1): p. 99-110.

237. Li, B.-j., et al., Influences of ultrasonic vibration on morphology and photoelectric properties of F-doped SnO2 thin films during laser annealing. Applied Surface Science, 2018. 458: p. 940-948.

238. Tran, Q.-P., J.-S. Fang, and T.-S. Chin, Properties of fluorine-doped SnO2 thin films by a green sol–gel method. Materials Science in Semiconductor Processing, 2015. 40: p. 664-669.

239. Fauzia, V., et al., High figure of merit transparent conducting Sb-doped SnO2 thin films prepared via ultrasonic spray pyrolysis. Journal of Alloys and Compounds, 2017. 720: p. 79-85.

240. Chan y Díaz, E., et al., Influence of the oxygen pressure on the physical properties of the pulsed-laser deposited Te doped SnO2 thin films. Journal of Alloys and Compounds, 2010. 508(2): p. 342-347.

241. Graužinytė, M., S. Goedecker, and J.A. Flores-Livas, Computational Screening of Useful Hole–Electron Dopants in SnO2. Chemistry of Materials, 2017. 29(23): p. 10095-10103.

242. Lai, K., et al., Effect of oxygen vacancy and Al-doping on the electronic and optical properties in SnO2. Physica B: Condensed Matter, 2013. 428: p. 48-52.

243. Ni, J., et al., Electrical, structural, photoluminescence and optical properties of p-type conducting, antimony-doped SnO2 thin films. Acta Materialia, 2009. 57(1): p. 278-285.

244. T., L., et al., A study of structural, electrical, and optical properties of p-type Zn-doped SnO2 films versus deposition and annealing temperature. J. Phys. D: Appl. Phys., 2017. 50: p. 145102.

245. C.-Y., T. and L. S.-C., Fabrication of p-type conductivity in SnO2 thin films through Ga doping. J. Alloys Compd., 2015. 622: p. 644.

246. Albanese, E., et al., Nature of Paramagnetic Species in Nitrogen-Doped SnO2: A Combined Electron Paramagnetic Resonance and Density Functional Theory Study. The Journal of Physical Chemistry C, 2015. 119(48): p. 26895-26903.

247. Watanabe, K., et al., p-type conversion of distorted SnOx thin film by mild thermal annealing treatment in pure N2 environment. AIP Advances, 2022. 12(10): p. 105102.

248. Pan, S.S., et al., Atomic nitrogen doping and p-type conduction in SnO2. Applied Physics Letters, 2009. 95(22): p. 222112.

249. Kim, Y., et al., Nitrogen-doped transparent tin oxide thin films deposited by sputtering. Current Applied Physics, 2011. 11(4, Supplement): p. S139-S142.

250. Ding, X., F. Fang, and J. Jiang, Electrical and optical properties of N-doped SnO2 thin films prepared by magnetron sputtering. Surface and Coatings Technology, 2013. 231: p. 67-70.

251. Fang, F., et al., Electrical and optical properties of nitrogen doped SnO2 thin films deposited on flexible substrates by magnetron sputtering. Materials Research Bulletin, 2015. 68: p. 240-244.

252. Sun, X., et al., Structural, Electronic, and Optical Properties of N-doped SnO2. The Journal of Physical Chemistry C, 2008. 112(26): p. 9861-9864.

253. Dang, H.P., et al., Eliminating the charge compensation effect in Ga-doped SnO2 films by N doping. Journal of Alloys and Compounds, 2019. 776: p. 276-286.

254. Liu, X., et al., Preparation and characterization of p-type semiconducting tin oxide thin film gas sensors. Journal of Applied Physics, 2010. 107(6): p. 064309.

255. Yang, T., et al., Preparation and characterization of p-type transparent conducting SnO thin films. Materials Letters, 2015. 139: p. 39-41.

256. Bao, S., et al., Zn-doped Tin monoxide nanobelt induced engineering a graphene and CNT supported Zn-doped Tin dioxide composite for Lithium-ion storage. Journal of Colloid and Interface Science, 2022. 608: p. 768-779.

257. Lee, H.-N., H.-J. Kim, and C.-K. Kim, p-Channel Tin Monoxide Thin Film Transistor Fabricated by Vacuum Thermal Evaporation. Japanese Journal of Applied Physics, 2010. 49(2R): p. 020202.

258. Caraveo-Frescas, J.A., et al., Record Mobility in Transparent p-Type Tin Monoxide Films and Devices by Phase Engineering. ACS Nano, 2013. 7(6): p. 5160-5167.

259. Liao, M., et al., Effects of Pb Doping on Hole Transport Properties and Thin-Film Transistor Characteristics of SnO Thin Films. ECS Journal of Solid State Science and Technology, 2015. 4(3): p. Q26.

260. Kim, H.J., et al., Charge Transport Mechanism in p-Channel Tin Monoxide Thin-Film Transistors. IEEE Electron Device Letters, 2017. 38(4): p. 473-476.

261. Rockelé, M., et al., Integrated Tin Monoxide P-Channel Thin-Film Transistors for Digital Circuit Applications. IEEE Transactions on Electron Devices, 2018. 65(2): p. 514-519.

262. Ogo, Y., et al., Tin monoxide as an s-orbital-based p-type oxide semiconductor: Electronic structures and TFT application. physica status solidi (a), 2009. 206(9): p. 2187-2191.

263. Barros, R., et al., Role of Structure and Composition on the Performances of P-Type Tin Oxide Thin-Film Transistors Processed at Low-Temperatures. Nanomaterials, 2019. 9(3): p. 320.

264. Hsu, P.-C., et al., Sputtering deposition of P-type SnO films using robust Sn/SnO2 mixed target. Thin Solid Films, 2014. 555: p. 57-61.

265. Kim, T., et al., Origin of Ambipolar Behavior in p-Type Tin Monoxide Semiconductors: Impact of Oxygen Vacancy Defects. IEEE Transactions on Electron Devices, 2021. 68(9): p. 4467-4472.

266. Toyama, T., et al., Optical absorption spectra of P-type Tin monoxide thin films around their indirect fundamental gaps determined using photothermal deflection spectroscopy. Thin Solid Films, 2014. 555: p. 148-152.

267. Kim, Y., et al., Nitrogen doped p-type SnO thin films deposited via sputtering. Materials Science and Engineering: B, 2012. 177(16): p. 1470-1475.

268. Hsu, P.-C., et al., Sputtering Deposition of P-Type SnO Films with SnO2 Target in Hydrogen-Containing Atmosphere. ACS Applied Materials & Interfaces, 2014. 6(16): p. 13724-13729.

269. Um, J. and S.E. Kim, Homo-Junction pn Diode Using p-Type SnO and n-Type SnO2 Thin Films. ECS Solid State Letters, 2014. 3(8): p. P94.

270. Sanal, K.C. and M.K. Jayaraj, Growth and characterization of tin oxide thin films and fabrication of transparent p-SnO/n-ZnO p–n hetero junction. Materials Science and Engineering: B, 2013. 178(12): p. 816-821.

271. Hsu, P.-C., et al., Film Texture, Hole Transport and Field-Effect Mobility in Polycrystalline SnO Thin Films on Glass. ECS Journal of Solid State Science and Technology, 2014. 3(9): p. Q3040.

272. Hosono, H., et al., Bipolar Conduction in SnO Thin Films. Electrochemical and Solid-State Letters, 2011. 14(1): p. H13.

273. Patil, R.B., R.K. Puri, and V. Puri, Physical properties of tin oxide thin films improved by vapour chopping. Journal of Alloys and Compounds, 2008. 463(1): p. 453-457.

274. Geurts, J., et al., SnO films and their oxidation to SnO2: Raman scattering, IR reflectivity and X-ray diffraction studies. Thin Solid Films, 1984. 121(3): p. 217-225.

275. Ullah, S., et al., Structure and electronic properties of tin monoxide (SnO) and lithiated SnO terminated diamond (100) and its comparison with lithium oxide terminated diamond. Applied Surface Science, 2021. 559: p. 149962.

276. Guo, W., et al., Microstructure, optical, and electrical properties of p-type SnO thin films. Applied Physics Letters, 2010. 96(4): p. 042113.

277. Liang, L.Y., et al., Microstructural, Optical, and Electrical Properties of SnO Thin Films Prepared on Quartz via a Two-Step Method. ACS Applied Materials & Interfaces, 2010. 2(4): p. 1060-1065.

278. Liu, Q., et al., Tunable crystallographic grain orientation and Raman fingerprints of polycrystalline SnO thin films. Journal of Materials Chemistry C, 2015. 3(5): p. 1077-1081.

279. Myeonghun, U., et al., High Performance p-type SnO thin-film Transistor with SiO_x Gate Insulator Deposited by Low-Temperature PECVD Method. JOURNAL OF SEMICONDUCTOR TECHNOLOGY AND SCIENCE, 2014. 14(5): p. 666-672.

280. Han, J.H., et al., Growth of p-Type Tin(II) Monoxide Thin Films by Atomic Layer Deposition from Bis(1-dimethylamino-2-methyl-2propoxy)tin and H2O. Chemistry of Materials, 2014. 26(21): p. 6088-6091.

281. Dai, G., et al., Structure and magnetic properties of Cr-Doped tin monoxide prepared by hydrothermal method. Ceramics International, 2020. 46(9): p. 13350-13355.

282. Eqbal, E. and E.I. Anila, Properties of transparent conducting tin monoxide(SnO) thin films prepared by chemical spray pyrolysis method. Physica B: Condensed Matter, 2018. 528: p. 60-65.

283. Sun, J., et al., Formaldehyde assisted reduction achieved p-type orthorhombic tin oxide film prepared by an inexpensive chemical method. Materials Research Express, 2017. 4(11): p. 116411.

284. The Materials, P., Materials Data on SnO by Materials Project. 2020: United States.

285. Saji, K.J., et al., P-type SnO thin films and SnO/ZnO heterostructures for all-oxide electronic and optoelectronic device applications. Thin Solid Films, 2016. 605: p. 193-201.

286. Walsh, A., et al., Stereochemistry of post-transition metal oxides: revision of the classical lone pair model. Chemical Society Reviews, 2011. 40(9): p. 4455-4463.

287. McLeod, J.A., et al., Chemical Bonding and Hybridization in 5p Binary Oxide. The Journal of Physical Chemistry C, 2012. 116(45): p. 24248-24254.

288. Li, K., et al., Crystal and electronic structure engineering of tin monoxide by external pressure. Journal of Advanced Ceramics, 2021. 10(3): p. 565-577.

289. Graužinytė, M., S. Goedecker, and J.A. Flores-Livas, Towards bipolar tin monoxide: Revealing unexplored dopants. Physical Review Materials, 2018. 2(10): p. 104604.

290. Allen, J.P., et al., Understanding the defect chemistry of tin monoxide. Journal of Materials Chemistry C, 2013. 1(48): p. 8194-8208.

291. Togo, A., et al., First-principles calculations of native defects in tin monoxide. Physical Review B, 2006. 74(19): p. 195128.

292. Wang, Y.R., S. Li, and J.B. Yi, Transition Metal-Doped Tin Monoxide Monolayer: A First-Principles Study. The Journal of Physical Chemistry C, 2018. 122(8): p. 4651-4661.

293. Granato, D.B., et al., Enhancement of p-type mobility in tin monoxide by native defects. Applied Physics Letters, 2013. 102(21): p. 212105.

294. Meyer, M., et al., Ab initio pseudopotential calculation of the equilibrium structure of tin monoxide. Physical Review B, 2001. 64(4): p. 045119.

295. Kripalani, D.R., et al., Vacancies and dopants in two-dimensional tin monoxide: An ab initio study. Applied Surface Science, 2021. 538: p. 147988.

296. Allen, J.P., et al., Tin Monoxide: Structural Prediction from First Principles Calculations with van der Waals Corrections. The Journal of Physical Chemistry C, 2011. 115(40): p. 19916-19924.

297. Wanzhong, L., S. Jian, and D. Chong, Layer-dependent electronic and optical properties of tin monoxide: a potential candidate in photovoltaic applications. Physical Chemistry Chemical Physics, 2022. 24(13): p. 7611-7616.

298. Tariq, Z., et al., First-principles study of electronic and optical properties of sulfur doped tin monoxide: A potential applicant for optoelectronic devices. Ceramics International, 2019. 45(6): p. 7495-7503.

299. Watson, G.W., The origin of the electron distribution in SnO. The Journal of Chemical Physics, 2001. 114(2): p. 758-763.

300. Fortunato, E., P. Barquinha, and R. Martins, Oxide Semiconductor Thin-Film Transistors: A Review of Recent Advances. Advanced Materials, 2012. 24(22): p. 2945-2986.

301. Haacke, G., *New figure of merit for transparent conductors.* Journal of Applied Physics, 1976. **47**(9): p. 4086-4089.

Chapter 2: Growth and Characterization of undoped tin oxide (SnO_x) films

2. Growth and Characterization of undoped tin oxide (SnO_x) films

2.1. Introduction

Transparent conductive oxides (TCOs) are imperative materials in various technologies requiring optical transparency and electrical conductivity. In addition to these two characteristics, TCOs combine a third property, namely a high chemical stability. More specifically, owing to its optoelectronic properties and its production scalability, tin-doped indium oxide (ITO) is a preferred TCO for industrial applications and it has been extensively employed as transparent electrodes for various solar cell technologies, light emitting diodes and flat panel displays[1-11]. However, researchers are working on the development of alternatives materials to ITO due to the Indium (In) supply challenges in the future. Tin, instead, is a low-cost material of much higher earth abundance than Indium. Two stoichiometric tin oxide compounds, namely SnO and SnO_2, are known to be wide band gap oxide semiconductors with tetragonal litharge and rutile type structures, respectively. Tin in SnO_x has two chemical states of Sn^{2+} for SnO phase and Sn^{4+} for the SnO_2 one. The first is intrinsically p-type semiconductor while the second is n-type[12, 13].

In particular, SnO_x has been largely investigated in applications of gas sensors, solar cells, transparent electrodes, and thin film transistors [11, 14-20]. Moreover, in the past decades, SnO has been the key material for anode materials [21], coatings [22], catalysis [23], and precursors for the production of SnO_2 [24, 25], because of its properties of gas-sensitivity and metastability to transform into SnO_2 at O_2-rich ambient. Recently, SnO has been drawn back into attention mainly because of the difficulty in obtaining high-quality p-type such as doped ZnO [26, 27], NiO [28, 29], Cu_2O [30]. Previous studies show that the maximum hole mobility of SnO films is about 2.6 $cm^2/V\cdot s$, fairly high among p-type conductive oxides, and it can be further improved via proper doping [19]. Those properties render SnO a promising candidate to be a next p-type oxide semiconductor for advanced optoelectronic devices. Several techniques have been used to grow SnO_x films on various substrates, including reactive RF magnetron sputtering (MS) [31], e-beam evaporation [18], laser ablation [25], and atomic layer deposition [32]. However, the prepared SnO_x films are often mixed with some impurity phases, including metallic Sn, SnO_2, and intermediate oxides containing both 2^+ and 4^+ valences [31, 33, 34]. The reason is that SnO can decompose according to the disproportion at ion reaction even in the absence of oxygen at suitable temperature [16, 17]. Consequently, deposition conditions and growth temperature are of great importance in the fabrication of single phase SnO_x films.

In this chapter, the synthesis of tin oxide thin films to achieve both phases of Sn(IV)O_2 and Sn(II)O is presented in detail. The SnO_x synthesis is carried out by reactive magnetron sputtering via two routes. The first is to deposit SnO_x by reactive sputtering of oxidized target of SnO while the second route is the deposition by reactive sputtering of metallic target. Through these two routes, different growth conditions and post-deposition annealing effects are investigated with material characterization techniques. In addition to the sputtering target material, the growth conditions, to be varied, are substrate temperature, O_2/Ar flow rate ratio, and post-deposition thermal annealing. All samples are deposited on amorphous quartz which is highly resistive and has a constant high optical transmittance in infrared, visible and a significant part of the ultraviolet to avoid any electrical or optical interference with the grown tin oxide films.

In the first part, different polycrystalline SnO_x thin films were fabricated on quartz substrates by a two-step method, i.e., RF MS from high-purity SnO source target first and subsequent air and vacuum annealing treatments. The optimized conditions were clearly defined and discussed thoroughly. In the second part, different polycrystalline SnOx thin film were synthetised using one step-method of magnetron sputtering where the effect of O_2/Ar flow rate ratio and substrate temperature at poor-oxygen condition were investigated. In the third part, the effect of thermal annealing on grown SnO_x thin film by magnetron sputtering was explored to achieve and understand the mechanism to form a p-type conductivity. In the last part, the ageing and heating effects were assessed to investigate certain aspects of instability related to grown SnO_x thin films.

In this chapter, material characterization will be conducted on all samples to explore their morphology, crystal phase, chemical composition, optical, and electrical properties of the obtained SnO_x thin films were characterized by Grazing Incidence X-Ray Diffraction (GIXRD), Scanning Electron Microscopy (SEM), Transmitting Electron Microscopy (TEM), UV-Visible spectroscopy (UV-Vis), and Hall effect measurement, X-ray Photoelectron Spectroscopy (XPS), Transmission Electron Microscopy (TEM) as detailed in the experimental section.SnO_x sputtered using an oxidized target (SnO)

2.2. Materials and Methods

2.2.1. Material Synthesis

As part of this thesis work, various deposition techniques were explored to synthetize, tune and optimize SnO_x thin films, namely, hydrothermal process, spin coating, ion layer gas reaction (ILGAR) set-up, e-beam evaporator, and magnetron sputtering. While this exercise was worthwhile to be exposed to the advantages and challenges of each deposition techniques, magnetron sputtering stood out as the most effective technique as it is an affordable and scalable physical vacuum-based technique which enables the deposition of consistent, reproducible, high purity and quality films and it has several parameters of adjustment which allows the tuning of the material properties. In the following, the synthesis of SnO_x films was achieved using two magnetron sputtering instruments namely, Orion 3 device from AJA International Co. and Torr International system. The parameters of magnetron sputtering for each study will be presented in detail in each section.

2.2.2. Material Characterization

Several characterization techniques were employed to investigate the micro-structure, crystalline structure, optical transmittance and bandgap, resistivity, charge carrier concentration and mobility, and elemental depth profiles.

GIXRD has been conducted using Rigaku – Smartlab along with ICCD – PDF crystallography data base. The X-ray source is Cu K-alpha at 1.54 Å, the 2θ scans of the detector are from 15 to 65°, the step and the speed are 0.02° and 2°/min while the X-ray incident beam was kept at 0.55°. UV-Visible Spectroscopy was performed using Perkin Elmer - Lamda 1050, using 4 nm steps. Electrical properties were conducted for all samples using benchtop four-point probe system and Hall effect - Lakeshore 8400. Depth profiles were obtained using ToF-SIMS[5] - IONTOF. Scanning/Transmission Electron Microscopy (SEM/TEM) images were obtained using FEI - Quanta 650/Talos, respectively. TEM lamella has been prepared by Focused Ion Beam (FIB)/SEM. The process consists of coating the SnO_x film by a protective Pt layer. Then, the whole stack Pt/SnO_2/Substrate undergoes the thinning process to reach a convenient vertical thickness for the TEM imaging. TOF-SIMS analysis was performed by positive Bi^+ ion primary beam at 30 keV and ~1.3 pA current over a 100×100 μm^2 analysed area using random rastering mode while the sputtering was achieved using Cs^+ ion beam at 30 keV over 400 x 400 μm^2. The depth profile has been conducted in positive polarity which targets the positive ions emerging from the surface at each etched level. The chemical state analysis of all samples was conducted by X-ray Photoelectron Spectroscopy (XPS) (ESCALAB250Xi Thermo-Fisher-Scientific - UK) using Avantage software and database as well as XPS NIST database. Pass Energy for high resolution scans is 20 eV and for survey scans is 100 eV. XPS equipment was calibrated using triple high purity standards (Gold, Silver, and Copper). All samples were referenced using C1s at 284.8 eV.

2.3. SnO_x sputtered using an oxidized target (SnO)

2.3.1. SnO_x thin film synthesis

The SnO_x thin films were prepared in two subsequent steps. The first step consists of the thin film deposition by Radio Frequency (RF) magnetron sputtering, manufactured by Torr (described in the appendix in section 1.3.), with a high purity SnO (99.99%) 2”- diameter sputtering target (Manufactured by Codex International) on 1” × 3” cleaned quartz substrates at two different temperatures, namely 100 and 250 °C, under different O_2 to Ar flow rates ratios O_2/Ar = 0, 0.005, 0.015, 0.025, 0.045 and 0.075. The Ar flow rate was fixed at 200 sccm. Each sample was cut into three 1” × 1” smaller samples.

The second step consists of two different post deposition annealing at 400 °C for 1 h, one in air and the other one in a controlled moderate vacuum (with a constant Ar flow of 5 sccm) at 6.66 x 10^{-2} Pa as shown in Diagram 1 and table 1.

The depositions conditions using RF magnetron sputtering were: 50 W power, 200 sccm of Ar flow and 30 min deposition time for all samples. The first batch was deposited at 100 °C, and the second batch was deposited at 250 °C. Prior to the deposition, the base pressure of 6.66 × 10^{-3} Pa was first achieved, and the deposition pressure, which depends on the variable oxygen flow rate, varied from 0.59 to 0.68 Pa for the chamber's pumping.

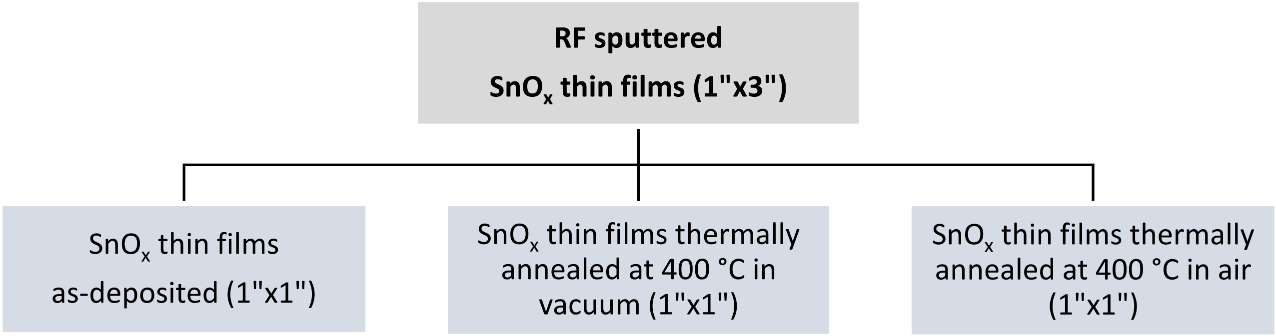

Diagram 1: Samples preparation, growth and annealing conditions.

Sample	Substrate Temp (°C)	O_2/Ar (Ar:O_2 sccm)	Depos. Pressure (Pa)	Thickness (nm)
S0	100	0 (200:0)	0.59	100
S1		0.005 (200:1)	0.60	242
S2		0.015 (200:3)	0.61	255
S3		0.025 (200:5)	0.63	277
S4		0.045 (200:9)	0.67	199
S5		0.075 (200:15)	0.68	153
E0	250	0 (200:0)	0.59	143
E1		0.005 (200:1)	0.60	170
E2		0.015 (200:3)	0.61	149
E3		0.025 (200:5)	0.63	181
E4		0.045 (200:9)	0.65	108
E5		0.075 (200:15)	0.68	163

Table 1: Summary of the RF sputtering conditions and thickness of samples.

Following a first visual observations just after the SnO_x deposition, all the samples looked homogenous and most of the films had the yellowish colour which is a typical characteristic of SnO_x material.

2.3.2. Structural properties by GIXRD

For the as-deposited SnO_x at 100 °C, the samples do not show any XRD sharp peak, thereby indicating the low crystalline quality and/or the amorphous structure of this series (Figure 1a). The sample deposited without O_2 flow has a broad peak at around 30° revealing the presence of a very low crystalline structure of SnO. The XRD pattern for SnO_x samples deposited in presence of O_2 show a low crystalline SnO_2 phase due to the shift of the broad peak from 30 to 34°. It is worth to note that the XRD pattern did not change while increasing the O_2/Ar flow rate ratio from 0.005 to 0.075, which may indicate that increasing the O_2 flow does not improve the crystalline microstructure of SnO_x at this deposition temperature of 100 °C.

For SnO_x samples deposited at 100 °C and annealed at 400 °C under air, all samples show a remarkable improved crystallinity (Figure 1e). For air annealed SnO_x deposited without O_2 flow, there are two highly crystalline phases of SnO and SnO_2 as revealed by the presence of sharp peaks located at 29.9° indicating SnO and at 33.9° indicating SnO_2. The crystallite size related to SnO_2 (110) peak drastically decreases from 116 Å to 51 Å when O_2/Ar goes from 0 to 0.005. Then, it increases slightly up to 62 Å when O_2/Ar varies from 0.005 to 0.025 and it decreases to 57 Å when O_2/Ar goes from 0.025 to 0.075. The sharp peak located at 26.6° and corresponding to the (110) plane of SnO_2 deposited without O_2, represents the highest crystallite size of all the deposited SnO_x samples.

For as-deposited SnO_x at 250 °C (Figure 1b), the samples deposited at O_2/Ar ratios equal or above 0.005 have an XRD pattern which shows at least one peak, and the most intense peak located at 34° and corresponding to the (101) plane is observed for deposition at O_2/Ar = 0.015. This sample deposited at O_2/Ar = 0.015 also exhibits the highest crystallite size at 56 Å for the (110) plane. The crystallite size decreases to 45 nm while increasing the O_2/Ar from 0.015 to 0.045. The crystallite size was not calculated for the other samples due to poor peak definition as shown in Table 2. It is also expected that the growth conditions in the absence of O_2 flow would favour the presence of SnO due to the material of the sputtering target. Furthermore, the growth under O_2 flow has formed a SnO_2 phase and hence, increasing the growth temperature has clearly improved the crystalline quality of SnO_2 as concluded from XRD analysis.

For SnO_x samples deposited at 100 °C and annealed at 400 °C under moderate vacuum, similarly to as-deposited samples at 100 °C without O_2 flow, the XRD pattern shows a broad peak at around 30° revealing the presence of low crystalline SnO for the sample deposited without O_2 flow (Figure 1c). The XRD pattern also shows a broad peak at around 34° related to the presence of low crystalline SnO_2 phase for the samples deposited in the presence of O_2. For O_2/Ar above 0.005, there is a small peak located at 34° and associated to the (101) plane. No noticeable change was then observed while varying the O_2/Ar.

For SnO_x samples deposited at 250 °C and annealed at 400 °C under moderate vacuum, similarly to previous samples deposited without O_2 flow, there is a clear indication of a low crystalline SnO phase (Figure 1d). While varying the O_2/Ar from 0.005 to 0.075, there is a clear crystalline microstructure as indicated by XRD pattern. The crystallite size related to SnO_2 (110) peak decreases from 61 Å to 56 Å when O_2/Ar goes from 0.015 to 0.025 and then it remains constant for higher O_2/Ar ratios as revealed by Table 2. It was noticed that the vacuum annealing has slightly improved the crystallinity of the SnO_x samples deposited in the presence of O_2.

For SnO_x samples deposited at 250 °C and annealed at 400 °C under air, all samples show an improved crystallinity compared to as-deposited SnO_x (Figure 1f). For air annealed SnO_x deposited without O_2 flow, there are also two high crystalline phases of SnO and SnO_2 as revealed by the presence of sharp peaks located at 29.9° indicating SnO and at 33.9° indicating SnO_2. The crystallite size of SnO_2 drastically decreases from 109 Å to 54 Å when O_2/Ar goes from 0 to 0.005. Then, it slightly stabilizes around the value of 53 Å when O_2/Ar goes from 0.005 to 0.075. Air annealing has clearly improved the crystallinity of SnO_x samples which were deposited at 100°C compared to vacuum annealing process. It is worth to note that SnO peaks were only observed in both air annealed samples deposited without O_2 flow.

To sum-up, the as-deposited samples have shown that the relatively high temperature of 250 °C (i.e. as compared to 100 °C) has improved the crystalline microstructure for all the samples deposited with the presence of O_2. This is due to the improved crystallization of SnO_x and the reduction of the microstructure disorder [31]. Vacuum annealing has then slightly improved the crystallinity for samples deposited at 100°C due to the higher annealing temperature of 400 °C. However, there is no clear improvement of the crystalline microstructure of the samples deposited at 250 °C. The air annealing has remarkably improved the SnO_x microstructure for all samples deposited at 100 °C due to the higher annealing temperature of 400 °C, compared to the deposition temperature, and to the abundant presence of O_2 which enabled the crystallization of SnO_x. Air annealing for SnO_x sample deposited at 250 °C without O_2 has substantially improved the crystallinity of SnO_x due to the presence of O_2 at higher temperature of 400 °C. Moreover, further crystallization was less extensive under air annealing for other samples deposited in presence of O_2. This is likely due to the small temperature gradient between the deposition and the annealing processes, as well as the presence of O_2 in both processes. SnO crystallinity was neither achieved when depositing SnO without O_2 at both temperatures of 100 and 250 °C, nor after annealing these samples under vacuum. However, SnO phase appeared in both samples deposited at 100 and 250 °C without O_2 and annealed under air. This indicates that SnO crystallinity may be improved using a controlled annealing process under inert gas at atmospheric pressure and in absence of O_2 which can lead to crystallization of SnO without any further oxidation to SnO_2 phase[31, 32, 35-38]. Experimental work related to SnO_x annealing under inert gas will be discussed later in this chapter. The different observations extracted from XRD are summarized in Table 3.

O_2/Ar ratio	Crystallite Size (Å)					
	Deposition Temperature (°C)					
	100	250	100	250	100	250
	As deposited		Vacuum Annealing at 400 °C		Air Annealing at 400 °C	
0	*	*	*	*	116	109
0.005	*	*	*	*	51	54
0.015	*	56	*	61	56	52
0.025	*	54	*	56	62	53
0.045	*	45	*	56	61	55
0.075	*	*	*	56	57	55

Table 2: Crystallite size for SnO_x sample using Scherrer equation for the peak SnO_2 (110).

O_2/Ar ratio	Deposition Temperature (°C)					
	100	250	100	250	100	250
	As deposited		Vacuum Annealing at 400 °C		Air Annealing at 400 °C	
0	(SnO_x) Low crystallinity	(SnO_x) Low crystallinity	(SnO_x) Low crystallinity	(SnO_x) Low crystallinity	* Higher crystallinity	Higher crystallinity
0.005	Low crystallinity	Poorly crystallized	Poorly crystallized	Lower crystallinity	Lower crystallinity ↓ High crystallinity ↓ Lower crystallinity	Average crystallinity
0.015		Average crystallinity ↓ Lower crystallinity		+ High crystallinity ↓ Lower crystallinity		
0.025						
0.045						
0.075						

Table 3: Summary of SnO_x crystallinity samples using XRD and Scherrer equation for peak (101).

+: best conductivity of SnO_x deposited at 250 °C and 0.015 O_2/Ar ratio followed by vacuum annealing.

*:best crystallinity of SnO_x deposited at 100 °C and without O_2 flow followed by air annealing.

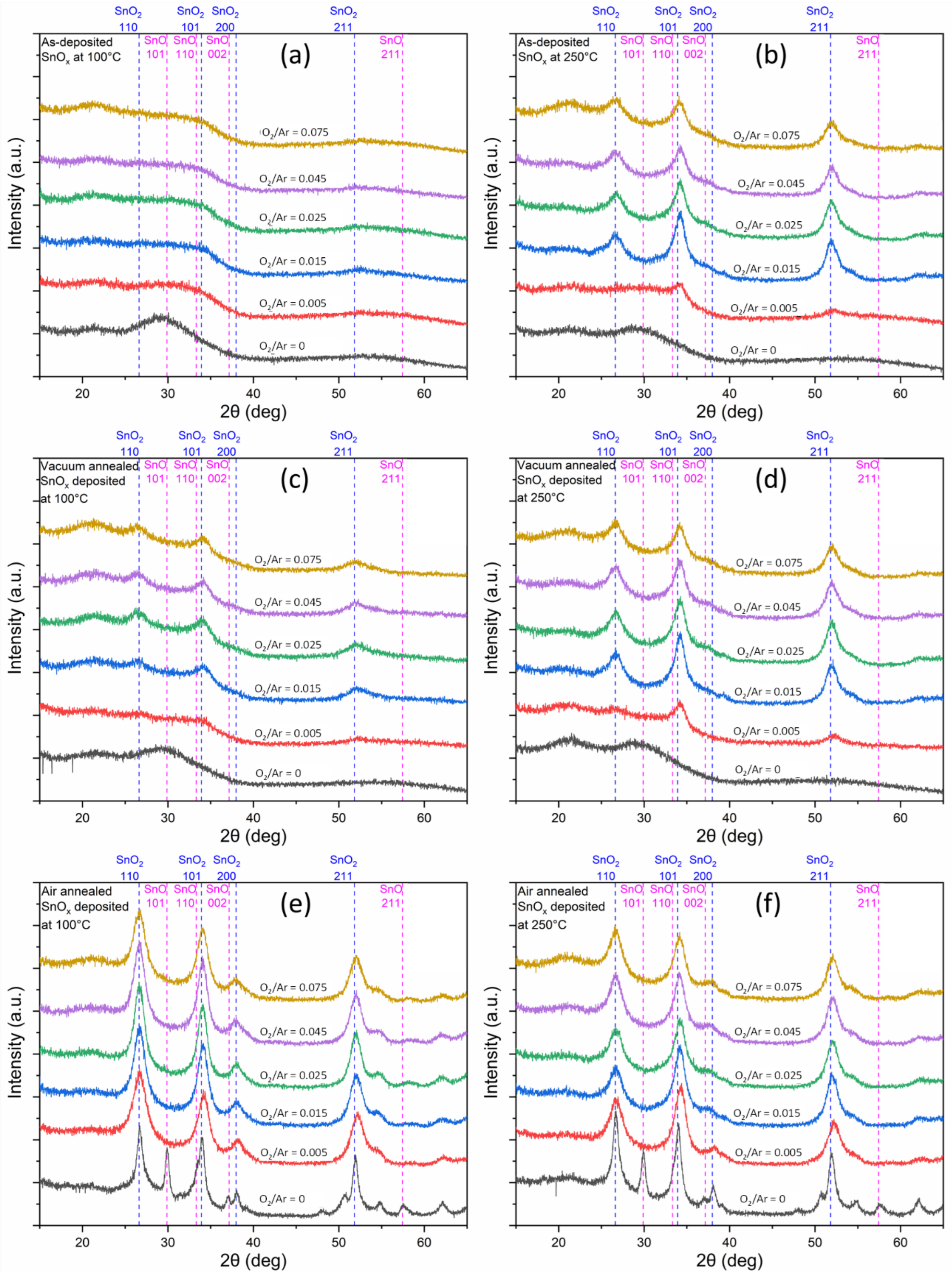

Figure 1: GIXRD patterns of SnO$_x$ samples (a) as deposited (as-dep) at 100 °C, (b) as-dep at 250 °C, (c) as-dep at 100°C and annealed in vacuum at 400 °C, (d) as-dep at 250°C and annealed in vacuum at 400 °C, (e) as-dep at 100 °C and annealed in air at 400 °C, and (f) as-dep at 250 °C and annealed in air at 400 °C.

2.3.3. Surface chemical state analysis by XPS

Chemical state analysis was performed for all 36 SnO_x thin film samples using X-ray photoelectron spectroscopy which is a surface sensitive technique analysing the surface of around 5 nm thickness. As expected, the surface of thin films gets oxidized at the surface once exposed to the air. However, this technique can provide an important indication of the present chemical states of the overall film. As expected, all XPS spectra for $Sn3d_{5/2}$ show only the presence of the two chemical states Sn(II) and Sn(IV). The peak position of $Sn3d_{5/2}$ related to Sn(II) is around 486.5 (+/- 0.15) eV while the one for Sn(IV) is around 486.9 (+/- 0.15) as shown in Figures 2, 3. It is worth noting that all samples were subject to low energy Ar ion cluster cleaning where the adventitious carbon was reduced drastically which improved the Sn and O from lattice and defect oxide. XPS equipment was calibrated using triple high purity metals Au/Ag/Cu and the XPS spectra were referenced using C 1s main peak at 284.8 eV.

For SnO_x deposited at 100 °C, the chemical state analysis revealed that the presence of Sn(II) in SnO_x deposited without O_2 flow is around 66.3% while Sn(IV) is around 33.7%. The presence of Sn(II) decreases drastically once we introduce O_2 flow and it reaches 18.7% for O_2/Ar ratio of 0.005 while Sn(IV) increases to 81.3%. Sn(II) presence decreases to 5.1% for O_2/Ar of 0.015 while Sn(IV) increases to 94.9%. Sn(II) continues to decrease while increasing the O_2/Ar flow rate ratio till it reaches 3% while O_2/Ar ratio reaches 0.075. Sn(IV) increases and reaches 97% for O_2/Ar ratio of 0.075. This decrease in Sn(II) (increase in Sn(IV)) was expected due to the increase of the oxidation state while introducing and increasing the O_2 flow rate. Vacuum annealing has kept the Sn(II) presence very similar to the as-deposited samples. However, the Sn(II) percentages slightly decreases except for O_2/Ar ratio of 0.005 where vacuum annealing led to a significant decrease 6.5% compared to 18.7% for as-deposited. The vacuum annealing at 400°C has proven to slightly improve the crystallinity for SnO_x deposited in presence of O_2 and favours more SnO_2 phase as revealed by GIXRD which explains the higher percentage of Sn(IV). Air annealing has led to a substantial increase of Sn(IV) for SnO_x deposited without O_2 flow and for O_2/Ar ratio of 0.005 compared to as-deposited SnO_x films while all other SnO_x were subject to a slight increase. Air annealing has led to a high crystalline SnO_2 phase as shown by GIXRD. These results are matching the structural findings discussed in the previous section.

For SnO_x deposited at 250 °C, the chemical state analysis revealed that the presence of Sn(II) in SnO_x deposited without O_2 flow is around 65.6% while Sn(IV) is around 34.3%. The presence of Sn(II) decreases drastically once we introduce O_2 flow and it reaches 10% for O_2/Ar ratio of 0.005 while Sn(IV) increases to 90%. Sn(II) presence decreases to 5.5% for O_2/Ar ratio of 0.015 while Sn(IV) increases to 94.5%. Sn(II) continue to decrease while increasing the O_2/Ar flow rate ratio till it reaches 3.7% while O_2/Ar ratio reaches 0.075. Sn(IV) increases and reaches 96.3% for O_2/Ar ratio of 0.075. Similar to the previous SnO_x series, this decrease in Sn(II) (increases in Sn(IV)) was expected due to the increase of the oxidation state while introducing and increasing the O_2 flow rate. Vacuum annealing has kept the Sn(II) presence trend very similar to the as-deposited samples. However, the Sn(II) percentages slightly increases which might be due to vacuum annealing and the small temperature gradient. The vacuum annealing at 400 °C has proven to slightly improve the presence of Sn(II) phase.

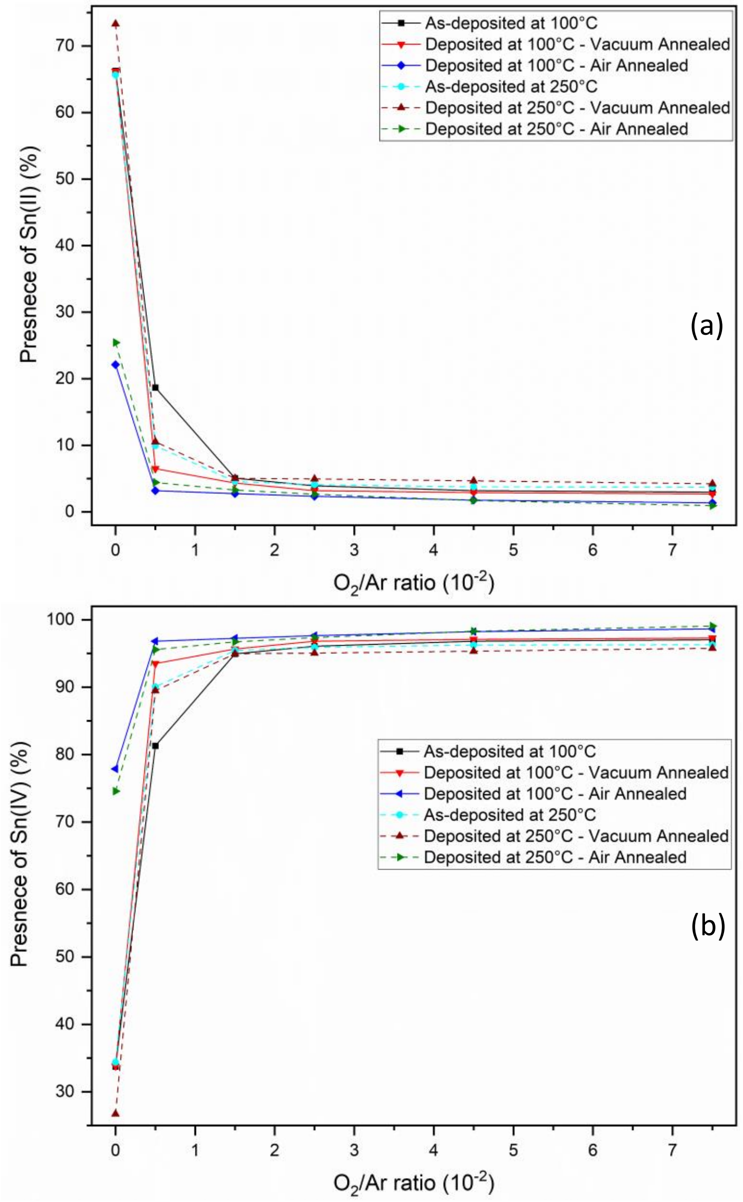

Figure 2: XPS chemical state (a) Sn(II) and (b) Sn(IV) quantification using $Sn3d_{5/2}$ spectra fitting for SnO_x as a function of O_2/Ar ratio and deposition temperature in different annealing conditions.

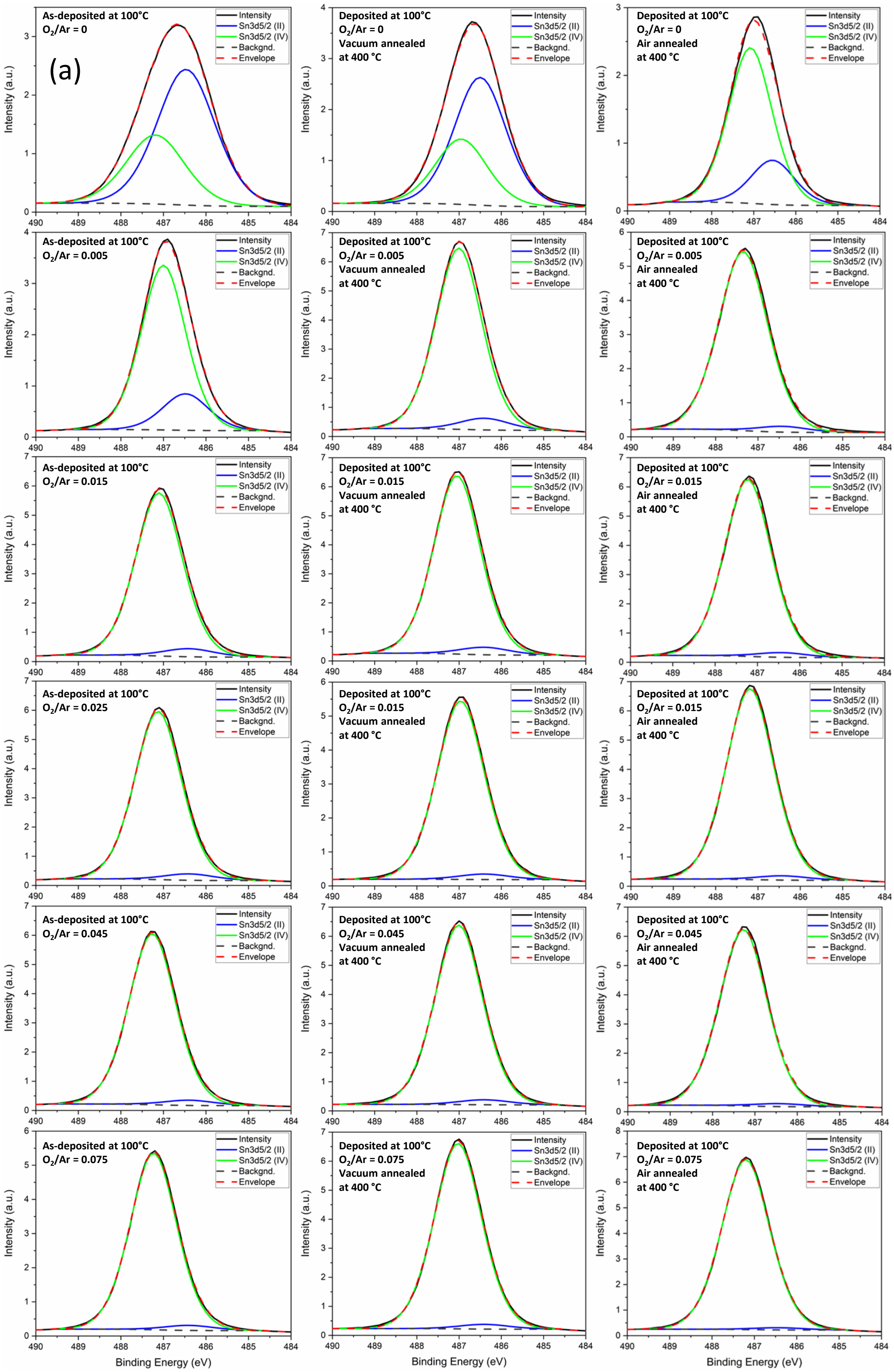
(a)
As-deposited at 100°C
O_2/Ar = 0
Deposited at 100°C
O_2/Ar = 0
Vacuum annealed
at 400 °C
Deposited at 100°C
O_2/Ar = 0
Air annealed
at 400 °C
As-deposited at 100°C
O_2/Ar = 0.005
Deposited at 100°C
O_2/Ar = 0.005
Vacuum annealed
at 400 °C
Deposited at 100°C
O_2/Ar = 0.005
Air annealed
at 400 °C
As-deposited at 100°C
O_2/Ar = 0.015
Deposited at 100°C
O_2/Ar = 0.015
Vacuum annealed
at 400 °C
Deposited at 100°C
O_2/Ar = 0.015
Air annealed
at 400 °C
As-deposited at 100°C
O_2/Ar = 0.025
Deposited at 100°C
O_2/Ar = 0.015
Vacuum annealed
at 400 °C
Deposited at 100°C
O_2/Ar = 0.015
Air annealed
at 400 °C
As-deposited at 100°C
O_2/Ar = 0.045
Deposited at 100°C
O_2/Ar = 0.045
Vacuum annealed
at 400 °C
Deposited at 100°C
O_2/Ar = 0.045
Air annealed
at 400 °C
As-deposited at 100°C
O_2/Ar = 0.075
Deposited at 100°C
O_2/Ar = 0.075
Vacuum annealed
at 400 °C
Deposited at 100°C
O_2/Ar = 0.075
Air annealed
at 400 °C
Intensity
Sn3d5/2 (II)
Sn3d5/2 (IV)
Backgnd.
Envelope
Intensity (a.u.)
Binding Energy (eV)
490
489
488
487
486
485
484

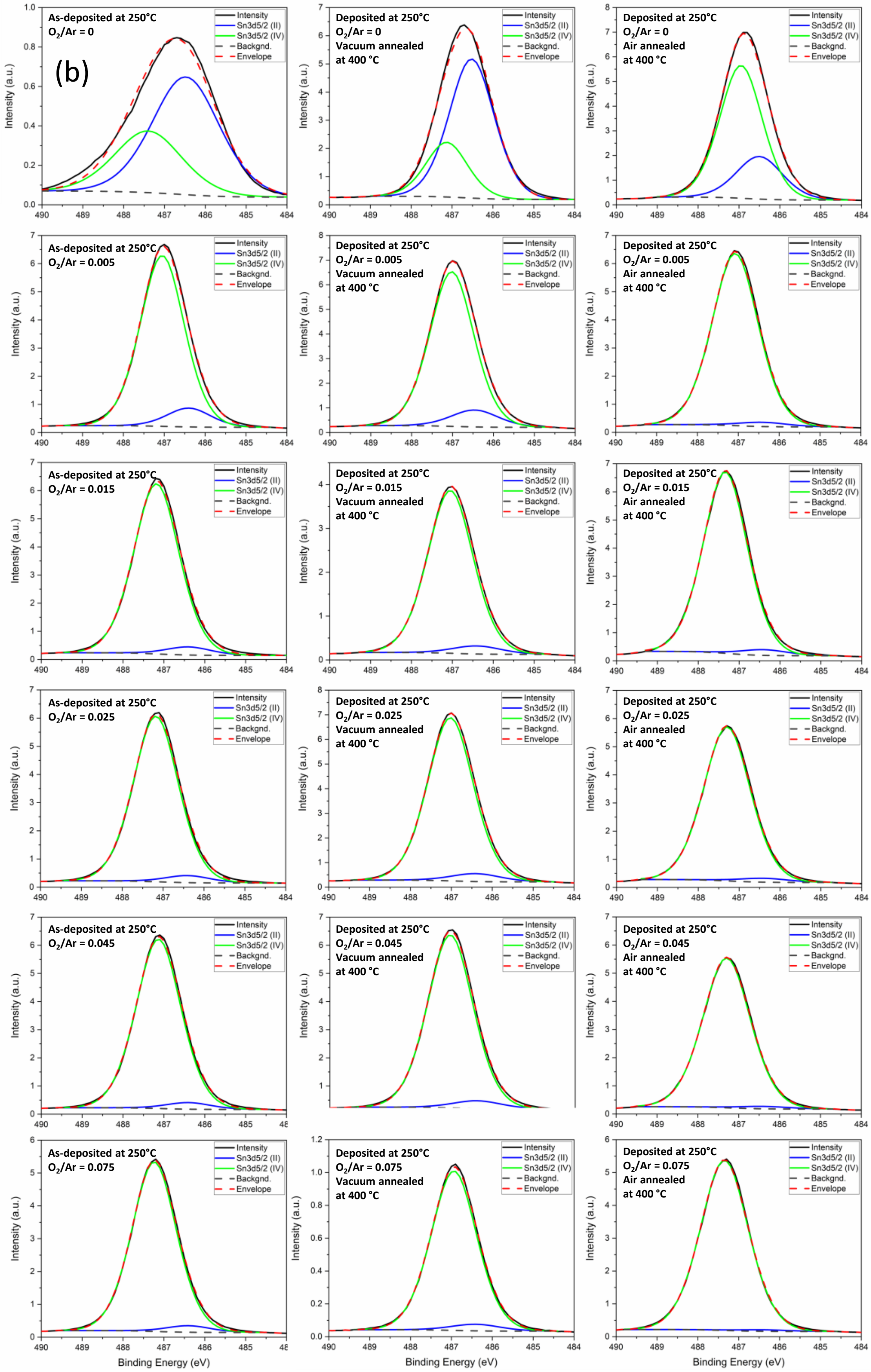

Figure 3: XPS spectra for Sn3d$_{5/2}$ for (a) SnO$_x$ deposited at 100°C as a function of O$_2$:Ar in different annealing conditions, (b) SnO$_x$ deposited at 250 °C as a function of O$_2$:Ar in different annealing conditions.

2.3.4. Electrical transport properties

The electrical properties were investigated initially using the four-point probe IV tool then through the Hall effect measurements. Four-point probe measurements were performed on all samples using three-point statistics method. The obtained results revealed a very high resistivity around 10^8 Ω·cm for SnO_x deposited without the presence of O_2 for both as-deposited series at 100°C and 250 °C. As revealed by XRD results, this may be attributed to the low crystallinity of the SnO_x films. The resistivity decreases to its lowest value of 47 Ω·cm at $O_2/Ar = 0.005$ for SnO_x samples deposited at 100°C and to its lowest value of 4.5 Ω·cm at $O_2/Ar = 0.015$ for SnO_x samples deposited at 250 °C. The lower value of resistivity for samples deposited at 250 °C is matching with the highest crystallite size which indicated as discussed earlier the improvement of the crystalline microstructure.

For SnO_x deposited at 100 °C, the resistivity increases significantly from $O_2/Ar = 0.005$ to 0.015 and it relatively stabilizes at higher O_2/Ar starting from 0.015 (Figure 2). For SnO_x as deposited at 250 °C, the same behaviour is observed, where the resistivity increases significantly from O_2/Ar =0.015 to 0.025 and it relatively decreases towards higher O_2/Ar starting from 0.025. In the presence of O_2, all deposited SnO_x samples at 250 °C show a better electrical conductivity compared to films grown at 100°C.

Vacuum annealed samples were found to follow similar pattern as the as-deposited SnO_x at both deposited temperatures where the best crystalline as-deposited SnO_x samples are still the most conductive ones. Moreover, the lowest recorded resistivity values are 0.14 Ω·cm for the best SnO_x deposited at 100 °C and 0.07 Ω·cm for the best SnO_x deposited at 250 °C of all the fabricated batches after vacuum annealing. Furthermore, as expected after annealing process, the best recorded resistivity values are significantly lower compared to the as-deposited ones. This improvement is likely attributed to the microstructure improvement leading to the conservation of charge carrier after the vacuum annealing of the samples.

For both air annealed series, the lowest resistivity of around 0.13 Ω·cm was observed for samples deposited without O_2 flow. The resistivity increases then significantly until $O_2/Ar = 0.015$ and slightly stabilizes for higher O_2/Ar starting from 0.015. The trend of resistivity with respect to O_2/Ar (of both air-annealed series) are very closely matching regardless the deposition temperature of SnO_x. However, the resistivity for SnO_x samples deposited at 250 °C is slightly lower for all O_2/Ar ratios except the two extreme values of 0 and 0.075 as shown in Figure 4.

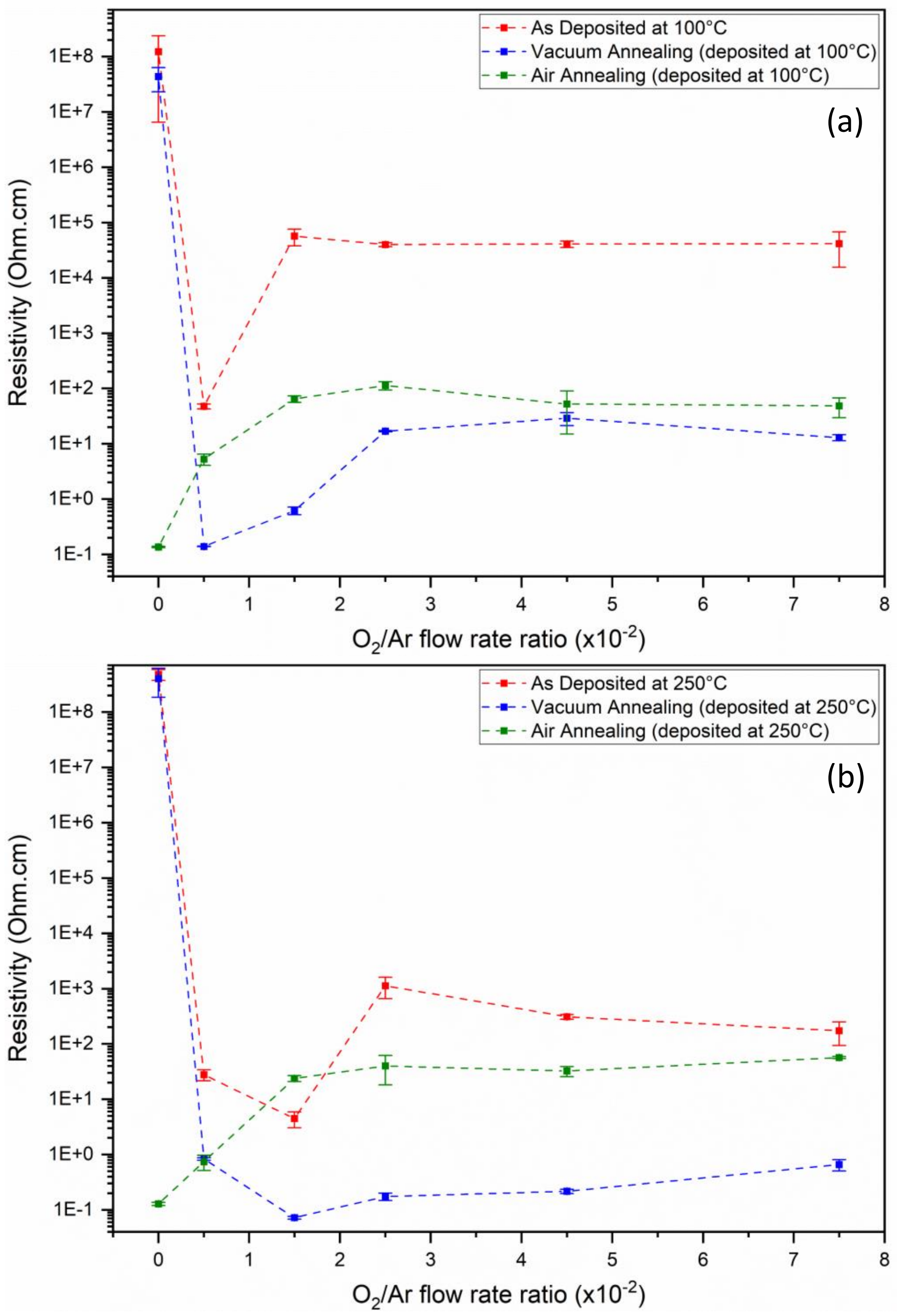

Figure 4: Resistivity as a function of O_2/Ar flow rate ratio in growth conditions for as-deposited, vacuum-annealed, and air-annealed SnO_x (a) deposited at 100°C and (b) deposited at 250°C.

The samples deposited at 250 °C followed by a moderate vacuum annealing at 400 °C showed the lowest resistivity of 0.07 Ω·cm at O_2/Ar = 0.015. Furthermore, the other SnO_x samples in the same series deposited with O_2/Ar ratio above 0.015 show substantially a lower resistivity compared to samples from other series with the same conditions of O_2/Ar. This can be attributed to the relatively higher crystallite size due to the annealing process, as well as the expected charge carrier concentrations due to the vacuum annealing [31, 37, 38].

Further analysis using Hall effect measurement were conducted solely on the best conductive samples identified by four-point probe method, both for vacuum and air annealed samples series. The electron mobility for the best conductive samples for each series were 1.07 $cm^2/V\cdot s$ for vacuum annealed series deposited at 100°C, 7.77 $cm^2/V\cdot s$ for vacuum annealed series deposited at 250°C, 2.11 $cm^2/V\cdot s$ for air annealed series deposited at 100 °C, and 2.58 $cm^2/V\cdot s$ for air annealed series deposited at 250°C. Their respective charge carrier concentrations were 1.47×10^{19} cm^{-3} for vacuum annealed series deposited at 100°C, 5.84×10^{18} cm^{-3} for vacuum annealed series deposited 250°C, 1.39×10^{19} cm^{-3} for air annealed series deposited at 100°C, and 1.26×10^{19} cm^{-3} for air annealed series deposited at 250°C as shown in Table 4. All these conductive samples were n-type semiconductors which is expected for vacuum annealed samples due to the presence of SnO_2 phase.

Series' best conductive sample	O_2/Ar ratio	Mobility ($cm^2/V\cdot s$)	electron carrier (cm^{-3})
As deposited at 100 °C / Vacuum annealed	0.005	1.07	1.47×10^{19}
As deposited at 250 °C / Vacuum annealed	0.015	7.77	5.84×10^{18}
As deposited at 100 °C / Air annealed	0	2.11	1.39×10^{19}
As deposited at 250 °C / Air annealed	0	2.58	1.26×10^{19}

Table 4: Hall effect measurements for SnO_x samples of each annealed series.

However, the n-type conductivity for air annealed samples reveals that the majority charge carriers are related to the SnO_2 phase. The best conductive SnO_x, which is deposited at 250 °C / O_2/Ar = 0.015 and annealed under vacuum at 400 °C is a result of a much higher mobility and an average charge carrier concentration compared to other samples.

Normally, scattering mechanisms are the main explanation for electron mobility. Furthermore, as per the grain-boundary scattering mechanism, the mobility increases while increasing the carrier concentration or the crystallite size. However, for higher values than 10^{20} cm^{-3} of charge carrier concentration, the mobility decreases due to the domination of ionized scattering mechanism [36, 39, 40]. Therefore, the grain-boundary scattering mechanism is likely the main mechanism responsible for the higher electron mobility of the best conductive SnO_x sample. As a matter of fact, Kim et al. [41] established that the grain boundary scattering was the dominant scattering mechanism for SnO_{2-x} thin films prepared by magnetron sputtering [41]. In another work performed on polycrystalline Gallium doped Zinc Oxide (GZO), Hall mobility measurements indicated that the mobility of electron carriers across many grains and grain boundaries within conduction path was limited by both scattering effects intra-grains and at grain boundaries[42]. The dominancy of the scattering effects varies with electron concentration. In the case of higher electron concentration above about 10^{20} cm^{-3}, the dominant scattering effect for μHall has been considered to be ingrain scattering (ionized-impurity scattering)[43, 44]. On the other hand, it is well established that μ_{opt} shows the electron mobility in ingrains. Thus, μ_{opt} is limited by the effect of ingrain scattering. In advanced investigations, comparing electron and optical mobilities (μHall and μopt) has been employed to highlight the contribution of grain boundary scattering on electron mobility, and this approach has frequently been used as a means to study the effect of ingrain and grain boundary scattering on electron transport properties in many TCOs[45-50].

2.3.5. Optical properties

The optical properties have been studied using UV-Visible spectroscopy. The optical transmittance measurements (Figure 4) were conducted on all the grown samples and the average optical transmittance between 400 and 700 nm is summarized in Table 5.

O_2/Ar ratio	Optical transmittance (%)					
	Deposition Temperature (°C)					
	100	250	100	250	100	250
	As-deposited		Vacuum Annealing at 400 °C		Air Annealing at 400 °C	
0	72	80	70	79	65	77
0.005	78	76	80	76	86	87
0.015	87	87	86	87	88	89
0.025	87	88	87	88	89	89
0.045	88	90	87	89	90	90
0.075	89	91	89	91	91	91

Table 5: Average optical transmittance between 400 and 700 nm for SnO_x samples with substrate.

The average optical transmittance of the reference Quartz substrate was initially measured at 93%. For SnO_x samples deposited at 100 °C, it is observed that the average optical transmittance from 400 to 700 nm (labelled transmittance) increases from 72 up to 89% when O_2/Ar increases from 0 to 0.075. Moreover, the transmittance increases from 70 to 89% after vacuum annealing and increases from 65 % to 91 % when O_2/Ar varies from 0 to 0.075 after air annealing. For SnO_x samples deposited at 250 °C, the transmittance in as-deposited and vacuum annealed samples decreases from around 80% to 76% when O_2/Ar varies from 0 to 0.005. Furthermore, the transmittance increases up to 91% for O_2/Ar increasing from 0.005 to 0.075. The transmittance increases from 77 % to 91 % for O_2/Ar varying from 0 to 0.075 after air annealing. These results are summarized in table 5.

It is established that the oxygen flow has a strong effect on the optical properties of SnO_x [36]. This can be directly observed by the blue shift of the absorption edge as well as the relative increase of transmittance when O_2/Ar is increasing as shown in Figure 5.

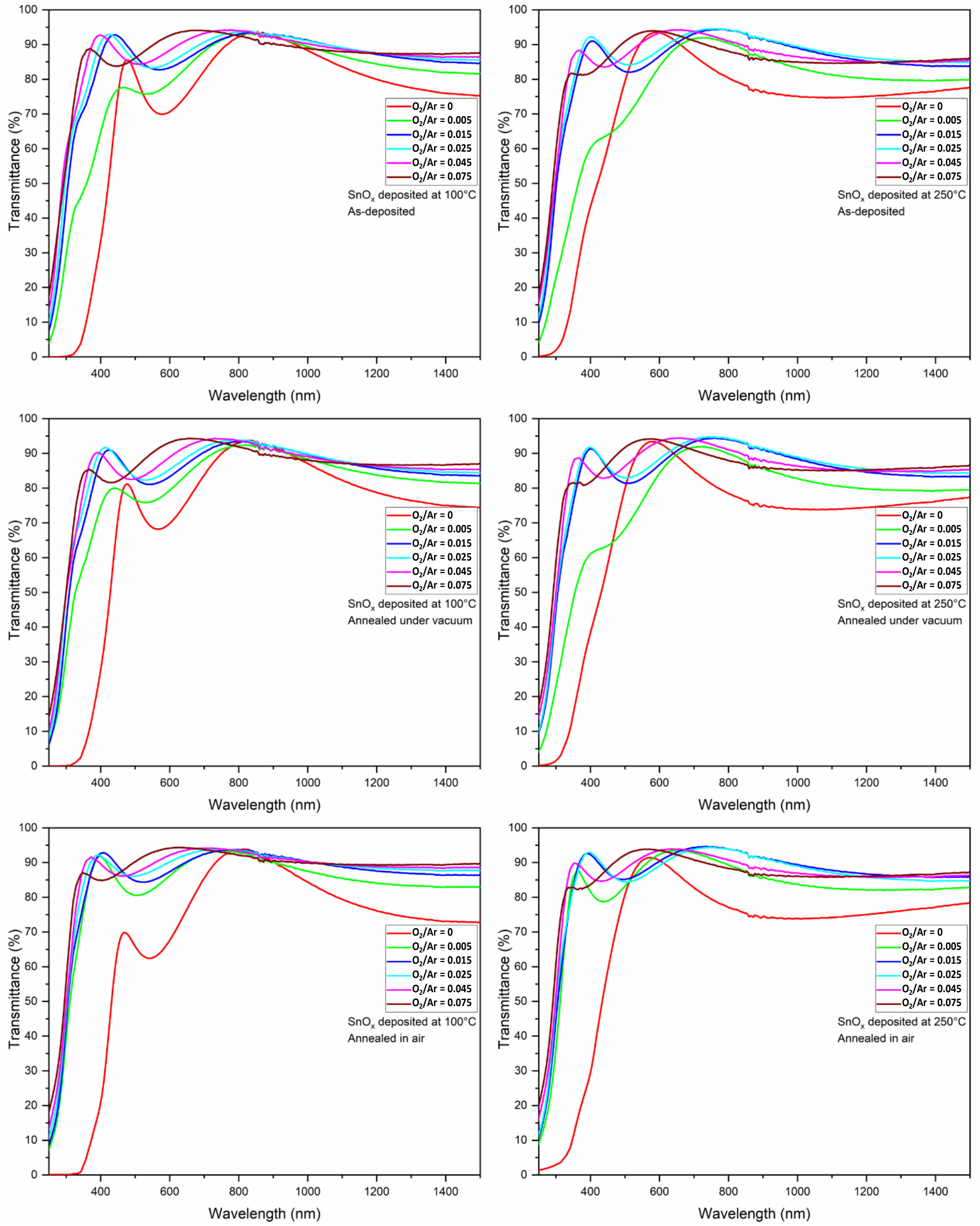

Figure 5: UV-Visible transmittance as a function of the wavelength for all the measured SnO_x samples.

Figures 6 shows Tauc plots for all samples considering the SnO_x thin films as a direct bandgap semiconductor. It can be concluded from Tauc plots that all the SnO_x films have a wide optical band gap varying from 3.3 to 4.5 eV.

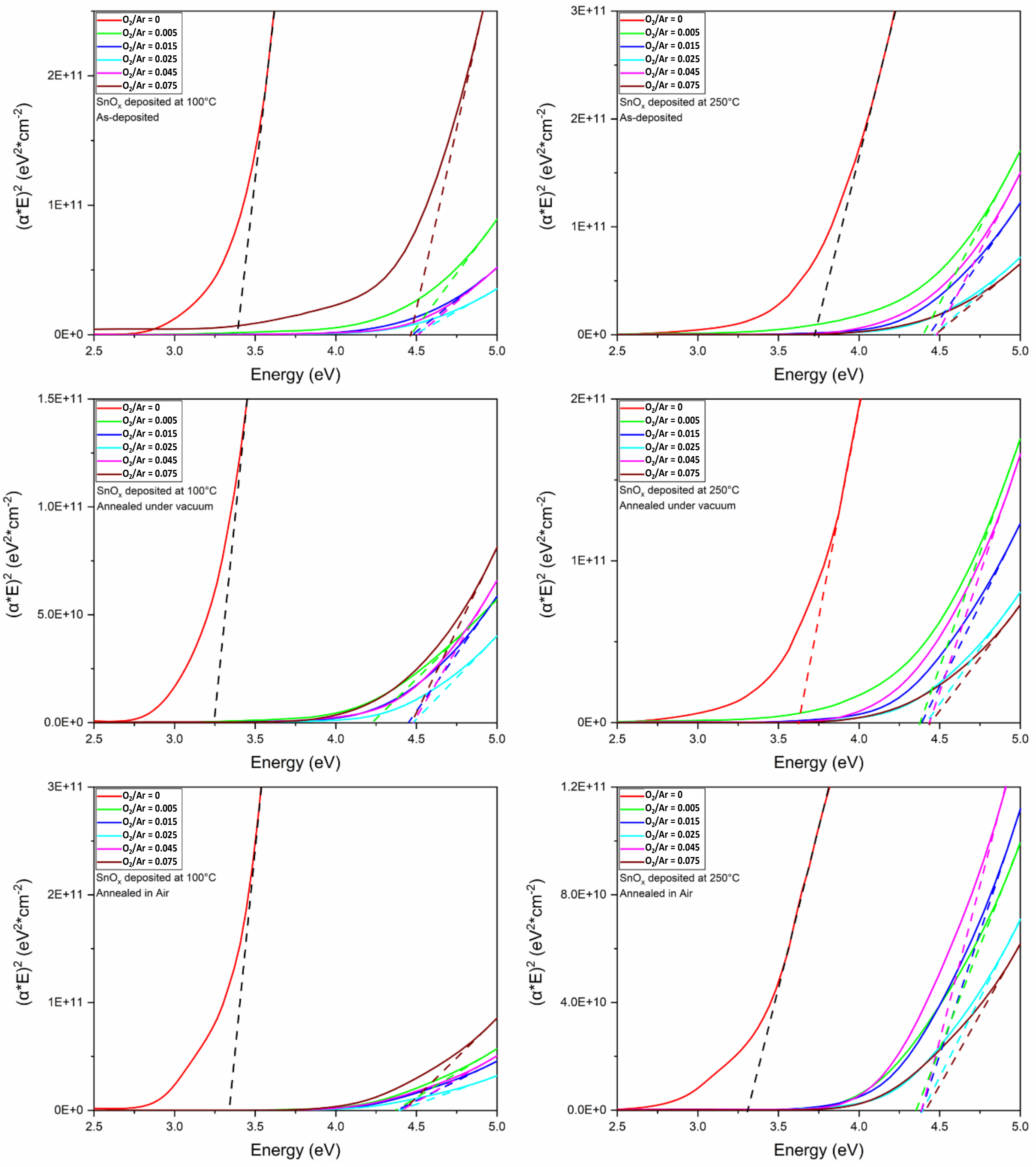

Figure 6: Tauc plots for all the measured SnO$_x$ samples showing the respective optical bandgaps.

Table 6 summarised the values of the optical band gap for all the samples, which are found to increase and then stabilise when O$_2$/Ar is increasing. The low optical bandgap for the SnO$_x$ samples deposited without the presence of O$_2$ compared to the other samples, is a typical characteristic for SnO and it was already reported in the literature varying from 2.6 to 3.4 eV [36]. These results corroborate well the XRD analysis and are confirming the major presence and the low crystallinity behaviour of the SnO phase for both the as-deposited and vacuum annealed samples. The measured bandgap above 4 eV for the rest of the samples is related to SnO$_2$ phase which is very close to the values reported in the literature. The band gap variation is mainly related to the difference of the stoichiometry of the SnO$_x$

films. However, the effect of the sample disorder can also decrease the bandgap of the SnO_x thin films[35, 36, 51].

The band gap of SnO_2 samples prepared in presence of O_2 is relatively very high compared to the literature where all samples reached 4.4~4.5 eV except one sample of SnO_2 deposited at 100 °C / 0.005 O_2/Ar and annealed under vacuum. These band gap values are related to the high oxidation of SnO_2 due to the oxidized sputtering target and the presence of oxygen during the growth.

O_2/Ar ratio	Optical Bandgap (eV)					
	SnO_x Deposition Temperature (°C)					
	100	250	100	250	100	250
	As-deposited		Vacuum Annealing at 400 °C		Air Annealing at 400 °C	
0	3.4	3.7	3.3	3.6	3.3	3.3
0.005	4.5	4.4	4.2	4.4	4.4	4.4
0.015			4.5			
0.025		4.5				
0.045						
0.075						

Table 6: Optical bandgap for SnO_x samples.

2.3.6. Optoelectronic performance

The optoelectronic performance for all SnO_x samples was evaluated using Haacke figure of merit (FoM) equation (1)[52] . The results are shown in Table 7. SnO_x samples have a relatively low figure of merit due to the moderate resistivity of the thin films. The highest figure of merit ϕ of 5.14×10^{-2} ($10^{-3}\ \Omega^{-1}$) is related to our best conductive SnO_x sample. Furthermore, the SnO_x samples deposited at 250 °C where the O_2/Ar ratio between 0.015 and 0.045 as well as SnO_x sample deposited at 100 °C and at 0.005 O_2/Ar ratio have shown figure of merit above 10^{-2} ($\times 10^{-3}\ \Omega^{-1}$). These results reveal that the vacuum annealing has improved the optoelectronic performance of the SnO_x thin films.

$$\phi = T^{10} / R_s \qquad (1)$$

where ϕ is figure of merit in Ω^{-1}, T is the average optical transmittance from 400 to 700 nm in %, and R_s is the sheet resistance in $\Omega \cdot \square^{-1}$.

O₂/Ar ratio	Figure of merit (10^{-3} Ω^{-1})					
	Deposition Temperature (°C)					
	100	250	100	250	100	250
	As-deposited		Vacuum Annealing at 400 °C		Air Annealing at 400 °C	
0	3.06×10^{-12}	3.21×10^{-12}	6.52×10^{-12}	3.38×10^{-12}	9.91×10^{-04}	8.17×10^{-03}
0.005	4.27×10^{-05}	3.93×10^{-05}	**1.87×10^{-02}**	1.32×10^{-03}	1.02×10^{-03}	5.70×10^{-03}
0.015	1.12×10^{-07}	8.31×10^{-04}	9.13×10^{-03}	**5.14×10^{-02}**	1.10×10^{-04}	1.96×10^{-04}
0.025	1.72×10^{-07}	4.45×10^{-06}	4.10×10^{-04}	**2.90×10^{-02}**	7.66×10^{-05}	1.42×10^{-04}
0.045	1.35×10^{-07}	1.22×10^{-05}	1.72×10^{-04}	**1.56×10^{-02}**	1.33×10^{-04}	1.17×10^{-04}
0.075	1.15×10^{-07}	3.70×10^{-05}	3.70×10^{-04}	9.66×10^{-03}	1.23×10^{-04}	1.12×10^{-04}

Table 7: Figure of merit for all SnO_x samples.

Table 1 in the appendix summarizes selected values from relevant literature of FoM for different doped SnO_2 thin films along with the doping type, synthesis method, band gap value, electrical resistivity and sheet resistivity, and optical transmittance[53-75]. Only two references of undoped films have been found in addition to our present work. Figure 7 highlights these FoM and band gap values as a function of the various references along with our present work in this section 2.3 and the next one 2.4. Highest FoM has been recorded for SnO_2 grown with spray pyrolysis and doped with fluorine, while the lowest value characterized SnO_2 was deposited by Pulsed Laser Deposition and doped with Tellurium. While our measured FoM belongs rather to the category of low values in Table 1 in the appendix, it is rather expected since our SnO_2 films are undoped and did not reach a low resistivity around 10^{-4} Ω·cm. However, the optical band gap was among the highest reported in the literature which is, as discussed previously, due to the high oxidation state of SnO_x.

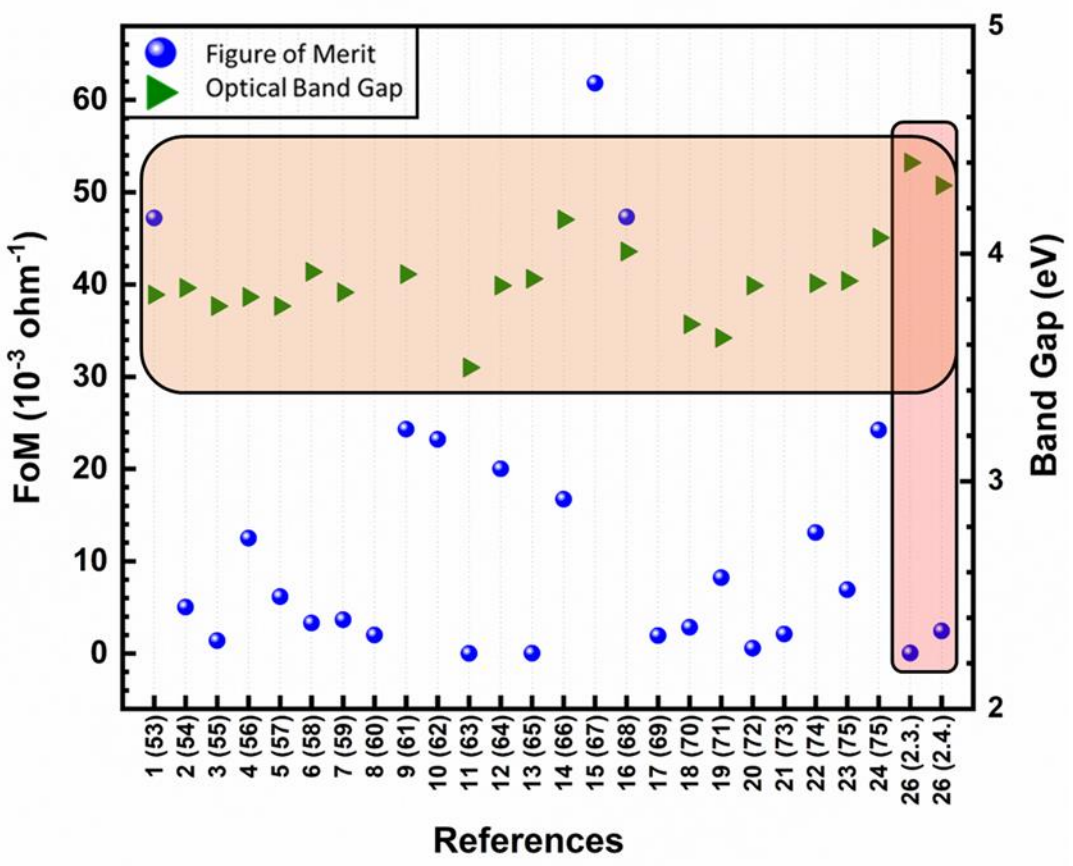

Figure 7: Summary of Figure of Merit values and bang gap as a function of the various references [53-75] as well as the results of this thesis work in sections 2.3. and 2.4.

2.3.7. Morphology, TEM imaging & diffraction, and mapping

SEM observations were conducted on the four samples from the annealed series showing the highest conductivity as well as their related SnO_x samples without annealing. All four samples show a crack-free SnO_x films. The annealing process did not change drastically the morphology of the SnO_x thin films. It can be clearly observed that the best conductive sample deposited at 250 °C with O_2/Ar = 0.015 and annealed under vacuum (Figure 8c) has the largest grain size compared to the other samples as shown in Figure 8. The large grain size has improved the conductivity of SnO_x as previously reported [36]. Following the discussion regarding the Hall effect results, the high mobility associated to these specific growth conditions is also attributed to the large grain size [33, 36]. The sample deposited at 100 °C and with O_2/Ar = 0.005 and annealed under vacuum (Figure 8a) has shown the smallest grain size compared to the other three SnO_x samples. This result is corroborating well the Hall effect measurement as it has shown the lowest mobility among the four selected samples.

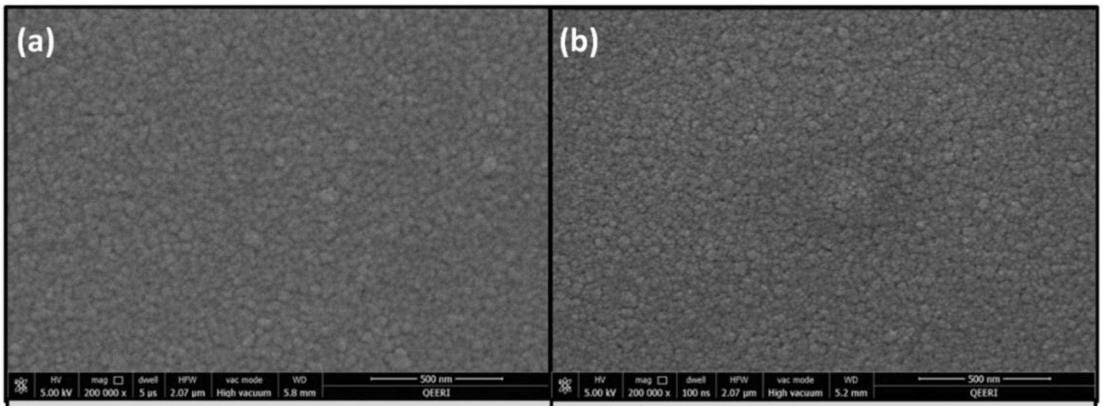

SnO$_x$ deposited at 100°C, at 0.005 O$_2$/Ar, annealed under vacuum

Same SnO$_x$ sample without annealing

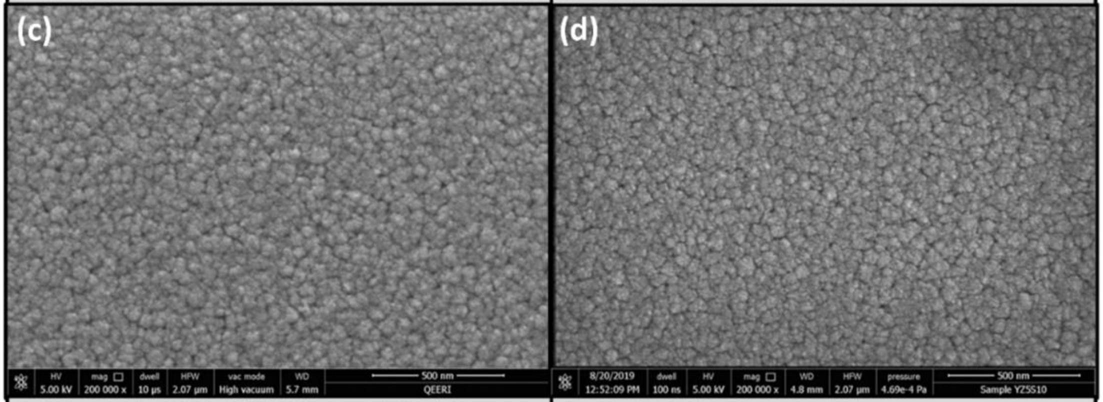

SnO$_x$ deposited at 250°C, at 0.015 O$_2$/Ar, annealed under vacuum

Same SnO$_x$ sample without annealing

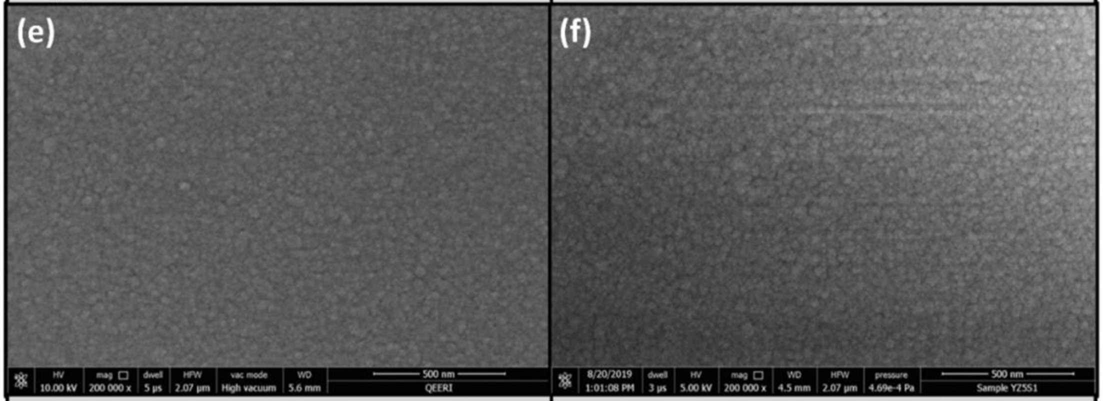

SnO$_x$ deposited at 100°C, at 0 O$_2$/Ar, annealed in air

Same SnO$_x$ sample without annealing

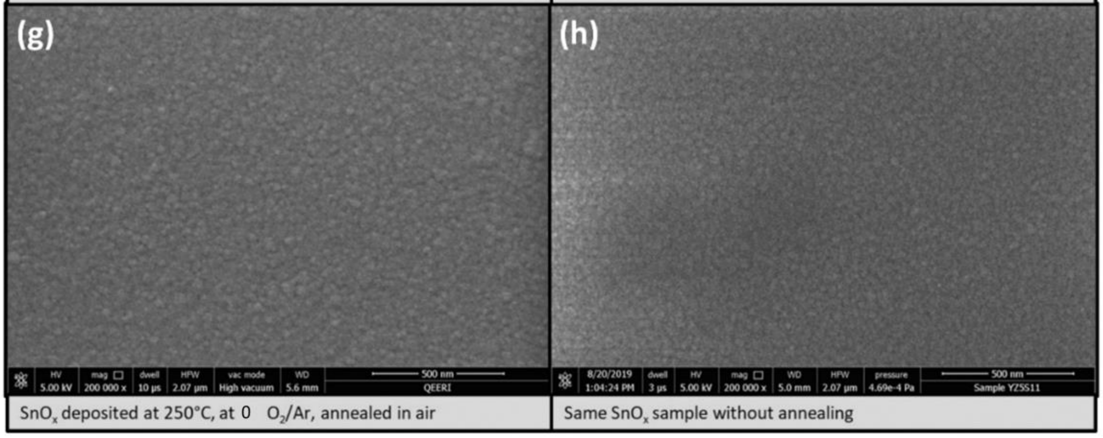

SnO$_x$ deposited at 250°C, at 0 O$_2$/Ar, annealed in air

Same SnO$_x$ sample without annealing

Figure 8: Representative SEM images for the most electrically conductive annealed samples and their related SnO$_x$ samples without annealing: (a) SnO$_x$ deposited at 100°C, O_2/Ar = 0.005, annealed under vacuum; (b) SnO$_x$ deposited at 100°C, O_2/Ar = 0.005, without annealing; (c) SnO$_x$ deposited at 250°C, O_2/Ar = 0.015, annealed under vacuum; (d) SnO$_x$ deposited at 250°C, O_2/Ar = 0.015, without annealing, (e) SnO$_x$ deposited at 100°C,

$O_2/Ar = 0$, annealed in air; (f) SnO_x deposited at 100°C, $O_2/Ar = 0$, without annealing; (g) SnO_x deposited at 250°C, $O_2/Ar = 0$, annealed in air; (h) SnO_x deposited at 250°C, $O_2/Ar = 0$, without annealing.

In order to confirm the multi-crystalline structure of the best conductive SnO_2 sample, we performed TEM imaging and mapping (Figure 9). The interplanar spacing could be measured directly from the image (Figure 9a) namely (110) and (101) planes, which is matching with the results revealed by XRD. Figure 9b shows the TEM diffraction pattern indexation revealing the intense patterns are related to (110) and (101) planes. High-angle annular dark-field imaging (HAADF) shown in Figure 9c has revealed a dense SnO_2 film with elongated column-shape crystalline structure towards the growth direction. EDS mapping (Figure 9d) has revealed the presence of a uniform layer of SnO_2 which is forming a sharp and clear interface with the quartz substrate grain size [33, 36].

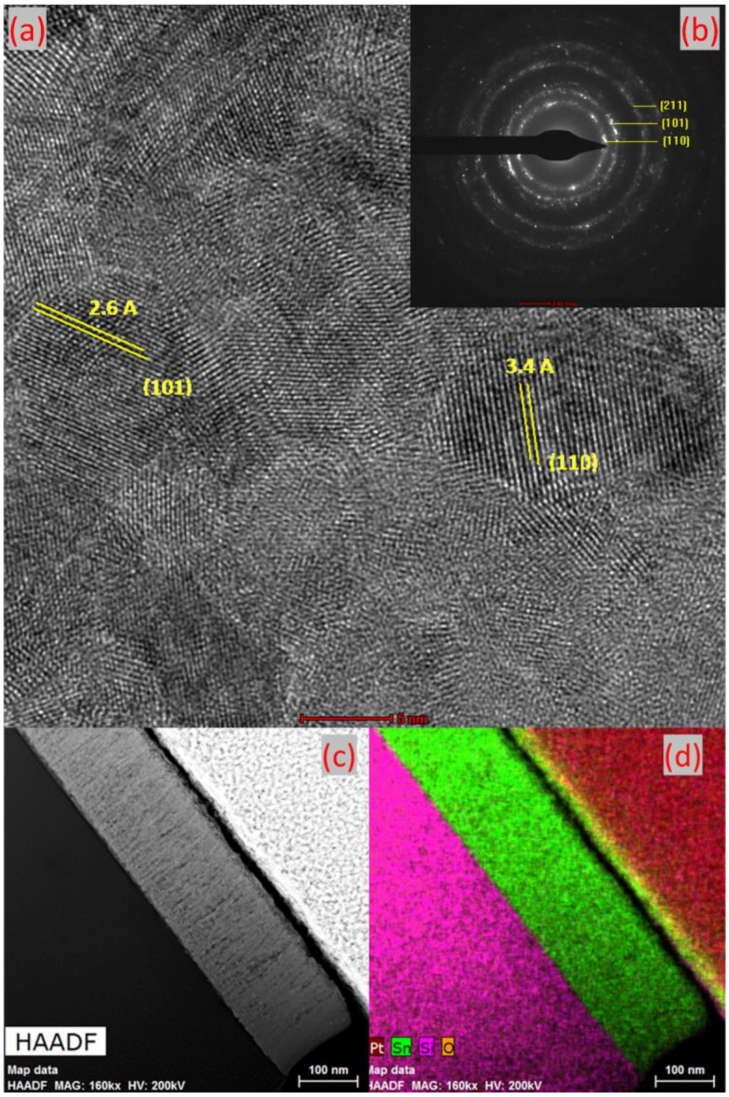

Figure 9: Cross-section TEM images for the best conductive SnO_x thin film deposited at 250°C and $O_2/Ar = 0.015$, annealed under vacuum (a) high resolution TEM image, (b) TEM diffraction pattern, (c) High-angle annular dark-field imaging (HAADF), (d) EDS mapping.

2.3.8. Thickness variation and elemental depth profiling

As reported in literature, the variation in thickness due to oxygen flow rate and temperature has been assessed using theoretical and experimental methods, and this variation depends on many factors. One of these factors is oxygen adsorption as oxygen flow rate increases from poor oxygen condition to the optimal condition which improves the deposition rate. On the other hand, one of the factors related to the decrease in deposition rate for higher O_2 flow rate (oxygen rich condition) is the further oxidation of the sputtering target surface[76].

After having investigated the structural properties with XRD and TEM, we further confirm the homogeneity of the samples by performing TOF-SIMS on the best conductive samples to show the presence of high quality SnO_x by the two constant intensities of Sn and O in the ToF-SIMS steady state conditions between the surface and the interface as shown in Figure 10. This analysis reveals the constant stoichiometry throughout the depth. The ion yield is much higher for Sn at the surface and the interface due to the matrix effect where the chemical environment changes as the secondary ion yields are strongly dependent on the chemical environment, which explains the high intensity of Sn at the surface and the interface. SIMS in general is inherently not a quantitative measurement technique. The secondary ion yields are strongly dependent on the chemical environment (matrix effect) and therefore, there is no direct correlation of elemental/compound intensity vs concentration. This technique also revealed the presence of H which slightly increases from the surface to the interface[77].

TOF-SIMS also confirmed the absence of organic or inorganic contamination throughout the depth and it shows also perfect interfaces between the SnO_x thin film and the quartz substrate.

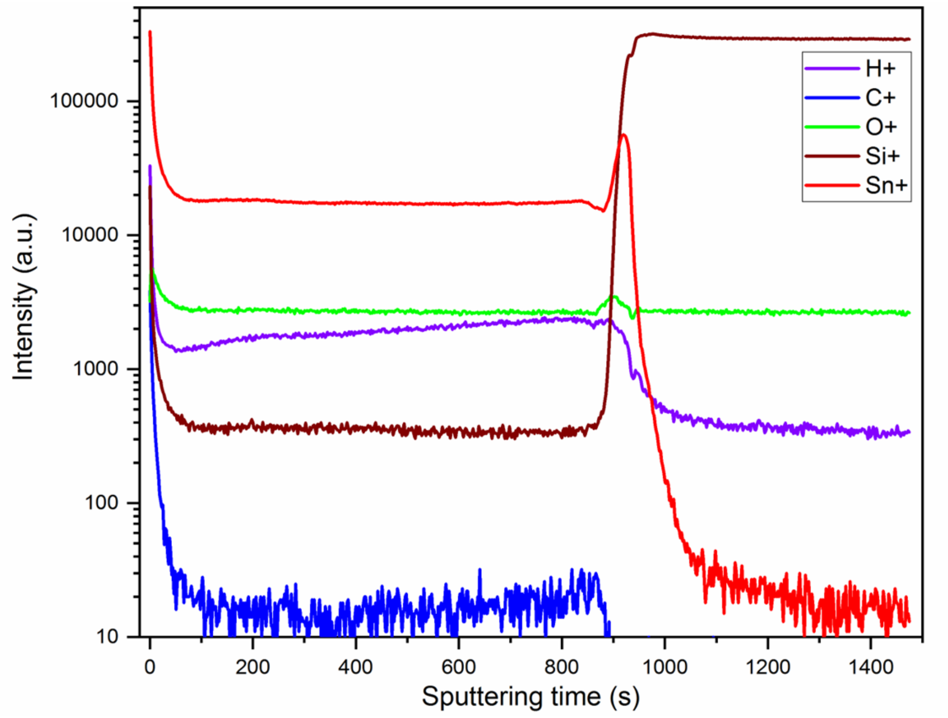

Figure 10: TOF-SIMS profiles for the best conductive sample (SnO_x thin film deposited at 250 °C, at O_2/Ar = 0.015, and annealed under vacuum at 400 °C).

2.3.9. Summary

For as-deposited SnO_x samples sputtered using a SnO target and based on their characterizations, it is suggested that such SnO_x is predominantly amorphous and/or showing low crystalline SnO in absence of additional O_2 in the chamber, owing to the nature of the sputtering target (SnO). This has led to lower electrical conductivity. At low O_2/Ar ratios, the predominating phase becomes SnO_2 and the crystallinity tended to improve at higher temperature of 250 °C as the O_2/Ar ratio increased from 0.005 to 0.015. The poor oxygen condition is suggested to form defects within SnO_x thin film, particularly oxygen vacancies, and these defects are expected to increase while improving the crystalline structure of SnO_2 by increasing the O_2/Ar ratio in the oxygen poor condition range (from 0.005 to 0.015 O_2/Ar). This has led to higher electrical conductivity. At higher O_2/Ar ratios, the crystallinity decreased at higher temperature of 250°C. The rich O_2 condition is expected to reduce the oxygen vacancy defects and eventually decreases the charge carrier concentration. This has led to lower electrical conductivity[78]. Both annealing processes are expected to improve the crystallinity of the films due to a thermal treatment at 400°C for 1 hour. However, vacuum annealing is expected to conserve the charge carrier concentration by preventing annihilation of the oxygen vacancies due to the lack of O_2. On the other hand, air annealing is found to reduce the charge carrier concentration by filling the oxygen vacancies with oxygen supplied from air.

The air annealing has shown a better crystallinity compared to vacuum annealing as all the samples have reported high crystallinity and two SnO_x samples deposited without O_2 recorded the highest crystallite size. Both SnO_x deposited without O_2 and annealed in air have revealed that the presence of both phases SnO and SnO_2, and it is clear that O_2 from the air atmosphere has oxidized significantly SnO to SnO_2. Moreover, as per crystallite size reported in Table 2, it is found that the crystallite size is relatively higher after vacuum annealing for the SnO_x samples (deposited at 250°C). While for the annealing under vacuum, the charge carrier concentration which is mainly due to oxygen vacancies is found to be conserved. The combination of improved crystallite size and the conservation of charge carrier are the key factors for improving the electrical conductivity as compared to SnO_x samples from other series with same O_2/Ar ratio.

The first part of the chapter highlighted the structure/performance correlations of SnO_x thin films grown by RF MS. High quality SnO_x samples were prepared using magnetron sputtering deposition method followed by thermal annealing processes. Crystalline microstructure, electrical and optical properties were characterised in-depth. Both SnO_2 and mixed SnO/SnO_2 thin films were synthetized using RF sputtering. The **most electrically conductive sample** was obtained by using O_2/Ar = 0.015 during the growth at 250 °C and followed by a moderate vacuum post annealing at 400 °C / 6.66×10^{-2} Pa. This SnO_x film has shown a compact and dense morphology without presence of pinholes or cracks, and its grain sizes were relatively larger compared to other samples, which clearly improved the electron mobility. Its average optical transmittance between 400 and 700 nm was measured to be above 80%. The **best optical transmittance** of 91% is achieved only using the highest O_2/Ar ratio of 0.075 for deposited SnO_x at 250°C without annealing and with vacuum annealing as well as both air annealed samples. Vacuum annealing provided a higher electrical conductivity compared to the as-deposited and air-annealed processes. This is attributed to the improvement of crystalline microstructure as well as the presence of oxygen lattice vacancies which has led to a high charge carrier concentration. These growth conditions summarise a good compromise between a high grain size, higher crystalline structure, and high charge carrier concentration. The most conductive SnO_x sample obtained by using O_2/Ar = 0.015 during the growth at 250 °C and followed by a moderate vacuum post annealing have also enabled the best optoelectronic performance as assessed by FoM.

2.4. SnO_x sputtered using a Sn target

In this study, the SnO_x thin films were prepared using reactive magnetron sputtering, manufactured by AJA International Co. (described in the appendix in section 1.3.), with a high purity Sn (99.999%) 2".

2.4.1. Effect of O_2 flow rate during the growth on SnO_x

The aim of this study is to investigate the effect of O_2 flow rate while using magnetron sputtering on deposited SnO_x using Sn metallic sputtering target while setting the other parameters, namely power at 50 W, Ar flow rate at 12 sccm, deposition temperature at 100 °C and deposition pressure at 0.45 Pa. The deposition time was kept constant for low O_2 flow rate at 12 minutes. However, it was slightly increased to 15 minutes at higher O_2 flow rates to adjust the expected decrease in deposition rate. The targeted thickness is slightly above 100 nm. The ultimate objective is to explore the SnO_x thin film properties from low O_2 flow rates to higher one to study the structural and optoelectronic properties while varying the O_2 at low flow rate. The samples synthesis parameters are presented in table 8.

Sample name	Power (W)	Substrate Temperature (°C)	Deposition time (min)	O_2/Ar (O_2:Ar sccm)	Deposition Pressure (Pa)
6S1D	50	100	12 (100nm target)	0.17 (2:12)	0.45
6S2D				0.21 (2.5:12)	
6S3D				0.25 (3:12)	
6S4D			15 (100nm target)	0.29 (3.5:12)	
6S5D				0.33 (4:12)	

Table 8: SnO_x thin film deposition parameters using radio-frequency magnetron sputtering.

a) Structural properties and chemical state analysis

Grazing incidence X-ray diffraction was performed to probe the crystalline microstructure of the SnO_x thin films in different O_2 partial pressures during the growth. Both SnO_x samples deposited at 0.17 and 0.21 O_2/Ar flow rate ratios have shown a broad peak around 30° which indicate the presence of low crystalline or amorphous SnO phase. Similar results were reported in a previous section of this chapter. For SnO_x deposited at 0.25 O_2/Ar flow rate ratio the peak become broader which indicate the presence of either or both low crystalline or amorphous phases SnO and SnO_2. Samples deposited at 0.29 and 0.33 O_2/Ar ratios have revealed a clear crystalline microstructure by the presence of XRD peaks (110), (101), (200) and (211) related to SnO_2 phase only. It is worth noting that the sharpest peak was (200) observed for SnO_x deposited at 0.29 O_2/Ar flow rate ratio as shown in Figure 11. The poor oxygen condition during the growth has enabled the formation of SnO which the lower oxidation state of SnO_x. Increasing the O_2 partial pressure in the growth atmosphere has increased the oxidation state of SnO_x which led to a dominant phase of SnO_2. The crystallization of the SnO phase was not achieved in this study as the SnO_x tend to change the phase from SnO to SnO_2 while increasing the O_2 partial pressure. On the other hand, increasing the O_2 partial pressure to richer condition enabled the crystallization of SnO_2 for samples grown at 0.29 and 0.33 O_2/Ar flow rate ratios.

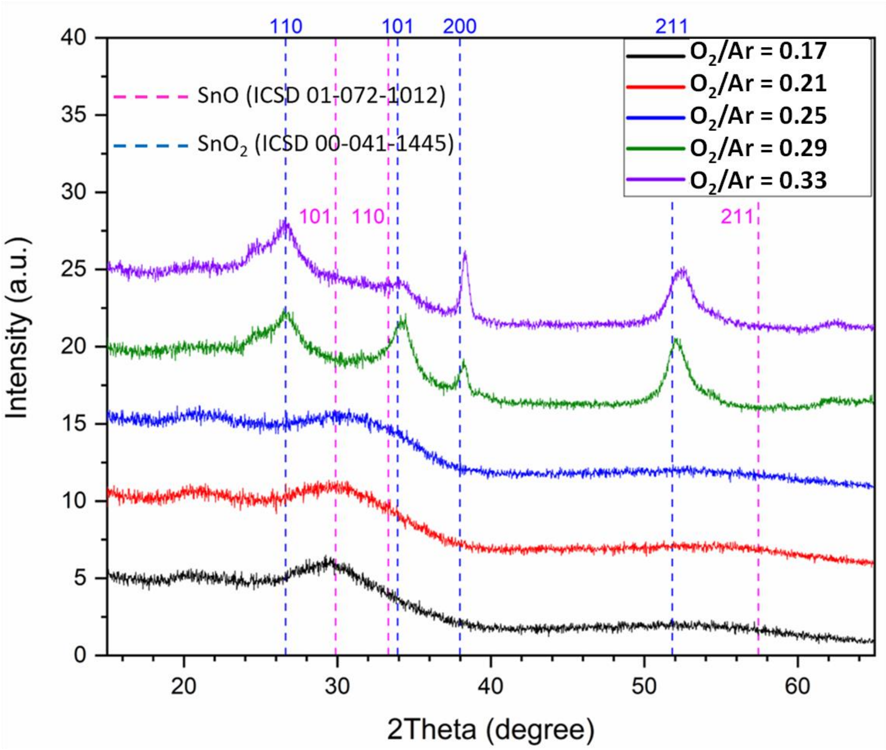

Figure 11: GIXRD pattern for SnO_x sample using different O_2 flow rates during the growth.

Chemical state analysis was performed using X-ray photoelectron spectroscopy which is a surface sensitive technique analysing the surface of around 5 nm thickness. As expected, the surface of thin films gets oxidized at the surface once exposed to the air. However, the technique can provide an important indication of the present chemical states of the overall film. All XPS spectra for $Sn3d_{5/2}$ show only the presence of the two chemical states Sn(II) and Sn(IV) without any presence of Sn(0) which indicates that the Sn sputtering deposition is completely oxidized and there is no indication of metallic Sn presence within the surface of SnO_x. The peak position of $Sn3d_{5/2}$ related to Sn(II) is around 486.5 (+/- 0.1) eV while the one for Sn(IV) is around 486.9 (+/- 0.1) as shown in Figure 12. The chemical state analysis revealed that the presence of Sn(II) in SnO_x at 0.17 O_2/Ar flow rate ratio is around 47% while Sn(IV) is 53%. Sn(II) percentage decreases to 40% while the O_2/Ar flow rate ratio increases to 0.29 and Sn(IV) increases to 60%. Sn(II) percentage decreases drastically to 22% while the O_2/Ar flow rate ratio increases to 0.25 and Sn(IV) increases to 78%. Sn(II) percentage continue decreasing to 8% while the O_2/Ar flow rate ratio reaches 0.29 and Sn(IV) increases to 92%. Sn(II) percentage slightly increasing to 10% at O_2/Ar flow rate ratio of 0.33 while Sn(IV) decreases to 90%. XPS results shows that the chemical state of SnO_x thin film made from metallic Sn sputtering target follows the same pattern of SnO_x made from oxidised SnO target. It can be summarised by the presence of mainly SnO as revealed by Sn(II) at low O_2/Ar flow rates along with the presence of Sn(IV) at the surface. It is worth noting that the surface of thin films would always oxidise to a higher chemical state due to the presence of oxygen in air. The main chemical state of SnO_x becomes SnO_2 as revealed by Sn(IV) in O_2 rich conditions for O_2/Ar ratio at 0.25 or higher. These results are matching with the XRD results discussed previously.

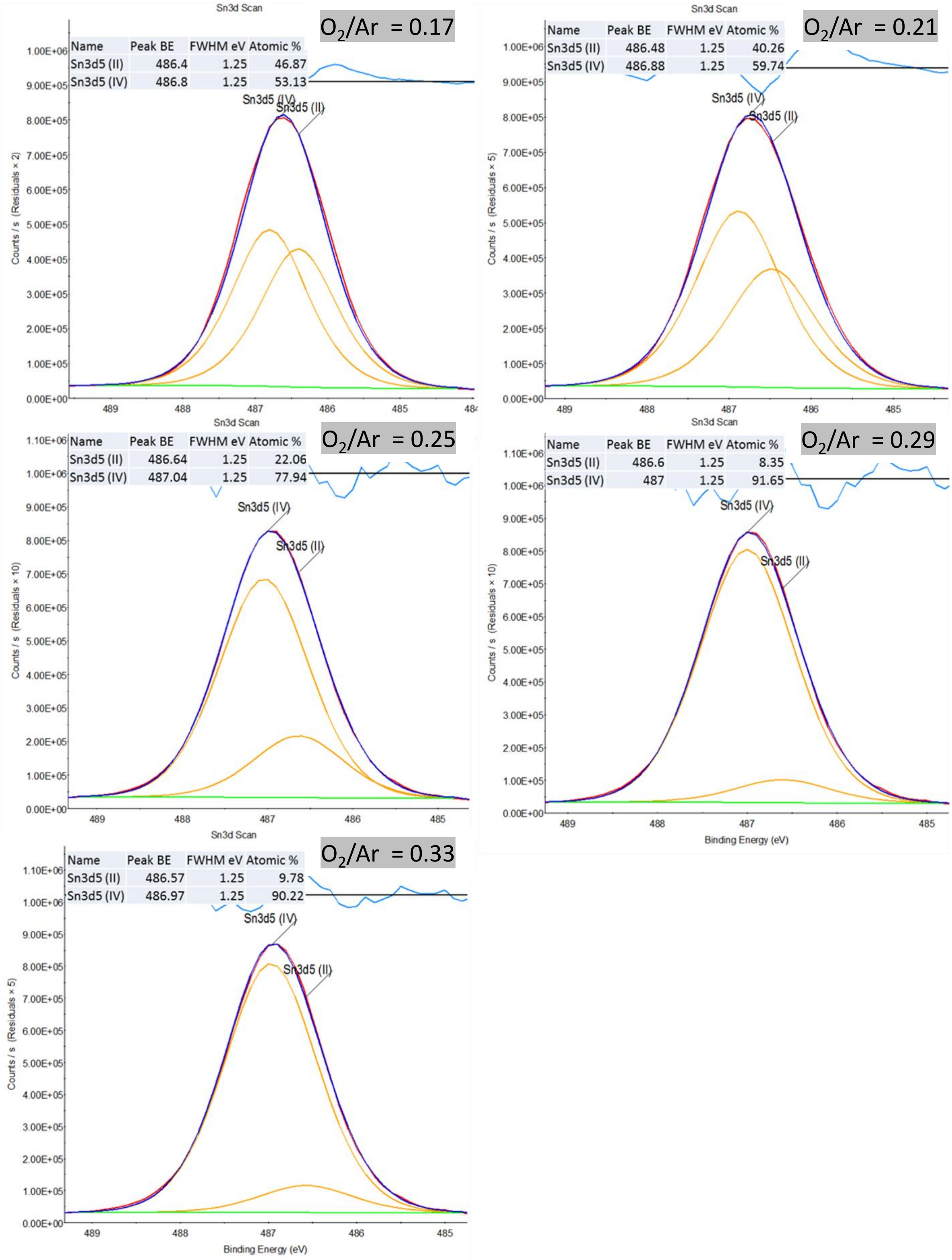

Name	Peak BE	FWHM eV	Atomic %
Sn3d5 (II)	486.4	1.25	46.87
Sn3d5 (IV)	486.8	1.25	53.13

Name	Peak BE	FWHM eV	Atomic %
Sn3d5 (II)	486.48	1.25	40.26
Sn3d5 (IV)	486.88	1.25	59.74

Name	Peak BE	FWHM eV	Atomic %
Sn3d5 (II)	486.64	1.25	22.06
Sn3d5 (IV)	487.04	1.25	77.94

Name	Peak BE	FWHM eV	Atomic %
Sn3d5 (II)	486.6	1.25	8.35
Sn3d5 (IV)	487	1.25	91.65

Name	Peak BE	FWHM eV	Atomic %
Sn3d5 (II)	486.57	1.25	9.78
Sn3d5 (IV)	486.97	1.25	90.22

Figure 12: XPS peak fitting for SnO_x samples using different O_2 flow rates during the growth.

b) Optical properties

The optical transmittance in UV-Visible-Infrared range for SnO_x thin film samples is shown in Figure 13(a). Both average of optical transmittance from 400 to 700 nm and from 500 to 800 nm as well as the optical transmittance at 550 nm and the optical bandgap are defined in Table 9. The average optical transmittance from 500 to 800 nm is 82% for SnO_x thin film sample with O_2/Ar flow rate ratio at 0.17. This transmittance decreases to 80% at O_2/Ar of 0.21 and continues to decrease to 76.5% at O_2/Ar of 0.25. The optical transmittance increases to 85.3% when the O_2/Ar flow rate ratio increases to 0.29 and it continues to increase to 89.7% for O_2/Ar ratio at 0.33. The optical transmittance spectra show that cut-on edge is towards higher wavelength with oxygen poor growth conditions for SnO_x thin film grown samples and it is towards lower wavelength for the relatively oxygen rich conditions grown SnO_x thin film samples. The optical transmittance is relatively high which is above than 80% for four samples out of five without excluding the absorbance/reflection contribution of the quartz substate. The highest optical transmittance is achieved by the SnO_x thin sample which has the highest O_2 flow rate during the growth which is related to highest oxidized SnO_x.

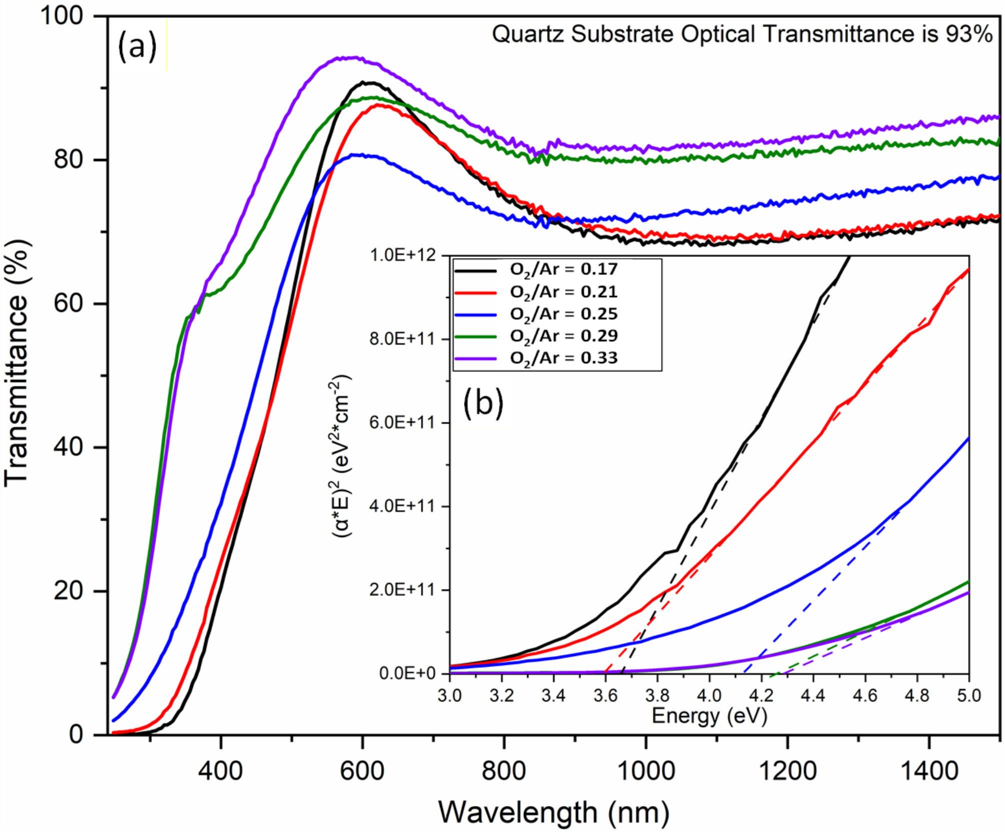

Figure 13: (a) UV-Vis transmittance spectra and (b) Tauc plot for SnO_x samples using different O_2/Ar flow rate ratio during the growth.

Tauc plot for SnO_x thin film samples is shown in Figure 13(b) and their related optical bandgap is defined in Table 10. Tauc plot was established for both direct and indirect bandgap. Only the direct bandgap plot had a clear linear region which could be extrapolated to the abscissa. Therefore, the SnO_x thin film samples are direct bandgap. The SnO_x sample of oxygen poor condition during the growth, namely for O_2/Ar ratio at 0.17 and 0.21, have a lower bandgap which is 3.7 and 3.6 eV respectively. The oxygen rich condition during the growth, namely for O_2/Ar ratio at 0.25, 0.29 and 0.33, have a higher bandgap which is 4.1, 4.3 and 4.3 eV, respectively. The optical bandgap results, and as per the literature, are interpreted as the SnO_x thin films grown at O_2/Ar ratio of 0.17 and 0.21 are mainly SnO and the SnO_x thin films grown at O_2/Ar ratio of 0.25, 0.29 and 0.33 are mainly SnO_2. It is worth mentioning that 4.3 eV one of the highest results reported in the literature as shown previously in the summary (Figure 7).

O_2/Ar (O_2:Ar sccm)	Optical Transmittance (%)			Optical Bandgap (eV)
	Average 400–700 nm	Average 500–800 nm	At 550 nm	
0.17 (2:12)	68.8	82.0	82.3	3.7
0.21 (2.5:12)	66.9	80.0	76.6	3.6
0.25 (3:12)	68.2	76.5	78.1	4.1
0.29 (3.5:12)	80.5	85.3	85.5	4.3
0.33 (4:12)	86.7	89.7	93.4	4.3

Table 9: Average optical transmittance from 400 to 700 nm and from 500 to 800 nm, optical transmittance for 550 nm, and optical bandgap for SnO_x thin film samples.

c) Electrical properties

Hall effect measurements on SnO_x thin films shown in Table 10 have revealed that poor oxygen condition led to a very high electrical resistivity and further measurements were not possible. The relatively oxygen richer condition, namely for SnO_x thin films grown at O_2/Ar ratio of 0.29 and 0.33, has provided a very low electrical resistivity below 5×10^{-3} Ω·cm. The SnO_x sample grown at O_2/Ar ratio of 0.25 has an average electrical resistivity of 2.84×10^{-1} Ω·cm.

The high electrical resistivity of SnO_x thin films, grown at O_2/Ar ratio of 0.17 and 0.21, is mainly related to the amorphous character of the dominant phase SnO as revealed by XRD, XPS and UV-Vis. The low electrical resistivity of SnO_x thin films, grown at O_2/Ar ratio of 0.29 and 0.33, is related to both high mobility which is mainly a result of the crystalline microstructure of SnO_2 dominant phase and intrinsic charge carrier of SnO_2 due to the oxygen vacancies[36]. The moderate electrical resistivity of SnO_x thin film, grown at O_2/Ar ratio of 0.25, is related to the amorphous character of the dominant SnO_2 phase which has led to a relatively smaller electron mobility of 1.51 cm^2/V·s compared to both 18.1 and 24.4 cm^2/V·s for rich oxygen conditions.

O_2/Ar (O_2:Ar sccm)	Thickness (nm)	Rate (nm/min)	Resistivity (Ω.cm)	Sheet resistance (Ω/□)	Mobility (cm^2/V·s)	Charge concentration (cm^{-3}) – (carrier type)
0.17 (2:12)	132	11	N/A*	N/A	N/A	N/A
0.21 (2.5:12)	125	10.42	N/A*	N/A	N/A	N/A
0.25 (3:12)	113	9.42	2.84×10^{-1}	2.51×10^{4}	1.51	1.64×10^{19} - (n-type)
0.29 (3.5:12)	136	9.07	4.93×10^{-3}	3.63×10^{2}	18.1	9.52×10^{19} - (n-type)
0.33 (4:12)	145	9.67	3.00×10^{-3}	2.07×10^{2}	24.4	1.24×10^{20} - (n-type)

Table 10: Electrical properties of SnO_x thin film samples using different O_2 flow rate ratios during the growth.

* Very high resistivity.

d) Optoelectronic performance

Table 11 shows the Figure of Merit (FoM) for SnO_x thin film samples. The poor oxygen conditions of grown SnO_x thin film at O_2/Ar ratio of 0.17 and 0.21 led to a high resistivity which is due to the amorphous character of the dominant phase SnO. Thus, their FoM could not be computed, and it is expected to be very low. However, richer oxygen condition grown SnO_x thin film at O_2/Ar ratio of 0.29 and 0.33 have shown relatively high optoelectrical performance by their high FoM. The SnO_x thin film grown at O_2/Ar ratio of 0.25, has a relatively low optoelectrical performance due to the moderate electrical resistivity. It is worth noting that as per the literature and to the best of our knowledge, SnO_x thin film grown O_2/Ar ratio of 0.33 of 2.44×10^{-3} Ω^{-1} has one of the highest reported optoelectrical performance for undoped SnO_x as indicated in the summary of Figure 7.

O_2/Ar (O_2:Ar sccm)	Figure of merit (10^{-3} Ω^{-1})		
	Average Transmittance 400 – 700 nm	Average Transmittance 500 – 800 nm	Transmittance at 550 nm
0.17 (2:12)	N/A	N/A	N/A
0.21 (2.5:12)	N/A	N/A	N/A
0.25 (3:12)	8.67×10^{-4}	2.73×10^{-3}	3.36×10^{-3}
0.29 (3.5:12)	0.315	0.562	0.575
0.33 (4:12)	1.16	1.63	2.44

Table 11: Figure of Merit for SnO_x thin film samples using different O_2 flow rates during the growth.

2.4.2. Effect of deposition temperature on SnO_x using Sn metallic target

After assessing the effect O_2 flow rate during the growth on SnO_x, this study is mainly focusing on the effect of deposition temperature during the growth on SnO_x thin films in poor oxygen condition. All parameters were kept fixed except the deposition temperature. The fixed parameters are power at 50 W, Ar flow rate at 12 sccm, deposition pressure at 0.45 Pa, and O_2/Ar flow rate ratio at 0.21. This last parameter was chosen because it is just below the poor oxygen condition point for the SnO_x thin film grown at O_2/Ar of 0.25 that provided a predominant SnO_2 phase. The deposition temperature used in this study, are room temperature (RT), 100, 200 and 400°C. The deposition time was kept constant at 12 minutes for all samples. The targeted thickness is slightly above 100 nm. The objective of this study is also to assess the possibility to improve the crystallinity of the dominant SnO phase and eventually improve the electrical conductivity. The samples synthesis parameters are presented in Table 12.

Sample name	Mode/target	Power (W)	Substrate Temperature	Deposition time (min)	O_2/Ar (O_2:Ar sccm)	Depos. Pressure (Pa)
7S1D	RF/Sn (2”)	50	RT	12 (100nm target)	0.21 (2.5:12)	0.45
7S2D			100°C			
7S3D			200°C			
7S4D			400°C			

Table 12: SnO_x thin film deposition parameters using radio-frequency magnetron sputtering.

a) Structural properties and chemical state analysis

Grazing incidence X-ray diffraction, shown in Figure 14, was performed to probe the crystalline structure of the SnO_x thin films in different deposition temperatures during the growth. All SnO_x samples have shown a broad peak around 30° which indicate the presence of low crystalline or amorphous SnO phase. In addition, GIXRD pattern of SnO_x deposited at 400°C has shown a small peak at 34° related to SnO_2 (101) and a smaller peak at 52° related to SnO_2 (211). Both these peaks indicate a small presence of SnO_2 crystalline phase. Varying the deposition temperature did not change the amorphous microstructure of the SnO at RT, 100°C and 200°C. However, the deposition temperature at 400°C enabled the formation of a small crystalline phase of SnO_2 along with predominant amorphous SnO.

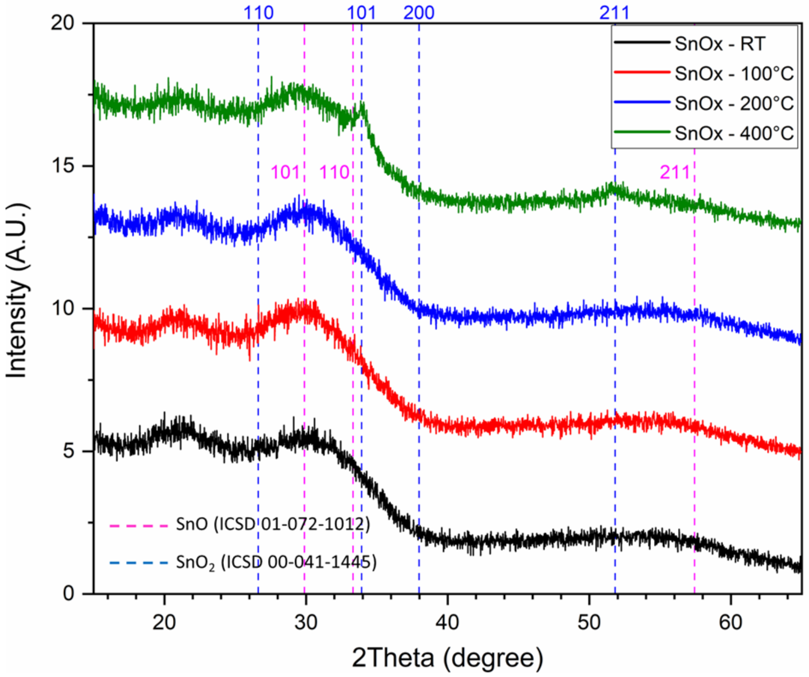

Figure 14: GIXRD pattern for SnO_x sample using different deposition temperatures during the growth.

Surface sensitive chemical state analysis was performed using X-ray photoelectron spectroscopy. Similar to the previous study, it is expected to get higher oxidation state at the surface of thin films due to the air exposure. All XPS spectra for Sn3$d_{5/2}$ show only the presence of the two chemical states Sn(II) and Sn(IV) without any presence of Sn(0) which indicates that the Sn sputtering deposition is completely oxidized and there is no indication of metallic Sn presence within the surface of SnO_x. The peak position of Sn3$d_{5/2}$ related to Sn(II) is around 486.5 (+/- 0.1) eV while the one for Sn(IV) is around 486.9 (+/- 0.1) as shown in Figure 15. The chemical state analysis revealed that the presence of Sn(II) in SnO_x deposited at room temperature is around 29% while Sn(IV) is 71%. Sn(II) percentage increases to 40% and Sn(IV) increases to 60% for SnO_x deposited at 100°C. Sn(II) percentage slightly decreases to 38% and Sn(IV) increases to 62% for SnO_x deposited at 200°C. For SnO_x deposited at 400°C, Sn(II) percentage slightly increasing to 41% and Sn(IV) decreases to 59%. XPS results the chemical states distribution of Sn(II) and Sn(IV) were very closely matching in samples deposited at 100, 200 and 400°C. While SnO_x deposited at room temperature was more oxidized to the higher oxidation state as revealed by the lower Sn(II) and the higher Sn(IV) chemical states. As stated before, the presence of higher oxidation states at the surface is likely related to the post deposition oxidation of SnO_x once exposed to the air. These results along the XRD ones have revealed that there is a major presence of Sn(II) chemical state as SnO except at the surface, and the temperature deposition did not change drastically the chemical state except for the room temperature deposition which favours more the Sn(IV) chemical state. It is also worth noting that the higher temperature 400°C enables the crystallization of the phase SnO_2.

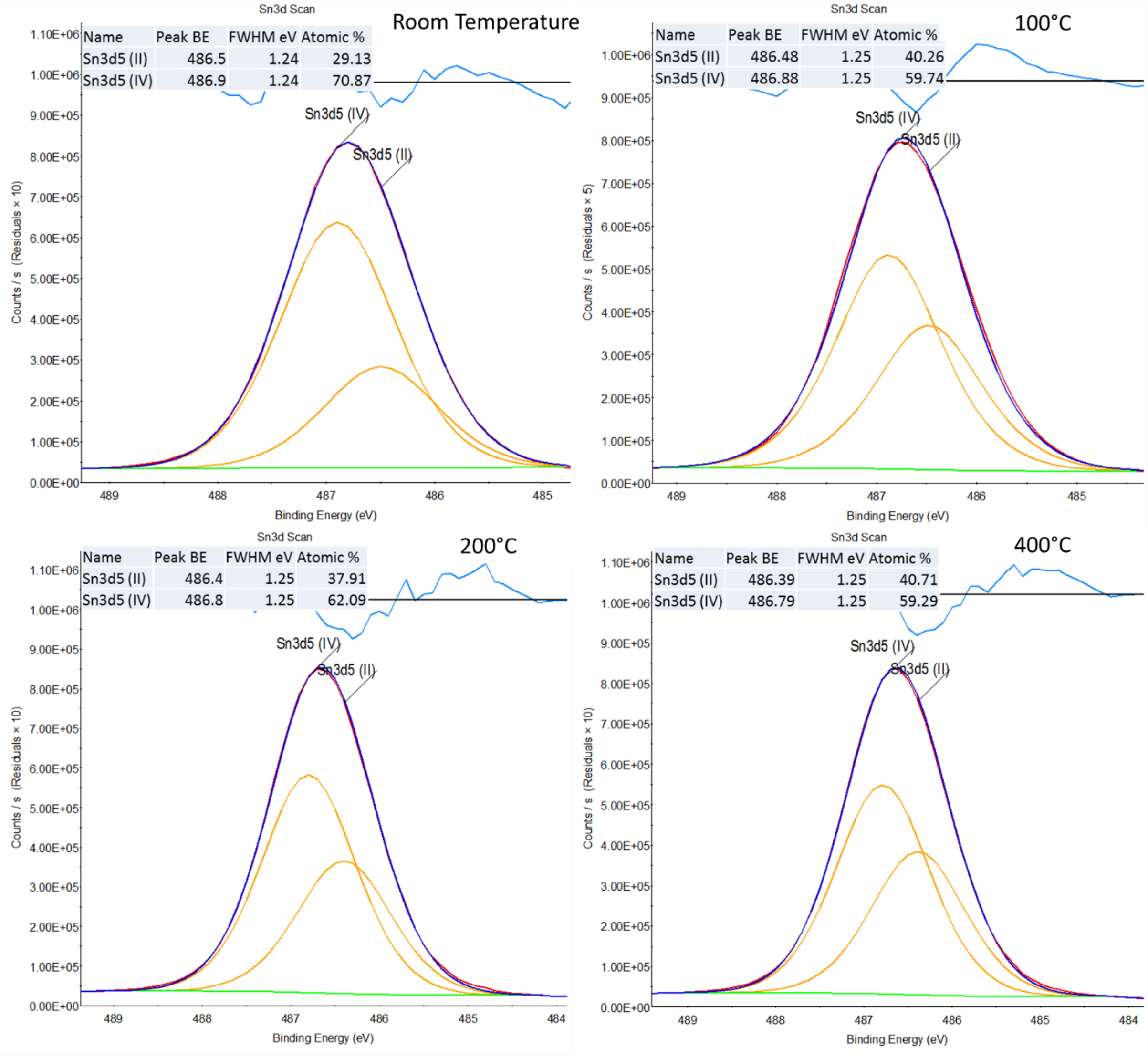

Room Temperature

Name	Peak BE	FWHM eV	Atomic %
Sn3d5 (II)	486.5	1.24	29.13
Sn3d5 (IV)	486.9	1.24	70.87

100°C

Name	Peak BE	FWHM eV	Atomic %
Sn3d5 (II)	486.48	1.25	40.26
Sn3d5 (IV)	486.88	1.25	59.74

200°C

Name	Peak BE	FWHM eV	Atomic %
Sn3d5 (II)	486.4	1.25	37.91
Sn3d5 (IV)	486.8	1.25	62.09

400°C

Name	Peak BE	FWHM eV	Atomic %
Sn3d5 (II)	486.39	1.25	40.71
Sn3d5 (IV)	486.79	1.25	59.29

Figure 15: XPS peak fitting for SnO_x samples using different deposition temperatures during the growth.

b) Optical properties

The optical properties were probed by UV-Visible spectrometer. The optical transmittance in UV-Visible-Infrared range for SnO_x thin film samples is shown in Figure 16(a). The average of optical transmittance from 400 to 700nm, from 500 to 800nm, the optical transmittance at 550nm and the optical bandgap are defined in Table 13. The average optical transmittance from 500 to 800nm is 75.5% for SnO_x thin film sample deposited at room temperature. This transmittance increases to 80% for SnO_x deposited at 100°C and it decreases to 75.9% for SnO_x deposited at 200°C. The optical transmittance increases to 83.2% when the deposition temperature of SnO_x increases to 400°C. The optical transmittance spectra show that cut-on edges for all samples is very close to each other. The optical transmittance is relatively high which is above than 75% for all samples without excluding the absorbance/reflection contribution of the quartz substate. The highest optical transmittance is obtained with the SnO_x thin film sample grown at 400°C. This is due to the better microstructural ordering and disorder reduction[35, 36, 51, 79].

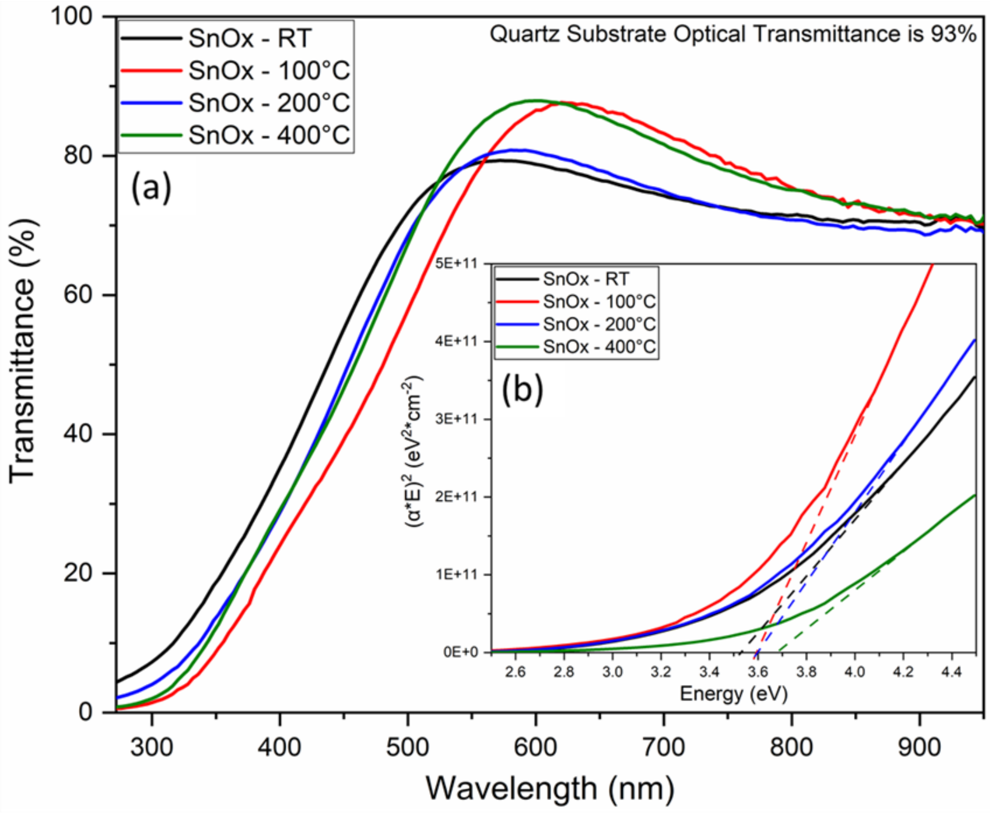

Figure 16: (a) UV-Vis transmittance spectra and (b) Tauc plot for SnO_x samples using different deposition temperatures during the growth.

Tauc plot for SnO_x thin film samples is shown in Figure 16(b) and their related optical bandgap is defined in Table 13. Tauc plot was established for both direct and indirect bandgap. Similar to the previous study, only the direct bandgap plot had a clear linear region for all samples which could be extrapolated to the abscissa. Therefore, the SnO_x thin film samples are direct bandgap. All SnO_x samples have very similar optical bandgap of about 3.6 (+/- 0.1) eV. SnO_x deposited at room temperature have shown a bandgap of 3.5 eV. Both SnO_x samples deposited at 100 and 200°C have exhibited an optical bandgap of 3.6 eV while SnO_x deposited at 400°C show an optical bandgap of 3.7 eV. The optical bandgap difference between the four samples is very small. However, this study shows that increasing the temperature can increase even slightly the optical bandgap which is more due to the microstructural ordering and defect reduction. It is worth mentioning that the presence of defects can form shallow energy levels which reduces the optical bandgap. As per the literature, the optical bandgaps of 3.6 (+/- 0.1) eV reveal that predominant phase in the SnO_x thin film samples is SnO which is expected to the poor oxygen condition during the growth of SnO_x. This predominant SnO phase was not significantly affected by the deposition temperature variation from RT to 400°C[35, 36, 51, 79].

Deposition Temperature	Optical Transmittance (%)			Optical Bandgap (eV)
	Average 400-700nm	Average 500-800 nm	At 550nm	
RT	69.4	75.5	78.7	3.5
100°C	66.9	80.0	76.6	3.6
200°C	67.8	75.9	79.1	3.6
400°C	71.1	81.4	83.2	3.7

Table 13: Average optical transmittance from 400 to 700nm and from 500 to 800nm, optical transmittance for 550nm, and optical bandgap for SnO_x thin film samples using different deposition temperatures during the growth.

c) Electrical properties

Hall effect measurements were not possible due to the high resistivity of the SnO_x thin film samples as shown in table 14. The deposition temperature did not improve the electrical conductivity at poor oxygen condition during the growth. The high resistivity is likely related to the amorphous character of the SnO. Improving the SnO crystallinity can be a key factor to improve the electrical and optoelectrical performance of the SnO samples. Further studies related to this topic will be presented and discussed in this thesis.

Deposition Temperature	Thickness (nm)	Rate (nm/min)	Resistivity (Ω*cm)	Sheet resistance (Ω/sq)	Mobility (cm^2/Vs)	Charge concentration (cm^{-3})
RT	100	8.33	N/A*	N/A	N/A	N/A
100°C	125	10.42	N/A*	N/A	N/A	N/A
200°C	116	9.67	N/A*	N/A	N/A	N/A
400°C	205	17.08	N/A*	N/A	N/A	N/A

Table 14: Electrical properties of SnO_x thin film samples using different deposition temperatures during the growth. * Very high resistivity.

d) Optoelectronic performance

The Figure of Merit which reveals the optoelectrical performance of the SnO_x thin film samples were not calculated due to the very high resistivity of the SnO_x thin films. Figure of Merit is expected to be extremely low.

2.4.3. Summary

SnO_x thin film samples, with different O_2/Ar flow rate ratios during the growth, have shown very different structural, optical and electrical properties. At poor oxygen condition during the growth, SnO_x were mainly amorphous SnO phase, the optical transmittance was equal or above 80%. However, the electrical resistivity was very high. At higher oxygen condition during the growth, the predominant phase was SnO_2, the optical transmittance varied from 76.8 to 89.7 % and the resistivity varied from 2.84×10^{-1} to 3×10^{-3} Ω·cm. All samples deposited at higher O_2/Ar flow rate ratios were n-type conductive. The optoelectrical performance has improved while increasing the O_2/Ar flow rate ratios.

At relatively poor oxygen condition, SnO_x thin film samples deposited at different temperature have shown the presence of a predominant amorphous SnO phase. Furthermore, SnO_x deposited at 400°C has shown a small presence of SnO_2. The optical properties have shown a relatively high optical transmittance and very similar bandgaps for all the SnO_x which related SnO. However, the electrical resistivity was very high for all samples at different deposition temperatures[36].

As per both studies related to O_2 flow effect and growth temperature, it can be concluded that the high electrical resistivity of the predominant SnO phase thin film is due to the amorphous microstructure regardless of the deposition temperature during the growth. The predominant amorphous SnO_2 phase is moderately resistive due to the amorphous microstructure. However, predominant crystalline SnO_2 thin film is highly conductive. Tuning the deposition temperature at poor oxygen condition during the growth of SnO_x did not improve the crystalline microstructure of SnO_x thin film samples. Thus, the electrical properties could not be improved. Improving additional parameters during the growth and/or post annealing might be required to achieve a crystalline SnO phase.

2.5. Effect of thermal annealing of sputtered SnO_x under Ar atmosphere

The objective of this part is to explore the possibility of achieving SnO_x p-type conductivity through thermal annealing using inert gas, namely Ar, to avoid any reaction with the SnO_x during the process. For this study, the SnO_x films were synthetized using the method described in part 2.3. More specifically, the SnO_x thin films were prepared using magnetron sputtering, manufactured by Torr Int. (described in the appendix in section 1.3.) with a high purity SnO (99.99%) 2”- diameter target (Manufactured by Codex International) on cleaned quartz substrates at a temperature of 250 °C, under different O_2/Ar flow rates ratios where $O_2/Ar = 0.015$, 0.035, 0.055, 0.065 and 0.075. The other deposition conditions were fixed, at 50 W as a power, 200 sccm of Ar flow rate and 30 min deposition duration time for all samples. Prior deposition, the base pressure was around 6.66×10^{-3} Pa while the deposition pressure was approximately 0.66 Pa as summarized in Table 15. The as-deposited samples were subject to different annealing processes as summarized in Diagram 2.

The thermal annealing process was carried out using a tube furnace (made by Carbolite, UK) and high purity Ar gas which is used as process gas. Diagram 2 below shows the summary of the applied thermal annealing processes. The annealing temperature varied from 400 to 600°C and duration time from 20 to 120 min. As the objective of this study is to explore the possibility of p-type conductivity, the main used characterization technique is the Hall effect probe.

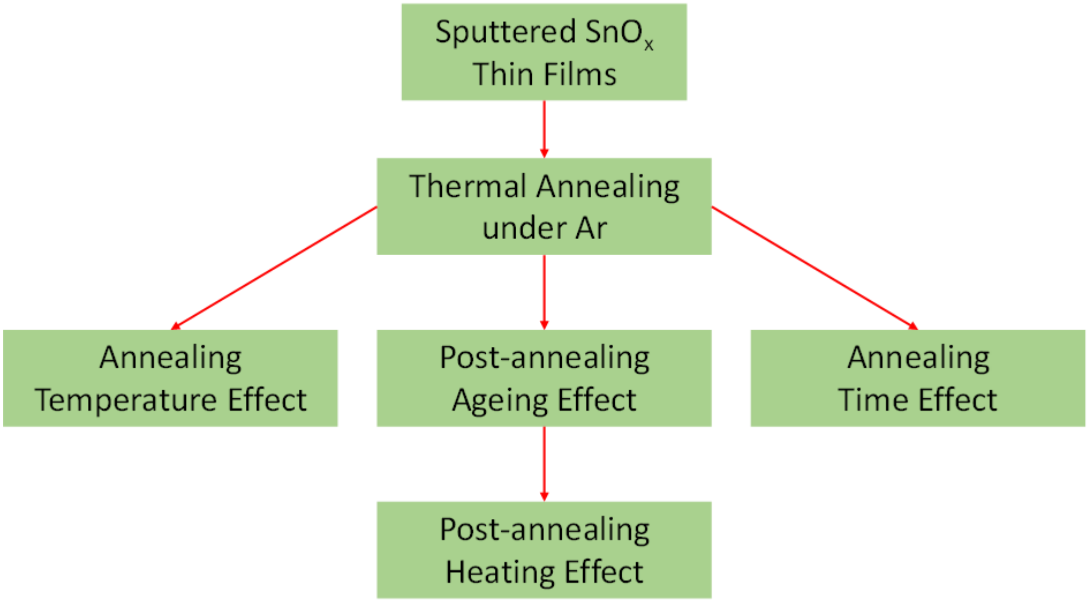

Diagram 2: Different experiments conducted using Ar thermal annealing.

Sample	Substrate Temp (°C)	Power (W)	O_2/Ar (O_2:Ar sccm)	Depos. Pressure (Pa)	Deposition time (min)
S1	250	50	0.015 (3:200)	0.66	30
S2			0.035 (7:200)		
S3			0.055 (11:200)		
S4			0.065 (13:200)		
S5			0.075 (15:200)		

Table 15: Summary of the magnetron sputtering conditions of SnO$_x$ thin film samples.

2.5.1. Annealing temperature effect on SnO$_x$ thin films

The aim of this experiment using different annealing temperatures is to define if there is an effect of the annealing temperature on the electrical properties of SnO$_x$ thin films. The annealing processes temperatures were 400, 500 and 600 °C and all other parameters were kept fixed, namely Ar flow rate and annealing time as shown in Table 16.

Annealing	Flow rate (sccm)	Temperature (°C)	Time (min)
A400	57 (Ar)	400	50
A500	57 (Ar)	500	50
A600	57 (Ar)	600	50

Table 16: Summary of the annealing conditions of SnO$_x$ thin film samples.

The as-deposited samples have shown a high resistivity for O_2/Ar ratio of 0.015 and 0.035. However, the SnO_x samples were very high resistive for higher O_2/Ar ratios and their conductivity type and electrical parameters could not be determined as shown in Table 17.

Furthermore, the thermal annealing at 400 °C in Ar atmosphere has improved remarkably the electrical conductivity for all samples to a moderate resistivity except for SnO_x deposited at O_2/Ar of 0.035 which has slightly improved the resistivity from 2.4×10^2 to 1.6×10^2 Ω.cm. Similarly, while the mobility of all samples are in the range of 10^{-1} $cm^2/V{\cdot}s$, that of SnO_x deposited at O_2/Ar ratio of 0.035 has a high mobility of 2.6 $cm^2/V{\cdot}s$. The charge carrier concentration for all samples is relatively high in the range of 10^{18} cm^{-3} whereas SnO_x deposited at O_2/Ar ratio of 0.035 exhibited a lower concentration of about 1.5×10^{16} cm^{-3}. All thermally annealed SnO_x samples at 400 °C have n-type conductivity. The improvement in conductivity is mainly related to the improvement of the n-type charge carrier concentration at least for the SnO_x thin films deposited at O_2/Ar ratio of 0.015 and 0.035.

The thermal annealing at 500 °C has improved the electrical resistivity for all samples. However, this improvement is less important compared to the thermal annealing at 400 °C. The SnO_x samples deposited at O_2/Ar ratio of 0.015 and 0.035, and annealed at 500 °C, have demonstrated a n-type conductivity with electrical resistivity of 22 and 69 Ω·cm, respectively. The SnO_x thin films deposited at O_2/Ar ratio of 0.055 and 0.065, and annealed at 500 °C, have shown a p-type conductivity with electrical resistivity of 2×10^2 and 2.2×10^2 Ω·cm, respectively. Increasing further the O_2/Ar ratio to 0.075 followed by an annealing at 500 °C led to a mixture of n-type and p-type conductivity with electrical resistivity of 42 Ω·cm. As for the carriers mobility of annealed samples, it decreased for SnO_x film deposited at O_2/Ar ratio of 0.015 while it slightly increased for the SnO_x deposited at O_2/Ar of 0.035. Increasing the O_2/Ar ratio to 0.055 and 0.065 led to relatively good mobility of 8.3 and 14 $cm^2/V{\cdot}s$, respectively. The mobility is found to be as low as 0.11 $cm^2/V{\cdot}s$ for SnO_x deposited at O_2/Ar ratio of 0.075 followed by thermal annealing. The n-type charge carrier concentration has relatively improved for SnO_x deposited at O_2/Ar ratio of 0.015 and 0.035 after thermal annealing at 500 °C while the conductivity type of SnO_x deposited at O_2/Ar ratio of 0.055 and 0.065 have changed from n-type to p-type after this thermal annealing.

The thermal annealing at 600 °C has slightly improved the electrical resistivity for SnO_x thin films deposited at O_2/Ar of 0.015 and 0.035, and significantly improved the electrical resistivity for the rest of the samples. However, this thermal annealing has enabled p-type conductivity for all samples except for the oxygen rich grown SnO_x deposited at O_2/Ar of 0.075. The electrical resistivity for all samples is between 1.1×10^2 and 2×10^2 Ω·cm which is relatively high. The mobility is ranging between 0.13 to 1.4 $cm^2/V{\cdot}s$. The charge carrier concentration ranges from 3×10^{16} to 4.5×10^{17} cm^{-3} for the p-type conductive SnO_x thin films, while it is 2.5 x 10^{16} cm^{-3} for the n-type conductive SnO_x. All electrical measurements data for this post-annealing study are reported in Table 17.

Charge carrier concentration (cm^{-3})

O_2/Ar	As-deposited	Annealed at 400°C 50 minutes	Annealed at 500°C 50 minutes	Annealed at 600°C 50 minutes
0.015	-1.34E+15	-2.60E+18	-7.30E+17	2.30E+17
0.035	N/A**	-1.50E+16	-3.40E+16	3.00E+16
0.055	N/A*	-3.90E+18	4.00E+15	4.50E+17
0.065	N/A*	-3.20E+18	2.00E+15	4.40E+16
0.075	N/A*	-3.00E+18	N/A**	-2.50E+16

Resistivity (Ω·cm)

O_2/Ar	As-deposited	Annealed at 400°C 50 minutes	Annealed at 500°C 50 minutes	Annealed at 600°C 50 minutes
0.015	2.00E+02	2.70E+00	2.20E+01	1.90E+02
0.035	2.39E+02	1.60E+02	6.90E+01	1.60E+02
0.055	N/A*	3.50E+00	2.00E+02	1.40E+02
0.065	N/A*	3.20E+00	2.20E+02	1.10E+02
0.075	N/A*	3.20E+00	4.20E+01	2.00E+02

Mobility ($cm^2/V \cdot s$)

O_2/Ar	As-deposited	Annealed at 400°C 50 minutes	Annealed at 500°C 50 minutes	Annealed at 600°C 50 minutes
0.015	2.38E+01	8.90E-01	4.00E-01	2.00E-01
0.035	4.48E+00**	2.60E+00	4.40E+00	1.40E+00
0.055	N/A*	4.70E-01	8.30E+00	1.30E-01
0.065	N/A*	6.20E-01	1.40E+01	1.30E+00
0.075	N/A*	6.50E-01	1.10E-01**	1.30E+00

Table 17: Hall effect measurement for as deposited and thermally annealed SnO_x.

* Values with orange background represent n-type conductive samples and blue represent p-type conductive samples. Values with white background represent the samples where the conductivity type could not be determined. The samples with the mark. N/A*: high resistivity SnO_x. **: conductivity type could not be determined.

To sum up, the thermal annealing under inert atmosphere namely Ar, has improved the n-type conductivity at 400 °C and converted the n-type conductivity to p-type for four samples out of five at the annealing temperature of 600 °C. It is clear that increasing the annealing temperature has enabled the conductivity type conversion from n-type to p-type through enabling the formation of hole charge carrier due to the phase change from SnO_2 to SnO. The low charge carrier concentration is likely due to the charge compensation effect[13, 18, 19, 34, 80-82].

SnO_x thin film deposited at O_2/Ar ratio of 0.015 has shown a clear n-type conductivity and has changed its conductivity type to p-type upon thermal annealing at 600 °C for 50 min. In order to understand the changes, UV-Visible spectra related Tauc plot calculation was conducted on both as deposited and thermally annealed SnO_x deposited O_2/Ar ratio of 0.015 as depicted in Figure 17. Tauc plot shows that the as-deposited SnO_x is mainly SnO_2 as the optical bandgap is above 4 eV and the optical bandgap annealed SnO_x is less than 4 eV which indicates the presence of SnO phase that decreases the optical bandgap. After thermal annealing at 600 °C, there is a clear redshift of the SnO_x optical bandgap. As discussed previously in Chapter 1, thermal annealing at high temperature is expected to reduce the disorder which increases the optical bandgap. However, in this case the optical bandgap has reduced to a lower value below 4 eV which indicates the formation of SnO phase during the thermal annealing[35, 36, 51, 79].

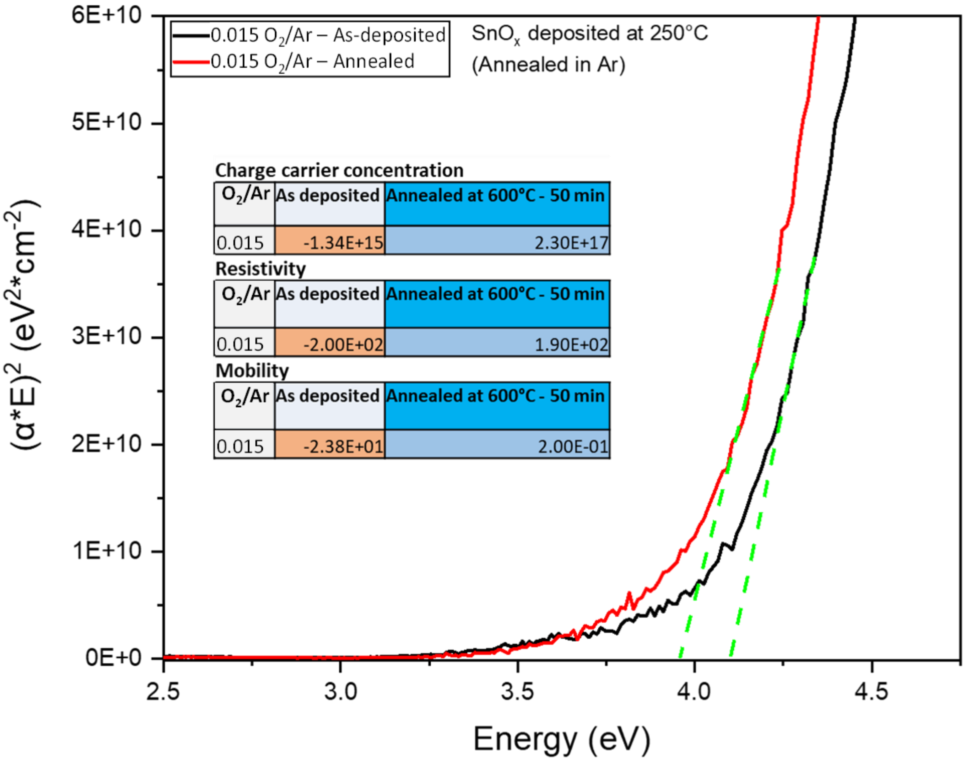

Charge carrier concentration

O_2/Ar	As deposited	Annealed at 600°C - 50 min
0.015	-1.34E+15	2.30E+17

Resistivity

O_2/Ar	As deposited	Annealed at 600°C - 50 min
0.015	-2.00E+02	1.90E+02

Mobility

O_2/Ar	As deposited	Annealed at 600°C - 50 min
0.015	-2.38E+01	2.00E-01

Figure 17: Tauc plot of as deposited and thermally annealed at 600°C SnO_x deposited O_2/Ar ratio of 0.015.

To understand the changes at the crystalline structure, High Resolution - Transmission Electron Microscopy (TEM) in-situ thermal annealing was performed on the SnO_x prepared at 0.015 O_2/Ar ratio where the substrate temperature was set at 250°C. The in-situ study consists of performing the TEM imaging and diffraction for as-deposited SnO_x followed by increasing the temperature from room temperature to 600°C for 10 minutes to complete the annealing process, and then reducing the temperature to 500°C to be able to perform the TEM imaging and diffraction at high temperature (maximum 500°C), and finally slowing down to room temperature to access the changes after the annealing process. The TEM images are shown in Figure 18. It is worth noting that high resolution imaging and diffraction of this TEM can be performed at maximum temperature of 500°C without the cooling system. However, the cooling system is required for higher temperatures, and it induces a certain level of vibration that reduces the resolution of TEM.

As expected, the as-deposited SnO_x sample shows an amorphous microstructure which is confirmed by the TEM images in Figure 18 (a, d) as well as the diffraction pattern in Figure 18 (g) due to the presence of large diffraction bands along. Nevertheless, the presence of some diffraction spots indicates the low crystallinity of SnO_x thin film. Upon thermal annealing and after cooling back to 500°C, there is clearly an improvement in crystallization of SnO_x due to the presence of much larger crystallites in Figure 18 (b) and by clear atomic planes in Figure 18 (e). The diffraction pattern has revealed a polycrystalline structure of SnO_x as witnessed by the presence of multiple sharp rings as well as some bright spots mainly within these rings. Upon returning to room temperature, the crystalline structure has been kept after the thermal annealing as shown in Figure 18 (c, f). TEM diffraction pattern has also revealed a polycrystalline structure by the presence of sharp rings. These rings are slightly thinner compared to the ones recorded at 500°C[83, 84].The diffraction pattern analysis was performed using diffractGUI to define the analysis zone axis and ringGUI to determine the crystallographic planes related to the rings in the diffraction pattern as shown in figure 19 and table 18. The diffraction pattern of SnO_x thin film at 500°C (after thermal annealing at 600°C) and after returning to room temperature is closely matching with SnO phase theoretical positions. This indicates the presence of polycrystalline SnO. These results also show that the amorphous as-deposited SnO_x has been crystallized to SnO and it has kept this SnO phase after the thermal annealing process. One of the lessons from this In-Situ TEM study is that the formed SnO at high temperature is unlikely to be subject to further oxidation while returning back to room temperature in the presence of O_2 as SnO_x sample was constantly under high vacuum in TEM system. This might also explain the non-stability of SnO_x after thermal annealing as well as the ageing affect[85-88].

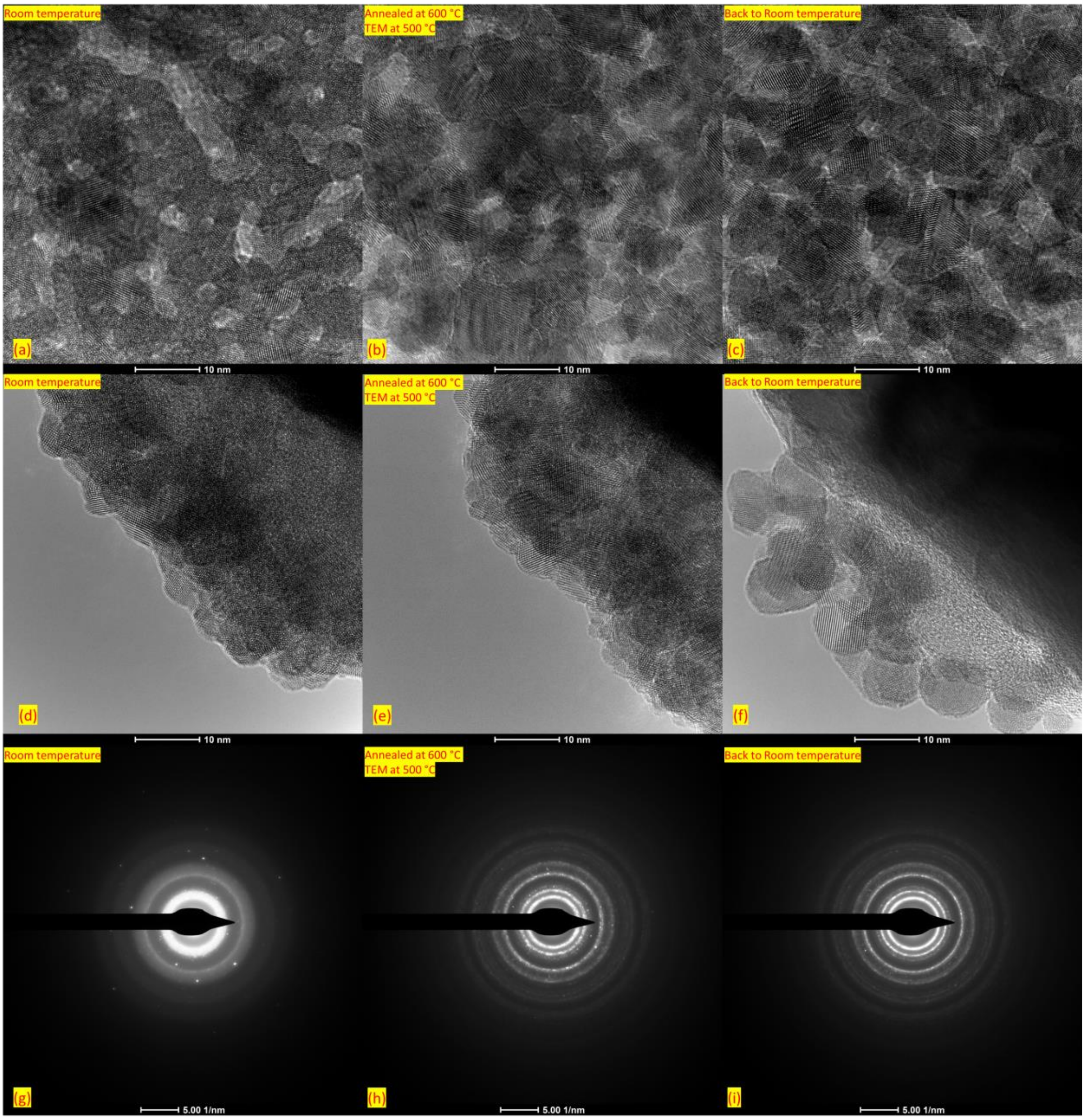

Figure 18: In-Situ Transmission Electron Microscopy imaging and diffraction: (a, d, g) as deposited SnO_x, (b, e, h) in-situ at 500 °C, (c, f, i) back to room temperature.

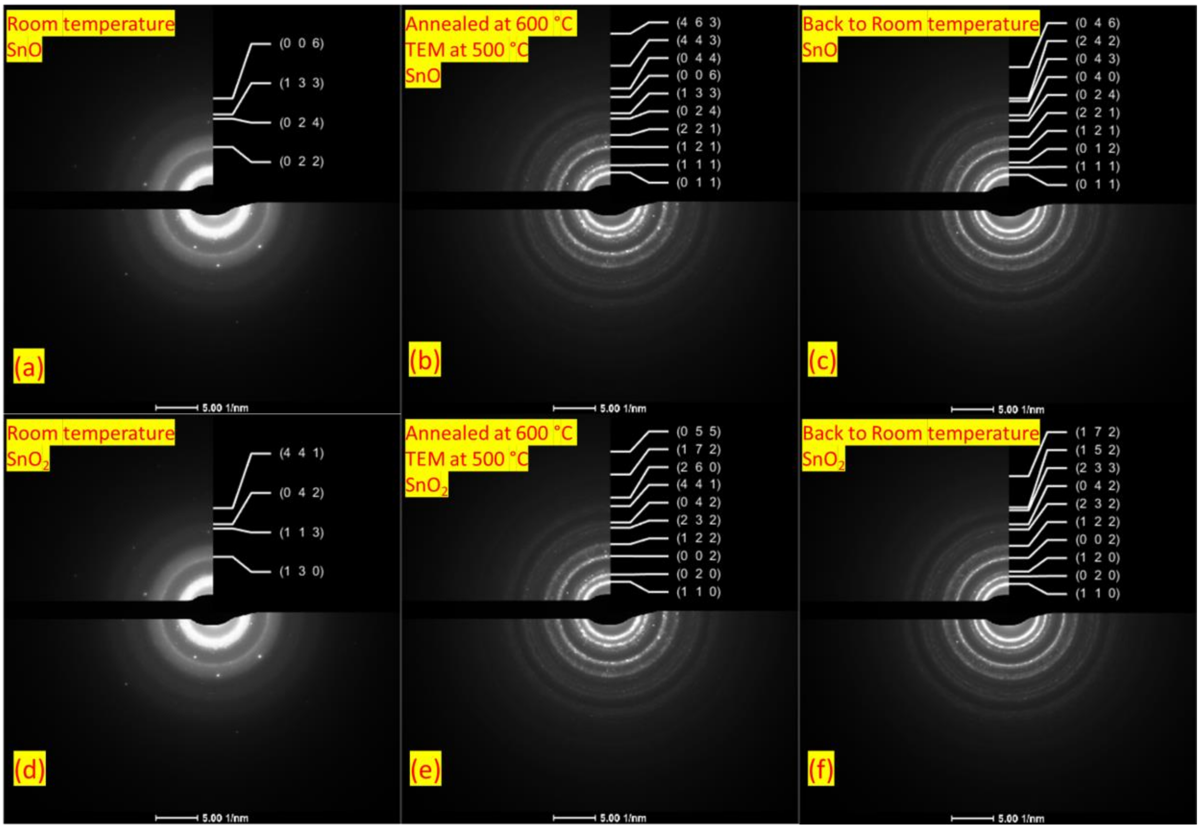

Figure 19: In-Situ Transmission Electron Microscopy diffraction analysis: for SnO indexation (a) as deposited SnO_x, (b) annealed SnO_x at 600 °C and returned to 500 °C, (c) annealed SnO_x at 600 °C and back to room temperature. for SnO_2 indexation (d) as deposited SnO_x, (e) annealed SnO_x at 600 °C and returned to 500 °C, (f) annealed SnO_x at 600 °C and back to room temperature.

	SnO Phase Indexation					SnO_2 Phase Indexation				
Room temperature	Ring identification					Ring identification				
	Plane	Radius [1/nm]		d-spacing [nm]		Plane	Radius [1/nm]		d-spacing [nm]	
		theor.	measured	theor.	measured		theor.	measured	theor.	measured
	(0 2 2)	6.691	6.499	0.149	0.154	(1 3 0)	6.675	6.499	0.15	0.154
	(0 2 4)	9.802	9.892	0.102	0.101	(1 1 3)	9.877	9.892	0.101	0.101
	(1 3 3)	10.376	10.418	0.096	0.096	(0 4 2)	10.521	10.418	0.095	0.096
	(0 0 6)	12.407	12.33	0.081	0.081	(4 4 1)	12.347	12.33	0.081	0.081
Annealed at 600 °C & TEM Diffraction at 500 °C	Ring identification					Ring identification				
	Plane	Radius [1/nm]		d-spacing [nm]		Plane	Radius [1/nm]		d-spacing [nm]	
		theor.	measured	theor.	measured		theor.	measured	theor.	measured
	(0 1 1)	3.346	3.345	0.299	0.299	(1 1 0)	2.985	3.345	0.335	0.299
	(1 1 1)	4.256	4.205	0.235	0.238	(0 2 0)	4.222	4.205	0.237	0.238
	(1 2 1)	6.234	6.404	0.16	0.156	(0 0 2)	6.277	6.404	0.159	0.156
	(2 2 1)	7.721	7.837	0.13	0.128	(1 2 2)	7.853	7.837	0.127	0.128

	(0 2 4)	9.802	9.797	0.102	0.102	(2 3 2)	9.865	9.797	0.101	0.102
	(1 3 3)	10.376	10.418	0.096	0.096	(0 4 2)	10.521	10.418	0.095	0.096
	(0 0 6)	12.407	12.377	0.081	0.081	(4 4 1)	12.347	12.377	0.081	0.081
	(0 4 4)	13.383	13.381	0.075	0.075	(2 6 0)	13.351	13.381	0.075	0.075
	(4 4 3)	16.12	16.105	0.062	0.062	(1 7 2)	16.192	16.153	0.062	0.062
	(4 6 3)	19.955	19.928	0.05	0.05	(0 5 5)	18.911	18.877	0.053	0.053
Back to Room temperature	Ring identification					Ring identification				
	Plane	Radius [1/nm]		d-spacing [nm]		Plane	Radius [1/nm]		d-spacing [nm]	
		theor.	measured	theor.	measured		theor.	measured	theor.	measured
	(0 1 1)	3.346	3.345	0.299	0.299	(1 1 0)	2.985	3.345	0.335	0.299
	(1 1 1)	4.256	4.253	0.235	0.235	(0 2 0)	4.222	4.253	0.237	0.235
	(0 1 2)	4.901	4.827	0.204	0.207	(1 2 0)	4.72	4.827	0.212	0.207
	(1 2 1)	6.234	6.452	0.16	0.155	(0 0 2)	6.277	6.452	0.159	0.155
	(2 2 1)	7.721	7.885	0.13	0.127	(1 2 2)	7.853	7.885	0.127	0.127
	(0 2 4)	9.802	9.845	0.102	0.102	(2 3 2)	9.865	9.845	0.101	0.102
	(0 4 0)	10.521	10.466	0.095	0.096	(0 4 2)	10.521	10.466	0.095	0.096
	(0 4 3)	12.214	12.138	0.082	0.082	(2 3 3)	12.107	12.138	0.083	0.082
	(2 4 2)	12.468	12.473	0.08	0.08	(1 5 2)	12.46	12.473	0.08	0.08
	(0 4 6)	16.267	16.2	0.061	0.062	(1 7 2)	16.192	16.2	0.062	0.062

Tables 18: In-Situ Transmission Electron Microscopy diffraction rings indexation for SnO and SnO_2.

The p-type conduction character reached at higher annealing temperature, revealed by Hall effect measurements, can be attributed to the formation of SnO phase which is known to form hole related charge carriers and enable the p-type conductivity. In the next experiment, the duration of the thermal annealing at 600 °C will be assessed.

2.5.2. Annealing time effect on SnO_x thin films

The aim of this experiment is to define if there is an effect of the annealing time on the electrical properties of SnO_x thin films. The thermal annealing durations were 20, 35, 50 (already established) and 120 minutes while all other parameters were kept fixed, namely Ar flow rate and annealing temperature at 600 °C as shown in Table 19.

Annealing	Flow rate (sccm)	Temperature (°C)	Time (min)
AT020	57 (Ar)	600	20
AT035	57 (Ar)	600	35
AT050	57 (Ar)	600	50
AT120	57 (Ar)	600	120

Table 19: Summary of the annealing conditions of SnO_x thin film samples.

The SnO_x samples deposited at O_2/Ar flow rate ratio of 0.015 and 0.035, and thermally annealed at 600 °C for 20 minutes have shown a relatively high resistivity similar to the as-deposited SnO_x ones with a very minor change. In contrast, the SnO_x deposited at O_2/Ar ratio of 0.065 and 0.075, and thermal annealed at 600°C for 20 minutes have shown an improvement in electrical conductivity with resistivity values around 2.2×10^2 Ω·cm for both samples. The SnO_x thin film deposited at O_2/Ar ratio of 0.035, has kept its high resistivity after the thermal annealing at 600 °C for 20 minutes and its conductivity type could not be determined as well as the mobility and the charge carrier concentration. The SnO_x thin films deposited at O_2/Ar ratio of 0.015, 0.065 and 0.075, and thermally annealed at 600 °C are found to have p-type conductivity, with hole carriers' mobility ranging from 2.2 to 6.3 cm^2/V·s and charge carrier concentration ranging from 5.1×10^{15} to 2.2×10^{16} cm^{-3}. Surprisingly, the sample deposited at 0.035 and annealed at 600 °C is found to have n-type conductivity, an electron mobility of 10 cm^2/V·s and a charge carrier concentration of 2.9×10^{15} cm^{-3}.

For SnO_x thin films thermally annealed at 600 °C for 35 minutes and deposited at O_2/Ar ratio of 0.015, 0.055 and 0.075 were found to be p-type conductive, with charge carrier concentration of 1.5×10^{16}, 8.2×10^{17} and 10^{16} cm^{-3}, respectively. Their resistivity values were found to range between 1.7×10^2 and 1.9×10^2 Ω·cm. The mobility is 3.3 and 3.4 cm^2/V·s for the SnO_x films deposited at O_2/Ar ratio of 0.015 and 0.075 while it is as low as 0,07 cm^2/V·s when the O_2/Ar ratio is 0.055. Surprisingly, the SnO_x thin films deposited at O_2/Ar ratio of 0.035 and 0.065 followed by the thermal annealing process, are found to have a n-type conductivity, their electrical resistivity is respectively 1.9×10^2 and 1.3×10^2 Ω·cm, their charge carrier concentration is respectively 2.1×10^{16} and 1.4×10^{17} cm^{-3}, and their mobility is respectively 1.7 and 0.35 cm^2/V·s.

For the thermal annealing at 600 °C for 120 minutes, all SnO_x samples have shown a n-type conductivity except the SnO_x grown at O_2/Ar ratio of 0.075 whose the conductivity type could not be determined. The measured electrical resistivity for SnO_x thin films deposited at O_2/Ar flow ratio of 0.015, 0.035, 0.055, and 0.065 followed by the thermal annealing is 78.7, 98.7, 26.5, and 29.2 Ω·cm, the charge carrier concentration is 2.3×10^{16}, 8.4×10^{15}, 2.4×10^{18} and 2×10^{18} cm^{-3}, and the mobility is 3.7, 7.6, 0.099 and 0.14 cm^2/V·s, respectively. Thus, the prolonged thermal annealing at 600 °C of two hours has led to a counter effect and kept the n-type conductivity while shorter duration annealing less than 50 minutes did not have a clear effect. All the results are shown in Table 20.

Charge carrier concentration (cm^{-3})

O_2/Ar	As deposited	Annealed at 600°C 20 minutes	Annealed at 600°C 35 minutes	Annealed at 600°C 50 minutes	Annealed at 600°C 120 minutes
0.015	-1.34E+15	2.17E+16	1.51E+16	2.30E+17	-2.27E+16
0.035	N/A**	-2.91E+15	-2.13E+16	3.00E+16	-8.41E+15
0.055	N/A*	N/A*	8.24E+17	4.50E+17	-2.41E+18
0.065	N/A*	5.13E+15	-1.37E+17	4.40E+16	-1.95E+18
0.075	N/A*	1.38E+16	1.01E+16	-2.50E+16	N/A**

Resistivity (Ω·cm)

O_2/Ar	As deposited	Annealed at 600°C 20 minutes	Annealed at 600°C 35 minutes	Annealed at 600°C 50 minutes	Annealed at 600°C 120 minutes
0.015	2.00E+02	2.43E+02	1.68E+02	1.90E+02	7.87E+01
0.035	2.39E+02**	2.42E+02	1.91E+02	1.60E+02	9.87E+01
0.055	N/A*	N/A*	1.66E+02	1.40E+02	2.65E+01
0.065	N/A*	2.18E+02	1.31E+02	1.10E+02	2.92E+01
0.075	N/A*	2.24E+02	1.86E+02	2.00E+02	3.32E+01

Mobility (cm^2/V·s)

O_2/Ar	As deposited	Annealed at 600°C 20 minutes	Annealed at 600°C 35 minutes	Annealed at 600°C 50 minutes	Annealed at 600°C 120 minutes
0.015	2.38E+01	3.07E+00	3.27E+00	2.00E-01	3.69E+00
0.035	4.48E+00**	1.03E+01	1.67E+00	1.40E+00	7.56E+00
0.055	N/A*	N/A*	6.90E-02	1.30E-01	9.94E-02
0.065	N/A*	6.27E+00	3.53E-01	1.30E+00	1.44E-01
0.075	N/A*	2.18E+00	3.40E+00	1.30E+00	6.84E-01

Table 20: Hall effect measurement for as deposited and thermally annealed SnO_x.

* Values with orange background represent n-type conductive samples and blue represent p-type conductive samples. Values with white background represent the samples where the conductivity type could not be determined. The samples with the mark. N/A*: high resistivity SnO_x. **: conductivity type could not be determined.

2.5.3. Post-annealing ageing and heating effect on SnO_x thin films

The stability of SnO_x in terms of electrical properties is very important to assess optoelectrical performance of the SnO_x samples. Therefore, a set of three samples was kept in air for seven days before performing a second Hall effect measurement as shown in Table 21.

All three samples have shown a better electrical conductivity after seven days of ageing while being exposed to air. The electrical resistivity is found to be 16.7, 22.5 and 26.7 Ω·cm for SnO_x samples deposited at O_2/Ar ratio of 0.055, 0.065 and 0.075, thermally annealed at 600 °C for 50 minutes and aged in air for seven days, respectively. All samples have shown an n-type conductivity including two SnO_x thin films which were p-type before the ageing. The corresponding electron mobility is 0.16, 0.17 and 0.17 $cm^2/V{\cdot}s$ and the charge carrier concentration is found to be 2.4×10^{18}, 1.7×10^{18} and 1.5×10^{18} cm^{-3} , respectively.

It is worth noting that the charge carrier concentration has increased significantly for all samples which is the main factor for improving the electrical conductivity. The mobility has decreased for the SnO_x thin films deposited at O_2/Ar ratio of 0.065 and 0.075, thermally annealed at 600 °C for 50 minutes and aged in air for seven days while it increased slightly for the other sample grown at 0.055 and thermally annealed at 600°C. The increase in the electrical conductivity can be related to the further oxidation which took place in the SnO_x in presence of O_2 in air. This oxidation is expected to change the crystalline structure towards mainly SnO_2. The intrinsic formation of oxygen vacancies has led to form electron charge carriers within the SnO_x which compensate the presence of hole charge carriers and eventually improve the electrical conductivity by the increasing of n-type carriers.

The air ambient also contains moisture which can affect the chemistry of the SnO_x thin films. Therefore, we carried out an experiment to evaluate if there is a reversable effect of exposure to moisture within the SnO_x tin films. Thus, the aged three samples were subject to a heating process at 150 °C for 50 minutes. Similar to previous studies, the resistivity, mobility and charge carrier concentration for SnO_x thin films deposited at O_2/Ar ratio of 0.055, 0.065 and 0.075, annealed at 600 °C for 50 minutes, aged for seven days in air and finally heated at 150 °C for 50 minutes in air as shown in Table 23. All three samples have kept their n-type conductivity character and show a better electrical conductivity after the heating. The electrical resistivities of the treated samples are found to be 1.1, 1.4 and 1.7 Ω·cm, and the corresponding charge carrier concentrations are measured to be 1.1 x 10^{19}, 5 x 10^{18} and 5.3 x 10^{18} cm^{-3}, for O_2/Ar flow rate of 0.055, 0.065 and 0.075, respectively.

The heating, in presence of air, which might have reduced the moisture adsorption in the SnO_x thin films, has likely increased the oxidation state of the SnO_x towards SnO_2 which led to a clear improvement in terms of mobility and charge carrier concentration. This improvement is reflected in the electrical resistivity which has decreased significantly.

Charge carrier concentration (cm^{-3})

O_2/Ar	As deposited	Annealed at 600°C 50 minutes	Annealed at 600°C for 50 min Aged for 7 days	Annealed at 600°C for 50 min Aged for 7 days heating at 150°C
0.055	N/A*	4.50E+17	-2.36E+18	-1.11E+19
0.065	N/A*	4.40E+16	-1.72E+18	-4.97E+18
0.075	N/A*	-2.50E+16	-1.46E+18	-5.29E+18

Resistivity (Ω·cm)

O_2/Ar	As deposited	Annealed at 600°C 50 minutes	Annealed at 600°C for 50 min Aged for 7 days	Annealed at 600°C for 50 min Aged for 7 days heating at 150°C
0.055	N/A*	1.40E+02	1.67E+01	1.12E+00
0.065	N/A*	1.10E+02	2.25E+01	1.36E+00
0.075	N/A*	2.00E+02	2.67E+01	1.68E+00

Mobility (cm^2/V·s)

O_2/Ar	As deposited	Annealed at 600°C - 50 minutes	Annealed at 600°C for 50 min Aged for 7 days	Annealed at 600°C for 50 min Aged for 7 days heating at 150°C
0.055	N/A*	1.30E-01	1.61E-01	5.95E-01
0.065	N/A*	1.30E+00	1.66E-01	9.23E-01
0.075	N/A*	1.30E+00	1.65E-01	7.12E-01

Table 21: Hall effect measurement for as deposited, thermally annealed, aged, and heated SnO_x samples.

* Values with orange background represent n-type conductive samples and blue represent p-type conductive samples. Values with white background represent the samples where the conductivity type could not be determined. The samples with the mark. N/A*: high resistivity SnO_x.

2.5.4. Summary

The study of thermal annealing under Ar atmosphere has shown that the higher temperature of 500 and 600°C has enabled p-type conductive samples while for treatment at 400°C no p-type conductive samples. This has confirmed the importance of both temperature and ambient during the annealing. It is also confirmed that the p-type character is correlated to the presence of SnO phase thanks to the transmission electron microscopy diffraction and to the optical measurements that revealed lower values of the optical bandgap. The annealing time experiments under Ar ambient has shown that p-type films are obtained for shorter time of annealing while extending the annealing duration to two hours conducted to the reverse effect where all samples become n-type.

On the other hand, the ageing effect under air ambient was assessed after seven days. We show that treatment have converted the SnO_x films from p-type to n-type conductivity and their resistivity has decreased. This could be explained by the further oxidation of SnO_x films from SnO towards SnO_2 and the increasing formation of the intrinsic n-type charge carriers which compensated the p-type charge carriers and increases the n-type carriers which reduced the resistivity. Finally, the effect of presence of moisture on tin oxide after seven days of the ageing has been assessed using heating process at 150°C in the presence of air. This process did not recover the p-type conductivity and instead it has led to further oxidation of SnO_x film and further decrease in resistivity by forming more n-type charge carriers.

2.6. General summary

This chapter show that it is possible to tune the structural, optical, and electrical properties of sputtered SnO_x films by optimising the growth conditions. This work has led to the synthesis of high conductive SnO_2 thin films with high optical transmittance which has enabled achieving a high optoelectronic performance as revealed by FoM. Thermal annealing for SnO_x thin films under Ar at a relatively high temperature around 600°C has shown a potential ability to convert n-type conductivity to p-type. Material properties of SnO_x before and after the annealing have shown that this conductivity is related to the formation of tin monoxide (SnO) phase.

In the next chapter, the performance assessment of perovskite solar cells using SnO_2 as Electron Transport Layer will be explored.

Reference

1. Lewis, B.G. and D.C. Paine, *Applications and Processing of Transparent Conducting Oxides.* MRS Bulletin, 2000. **25**(8): p. 22-27.

2. Ellmer, K., R. Mientus, and S. Seeger, *Metallic Oxides (ITO, ZnO, SnO2 , TiO2)*, in *Transparent Conductive Materials*. 2018. p. 31-80.

3. Nathan, A., et al., *Transparent Oxide Semiconductors for Advanced Display Applications.* Information Display, 2013. **29**(1): p. 6-11.

4. Jang, J., et al., *Thin-Film Optical Devices Based on Transparent Conducting Oxides: Physical Mechanisms and Applications.* Crystals, 2019. **9**(4): p. 192.

5. Park, J.S., et al., *Review of recent developments in amorphous oxide semiconductor thin-film transistor devices.* Thin Solid Films, 2012. **520**(6): p. 1679-1693.

6. Hosono, H., *68.3: Invited Paper: Transparent Amorphous Oxide Semiconductors for High Performance TFT.* SID Symposium Digest of Technical Papers, 2007. **38**(1): p. 1830-1833.

7. Kamiya, T. and H. Hosono, *Material characteristics and applications of transparent amorphous oxide semiconductors.* NPG Asia Materials, 2010. **2**(1): p. 15-22.

8. Nomura, K., et al., *Room-temperature fabrication of transparent flexible thin-film transistors using amorphous oxide semiconductors.* Nature, 2004. **432**(7016): p. 488-492.

9. Nathan, A., et al., *Amorphous Oxide Semiconductor TFTs for Displays and Imaging.* Journal of Display Technology, 2014. **10**(11): p. 917-927.

10. Fujiwara, H. and S. Fujimoto, *Transparent Conductive Oxide Materials*, in *Spectroscopic Ellipsometry for Photovoltaics: Volume 1: Fundamental Principles and Solar Cell Characterization*, H. Fujiwara and R.W. Collins, Editors. 2018, Springer International Publishing: Cham. p. 523-563.

11. Andrés, A.d., F. Jiménez-Villacorta, and C. Prieto, *The Compromise Between Conductivity and Transparency*, in *Transparent Conductive Materials*. 2018. p. 1-30.

12. Dalapati, G.K., et al., *Tin oxide for optoelectronic, photovoltaic and energy storage devices: a review.* Journal of Materials Chemistry A, 2021. **9**(31): p. 16621-16684.

13. Scanlon, D.O. and G.W. Watson, *On the possibility of p-type SnO2.* Journal of Materials Chemistry, 2012. **22**(48): p. 25236-25245.

14. Jiang, Q., X. Zhang, and J. You, *SnO2: A Wonderful Electron Transport Layer for Perovskite Solar Cells.* Small, 2018. **14**(31): p. 1801154.

15. Fukai, Y., et al., *Highly efficient dye-sensitized SnO2 solar cells having sufficient electron diffusion length.* Electrochemistry Communications, 2007. **9**(7): p. 1439-1443.

16. Calderer, J., et al., *Synthesis and characterisation of metal suboxides for gas sensors.* Microelectronics Reliability, 2000. **40**(4): p. 807-810.

17. Coles, G.S.V., G. Williams, and B. Smith, *The effect of oxygen partial pressure on the response of tin (IV) oxide based gas sensors.* Journal of Physics D: Applied Physics, 1991. **24**(4): p. 633-641.

18. Liang, L.Y., et al., *Phase and Optical Characterizations of Annealed SnO Thin Films and Their p-Type TFT Application.* Journal of The Electrochemical Society, 2010. **157**(6): p. H598.

19. Ogo, Y., et al., *p-channel thin-film transistor using p-type oxide semiconductor, SnO.* Applied Physics Letters, 2008. **93**(3): p. 032113.

20. Isono, T., et al., *Highly conductive SnO2 thin films for flat-panel displays.* Journal of the Society for Information Display, 2007. **15**(2): p. 161-166.

21. Odani, A., et al., *Development and testing of nanomaterials for rechargeable lithium batteries.* Journal of Power Sources, 2003. **119-121**: p. 517-521.

22. Han, Z., et al., *Solvothermal preparation and morphological evolution of stannous oxide powders.* Materials Letters, 2001. **48**(2): p. 99-103.

23. Liu, A., M. Zhu, and B. Dai, *A novel high-performance SnO2 catalyst for oxidative desulfurization under mild conditions.* Applied Catalysis A: General, 2019. **583**: p. 117134.

24. Pan, X.Q. and L. Fu, *Oxidation and phase transitions of epitaxial tin oxide thin films on (1012) sapphire.* Journal of Applied Physics, 2001. **89**(11): p. 6048-6055.

25. Fan, H. and S.A. Reid, *Phase Transformations in Pulsed Laser Deposited Nanocrystalline Tin Oxide Thin Films.* Chemistry of Materials, 2003. **15**(2): p. 564-567.

26. Kim, K.-K., et al., *Realization of p-type ZnO thin films via phosphorus doping and thermal activation of the dopant.* Applied Physics Letters, 2003. **83**(1): p. 63-65.

27. Zhang, T., et al., *Atomic layer deposited ZnxNi1−xO: A thermally stable hole selective contact for silicon solar cells.* Applied Physics Letters, 2018. **113**(26): p. 262102.

28. Bosman, A.J. and C. Crevecoeur, *Mechanism of the Electrical Conduction in Li-Doped NiO.* Physical Review, 1966. **144**(2): p. 763-770.

29. Hossain, M.A., et al., *Doped Nickel Oxide Carrier-Selective Contact for Silicon Solar Cells.* IEEE Journal of Photovoltaics, 2021. **11**(5): p. 1176-1187.

30. Pollack, G.P. and D. Trivich, *Photoelectric properties of cuprous oxide.* Journal of Applied Physics, 1975. **46**(1): p. 163-172.

31. Kim, C., S. Kim, and S.E. Kim, *Transparent SnOx thin films fabricated by radio frequency reactive sputtering with a SnO/Sn composite target.* Thin Solid Films, 2017. **634**: p. 175-180.

32. Sundqvist, J., et al., *Growth of SnO2 thin films by atomic layer deposition and chemical vapour deposition: A comparative study.* Thin Solid Films, 2006. **514**(1): p. 63-68.

33. Jiang, J.C., K. Lian, and E.I. Meletis, *Influence of oxygen plasma treatment on the microstructure of SnOx thin films.* Thin Solid Films, 2002. **411**(2): p. 203-210.

34. Guo, W., et al., *Microstructure, optical, and electrical properties of p-type SnO thin films.* Applied Physics Letters, 2010. **96**(4): p. 042113.

35. Jarzebski, Z.M. and J.P. Morton, *Physical Properties of SnO2 Materials: III . Optical Properties.* Journal of The Electrochemical Society, 1976. **123**(10): p. 333C-346C.

36. Tao, Y., et al., *The structural, electrical, and optical properties of SnO2 films prepared by reactive magnetron sputtering: Influence of substrate temperature and O2 flow rate.* Materials Chemistry and Physics, 2020. **250**: p. 123129.

37. Khan, A.F., et al., *Effect of annealing on electrical resistivity of rf-magnetron sputtered nanostructured SnO2 thin films.* Applied Surface Science, 2009. **255**(20): p. 8562-8565.

38. Sethi, R., et al., *Structural, optical and electrical properties of tin oxide thin films for application as a wide band gap semiconductor.* AIP Conference Proceedings, 2015. **1675**(1): p. 030039.

39. Zhu, B., et al., *Characteristics of Al-doped ZnO thin films prepared in Ar + H2 atmosphere and their vacuum annealing behavior.* Journal of Vacuum Science & Technology A, 2013. **31**(6): p. 061513.

40. Zhu, B.L., et al., *Investigation of Structural, Electrical, and Optical Properties for Al-Doped ZnO Films Deposited at Different Substrate Temperatures and H2Ratios.* Journal of The Electrochemical Society, 2012. **159**(5): p. H536-H544.

41. Kim, I.H., et al., *Scattering mechanism of transparent conducting tin oxide films prepared by magnetron sputtering.* Thin Solid Films, 2006. **515**(4): p. 2475-2480.

42. Yamada, T., et al., *Ingrain and grain boundary scattering effects on electron mobility of transparent conducting polycrystalline Ga-doped ZnO films.* Journal of Applied Physics, 2010. **107**(12): p. 123534.

43. Steinhauser, J., et al., *Transition between grain boundary and intragrain scattering transport mechanisms in boron-doped zinc oxide thin films.* Applied Physics Letters, 2007. **90**(14): p. 142107.

44. Fujiwara, H. and M. Kondo, *Effects of carrier concentration on the dielectric function of ZnO:Ga and In2O3:Sn studied by spectroscopic ellipsometry: Analysis of free-carrier and band-edge absorption.* Physical Review B, 2005. **71**(7): p. 075109.

45. Yamamoto, T., et al., *Dependence of carrier concentrations on oxygen pressure for Ga-doped ZnO prepared by ion plating method.* Thin Solid Films, 2004. **451-452**: p. 439-442.

46. Brehme, S., et al., *Free-carrier plasma resonance effects and electron transport in reactively sputtered degenerate ZnO:Al films.* Thin Solid Films, 1999. **342**(1): p. 167-173.

47. Hamberg, I. and C.G. Granqvist, *Evaporated Sn-doped In2O3 films: Basic optical properties and applications to energy-efficient windows.* Journal of Applied Physics, 1986. **60**(11): p. R123-R160.

48. Volintiru, I., M. Creatore, and M.C.M. van de Sanden, *In situ spectroscopic ellipsometry growth studies on the Al-doped ZnO films deposited by remote plasma-enhanced metalorganic chemical vapor deposition.* Journal of Applied Physics, 2008. **103**(3): p. 033704.

49. Ellmer, K., *Resistivity of polycrystalline zinc oxide films: current status and physical limit.* Journal of Physics D: Applied Physics, 2001. **34**(21): p. 3097-3108.

50. Minami, T., et al., *Conduction mechanism of highly conductive and transparent zinc oxide thin films prepared by magnetron sputtering.* Journal of Crystal Growth, 1992. **117**(1): p. 370-374.

51. Manifacier, J.C., et al., *Optical and electrical properties of SnO2 thin films in relation to their stoichiometric deviation and their crystalline structure.* Thin Solid Films, 1977. **41**(2): p. 127-135.

52. Haacke, G., *New figure of merit for transparent conductors.* Journal of Applied Physics, 1976. **47**(9): p. 4086-4089.

53. Fauzia, V., et al., *High figure of merit transparent conducting Sb-doped SnO2 thin films prepared via ultrasonic spray pyrolysis.* Journal of Alloys and Compounds, 2017. **720**: p. 79-85.

54. Islam, M.A., et al., *Highly transparent conducting and enhanced near-band edge emission of SnO2:Ba thin films and its structural, linear and nonlinear optical properties.* Optical Materials, 2020. **106**: p. 109996.

55. Hossain, M.F., et al., *Transparent conducting SnO2 thin films synthesized by nebulized spray pyrolysis technique: Impact of Sb doping on the different physical properties.* Materials Science in Semiconductor Processing, 2021. **121**: p. 105346.

56. Ramarajan, R., et al., *Substrate Temperature Dependent Physical Properties of Spray Deposited Antimony-Doped SnO2 Thin Films.* Thin Solid Films, 2020. **704**: p. 137988.

57. Ramarajan, R., et al., *Large-area spray deposited Ta-doped SnO2 thin film electrode for DSSC application.* Solar Energy, 2020. **211**: p. 547-559.

58. Sivakumar, P., et al., *Influence of Ga doping on structural, optical and electrical properties of transparent conducting SnO2 thin films.* Optik, 2021. **226**: p. 165859.

59. Sivakumar, P., et al., *Effect of Ti doping on structural, optical and electrical properties of SnO2 transparent conducting thin films deposited by sol-gel spin coating.* Optical Materials, 2021. **113**: p. 110845.

60. Tarighi, A. and A. Mashreghi, *Dependence of Photovoltaic Properties of Spray-Pyrolyzed F-Doped SnO2 Thin Film on Spray Solution Preparation Method.* Journal of Electronic Materials, 2019. **48**(12): p. 7827-7835.

61. Tran, Q.-P., J.-S. Fang, and T.-S. Chin, *Properties of fluorine-doped SnO2 thin films by a green sol–gel method.* Materials Science in Semiconductor Processing, 2015. **40**: p. 664-669.

62. Li, B.-j., et al., *Influences of ultrasonic vibration on morphology and photoelectric properties of F-doped SnO2 thin films during laser annealing.* Applied Surface Science, 2018. **458**: p. 940-948.

63. Chan y Díaz, E., et al., *Influence of the oxygen pressure on the physical properties of the pulsed-laser deposited Te doped SnO2 thin films.* Journal of Alloys and Compounds, 2010. **508**(2): p. 342-347.

64. Mrabet, C., et al., *Improvement of the optoelectronic properties of tin oxide transparent conductive thin films through lanthanum doping.* Journal of Alloys and Compounds, 2016. **666**: p. 392-405.

65. Joseph, D.P., et al., *Effect of Li doping on the structural, optical and electrical properties of spray deposited SnO2 thin films.* Thin Solid Films, 2009. **517**(21): p. 6129-6136.

66. Talaty, N.N., et al., *Characterization of Tin(IV) Oxide Thin Films Prepared by Atmospheric Pressure Chemical Vapor Deposition of cis-[SnCl4{OC(H)OC2H5}2].* Zeitschrift für anorganische und allgemeine Chemie, 2009. **635**(1): p. 53-63.

67. Moholkar, A.V., et al., *Effect of concentration of SnCl4 on sprayed fluorine doped tin oxide thin films.* Journal of Alloys and Compounds, 2008. **455**(1): p. 440-446.

68. Ramarajan, R., et al., *Boltzmann conductivity approach for charge transport in spray-deposited transparent Ta-doped SnO2 thin films.* Journal of Alloys and Compounds, 2022. **897**: p. 163159.

69. Moholkar, A.V., et al., *Properties of highly oriented spray-deposited fluorine-doped tin oxide thin films on glass substrates of different thickness.* Journal of Physics and Chemistry of Solids, 2007. **68**(10): p. 1981-1988.

70. El Radaf, I.M. and R.M. Abdelhameed, *Surprising performance of graphene oxide/tin dioxide composite thin films.* Journal of Alloys and Compounds, 2018. **765**: p. 1174-1183.

71. Adjimi, A., et al., *Gadolinium doping effect on SnO2 thin films optical and electrical properties.* Materials Research Express, 2019. **6**(9): p. 096405.

72. Belayachi, W., et al., *SnO2 Films Elaborated by Radio Frequency Magnetron Sputtering as Potential Transparent Conducting Oxides Alternative for Organic Solar Cells.* ACS Applied Energy Materials, 2022. **5**(1): p. 170-177.

73. Babar, A.R., et al., *Physical properties of sprayed antimony doped tin oxide thin films: The role of thickness.* Journal of Semiconductors, 2011. **32**(5): p. 053001.

74. Vishwakarma, S.R., J.P. Upadhyay, and H.C. Prasad, *Physical properties of arsenic-doped tin oxide thin films.* Thin Solid Films, 1989. **176**(1): p. 99-110.

75. Singh, S.K. and S. Basu, *Characterisation of conducting SnO2layers deposited by modified spray pyrolysis technique.* Materials Chemistry and Physics, 1988. **20**(4): p. 381-396.

76. Snyders, R., et al., *Correlation between the gas composition and the stoichiometry of SnOx films prepared by DC magnetron reactive sputtering.* Surface and Coatings Technology, 2001. **142-144**: p. 187-191.

77. Deline, V.R., et al., *Mechanism of the SIMS matrix effect.* Applied Physics Letters, 1978. **33**(9): p. 832-835.

78. De, A. and S. Ray, *A study of the structural and electronic properties of magnetron sputtered tin oxide films.* Journal of Physics D: Applied Physics, 1991. **24**(5): p. 719.

79. Jarzebski, Z.M. and J.P. Marton, *Physical Properties of SnO2 Materials: I . Preparation and Defect Structure.* Journal of The Electrochemical Society, 1976. **123**(7): p. 199C.

80. Barros, R., et al., *Role of Structure and Composition on the Performances of P-Type Tin Oxide Thin-Film Transistors Processed at Low-Temperatures.* Nanomaterials, 2019. **9**(3): p. 320.

81. Liu, X., et al., *Preparation and characterization of p-type semiconducting tin oxide thin film gas sensors.* Journal of Applied Physics, 2010. **107**(6): p. 064309.

82. Dang, H.P., et al., *Eliminating the charge compensation effect in Ga-doped SnO2 films by N doping.* Journal of Alloys and Compounds, 2019. **776**: p. 276-286.

83. Hur, K.-H., J.-H. Jeong, and D.N. Lee, *Microstructures and crystallization of electroless Ni-P deposits.* Journal of Materials Science, 1990. **25**(5): p. 2573-2584.

84. Klinger, M. and A. Jager, *Crystallographic Tool Box (CrysTBox): automated tools for transmission electron microscopists and crystallographers.* Journal of Applied Crystallography, 2015. **48**(6): p. 2012-2018.

85. Nicoletti, S., et al., *Tin Oxide Thin-Film Sensors for Aromatic Hydrocarbons Detection: Effect of Aging Time on Film Microstructure.* Journal of the American Ceramic Society, 1999. **82**(5): p. 1201-1206.

86. Patil, R.B., R.K. Puri, and V. Puri, *Physical properties of tin oxide thin films improved by vapour chopping.* Journal of Alloys and Compounds, 2008. **463**(1): p. 453-457.

87. Roman, L.S., et al., *Time-dependent structural modifications in tin oxide thin films under environmental conditions.* Journal of Materials Science: Materials in Electronics, 1996. **7**(6): p. 423-426.

88. Zhong, C.-W., et al., *Impact of gate dielectrics and oxygen annealing on tin-oxide thin-film transistors.* Japanese Journal of Applied Physics, 2016. **55**(4S): p. 04EG02.

Chapter 3: Study of Tin Oxide (SnO_2) Material as Electron Transport Layer (ETL) for Perovskite Solar Cells

3. Study of Tin Oxide (SnO_2) Material as Electron Transport Layer (ETL) for Perovskite Solar Cells

3.1. Introduction

The performance and cost-effectiveness fabrication of the perovskite solar cells (PSCs) are the two main assets which are increasingly attracting academic and industrial attention. Certified Power Conversion Efficiency (PCE) for the best solar cell efficiency has shown a 25.7% for PSCs as achieved by UNIST in 2021[1]. Focus is put nowadays on the PSCs commercialization [2], and this aim is still facing two main challenges, namely a descent device operational-stability and the fabrication scalability. The stability of the PSCs has been the cornerstone of extensive research and development over the last years. Nevertheless, this research effort has been found to be one of the most complex physico-chemical issues that involves multiple factors and various physical phenomena. These issues are also a subject of the device configuration and materials' characteristics. In fact, the device stability can directly be affected by the electrode material and its characteristics (work function, dimensions, etc.) [3], electron transport layer (ETL) and hole transport layer (HTL) properties [4, 5], the nature of the interface between the absorber-perovskite layer and the charge transport materials [6], and indeed, the stability of the perovskite material itself [7]. In 2016, Ahn et al. [8] proposed that the ETL based on TiO_2 is among the most responsible factors for the light-induced degradation in PSCs. This suggestion was also supported by the research outcome of Qiu and coworkers in 2018 [9]. On the other hand, SnO_2 as ETL has demonstrated its capability to replace the conventional TiO_2 due to the fact that a power conversion efficiency (PCE) of more than 21% has been already achieved using SnO_2 ETL [10]. SnO_2 shows several benefits over TiO_2, including a higher electron mobility and an excellent energy level matching [11]. More importantly, SnO_2 as ETL is highly efficient against the perovskite solar cells degradation, which is induced by TiO_2 ETL, thereby considerably improving the device operational lifetime under continuous light illumination at the maximum power point. In this context, Christians et al. [12] have recently demonstrated a much longer lifetime with un-encapsulated perovskite solar cells based on SnO_2 as ETL compared to TiO_2. On the other hand, the second big challenge deals with the scalability of the PSC fabrication, to reach the module scale (i.e. perovskite solar modules (PSMs)), while maintaining performance similar to PSCs of small areas [2]. As large-scale thin film growth processes for the PSCs fabrication have been introduced, the number of reports related to PSMs has drastically increased [13]. For instance, M. Green et al. have reported a PCE of 16 % with an aperture area (AA) of 16.29 cm^2 [14] and H. Chen et al. have achieved a certified PCE of 12.1% with a larger AA of 36.1 cm^2 [15]. Other key parameters are related to the cost-effectiveness and large-scale deposition processes of ETL [2]. Currently, the majority of PSMs are based on TiO_2 as ETL, which requires high processing temperature. TiO_2 is also the origin of many instability issues [16] due to its relatively higher resistance and a costly laser patterning method which is often used to remove TiO_2 coating from the interconnection paths between sub-cells [17]. This is required to avoid the rise in the series resistance value, thereby decreasing the overall PSM performance [18].

Unlike TiO_2 material, SnO_2 can be processed at much lower temperatures using different deposition technologies, including solution processes [11, 19, 20], electrodeposition, [21], electron-beam [22], atomic layer deposition [23] and magnetron sputtering [24]. It is worth noting that the majority of reports so far related to SnO_2 as ETL are only for small area devices [16]. Among all these thin film fabrication methods, magnetron sputtering (MS) is one of the most promising technologies due to its advantages related to cost-effectiveness and uniform large-scale SnO_2 thin films. Thus far, there are only a few reports about SnO_2 thin films, deposited by MS, as ETL for PSCs. For instance, F. Ali et al. have reported a PCE of 14% for an area of 0.09 cm^2 [25]. Furthermore, the film uniformity across large area MS is demonstrated as well as the superior electrical conductivity and electron mobility of SnO_2 versus that of TiO_2 which are also demonstrated as an advantage to improve the interconnection quality between different sub-cells in PSMs. On the other hand, the state-of-the-art related to PCE of PSC based on SnO_2 ETL is achieved by a very thin layer (~25 nm) of SnO_2 deposited by spin coating technique [26]. However, this deposition method associated with the very thin layer can lead to fringe effects, pinholes, and thickness non-uniformity related to large area thin films, especially for upscaling small devices into large PV modules.

Figure 1 displays the conduction band minimum (CBM) and valence band maximum (VBM) of commonly implemented inorganic metal materials as electron transport materials (ETLs) in perovskite solar cells (PSCs) where metal oxides, metal sulfide, CdSe and GaN were included. To deliver an efficient and reliable PSC, it is a essential to meet the following key characteristics: (i) good optical transmittance; (ii) a low photon-energy loss; (iii) an appropriate bandgap-matching/alignment; (iv) high electrical conductivity and electron mobility; (d) cost-effectiveness; and an acceptable rate of reproducibility (i.e. stability), [27, 28].

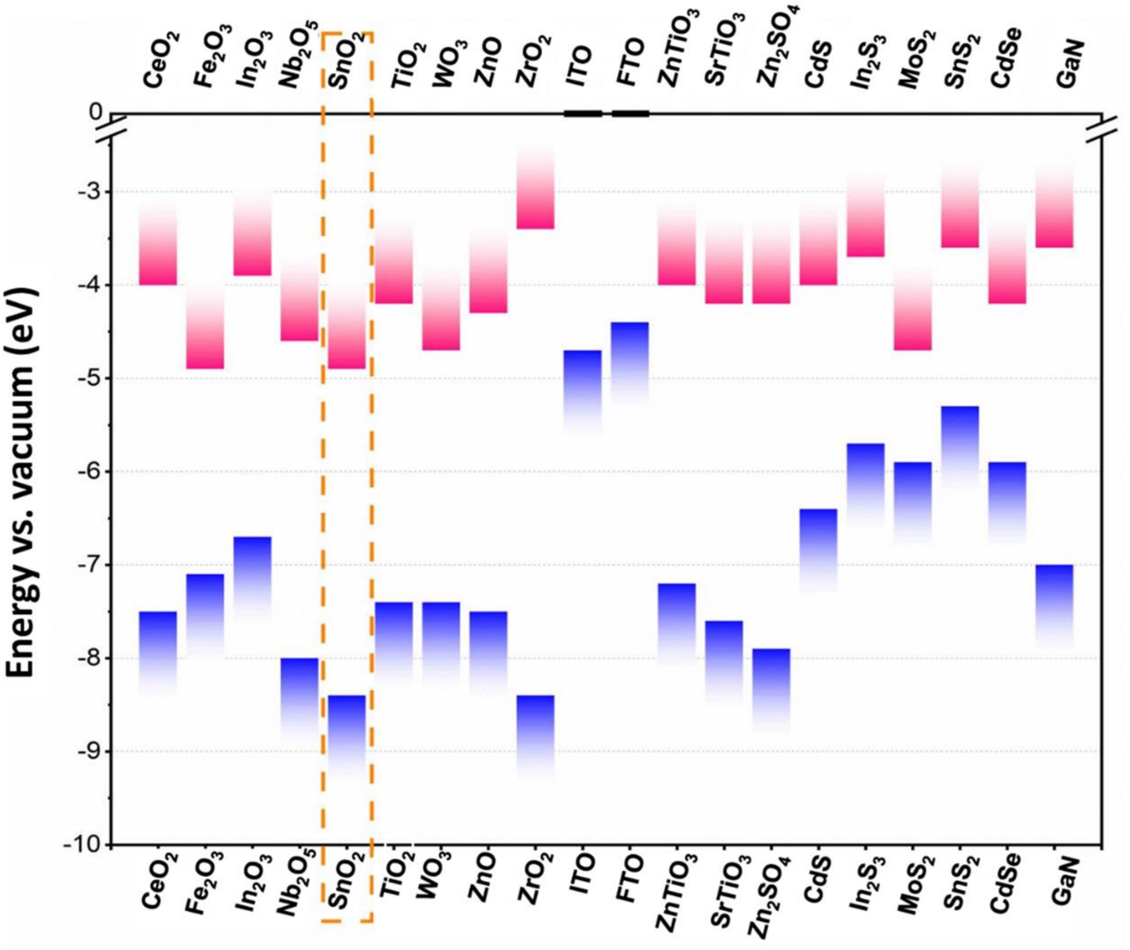

Figure 1: Schematic drawing showing the Conduction band (CB) and valence band (VB) of commonly employed inorganic materials as ETLs in PSCs. [29-39].

As a replacement to TiO_2, various materials, which offer particular optoelectronic properties, have already been studied. This has included binary metal oxides (ZnO, In_2O_3, Nb_2O_5, WO_3, Fe_2O_3 and CeO_2) [32], ternary metal oxides (Zn_2SnO_4, $BaSnO_3$ and $SrTiO_4$), [30] metal sulfides (MoS_2, CdS, In_2S_3, SnS_2 and Bi_2S_3), [29] as well as GaN, CdSe, and $InGaZnO_4$ [31]. Nevertheless, many pending issues are still to be addressed, including the low interfacial contact quality.

In 2015, the innovating work of Dai's group demonstrated -for the first time- a PSC based SnO_2 ETL with a PCE of 6.5 %. This was followed, in the same year, by the work of Wan et al. who reached a PCE of more than 15 % [20, 40]. The power conversion efficiency of PSC based on SnO_2 as electron transport material has recently achieved values above 20% [10]. This has demonstrated the SnO_2 as an attractive and promising ETL material from various point of views, especially for perovskite solar cell, and as an excellent substitute to the conventional TiO_2, owing to the following factors: (i) an optimized energy-level matching [41]; (ii) a significantly higher electron mobility than TiO_2; (iii) a high electrical conductivity [42, 43]; (iv) a large bandgap (3.6–4.5 eV); (v) a high transparency (i.e. optical transmittance) [44, 45]; (vi) a large flexibility in terms of processing temperature from relatively low temperature down to room temperature; (vii) a high stability under light (i.e. low photoactivity), and (viii) a high stability under heat and humidity [46, 47].

In addition, spin coating or spray methods are usually used for synthesis of TiO_2 ETL in PSC. This requires an elevated post-treatment temperature, generally above 450 °C, to enable the formation of the mesoporous layer with a dense structure, a crystalline structure, and a good electrical conductivity. Conversely, SnO_2 is routinely grown at much lower temperatures (≤ 250 °C) and in some cases it is grown at room temperature when the crystalline structure is not required. This advantage is very appealing for large-scale industrial applications.

3.2. SnO_2 thin film as ETL

To prepare metal-oxide thin films with a high quality, either in the lab- and/or at an industrial-scale, magnetron sputtering is demonstrated to be a reliable and mature deposition process, also offering the possibility to use low-cost materials' targets. The SnO material is sputtered through high-energy argon-plasma ions, it reacts with oxygen and then it is deposited on the top of FTO layer under a continuous process. An accurate control of the film thickness and density can be achieved with MS via the deposition rate. It's a relatively cost-effective process, with a very low rate of waste. The thin film growth process is usually operated in a high vacuum chamber, which enables a high level of reproducibility [49].

Qiu et al. studied in a systematic way the physical and chemical properties of the sputtered SnO_2 [26]. The fabricated perovskite solar cells implementing SnO_2 as ETL were found to exhibit a PCE of about 20% and a stability of about 625 hours as measured under T80 standard, thereby demonstrating the enhanced electrical conductivity and stability thanks to SnO_2 [26]. On the other hand, Bai and co-workers highlighted the impact of the Ar/O_2 gas ratio on the structural and morphological characteristics of the sputtered SnO_2 films [50]. The level of the trap states and dynamics of the carrier transit were also investigated in their PSC devices, which demonstrated a champion PCE up to 18% [50]. Moreover, Otoufi and co-workers experimented the bilayer architecture made with sputtered SnO_2 on TiO_2 layer, which was found to improve charge collection capacity, which has led to a PCE of about 12%, which is 4 % higher than that obtained with only TiO_2 as ETL (~ 8%) [51]. It is worth noting at this level that the flowing gas during the deposition process plays a key role in controlling the oxygen vacancies [52]. In addition, defects states within the SnO_2 bandgap, which may originate from the amorphous and/or nano-crystallinity present in the films, might be effectively suppressed by a post-thermal annealing process under air, thereby leading to the passivation of the interface with the perovskite material.

In this work, we have achieved the implementation of moderate temperature radio frequency magnetron sputtered SnO_2 as electron transport layer for spin-coated triple-cation based perovskite solar cells. We demonstrated that both procedures of mesoporous-scaffold and high-temperature processing are not essential in order to achieve high PSC device performance. Furthermore, no passivation process has been performed and no encapsulation has been used. Nevertheless, a PSC of more than 17% PCE has been demonstrated.

We have explored the material's properties of SnO_2, namely structural, morphological, electrical and optical properties, as well as its chemical states. We have also studied the temperature dependency of the perovskite layer performance through PL measurement under various temperature, which has suggested an interplay of different physical phenomena, including charge transfer dynamics and charge recombination. Our developed MS SnO_2 ETL is demonstrated to achieve a good device photovoltaic performance and a relatively good lifetime, which also could help for further development and integration of SnO_2 films into PSMs.

3.3. Experiments and Characterization

Electron Transport Layer (ETL): The glass coated FTO substrates with 7Ω/□ sheet resistance were first cleaned with 1 wt.% Na dodecylsulfate aqueous, deionized water, acetone, and isopropyl alcohol prior to their utilization. SnO_2 thin films were grown on these Glass/FTO, using magnetron sputtering, manufactured by Torr Int. (described in the appendix in section 1.3.), at 200 °C with a high purity SnO target (purity 99.99%, 2" diameter, Codex International^{TM}), under O_2:Ar mixture at 4:200 sccm, and a power of 50 W for 10 min, where the aim for these conditions is to improve the electron mobility without compromising the charge carrier concentration. A base pressure of 6.66×10^{-3} Pa was first reached and then a deposition pressure which depends on the variable oxygen flow rate, was set around 0.66 Pa. As a sufficient oxygen flow was provided to assure the highest chemical state of Sn oxide in the grown film which are Sn(IV) oxide, the argon is necessary to form and maintain the magnetron plasma. The film thickness was about 40 nm. A deposition rate of about 4 nm min^{-1} was deliberately chosen for a better film' coverage. Films were then treated with UV-ozone for 15 min and then one SnO_2 sample was post annealed at 250 °C in air, for 30 min. Samples were then placed into a nitrogen-filled glovebox for the perovskite layer deposition. In order to study the material's properties, some ETL - SnO_2 thin films were deposited directly on glass substrates (as-deposited SnO_2) and some were air-annealed at 250 °C for 30 minutes.

Perovskite Absorber Layer: "The (FA, MA, and Cs: FMC) triple-cation mixed-halide perovskite was prepared inside glovebox conditions to maintain oxygen and H_2O levels under 1 ppm. The one-step and 'antisolvent' processes were employed to obtain FAPbI3 and FMC based films. $Cs_{0.05}MA_{0.10}FA_{0.85}Pb(I_{0.85}Br_{0.15})_3$ was prepared by dissolving the precursors in a 1:4 DMSO: DMF mixed solvent. A 1.4 M precursor solution was obtained by mixing CsI (0.07 M), FAI (1.13 M), PbI_2 (1.19 M), MABr (0.2 M), and $PbBr_2$ (0.2 M) in the DMSO: DMF solvent with a 5% excess of PbI2. The perovskite films were deposited onto the 40-nm SnO_2 layer by spin-coating. This process started at 1000 rpm, for 10 s with a first-step acceleration rate of 200 rpm/s, followed by a second step acceleration at 1500 rpm/s until reaching a final speed of 4000 rpm, and then maintained for 35 s. During the last 20 s of spinning, 120 µL of chlorobenzene was dropped onto the substrate. The obtained film was finally annealed at 100 °C for 60 min", this process is reported previously by A. Manekkathodi, B. Aïssa et al. [48].

Hole-Transport Layer (HTL): "The doped Spiro-OMeTAD was prepared by dissolving 65 mg of Spiro-OMeTAD in 1 mL of chlorobenzene. Then, 17.5 µL/mL of 26 mM solution of Li-dopant (bis(trifluoromethane)-sulfonimide lithium salt solution in acetonitrile) in acetonitrile, 21.9 µL/mL of 26 mM solution of cobalt-dopant (FK209) solution in acetonitrile, and 20 µL/mL of tert-butylpyridine were added as an additive. This solution was spin-coated at 4000 rpm for 20 s on the perovskite films immediately after their growth. After the Spiro-OMeTAD deposition, samples were taken out from the glovebox for oxidation purposes", this process is also reported previously by A. Manekkathodi, B. Aïssa et al. [48].

Back-Contact Electrode: Back-contact electrode of 100 nm Au film was thermally evaporated under vacuum to complete the device. Film thicknesses were measured by a stylus profiler (Bruker Dektak).

Optical Properties: UV and visible light Transmittance and Absorbance spectra were determined by UV-Visible spectrometry (Jasco V670).

Grazing Incidence X-ray Diffraction (GIXRD) has been performed for both as-deposited SnO_2 and the annealed samples. The incident angle of the x-ray source was fixed at 0.55° while the 2θ was scanned from 15 to 65° for both diffractograms. The step size was fixed at 0.02° and the scan speed was kept at 2°/min for both diffractograms. The X-ray source is Cu K-alpha, and its wavelength is 1.54 Å. GIXRD analysis was performed using Rigaku Smartlab (Japan).

X-ray photoelectron spectroscopy (XPS) has been conducted on both as-deposited and annealed SnO_2 thin film samples. High resolution spectra for Sn3d and O1s were performed using 20 eV pass energy, 0.1 eV Step size and 5 periods (average of 5 spectra) while survey spectra were achieved using 100 eV pass energy, 1 eV step size and 1 period (no averaging). Prior to the XPS analysis, both samples were first cleaned using low energy/atom argon cluster source to remove the surface contamination without altering the surface chemistry of the SnO_2 thin film samples, which is confirmed by reducing drastically the carbon contamination while keeping the Sn3d spectra intact. It is worth noting that XPS equipment is calibrated using triple pure standard samples of Au, Ag and Cu. During the measurements, all spectra were referenced using C1s to correct all the surface charging related shift. XPS analysis was performed using Thermo Fisher Scientific– Escalab 250Xi (United Kingdom).

Temperature-Dependent PL: An iHR320 fluorescence spectrometer (Horiba, Jobin Yvon iHR320) equipped with CCD camera was used for the photoluminescence (PL) spectra recording. To decouple the response of the absorbing material from any other influence, only perovskite films were grown on glass substrate following the same procedure depicted above. A green PL excitation source of 532 nm wavelength was used and based on a diode-pumped solid-state laser (from Laser Quantum).

The aim is to probe the temperature dependency of the PL response of the absorber films. To do so, the temperature was varied from RT to 75 ^{o}C with a ramping rate of 5 °C/min. At each temperature, we stabilize the sample's temperature for 5 min prior to its measurement. Laser was turned off during the heating and stabilization intervals to avoid any photo-degradation of the samples. For all the temperatures, the PL response was recorded from the same spot on the sample and with the same exposure and integration-time.

Solar Cell Device Performance: A standard AM1.5G AAA solar simulator with 100 mW/cm^2 and a certified reference Si solar cell was employed to analyze the PV performance (Newport, Inc.). Measurements were performed in ambient air. An appropriate mask designed an active area of 0.16 cm^2. I−V plots were recorded under different temperatures between 25 and 75 °C upon illumination (Keithley Model 2400 source meter). The temperature ramp/cooling rate of 3−5 °C/min was adopted through a solid-state heating/cooling system (ThermoCube). The PSCs were stabilized at each temperature setting for 10 min prior to launch the subsequent measurement. All the cooling and/or heating steps were performed under dark conditions.

A load resistance of 180 Ω was connected to the device for its stability. Current–voltage (I-V curve) scans were acquired. No filters have been used during the measurements. The stability measurement was performed at RH of 5% in a nitrogen box. The EQE scans were acquired by an IPCE measurement system.

PSC device configuration and cross-sectional imaging: The PSC device configuration is based on the conventional architecture where the layers on the glass substrate are fluorine doped tin oxide (FTO), SnO_2, perovskite, Spiro-OMETAD and Au, respectively as shown in Figure 2. FTO material and SnO_2 are used as anode and ETL, respectively, while the perovskite as the absorber layer. Spiro-OMETAD acts as HTL, and the metallic cathode is made of Au contact.

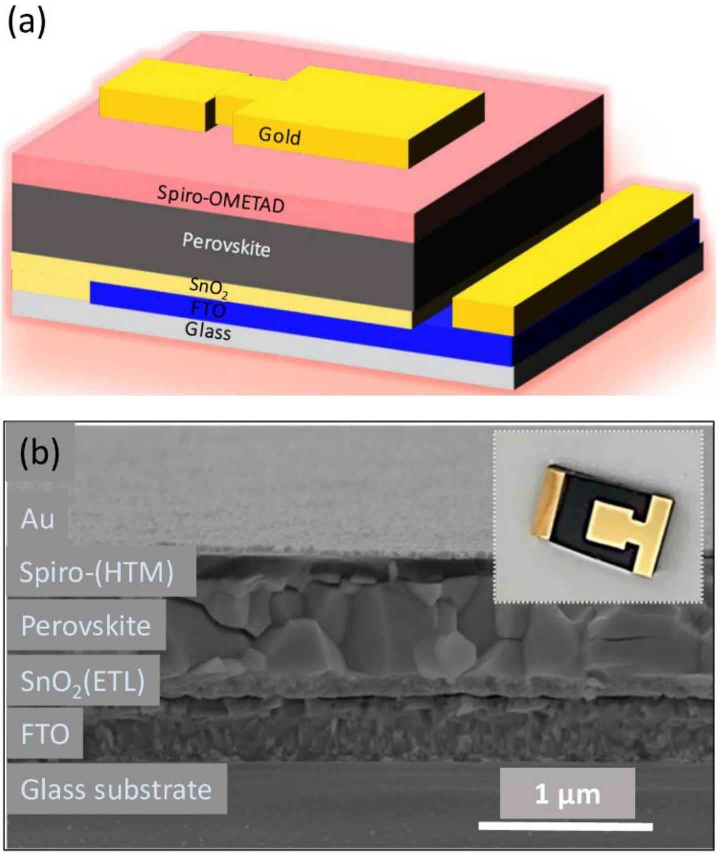

Figure 2: (a) Schematic diagram of the perovskite solar cell (PSC) used in this study. (b) Cross-sectional SEM image of $Cs_{0.05}MA_{0.10}FA_{0.85}Pb(I_{0.85}Br_{0.15})_3$ PSC. The inset shows a photograph of a PSC that is representative of those used in our experiments.

3.4. Results

3.4.1. Properties of the ETL-SnO_2 film

Figures 3a, 3b, 3c and 3d show representative top-view SEM images of as-deposited and thermally annealed SnO_2 films deposited onto glass substrate. SnO_2 samples demonstrate a uniform smooth surface morphology, with a large grain size, pinhole- and crack-free films. The thermal annealing treatment was found to have little or no impact on the morphology of the SnO_2 thin films. Figures 3e and 3f show the associated AFM images of these SnO_2 films.

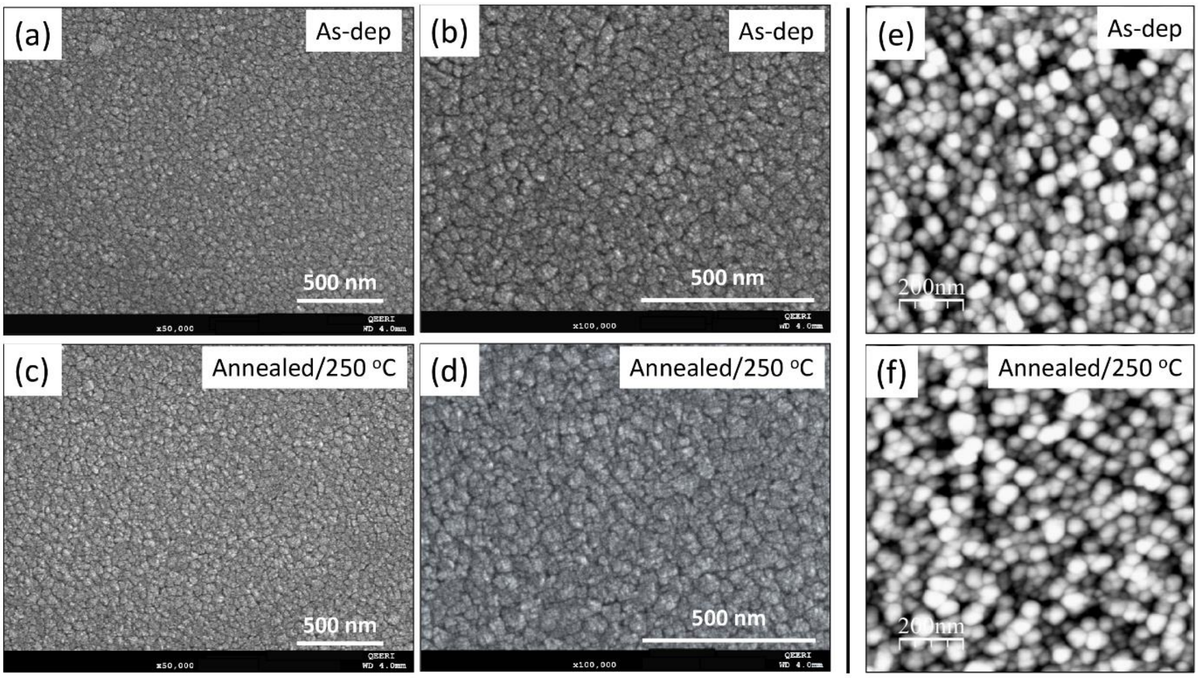

Figure 3: SEM (a-d) and AFM images (e, f): Top-view SEM images showing the SnO_2 films (a) as deposited magnified at x50k, (b) as deposited magnified at x100k, (c) annealed at 250 °C magnified at x50k, (d) annealed at 250 °C magnified at x100k; and AFM images of the SnO_2 films (e) as-deposited, (f) annealed at 250 °C.

The as-deposited SnO_2 thin films have shown a clear crystalline microstructure of the SnO_2 phase by displaying clear triple peaks of (110), (101) and (211) orientation planes, as shown in Figure 4. There is no presence of any secondary phases which reveals the high crystalline quality of this SnO_2 thin film. After the air annealing the SnO_2 thin film samples have kept their SnO_2 microstructural phase as revealed by the same observed triple peaks of (110), (101) and (211) (Figure 4). Furthermore, it is noticed that the crystallinity has enhanced after the air annealing as demonstrated by the slight decrease of the full width at half maximum (FWHM) related to the SnO_2 phase peak (101). By using the Scherrer equation, the calculated crystallite size of SnO_2 phase using (101) peak has increased from 60.7 Å for the as-deposited SnO_2 sample to 69.2 Å for the annealed SnO_2 sample. These results are shown in Table 1. As per the GIXRD analysis, it is clear that the growth conditions favored the formation of SnO_2 phase without any secondary phases. Furthermore, the post air annealing process has kept and enhanced the crystallinity of the SnO_2 phase without promoting any secondary phases. These results are matching with previously reported findings [52] where improved crystallinity of the SnO_2 films was demonstrated with respect to an air-thermal-annealing treatment, as more oxygen incorporated in the film increased its crystallinity.

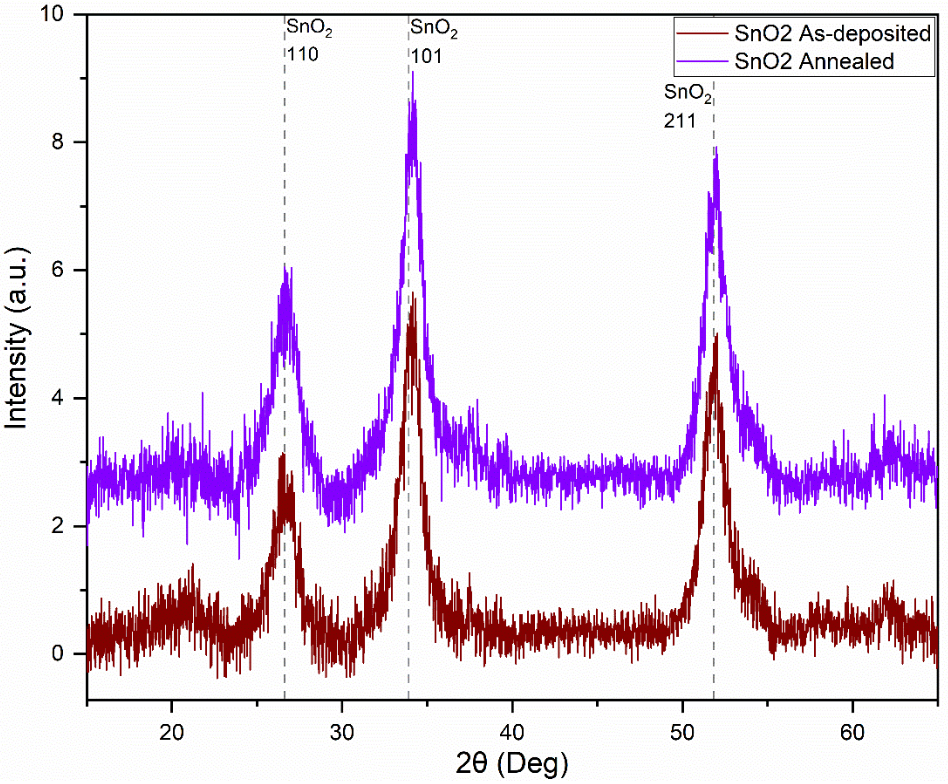

Figure 4: GIXRD for as-deposited SnO_2 and annealed SnO_2 thin film samples.

Sample	FWHM (°)	Crystallite size (Å)
SnO_2 as deposited	1.36	60.7
SnO_2 annealed	1.34	69.2

Table 1: Crystallite size calculation using SnO_2 phase peak (101) from Scherrer equation.

Survey XPS spectra has revealed the high purity of the SnO_2 thin film samples owing to the presence of only O and Sn as well as the low-to-absent content of C, particularly after the surface cleaning. All the peaks are related to Sn and O photoelectrons and Auger electrons as shown in Figure 5a. For the as deposited SnO_2 samples, $Sn3d_{5/2}$ peak is positioned on a higher binding energy at 486.7 eV, which indicates the presence of higher oxidation state related to Sn(IV). After the air annealing process, the peak position of $Sn3d_{5/2}$ has slightly shifted towards the higher binding energy at 486.8 eV, which indicates a slight increase in oxidation state after the annealing treatment as displayed by Figure 5b. These results match well with the crystallite size increase as discussed above. XPS related O 1s spectra have shown two main component peaks, the first peak is related to the photoelectrons originating from the oxygen atoms in the SnO_2 lattice, while the second peak is related to the other oxygen chemical states which might be defects in Sn oxide, or remaining surface organic molecules, and/or surface adsorbed moisture, as displayed in Figure 5c and 5d. For the as-deposited SnO_2 sample, the peak position of O related to the lattice SnO_2 is located at 530.6 eV, which confirms the presence of Sn(IV) oxide related to SnO_2. This is also corroborating well with the previous GIXRD results. The lattice oxide peak FWHM is of 1.26 eV, which is a reduced value that indicates the low chemical disorder as expected to be achieved by the vacuum-based material deposition.

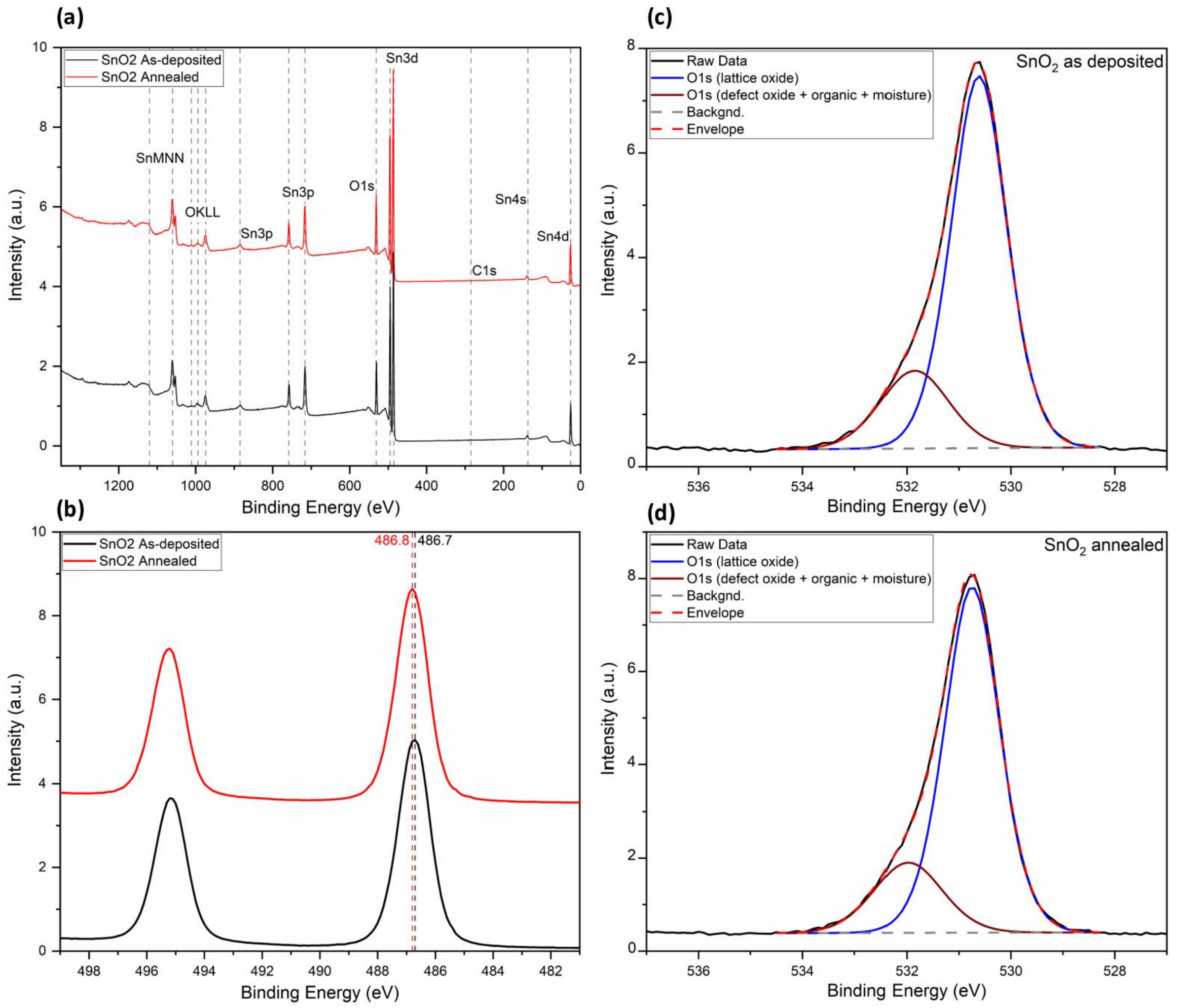

Figure 5: Post cleaned XPS spectra for as-deposited SnO_2 and annealed SnO_2 thin film samples: (a) surveys, (b) Sn3d, (c) O1s for as deposited SnO_2, (d) O1s for annealed SnO_2.

After the annealing, the peak position of O related to the lattice oxide has increased to 530.8 eV, which reveals the higher oxidation state of SnO_2 thin film after the annealing. Furthermore, the FWHM of O related to lattice oxide has slightly decreased from 1.26 to 1.25 eV, revealing a slight enhancement in the chemical disorder. The percentage of O related to lattice oxide has slightly increased from 79.8 to 80.1%, which also reveals that the thermal annealing process has improved the micro-structuring of the SnO_2 films as shown in Table 2 and it has enabled a slight reduction of the oxygen vacancies. Overall, this process has improved the surface chemistry of the SnO_2 thin film [53].

Sample	Binding Energy (eV)	FWHM (eV)	Chemical State	Percentage (%)
SnO_2 as deposited	530.6	1.26	Lattice Oxide	79.8
	531.9	1.54	Defect/Organic/H_2O	20.2
SnO_2 annealed	530.8	1.25	Lattice Oxide	80.1
	532.0	1.54	Defect/Organic/H_2O	19.9

Table 2: XPS O1s spectra fitting: peak positions, FWHM and percentage of chemical states.

As for the optical properties, the SnO_2 films have shown rather a high transmittance in the visible range which is higher than 80 %. The associated bandgap obtained from Tauc plot was about 3.95 eV, a value that is greater than that of TiO_2 and/or ZnO thin films (Figure 6). It is worth noting that larger bandgap can act as an efficient hole blocking and as a barrier against high-energy photons absorption, thereby decreasing the current losses, which is a requirement for stable halide perovskite solar cells. Indeed, both high optical transmittance and film quality are critical for an effective ETL layer for the *n-i-p* planar structure of PSCs [54].

Furthermore, Kam et al. [54] used a semiconductor band structure to calculate the position of the conduction band minimum (CBM) of a sputtered SnO_2 film, which was found to be -4.36 eV, which is even lower than that of TiO_2 and ZnO, where both are around -4.2 eV. More specifically, a deeper conduction band value will improve the electron transfer from the absorber layer, i.e. perovskite film, to the SnO_2 ETL layer. In the same context, Kam et al. calculations also showed the position of valance band maximum (VBM) at -8.08 eV [54], which is clearly deeper than that of TiO_2 and ZnO, which are at -7.4 eV and -7.6 eV, respectively. Here again, a deeper valence band of SnO_2 conjugated to its larger bandgap will enhance the capacity of the perovskite film to block the holes towards the SnO_2 ETL.

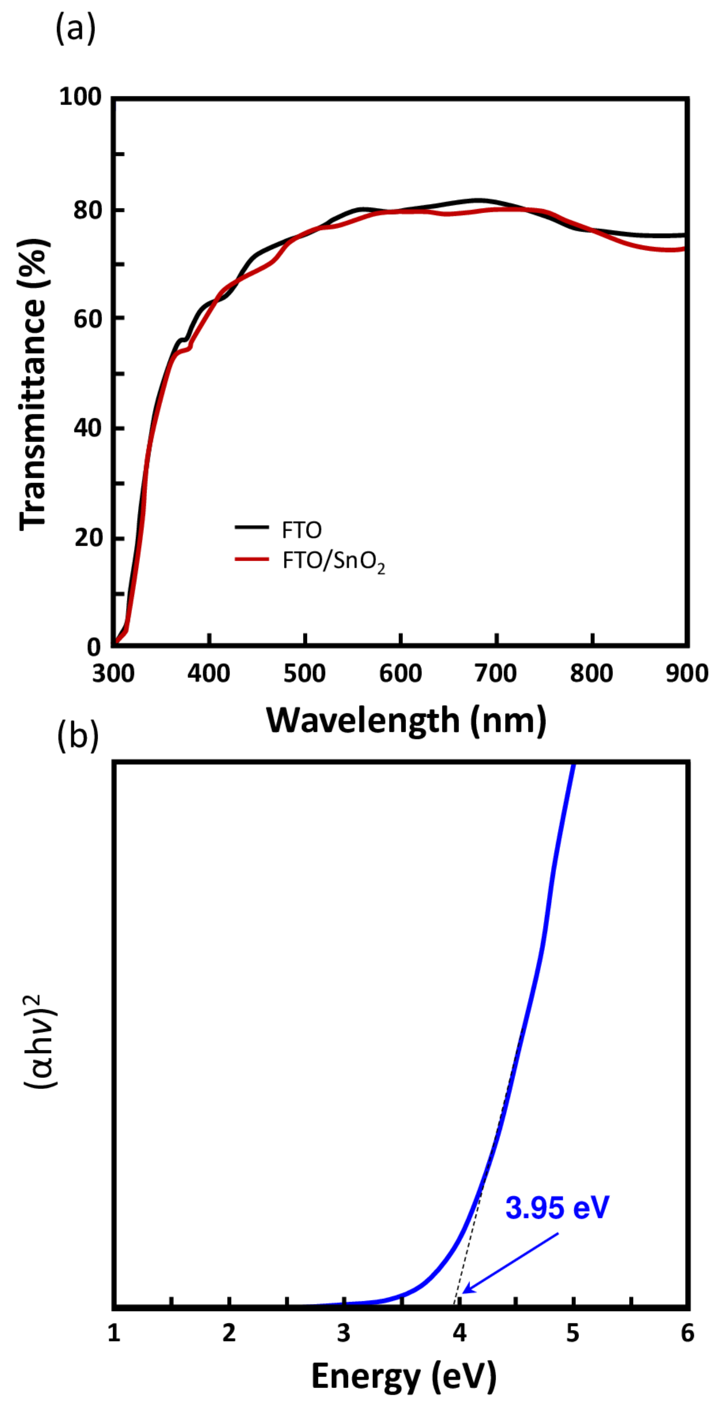

Figure 6: (a) Transmittance spectra % of the sputtered SnO_2 film deposited on fluorine doped tin oxide (FTO) glass and FTO on glass only. (b) Associated Tauc plot showing a bandgap of 3.95 eV.

On the other hand, the electrical resistivity of SnO_2 films has decreased from 0.245 Ω·cm (as-deposited) to 0.134 Ω·cm after a thermal annealing in air. The associated electron mobility has increased from 4.38 $cm^2/V·s$ as-deposited to 11.29 $cm^2/V·s$ after annealing treatment. However, the electron density has slightly decreased from 5.82×10^{18} cm^{-3} to 3.86×10^{18} cm^{-3}. The as-deposited and the annealed SnO_2 samples have negative charge carrier type (electrons). The thermal annealing process has clearly enhanced the electrical conductivity by significantly increasing the electron mobility and this finding is matching with the increase in crystallite size after the annealing process. The decrease in charge carrier concentration is related to the oxygen vacancy reduction as the thermal annealing in presence of oxygen in air enables the vacant oxygen site filling. On the other hand, its effect on the surface morphology is not very evident. The effect of the thermal annealing has also been highlighted and discussed above through microstructural study and chemical state analysis as well as the measurements of the average roughness as conducted by AFM (Figure 3e-f). In fact, the root mean square (RMS) roughness value was found to be in the low-level values, and it changed only slightly between the as-deposited and the annealed film (measured in the range of 1.45 to 1.33 nm). Moreover, from morphological point of view, the sputtered SnO_2 film was uniformly deposited, thereby showing rather a low value of surface roughness. This process is also boosted by thermal annealing treatment, and the obtained roughness values are highly accommodating for the solution-deposited perovskite on SnO_2/FTO/Glass. Therefore, this critical issue of the roughness effect has not been discussed in depth in the relevant literature. It is worth noting that a higher level of roughness of SnO_2 film will lead to inconstant rate for perovskite crystallization and hence leads ultimately to an increase of the carrier recombination probability between the perovskite absorber layer and the SnO_2 ETL.

3.4.2. Perovskite absorber layer

To highlight the impact of real-world conditions on these PSC devices, especially when they are subject to operate in a harsh condition, such as desert environment, a temperature-sensitive Photoluminescence (PL) study was conducted through PL spectroscopy to elucidate the correlation with the charge-carrier and bandgap dynamics. Figure 7a shows the temperature-dependency of the PL measurements of the tri-cation perovskite films deposited on glass substrates. A well-defined PL peak centered at ~773 nm is measured and is the fingerprint of the band-to-band recombination. It shows an associated bandgap of ~1.6 eV, corresponding typically to the tetragonal phase of the tri-cation perovskite material [13]. The variation in PL emission peak position (Figure 7a) as well as in PL emission peak broadening and intensity (Figure 7b) as a function of temperature, were investigated and the results are presented in Figure 7. The PL intensity was found to increase with respect to the temperature up to ~40 °C and then start decreasing when the temperature continues increasing from 40 to 75 °C.

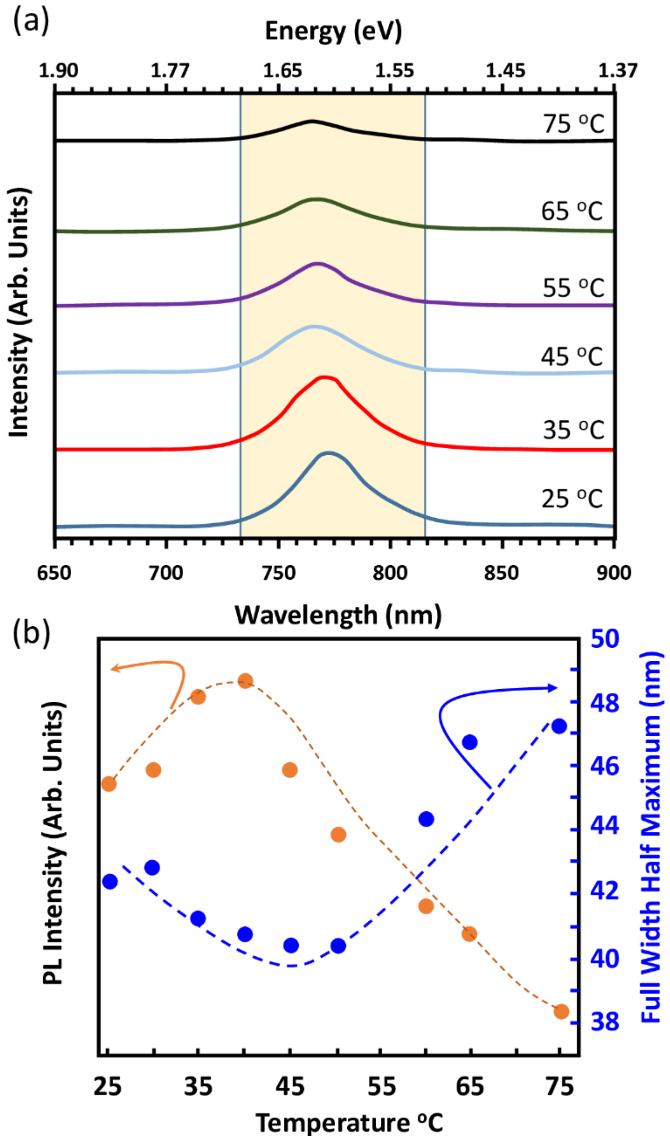

Figure 7: (a) Variation of the PL spectrum of the absorber perovskite films deposited on glass substrate. Measurements are performed in the range 25−75 °C. PL λ_{ext}= 532 nm. (b) Associated change in the PL peak intensity at ~773 nm and the FWHM as a function of temperature.

A rise in the PL emission intensity is generally the consequence of a decrease of the non-radiative recombination at traps and defects level in the bandgap, which lowers the band-to-band recombination rate and lower the charge−phonon coupling in the perovskite film [15, 55], leading thereby to an improvement of the V_{oc} and the fill factor (FF) values. Moreover, this decrease in the PL-emission-peak intensity while increasing the temperature above 40 °C is because of the charge trapping due to a boost of the charge−phonon coupling. This is also accompanied by a PL-emission-peak broadening (Figure 7a) [13]. The variations in the charge−phonon coupling and the orbital splitting, which are a direct consequence of the perovskite lattice expansion with respect to the temperature increasing, generate a singular bandgap broadening in addition to a blue shift of ~15 meV in the PL emission [13]. At this range of temperature, both the frequency and the population of the particular involved phonon modes increase with temperature [55] and support the suggestion that the charge trapping due to the electron−phonon coupling is dominant, which might be the reason behind the reduced PSC performance at elevated temperatures. Figure 7b shows an additional highlight of the temperature-dependency of the charge−phonon coupling [13, 56], namely the variation of the FWHM of the PL emission peak with respect to the temperature. The FWHM was found to decrease slightly from RT to 40 °C and then noticeably increase from 40 °C to 75 °C, denoting a higher charge−phonon interaction at this range of temperature. This broadening of the FWHM further supports the diagnosis and conclusion that PSC PV performance decrease for temperatures beyond 40 °C could be attributed to the charge trapping related to higher charge−phonon interactions. Overall, we attribute the PL changes up to 40 °C to the carrier accumulation near the perovskite/glass interface and/or to the diminution in the non-radiative charge traps, whereas higher charge−phonon interactions dominate at higher temperatures.

3.4.3. Perovskite solar cell device performance

Figure 8 displays the perovskite planar-junction solar-cell performance of the best device based on the optimized sputtered SnO_2 films integrated as ETL. Figure 8a shows the incident-photon-to-current efficiency (IPCE) and associated with the integrated current density. Following the optimization process of SnO_2 thin films using the growth and post-depositions conditions, an optimized SnO_2 ETL could be achieved through improving its material properties related to micro-structure, morphology and surface chemistry as well as the optoelectronic properties. Therefore, a PCE of 17.1% has been reached as shown in Figure 8b after the post-annealing treatment. The improvement of PCE from as-deposited SnO_2 ETL of 15.07% to thermally annealed SnO_2 ETL of 17.1% is a direct result of the improved microstructural and optoelectronic properties, including electrical conductivity and electron mobility. As discussed above, SnO_2 has high transmittance in visible light region and a deep valence band maximum position which has improved the hole-blocking process while minimizing the recombination at the SnO_2/perovskite interface. The high value related to J_{SC} of 22 mA cm^{-2} is corroborating well with the incident photon-to-electron conversion efficiency (Figure 8a) integrated J_{SC}, which also confirms the high transmittance of the SnO_2 ETL-layer.

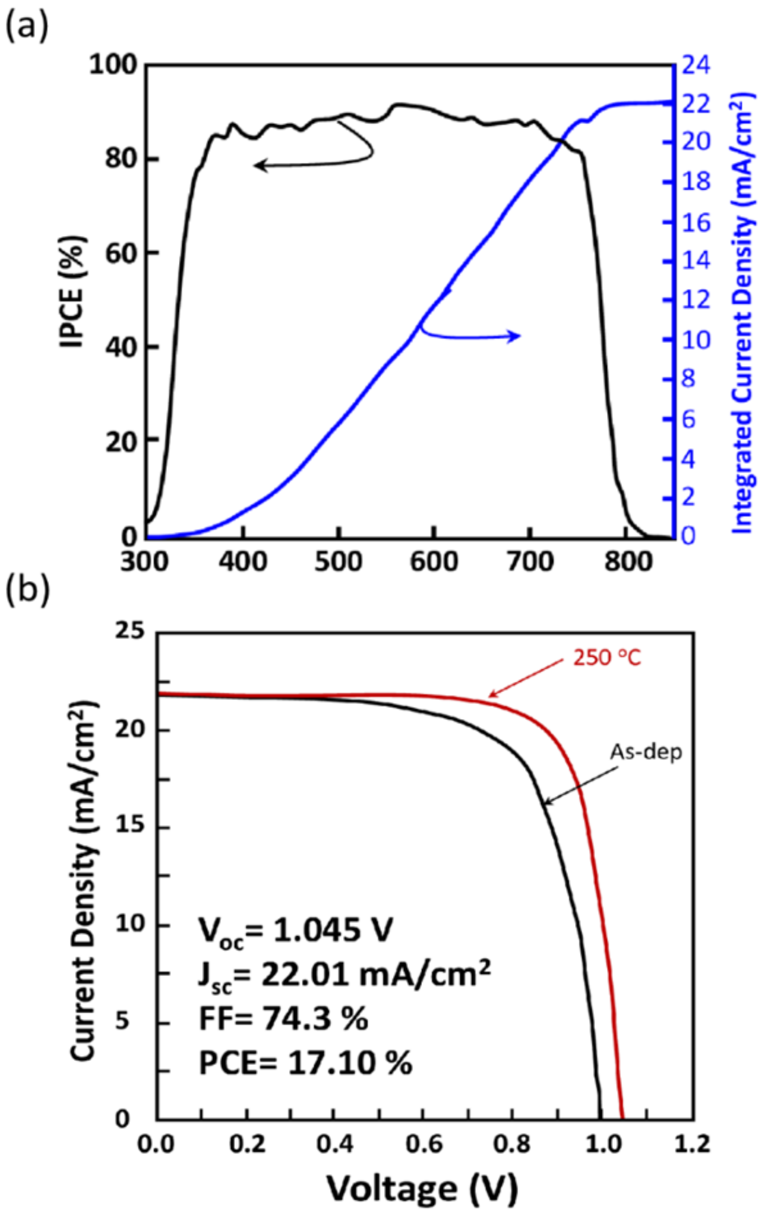

Figure 8: Perovskite solar cell device performance. a) IPCE and associated integrated current density of the best device based on the sputtered SnO_2 films as ETL. (b) *J–V* curves of the perovskite devices based on the SnO_2 films as-deposited and that annealed at 250 °C (device performance results are related to the annealed SnO_2 at 250 °C).

Another advantage of the SnO_2 as ETL for perovskite solar cells compared to TiO_2, is its longer operational stability and lifetime. Indeed, the operational lifetime of the solar cell based on SnO_2 ETL has been measured under its maximum power point, under a continuous light illumination, at 45 °C (the detailed results are not shown here but will be a subject for a separate report). The best-reached T80 (the time required to decrease to 80% of the initial efficiency) lifetime was 250 h and the average lifetime over 200 h. This protocol is also regarded to be the most reliable and reproducible way to test the operational stability[57].

Finally, Figure 9 summarizes a literature survey of various PCE values recorded for different PSC solar cells based SnO_2 ETL from about thirty references. In this literature survey, SnO_2 ETL was grown by different methods from different material sources. Only two references related to magnetron sputtering were found and show values comparable to our current work. Further optimization might be provided to enhance the PV properties through a systematic study by improving the microstructural and optoelectronic properties via post-deposition thermal annealing.

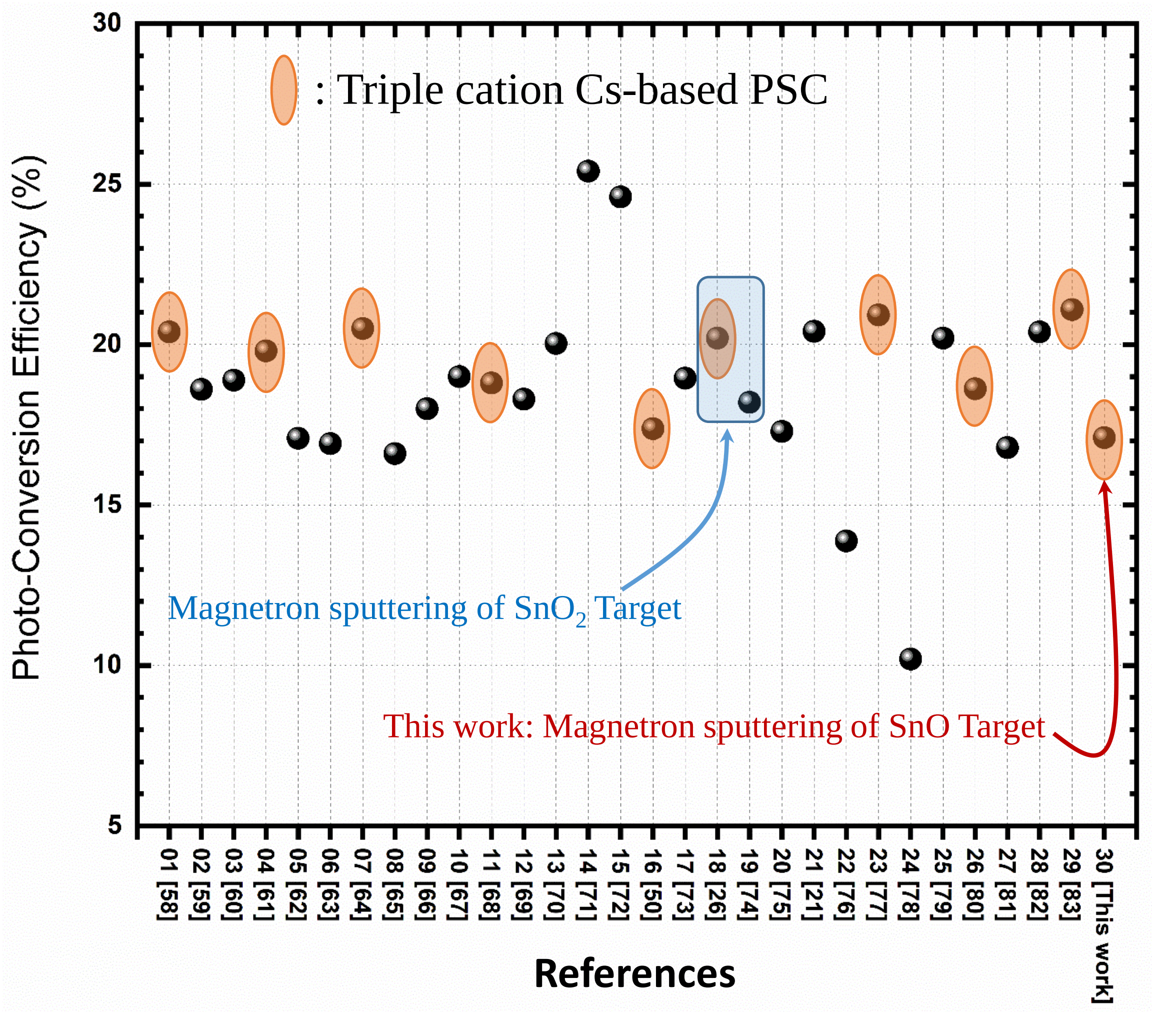

Figure 9: Summary of a literature survey of various PCE values recorded for different PSC solar cells based SnO_2 ETL. SnO_2 was grown by different methods from different sources [21, 26, 50, 58-82].

3.5. Summary

We have successfully employed the radio frequency magnetron sputtered SnO_2 as electron transport layer for spin-coated-(FA, MA, and Cs) triple cation-based perovskite solar cells on FTO substrates. We demonstrated that neither mesoporous scaffold nor high-temperature processing procedures were essential to achieve high device performance. In addition, no passivation process has been performed and no encapsulation has been used. Nevertheless, PSCs of 17.10% PCE have been achieved. Material's characterization study has demonstrated that the air annealing has enhanced the material's structural and electrical properties, particularly the improvement in crystallite size which led to an improvement in electron mobility. These enhancements have improved the overall performance of the PSC device. Our results on the temperature dependency suggested an interplay of different physical phenomena, including charge transfer dynamics and charge recombination that govern the PV performance at different temperature intervals. We attributed the PL changes up to 40 °C to the possible carrier accumulation near the SnO_2/perovskite interface and to the diminution in the non-radiative charge traps, whereas higher charge−phonon interactions are believed to be dominating at higher temperatures (i.e. from 40 °C to 75 °C). Our work offers a significant insight into the operational reliability and variability of the PV performance of PSCs, as well as the underlying mechanisms in perovskite materials, at real-world operating temperatures. More importantly, sputtered SnO_2 as ETL was demonstrated to enable a good device photovoltaic performance, stability and lifetime and could serve as a promising route for further development and integration of sputtered SnO_2 films into large-scale and cost-effective perovskite photovoltaics modules.

In the next chapter, nitrogen doping of SnO_x via a two-step method will be explored aiming at achieving a p-type conductivity where synthesis, conductions, materials characterization will be discussed thoroughly.

References

1. NREL, Best Research-Cell Efficiencies. 2022.

2. Qiu, L., L.K. Ono, and Y. Qi, Advances and challenges to the commercialization of organic–inorganic halide perovskite solar cell technology. Materials Today Energy, 2018. 7: p. 169-189.

3. Domanski, K., et al., Not All That Glitters Is Gold: Metal-Migration-Induced Degradation in Perovskite Solar Cells. ACS Nano, 2016. 10(6): p. 6306-6314.

4. Dkhissi, Y., et al., Stability Comparison of Perovskite Solar Cells Based on Zinc Oxide and Titania on Polymer Substrates. ChemSusChem, 2016. 9(7): p. 687-695.

5. Ono, L.K., et al., Pinhole-free hole transport layers significantly improve the stability of MAPbI3-based perovskite solar cells under operating conditions. Journal of Materials Chemistry A, 2015. 3(30): p. 15451-15456.

6. Manspeaker, C., et al., Role of interface in stability of perovskite solar cells. Current Opinion in Chemical Engineering, 2017. 15: p. 1-7.

7. Wang, S., et al., Accelerated degradation of methylammonium lead iodide perovskites induced by exposure to iodine vapour. Nature Energy, 2016. 2(1): p. 16195.

8. Ahn, N., et al., Trapped charge-driven degradation of perovskite solar cells. Nature Communications, 2016. 7(1): p. 13422.

9. Qiu, L., et al., Engineering Interface Structure to Improve Efficiency and Stability of Organometal Halide Perovskite Solar Cells. The Journal of Physical Chemistry B, 2018. 122(2): p. 511-520.

10. Yang, D., et al., High efficiency planar-type perovskite solar cells with negligible hysteresis using EDTA-complexed SnO2. Nature Communications, 2018. 9(1): p. 3239.

11. Jiang, Q., et al., Enhanced electron extraction using SnO2 for high-efficiency planar-structure HC(NH2)2PbI3-based perovskite solar cells. Nature Energy, 2016. 2(1): p. 16177.

12. Christians, J.A., et al., Tailored interfaces of unencapsulated perovskite solar cells for >1,000 hour operational stability. Nature Energy, 2018. 3(1): p. 68-74.

13. Jiang, Y., et al., Combination of Hybrid CVD and Cation Exchange for Upscaling Cs-Substituted Mixed Cation Perovskite Solar Cells with High Efficiency and Stability. Advanced Functional Materials, 2018. 28(1): p. 1703835.

14. Green, M.A., et al., Solar cell efficiency tables (version 52). Progress in Photovoltaics: Research and Applications, 2018. 26(7): p. 427-436.

15. Chen, H., et al., A solvent- and vacuum-free route to large-area perovskite films for efficient solar modules. Nature, 2017. 550(7674): p. 92-95.

16. Ding, B., et al., Low-temperature SnO2-modified TiO2 yields record efficiency for normal planar perovskite solar modules. Journal of Materials Chemistry A, 2018. 6(22): p. 10233-10242.

17. Palma, A.L., et al., Laser-Patterning Engineering for Perovskite Solar Modules With 95% Aperture Ratio. IEEE Journal of Photovoltaics, 2017. 7(6): p. 1674-1680.

18. Yang, M., et al., Highly Efficient Perovskite Solar Modules by Scalable Fabrication and Interconnection Optimization. ACS Energy Letters, 2018. 3(2): p. 322-328.

19. Anaraki, E.H., et al., Highly efficient and stable planar perovskite solar cells by solution-processed tin oxide. Energy & Environmental Science, 2016. 9(10): p. 3128-3134.

20. Ke, W., et al., Low-Temperature Solution-Processed Tin Oxide as an Alternative Electron Transporting Layer for Efficient Perovskite Solar Cells. Journal of the American Chemical Society, 2015. 137(21): p. 6730-6733.

21. Chen, J.-Y., et al., Low-temperature electrodeposited crystalline SnO2 as an efficient electron-transporting layer for conventional perovskite solar cells. Solar Energy Materials and Solar Cells, 2017. 164: p. 47-55.

22. Ma, J., et al., Highly Efficient and Stable Planar Perovskite Solar Cells With Large-Scale Manufacture of E-Beam Evaporated SnO2 Toward Commercialization. Solar RRL, 2017. 1(10): p. 1700118.

23. Xiao, C., et al., Junction Quality of SnO2-Based Perovskite Solar Cells Investigated by Nanometer-Scale Electrical Potential Profiling. ACS Applied Materials & Interfaces, 2017. 9(44): p. 38373-38380.

24. Tao, H., et al., Room-temperature processed tin oxide thin film as effective hole blocking layer for planar perovskite solar cells. Applied Surface Science, 2018. 434: p. 1336-1343.

25. Ali, F., et al., Tuning the Amount of Oxygen Vacancies in Sputter-Deposited SnOx films for Enhancing the Performance of Perovskite Solar Cells. ChemSusChem, 2018. 11(18): p. 3096-3103.

26. Qiu, L., et al., Scalable Fabrication of Stable High Efficiency Perovskite Solar Cells and Modules Utilizing Room Temperature Sputtered SnO2 Electron Transport Layer. Advanced Functional Materials, 2019. 29(47): p. 1806779.

27. Lin, L., et al., Inorganic Electron Transport Materials in Perovskite Solar Cells. Advanced Functional Materials, 2021. 31(5): p. 2008300.

28. Mahmood, K., S. Sarwar, and M.T. Mehran, Current status of electron transport layers in perovskite solar cells: materials and properties. RSC Advances, 2017. 7(28): p. 17044-17062.

29. Mahmood, K., et al., Electrospray deposited MoS2 nanosheets as an electron transporting material for high efficiency and stable perovskite solar cells. Solar Energy, 2020. 203: p. 32-36.

30. Sadegh, F., et al., Highly efficient, stable and hysteresis–less planar perovskite solar cell based on chemical bath treated Zn2SnO4 electron transport layer. Nano Energy, 2020. 75: p. 105038.

31. Wei, H., et al., Plasma-enhanced atomic-layer-deposited gallium nitride as an electron transport layer for planar perovskite solar cells. Journal of Materials Chemistry A, 2019. 7(44): p. 25347-25354.

32. Zhu, H., et al., Tailored Amphiphilic Molecular Mitigators for Stable Perovskite Solar Cells with 23.5% Efficiency. Advanced Materials, 2020. 32(12): p. 1907757.

33. Fares, C., et al., Valence and conduction band offsets for sputtered AZO and ITO on (010) (Al0.14Ga0.86)2O3. Semiconductor Science and Technology, 2019. 34(2): p. 025006.

34. Li, J. and N. Wu, Semiconductor-based photocatalysts and photoelectrochemical cells for solar fuel generation: a review. Catalysis Science & Technology, 2015. 5(3): p. 1360-1384.

35. Lu, Q., et al., 2D Transition-Metal-Dichalcogenide-Nanosheet-Based Composites for Photocatalytic and Electrocatalytic Hydrogen Evolution Reactions. Advanced Materials, 2016. 28(10): p. 1917-1933.

36. Marschall, R., Semiconductor Composites: Strategies for Enhancing Charge Carrier Separation to Improve Photocatalytic Activity. Advanced Functional Materials, 2014. 24(17): p. 2421-2440.

37. Stevanović, V., et al., Assessing capability of semiconductors to split water using ionization potentials and electron affinities only. Physical Chemistry Chemical Physics, 2014. 16(8): p. 3706-3714.

38. Yasuhiro Shirahata, T.O., Sakiko Fukunishi, Kazufumi Kohno, Fabrication of Perovskite-Type Photovoltaic Devices with Polysilane Hole Transport Layers. Materials Sciences and Applications, 2017. 8: p. 209-222.

39. Yip, H.-L. and A.K.Y. Jen, Recent advances in solution-processed interfacial materials for efficient and stable polymer solar cells. Energy & Environmental Science, 2012. 5(3): p. 5994-6011.

40. Li, Y., et al., Mesoporous SnO2 nanoparticle films as electron-transporting material in perovskite solar cells. RSC Advances, 2015. 5(36): p. 28424-28429.

41. Jiang, Q., X. Zhang, and J. You, SnO2: A Wonderful Electron Transport Layer for Perovskite Solar Cells. Small, 2018. 14(31): p. 1801154.

42. Kavan, L., L. Steier, and M. Grätzel, Ultrathin Buffer Layers of SnO2 by Atomic Layer Deposition: Perfect Blocking Function and Thermal Stability. The Journal of Physical Chemistry C, 2017. 121(1): p. 342-350.

43. Ke, W., et al., Effects of annealing temperature of tin oxide electron selective layers on the performance of perovskite solar cells. Journal of Materials Chemistry A, 2015. 3(47): p. 24163-24168.

44. Khan, A.F., et al., Characteristics of electron beam evaporated nanocrystalline SnO2 thin films annealed in air. Applied Surface Science, 2010. 256(7): p. 2252-2258.

45. Yeom, E.J., et al., Controllable synthesis of single crystalline Sn-based oxides and their application in perovskite solar cells. Journal of Materials Chemistry A, 2017. 5(1): p. 79-86.

46. Lin, S., et al., Efficient and stable planar hole-transport-material-free perovskite solar cells using low temperature processed SnO2 as electron transport material. Organic Electronics, 2018. 53: p. 235-241.

47. Qin, X., et al., Recent progress in stability of perovskite solar cells*. Journal of Semiconductors, 2017. 38(1): p. 011002.

48. Manekkathodi, A., et al., Unusual Bimodal Photovoltaic Performance of Perovskite Solar Cells at Real-World Operating Temperatures. The Journal of Physical Chemistry C, 2020. 124(17): p. 9118-9125.

49. Mo, Y., et al., Efficient Planar Perovskite Solar Cells via a Sputtered Cathode. Solar RRL, 2019. 3(9): p. 1900209.

50. Bai, G., et al., High performance perovskite sub-module with sputtered SnO2 electron transport layer. Solar Energy, 2019. 183: p. 306-314.

51. Otoufi, M.K., et al., Enhanced performance of planar perovskite solar cells using TiO2/SnO2 and TiO2/WO3 bilayer structures: Roles of the interfacial layers. Solar Energy, 2020. 208: p. 697-707.

52. Zakaria, Y., et al., Study of wide bandgap SnOx thin films grown by a reactive magnetron sputtering via a two-step method. Scientific Reports, 2022. 12(1): p. 15294.

53. Jung, K.-H., et al., Solution-processed SnO2 thin film for a hysteresis-free planar perovskite solar cell with a power conversion efficiency of 19.2%. Journal of Materials Chemistry A, 2017. 5(47): p. 24790-24803.

54. Kam, M., et al., Room-Temperature Sputtered SnO2 as Robust Electron Transport Layer for Air-Stable and Efficient Perovskite Solar Cells on Rigid and Flexible Substrates. Scientific Reports, 2019. 9(1): p. 6963.

55. Yu, H.Y., et al., Surface electronic structure of plasma-treated indium tin oxides. Applied Physics Letters, 2001. 78(17): p. 2595-2597.

56. Leng, D., et al., Preparation and Properties of SnO₂ Film Deposited by Magnetron Sputtering. International Journal of Photoenergy, 2012. 2012: p. 235971.

57. Domanski, K., et al., Systematic investigation of the impact of operation conditions on the degradation behaviour of perovskite solar cells. Nature Energy, 2018. 3(1): p. 61-67.

58. Lee, H.B., et al., Dopant-Free, Amorphous–Crystalline Heterophase SnO2 Electron Transport Bilayer Enables >20% Efficiency in Triple-Cation Perovskite Solar Cells. Advanced Functional Materials, 2020. 30(24): p. 2001559.

59. Zhang, D., et al., Efficient planar heterojunction perovskite solar cells with enhanced FTO/SnO2 interface electronic coupling. Journal of Alloys and Compounds, 2020. 831: p. 154717.

60. Xu, H., et al., Aged sol-gel solution-processed texture tin oxide for high-efficient perovskite solar cells. Nanotechnology, 2020. 31(31): p. 315205.

61. Smith, J.A., et al., Rapid Scalable Processing of Tin Oxide Transport Layers for Perovskite Solar Cells. ACS Applied Energy Materials, 2020. 3(6): p. 5552-5562.

62. Fan, X., et al., Spray-coated monodispersed SnO2 microsphere films as scaffold layers for efficient mesoscopic perovskite solar cells. Journal of Power Sources, 2020. 448: p. 227405.

63. Taheri, B., et al., Automated Scalable Spray Coating of SnO2 for the Fabrication of Low-Temperature Perovskite Solar Cells and Modules. Energy Technology, 2020. 8(5): p. 1901284.

64. Bu, T., et al., Universal passivation strategy to slot-die printed SnO2 for hysteresis-free efficient flexible perovskite solar module. Nature Communications, 2018. 9(1): p. 4609.

65. Gong, C., et al., Flexible Planar Heterojunction Perovskite Solar Cells Fabricated via Sequential Roll-to-Roll Microgravure Printing and Slot-Die Coating Deposition. Solar RRL, 2020. 4(2): p. 1900204.

66. Peng, Y., et al., Fully Doctor-bladed efficient perovskite solar cells in ambient condition via composition engineering. Organic Electronics, 2020. 83: p. 105736.

67. Chang, X., et al., Printable CsPbI3 Perovskite Solar Cells with PCE of 19% via an Additive Strategy. Advanced Materials, 2020. 32(40): p. 2001243.

68. Rohnacher, V., et al., Analytical Study of Solution-Processed Tin Oxide as Electron Transport Layer in Printed Perovskite Solar Cells. Advanced Materials Technologies, 2021. 6(2): p. 2000282.

69. Jeong, S., et al., Atomic layer deposition of a SnO2 electron-transporting layer for planar perovskite solar cells with a power conversion efficiency of 18.3%. Chemical Communications, 2019. 55(17): p. 2433-2436.

70. Lee, Y., et al., Efficient Planar Perovskite Solar Cells Using Passivated Tin Oxide as an Electron Transport Layer. Advanced Science, 2018. 5(6): p. 1800130.

71. Yoo, J.J., et al., Efficient perovskite solar cells via improved carrier management. Nature, 2021. 590(7847): p. 587-593.

72. Jeong, M.J., et al., Spontaneous interface engineering for dopant-free poly(3-hexylthiophene) perovskite solar cells with efficiency over 24%. Energy & Environmental Science, 2021. 14(4): p. 2419-2428.

73. Song, Z., et al., Low-Temperature Electron Beam Deposition of Zn-SnOx for Stable and Flexible Perovskite Solar Cells. Solar RRL, 2020. 4(2): p. 1900266.

74. Chen, Z., et al., Bulk heterojunction perovskite solar cells based on room temperature deposited hole-blocking layer: Suppressed hysteresis and flexible photovoltaic application. Journal of Power Sources, 2017. 351: p. 123-129.

75. Wang, C., et al., Understanding and Eliminating Hysteresis for Highly Efficient Planar Perovskite Solar Cells. Advanced Energy Materials, 2017. 7(17): p. 1700414.

76. Jia, J., et al., Combustion procedure deposited SnO2 electron transport layers for high efficient perovskite solar cells. Journal of Alloys and Compounds, 2020. 844: p. 156032.

77. Mohamad Noh, M.F., et al., Eliminating oxygen vacancies in SnO2 films via aerosol-assisted chemical vapour deposition for perovskite solar cells and photoelectrochemical cells. Journal of Alloys and Compounds, 2019. 773: p. 997-1008.

78. Mahmood, K., et al., Low-temperature electrospray-processed SnO2 nanosheets as an electron transporting layer for stable and high-efficiency perovskite solar cells. Journal of Colloid and Interface Science, 2018. 532: p. 387-394.

79. Xu, X., et al., High-performance planar perovskite solar cells based on low-temperature solution-processed well-crystalline SnO2 nanorods electron-transporting layers. Chemical Engineering Journal, 2018. 351: p. 391-398.

80. Guo, Y., et al., Vacuum thermal-evaporated SnO2 as uniform electron transport layer and novel management of perovskite intermediates for efficient and stable planar perovskite solar cells. Organic Electronics, 2019. 65: p. 207-214.

81. Sun, H., et al., Composition and Energy Band–Modified Commercial FTO Substrate for In Situ Formed Highly Efficient Electron Transport Layer in Planar Perovskite Solar Cells. Advanced Functional Materials, 2019. 29(11): p. 1808667.

82. Singh, M., et al., Facile synthesis of composite tin oxide nanostructures for high-performance planar perovskite solar cells. Nano Energy, 2019. 60: p. 275-284.

Chapter 4: Properties of Nitrogen doped Tin Oxide

4. Properties of Nitrogen doped Tin Oxide

4.1. Introduction

As elaborated in Chapter 1, transparent conductive oxides (TCOs) are very appealing materials due to their combined properties of optical transparency, electrical conductivity, and chemical stability. TCOs have been heavily investigated and are crucial materials in various optoelectronic applications such as solar cells, light emitting diodes (LEDs), flat panel display (FPDs)[1-8]. The widely studied TCOs are In-, Sn-, Zn-based oxides[9-15]. These oxides are known to be intrinsically n-type conductive materials. Nowadays, there is a huge demand for high quality p-type TCOs to achieve the next generation optoelectronic applications including all oxide devices[3, 16, 17]. In Chapter 2 , we have investigated the growth of undoped SnO_x films using two different magnetron sputtering methods that differ by the target material (SnO and Sn), deposition parameters and the atmosphere of the annealing process; The optimization of the grown and annealed undoped SnO_x has enabled a major improvement in optoelectronic properties as well as the ability to control the conductivity, n-type and p-type. In Chapter 3, the performance of SnO_2 thin film as an electron transport layer in perovskite solar cell has been assessed as well as the thermal annealing effect of this layer on the solar cell performance. In this chapter, the extrinsic doping of SnO_x using nitrogen will be evaluated to achieve the p-type conductivity.

There have been several reports about p-type TCO materials[18-21]. SnO_2 is a very attractive material due to its higher earth-abundance, wide bandgap, and higher exciton binding energy of 130 mV[22, 23]. P-type doping for SnO_2 have been reported using doping metals with lower valence cations such as In to substitute the Sn atoms and to act as acceptor defects[24, 25] or using nitrogen atoms as doping elements to substitute oxygen atoms[26-28]. Nitrogen doping is highly desirable due to its ion size, high solubility, electronegativity, earth-abundance, and non-toxicity. Nitrogen ionic radius of 1.71 Å is larger than oxygen ionic radius of 1.40 Å, so the nitrogen doping increases the lattice constant for the host SnO_2 and it requires a relatively higher temperature for the nitrogen incorporation into the oxygen lattice[22, 23, 26-32]. Nitrogen doped SnO_2 ($N:SnO_2$) has been synthetized previously by different methods. Jie et al.[31] reported $N:SnO_2$ thin films using Chemical Vapor Deposition. Bhawna et al.[33] reported $N:SnO_2$ nanoparticles using a wet chemistry synthesis process. Wang et al.[34] reported nanoparticles $N:SnO_2$ synthesis using a Laser Induced Pyrolysis process. There are several reports about nitrogen doped SnO_2 synthesis using magnetron sputtering and N_2 partial pressure during the growth. However, there are issues related to the incorporation of atomic nitrogen doping within the SnO host material, control of SnO_xN_Y stoichiometry and formation of Sn nitride phases[22, 23, 28-30, 32]. In addition, there is also a previous report about plasma post-treated p-type ZnO by Cao et al.[35]. Nitrogen incorporation in SnO_2 can result in different chemical states, particularly atomic nitrogen doping which substitutes oxygen in the host SnO_2 lattice and makes bonds with Sn(IV). This nitrogen atomic doping is reported to generate acceptor levels close to the valence band within the bandgap[22, 23, 27-30].

As reported in literature, reactive magnetron sputtering of Sn using a mixture of both reactive gases O_2 and N_2 can be challenging in terms of incorporating atomic nitrogen within the SnO_2 host material. In this study, we report on the synthesis of N:SnO_x using a two-step method. The first step consists of growing SnO_2 films by magnetron sputtering and the second one is a plasma treatment of the films under a high purity nitrogen precursor, namely ammonia (NH_3), nitrous oxide (N_2O), or nitrogen gas (N_2). The plasma treated SnO_x films were characterized by several techniques to monitor the effects of nitrogen treatment on the structural, composition, electrical and optical properties. We show that within our experimental conditions, the N_2 plasma treatment allowed the conversion from n-type character to p-type one.

4.2. Materials and Methods

4.2.1. Material Synthesis

SnO_x were synthetized using magnetron sputtering, manufactured by AJA Int. (described in the appendix in section 1.3.) on quartz substrates using Sn metallic target and O_2/Ar flow rate ratio at 0.25 where O_2:Ar is 3:12 sccm at a pressure of 0.45 Pa, for a deposition time of 12 minutes. The sputtering power was fixed at 50 W. The substrate temperature was set at 100 °C. SnO_x films were grown at 100 °C which is a low deposition temperature and using a relatively O_2 poor condition during the growth.

Upon deposition, the SnO_x thin films were submitted to plasma treatments using an electron cyclotron resonance - plasma enhanced chemical vapor deposition (ECR-PECVD) reactor. Its model is MycroSys 400 System from the manufacturer Roth & Rau as shown in Figure 1. The conditions of plasma treatments are summarized in the Table 1. The nitrogen gas precursors were NH_3, N_2O or N_2 with two levels of treatment for each precursor namely, moderate (NH_3-1, N_2O-1, N_2-1) and intense (NH_3-2, N_2O-2, N_2-2). The exposure time and microwave power were fixed at 30 min and 500 W, respectively, for all the treatments.

Figure 1: Photo of an electron cyclotron resonance - plasma enhanced chemical vapor deposition (ECR-PECVD) reactor.

Treatment	Flow rate (sccm)	Temperature (°C)	RF power (W)	Acceleration (V)
NH_3-1	10	100	30	70
NH_3-2	20	300	50	150
N_2O-1	10	100	30	70
N_2O-2	20	300	50	150
N_2-1	10	100	30	70
N_2-2	20	300	50	150

Table 1: Conditions of plasma treatments applied to SnO_x sputtered films.

4.2.2. Material Characterization

The structural properties of as-deposited (reference) and plasma treated SnO_x films were analysed using Grazing Incidence X-ray Diffraction (GIXRD Smartlab - Rigaku) where θ was fixed at 0.55° and 2θ scanned from 15 to 65°. Surface imaging has been conducted using Atomic Force Microscopy in ScanAsyst imaging mode (AFM Dimension Icon - Bruker). Depth profiling was conducted using Time of Flight - Secondary Ion Mass Spectroscopy (ToF.SIMS^5 - IONTOF) with negative polarity, Bi^+ 100 x 100 µm^2 as a primary scanning analysis beam and Cs^+ 400 x 400 µm^2 as a secondary scanning sputtering beam. The optical properties were analysed using UV-Visible Spectroscopy (UV-Vis Spectrometer

Lambda 19 - Perkin Elmer) scanning from 1000 to 248 nm with 4 nm step size. Finally, the electrical properties were monitored using a Hall Effect probe system (HMS 3000 - Ecopia).

In order to understand the chemistry of SnO_x films, a detailed study of elemental composition and the chemical states has been conducted using X-ray Photoelectron Spectroscopy (XPS Escalab 250Xi – Thermo Fisher Scientific) with a monochromated Al K alpha source at 1486.7 eV. XPS pass energy was 20 eV for high resolution scans and 100 eV for survey scans. Prior to performing the measurements, surface cleaning was performed using Argon cluster beam to remove the adventitious carbon contamination. The cleaning has enhanced the photoelectron intensities for N 1s, Sn $3d_{5/2}$, and O 1s. The remaining traces of surface adventitious carbon was used as a reference at 284.8 eV.

Previous reports about XPS analysis for N doped SnO_x suggest that the N 1s peak position related to nitride Sn-N bonds varies from 396.5 to 397.6 eV depending on the Sn chemical state. N 1s peak position for N incorporated within SnO_x is between 399 and 400 eV which is denoted as N:SnO_x where nitrogen atoms are expected to occupy oxygen vacancy sites. The higher binding energy compared to nitride Sn-N is mainly related to the oxygen rich environment with higher electronegativity. The N 1s peak position ranging from 402 to 404 eV is related to -NO_x adsorbed and/or substitution for oxygen sublattice which is denoted as NO_y:SnO_x. If the content of N is relatively small, nitrogen atoms are expected to fill the oxygen vacancies without altering the host SnO_2 chemical state. If nitrogen content becomes high, the chemical state of N is expected to be nitride by forming SnN_x regions. XPS related O 1s chemical state analysis for as-deposited and plasma treated SnO_x samples are expected to form mainly five chemical states for O 1s spectra representing: i) O-Sn(II) at 530.1 eV; ii) O-Sn(IV) at 530.6 eV are respectively related to SnO and SnO_2 lattice oxides, iii) O-Sn defect lattice oxide is around 531.7 eV, iv) oxygen related to organic and moister is around 532.3 eV, and v) O-Si related to SiO_2 O peak is expected around 532.8 eV. Sn $3d_{5/2}$ chemical state analysis for as-deposited and plasma treated SnO_x samples which reveals mainly three possible chemical states represented by peaks for Sn $3d_{5/2}$ spectra metallic related Sn(0) around 484.6 eV, Sn(II) around 486.4 eV and Sn(IV) around 486.9 eV[22, 26, 28, 29, 36-41].

4.3. Nitrogen doped SnO_x thin films

All SnO_x thin films were grown at 100 °C which is a low deposition temperature and using a relatively O_2 poor condition during the growth. These growth conditions (low temperature, poor O_2) were intentional to form a high concentration of oxygen vacancy defect which is supposed to enhance the incorporation of atomic nitrogen doping into the SnO_x thin film.

It has been reported that amorphous undoped tin oxide can exhibit a relatively high n-type conductivity due to the presence of high defect concentration related to oxygen vacancies[3, 5]. NH_3 treatments are expected to release nitrogen ions, by breaking N-H bonds, and incorporating these ions within the SnO_x host thin films. N_2O treatments are likely to produce nitrogen, oxygen and NO_y (where y is expected to be mainly 1) ions and to incorporate these ions within the host SnO_x thin films. NO_y is normally known by NO_x but we are denoting it NO_y to differentiate the x of the SnO_x. The oxidation state change is expected due to the potential oxygen stoichiometry increase. N_2 treatments are expected to break N-N bonds and deliver only nitrogen ions to be incorporated within the SnO_x host material.

The optical transmittance spectra in the UV-visible-NIR range of the as-deposited and N_2O and N_2 plasma treated SnO_x films will be plotted at each section. The measured average transmittance in the visible region from 500 to 800 nm and the optical bandgap as deduced from the Tauc plot will also be reported. The electrical properties and optoelectronic performance will also be presented for as-deposited and N_2O and N_2 plasma treated SnO_x films.

4.3.1. As-deposited SnO_x thin film (reference)

As elaborated previously in this chapter, the as-deposited SnO_x thin film (reference SnO_x) is intentionally grown at lower temperature with oxygen poor condition to be amorphous with a high oxygen vacancy concentration to facilitate the incorporation of nitrogen atoms within the SnO_x film. GIXRD of the SnO_x reference sample has not shown any peak confirming the amorphous microstructure character of this film. AFM image for the as-deposited SnO_x film did not show any clear crystalline morphology. However, this film has revealed a highly smooth surface with a sub-nanometre roughness of 0.5 nm using root mean square calculation method.

XPS spectra of the as-deposited SnO_x film shows a high quality SnO_x witnessed by the presence of only Sn and O in the survey spectrum. High resolution spectrum of Sn $3d_{5/2}$ shows that the chemical state is Sn(IV) except a very minor presence of Sn(II). The O 1s has revealed that majority of oxygen are related to SnO_2 lattice oxide and that a small portion are related SnO_x defect oxide. O-Sn(IV) bonds are about 91% of the total O and a small part related to O-Sn defect oxide around 7 %. There is a minor fraction of less than 1% of total O for O-Sn(II).

As-deposited SnO_x film has the average transmittance in the visible region from 500 to 800 nm of about 76.5% and its optical bandgap is 4.15 eV. The reference SnO_x film exhibits a resistivity of 0.25 Ω·cm, mobility of 1.45 cm^2/Vs, and a charge carrier concentration of 1.7×10^{19} cm^{-3}. The reached low mobility and relatively high charge carrier concentration are mainly due to the amorphous structure and oxygen vacancies, respectively.

These results related to as-deposited undoped SnO_x, will be presented as reference in the following sections along with the results of plasma treated SnO_x films.

4.3.2. Ammonia (NH_3) treatment for SnO_x thin films

Following a visual check for NH_3 plasma treated SnO_x films, it was clear that the ammonia treatments has led to a deterioration of the SnO_x thin films by the absence of yellowish mirror like surface of both SnO_x NH_3 treated films. In addition, a chemical alteration at the surface of the NH_3-2 treated SnO_x film has been observed due to the formation of a powdery material. As the NH_3 treated SnO_x samples were completely deteriorated, the following characterization was only conducted to understand the chemistry alterations that took place. Therefore, the material characterization for NH_3 plasma treated SnO_x films were limited to structural properties and chemical state analysis using GIXRD and XPS.

a) Structural Properties by GIXRD

Figure 2 plots the GIXRD patterns for the as-deposited and plasma treated SnO_x films using NH_3 as plasma gas precursor. The as-deposited SnO_x film has clearly an amorphous structure as witnessed by the large band in the range 25-35°. On the other hand, the SnO_x thin film subject to moderate treatment using NH_3 (NH_3-1) did not show any peaks except the typical broad peak related to amorphous quartz substrate around 21°. The intense NH_3-2 treatment for SnO_x has led to a formation of a crystalline metallic Sn as shown by the strong metallic Sn peaks features in the GIXRD pattern. This revealed that this plasma treatment has resulted in a reduction of SnO_x to metallic Sn. Furthermore, the presence of a broad amorphous quartz peak related to the substrate around 21° also confirms the etching to the SnO_x. The NH_3-1 sample does not exhibit even the Sn peaks suggesting a potential powerful etching of the SnO_x film. The presence of an intense SiO_2 broad peak confirm the etching of SnO_x. It is most likely that NH_3 treatment release a high concentration of atomic hydrogen that reacted with oxygen of the SnO_x film to form volatile OH species leaving behind unbonded Sn elements and/or resulting in an etching of the entire film.

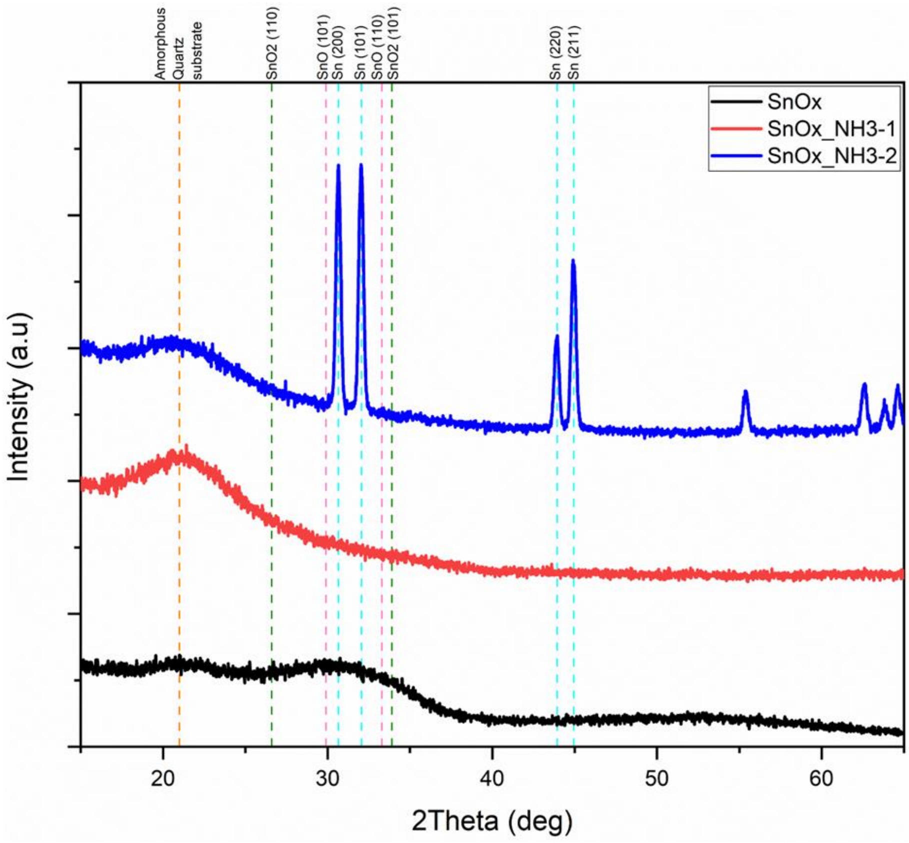

Figure 2: GIXRD patterns for as-deposited and NH3 plasma treated SnOx films.

b) Surface chemical state analysis by XPS

Figure 3 plots the XPS data for as-deposited SnO_x and NH_3 plasma treated SnO_x thin films. The main five nitrogen related chemical states for the treated SnO_x samples are represented by five peaks: (1) N 1s peak at 396.7 eV is related to nitride Sn(II)-N; (2) N 1s peak at 397.5 eV is related to nitride Sn(IV)-N; (3) N 1s related to Si-N chemical state that is expected to be around 398.2 eV. This higher binding energy is due to the higher ionicity of Sn-N compared to Si-N[37]. (4) The peak in the range from 399 to 400 eV is attributed to nitrogen atoms occupying oxygen vacancy site denoted N:SnO_x[22]; (5) N 1s peak around 403 eV is related to NO_y:SnO_x. The chemical states related to N-Sn(IV) and N:SnO_2 are reported to generate acceptor sites and contribute to p-type conductivity while NO_y:SnO_x and Sn(II)-N chemical states are reported to generate donor sites and contribute to n-type conductivity[22, 23, 27-30, 41].

The survey results displayed in Table 2 show the presence of mainly oxygen and silicon as well as a minor presence of N, Sn and C. The observed Si peak positioned at 103.2 and 103.4 eV for NH_3-1 and NH_3-2, respectively, are very close to the characteristic SiO_2 related peak position at 103.5 eV. This reveals that the SnO_x thin films have been substantially etched by NH_3 and the analysed surface is that of the substrate (quartz). Further analysis using high resolution Sn $3d_{5/2}$ spectra for both treatment conditions show the presence of Sn(IV), Sn(II) and metallic Sn related peaks. Therefore, the NH_3

treatments have etched and reduced the SnO_x films, which is in good agreement with XRD analysis. It should be noted that the quartz substrate and metallic Sn were only observed after exposure of SnO_x samples to NH_3 plasma. The NH_3 treatments has also formed some N-Si bonds at the quartz substrate. The summary of chemical state analysis is shown in Table 2.

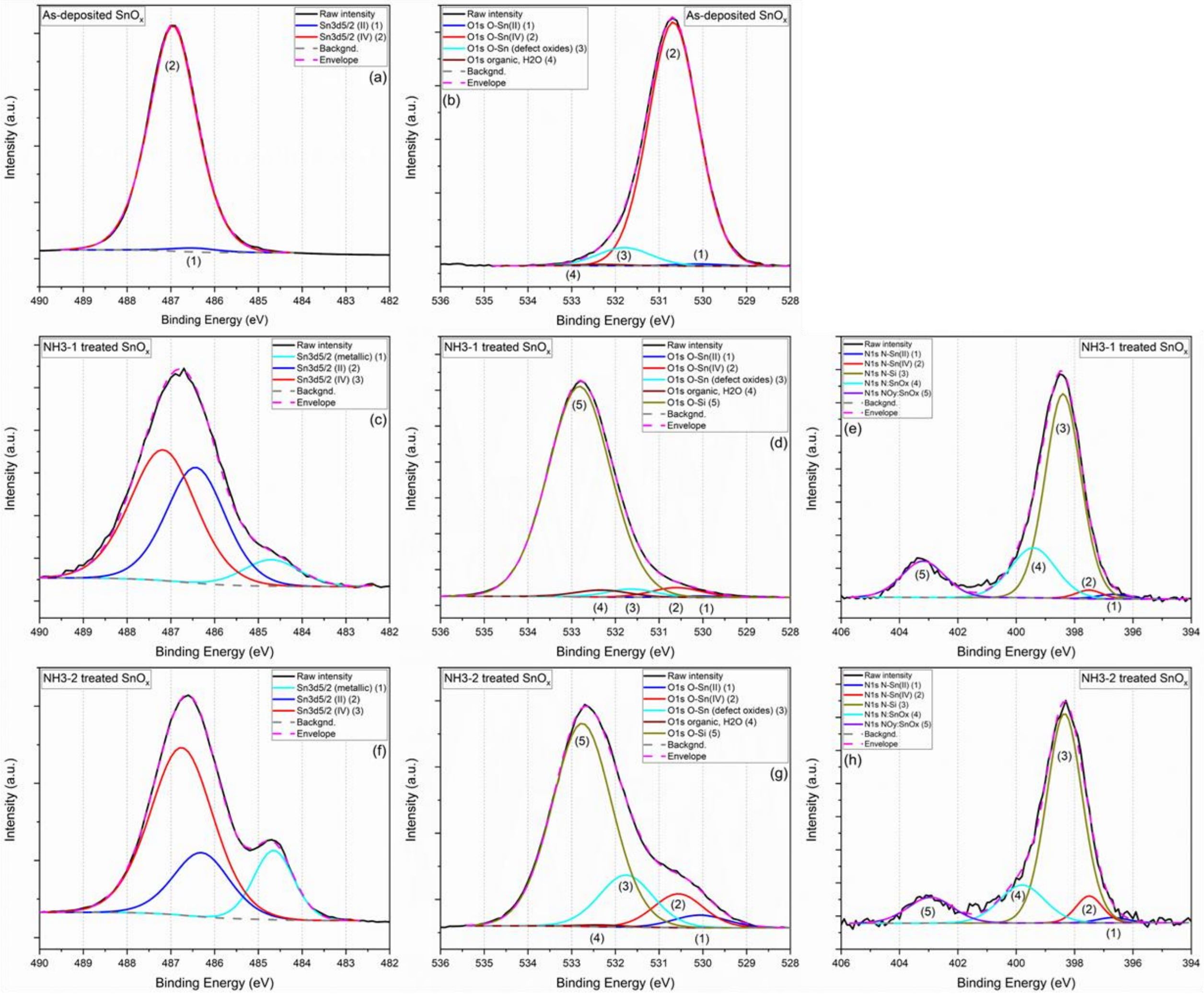

Figure 3: XPS $Sn3d_{5/2}$, O1s, and N1s spectra fitting for as-deposited and NH_3 plasma treated SnO_x films.

Sample	Survey spectra		High resolution spectra deconvolution				Total Atomic (%)
	Element	Atomic (%)	Chemical state	Binding Energy (eV)	Area (CPS.eV)	Area (%)	
SnO_x (as-deposited)	C 1s	0.87	--	--		--	0.9
	N 1s	0	--	--		--	0.0
	Sn 3d5/2	34.04	Sn(II)	486.5	19936	1.7	0.6
			Sn(IV)	487.0	1152286	98.3	33.5

	O 1s	65.09	O-Sn(II)	530.1	2256	0.79	0.5
			O-Sn(IV)	530.7	262011	91.32	59.4
			Defect oxide	531.8	21131	7.37	4.8
			Organic, H_2O	532.4	1505	0.52	0.3
						Total %	100
SnO_x_NH_3-1	Si 2p	31.8	--	--	--	--	31.8
	C 1s	2.31	--	--	--	--	2.3
	N 1s	6.68	N-Sn(II)	396.7	376	1.23	0.1
			N-Sn(IV)	397.5	603	2.1	0.1
			N-Si	398.4	19302	63.86	4.3
			$N:SnO_x$	399.4	5962	19.27	1.3
			$NO_Y:SnO_x$	403.2	4106	13.53	0.9
	Sn 3d5/2	0.97	Sn(0)	484.5	2795	2.87	0.0
			Sn(II)	486.4	11526	20.04	0.2
			Sn(IV)	486.9	44328	77.09	0.7
	O 1s	58.24	O-Sn(II)	530.1	2073	0.44	0.3
			O-Sn(IV)	530.6	15964	3.39	2.0
			Defect oxide	531.6	12926	2.74	1.6
			Organic, H_2O	532.3	12148	2.58	1.5
			SiO_2	532.8	428071	90.85	52.9
						Total %	100
SnO_x_NH_3-2	Si 2p	26.16	--	--	--	--	26.2
	C 1s	8.46	--	--	--	--	8.5
	N 1s	4.53	N-Sn(II)	396.7	215	1.4	0.1

			N-Sn(IV)	397.5	931	6.3	0.3
			N-Si	398.4	9882	66.6	3.0
			N:SnO_x	399.8	2270	15.2	0.7
			NO_y:SnO_x	402.9	1544	10.4	0.5
	Sn 3d5/2	5.44	Sn(0)	484.7	42012	10.2	0.6
			Sn(II)	486.3	54897	40.9	2.2
			Sn(IV)	486.8	161662	49.0	2.7
	O 1s	55.35	O-Sn(II)	530.1	11909	3.9	2.2
			O-Sn(IV)	530.6	29772	9.7	5.4
			Defect oxide	531.8	49353	16.1	8.9
			Organic, H_2O	532.3	1558	0.5	0.3
			SiO_2	532.8	213494	69.8	38.6
						Total %	100

Table 2: XPS survey and chemical states quantification for as-deposited and NH_3 plasma treated SnO_x films.

c) Summary

The ammonia treatment has led to the etching and the reduction of SnO_x films likely due to the formation of -OH related species induced by the presence of hydrogen. Therefore, the (moderate and intense) NH_3 plasma treatment with the used conditions is not suitable to form a nitrogen doped SnO_x.

4.3.3. Nitrous oxide (N_2O) treatment for SnO_x thin films

Exposure to N_2O plasma is expected to produce N, O and NO_x ions to be incorporated within the SnO_x. Consequently, the oxidation state is supposed to change due to the potential oxygen stoichiometry increase.

a) Structural Properties by GIXRD and surface morphology by AFM

SnO_x films after the plasma treatments under N_2O (both moderate N_2O-1 and intense N_2O-2) have revealed that the amorphous microstructure character has been kept after both treatments. This amorphous microstructure is revealed by the absence of any peak in GIXRD pattern as shown by Figure

4. Moreover, the structural properties by GIXRD did not show any sign of SnO_x film etching as the SiO_2 broad and intense peak was not observed.

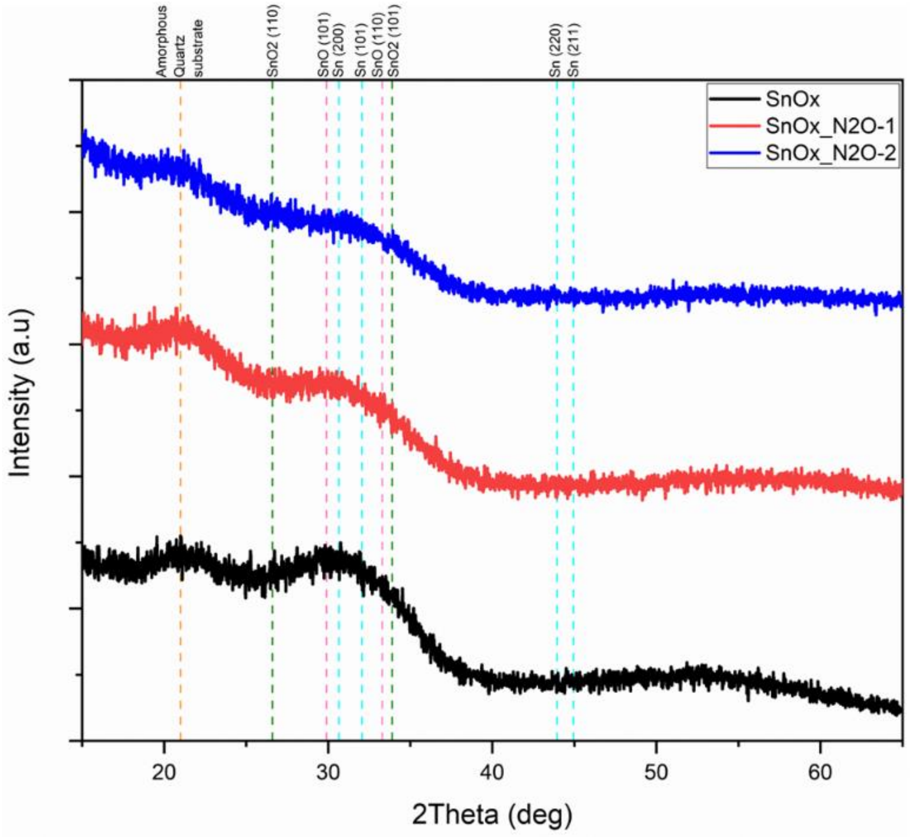

Figure 4: GIXRD patterns for as-deposited and N_2O plasma treated SnO_x films.

AFM analysis has further confirmed the results of the amorphous character related to N_2O plasma treated SnO_x. Indeed, AFM images after N_2O treatment have not revealed any crystalline microstructure formation as shown in Figure 5. The RMS roughness has slightly increased to 0.6 nm as compared to 0.5 nm for the reference SnO_x film.

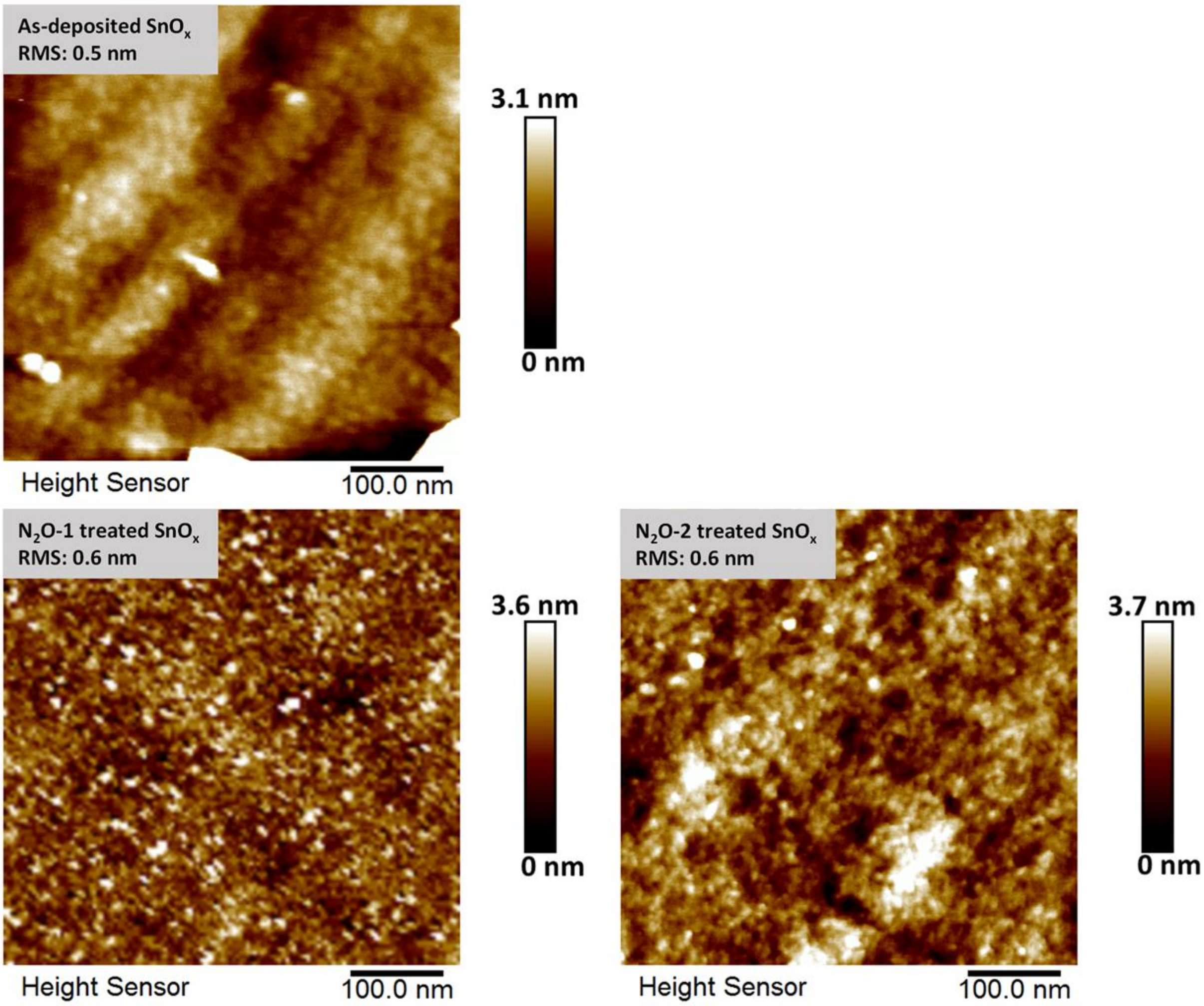

Figure 5: AFM images for as-deposited and N_2O plasma treated SnO_x films.

b) Surface chemical state analysis by XPS

The data analysis from survey spectra of N_2O treat SnO_x films has revealed the presence of essentially O and Sn, with a minor atomic concentration of C and N where the survey atomic concentrations related to the moderate treatment N_2O-1 for O, Sn, C and N are around 63.5, 30.8, 3.5 and 2.3 at.%, respectively. For the intense treatment N_2O-2, the survey atomic concentrations for O, Sn, C and N are around 64, 30.6, 3.6 and 1.8 at.%, respectively. Figure 6 shows the XPS spectra fitting following a chemical state analysis of Sn $3d_{5/2}$, O 1s and N 1s spectra for SnO_x films before and after both N_2O treatments namely, N_2O-1 and N_2O-2.

Sn $3d_{5/2}$ spectra for both N_2O treatment conditions reveal that the chemical state is mainly Sn(IV) with a smaller presence of Sn(II) and the absence of Sn(0). For the moderate treatment N_2O-1, the chemical state analysis shows that the presence of Sn(IV) is 92.4% while the presence of Sn(II) is 7.6%. For the intense treatment N_2O-2, the chemical state analysis shows that the presence of Sn(IV) is 86.5% while the presence of Sn(II) is 13.5%.

As per O 1s spectra, the moderate N_2O-1 treatment has kept the same chemical states within SnO_x which are O-Sn(II), O-Sn(IV), defect oxide, and organic/H_2O and their presence is 5.5%, 85.6%, 6.8%, 4.1%, respectively. Moreover, the moderate N_2O-1 treatment has led to a minor partial chemical state reduction for O-Sn(IV) which is the main chemical state. Conversely, the states of Sn(II) and defect oxide have increased. For N_2O-2 treated SnO_x, there is a similar distribution of same chemical states within SnO_x compared to N_2O-1 treated SnO_x which are O-Sn(II), O-Sn(IV), defect oxide, and organic/H_2O and their presence is 6.5%, 83.2%, 6.3%, 4%, respectively. The intense N_2O-2 treatment has also resulted in a minor partial chemical state reduction for O-Sn(IV). Nevertheless, O-Sn(IV) is remained the main chemical state. On the other hand, the states of Sn(II) and defect oxide have increased slightly more compared to the moderate N_2O-1 treatment.

As per N 1s spectra, the moderate N_2O-1 treatment has produced mainly molecular NO_Y^- (mainly NO^-) incorporation in the SnO_2 host film and N-Sn(IV) chemical state. The presence of the following chemical states N-Sn(II), N-Sn(IV), N:SnO_x, NO_Y:SnO_x is 4%, 45.4%, 12.2%, 38.4%, respectively. For the intense N_2O-2 treatment, the chemical state analysis has revealed similar results where the two main chemical states are molecular NO_Y^- (mainly NO^-) incorporation in the SnO_2 host film and N-Sn(IV) chemical state. However, the presence of molecular NO_Y^- is higher compared to the moderate N_2O-1 treatment. The other chemical states for this treatment are relatively minor. The presence of the following chemical states N-Sn(II), N-Sn(IV), N:SnO_x, NO_Y:SnO_x is 1.6%, 34.4%, 4%, 60%, respectively. All the chemical state analysis results are presented in table 3.

The majority of oxygen (around 84%) is bound to Sn(IV) forming the SnO_2 for both N_2O treatments. However, there is a small fraction of oxygen which is bound to Sn(II) forming the SnO. There is also a minor part of oxygen related to SnO_x defects oxide for both N_2O treatments. The latter include oxygen deficiency defect which are important for n-type electronic conductivity as well as Sn-NO_x defects [3, 5].

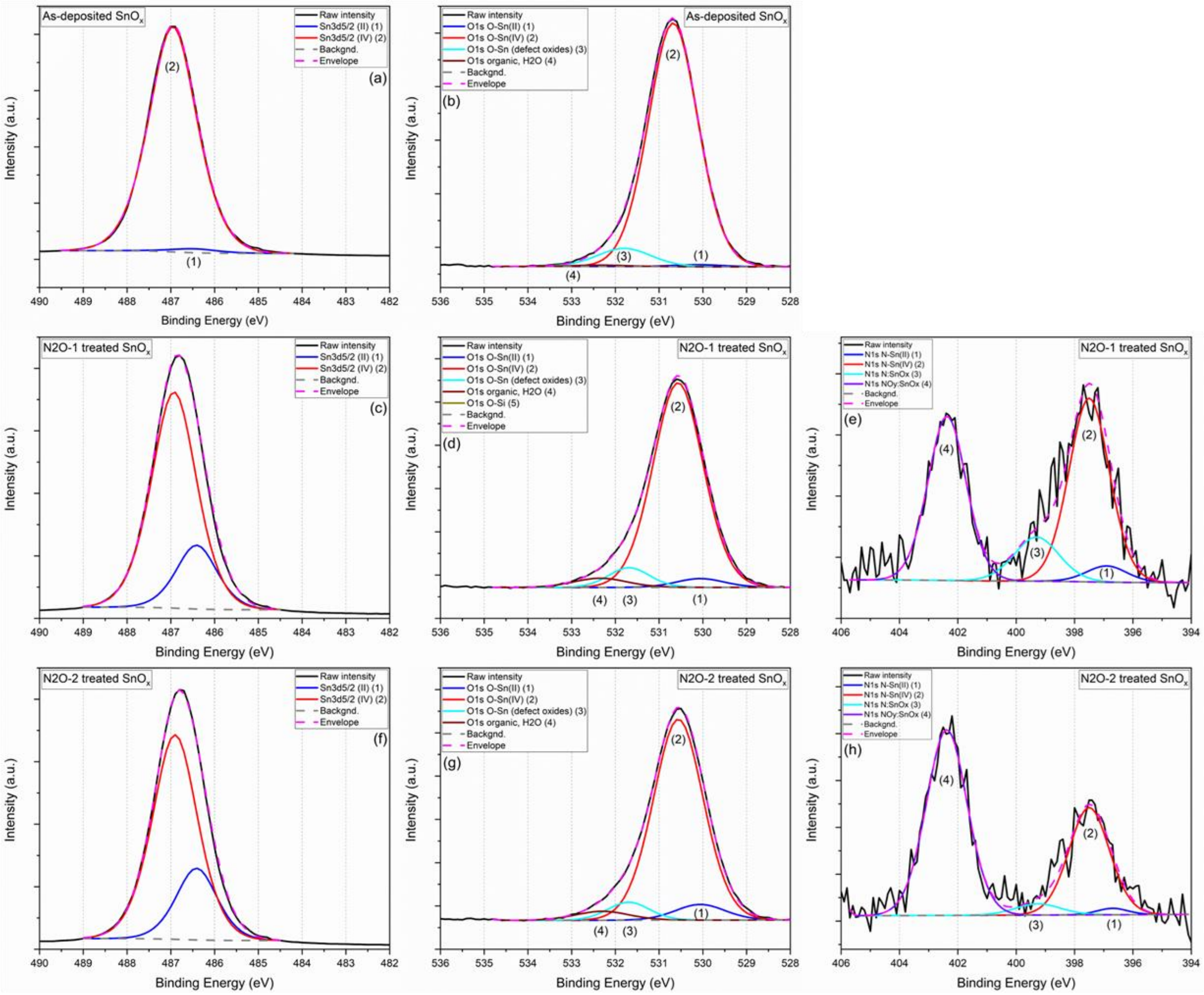

Figure 6: XPS Sn3d$_{5/2}$, O1s, and N1s spectra fitting for as-deposited and N_2O plasma treated SnO$_x$ films.

The summary of all XPS survey and chemical states quantification, shown in Table 3, reveals that N_2O treatments have increased oxygen atomic concentration and favoured the incorporation of nitrogen within the SnO$_x$ thin film at around 2 at. %.

Sample	Survey spectra		High resolution spectra deconvolution				Total Atomic (%)
	Element	Atomic (%)	Chemical state	Binding Energy (eV)	Area (CPS.eV)	Area (%)	
SnO$_x$ (as-deposited)	C 1s	0.87	--	--		--	0.9
	N 1s	0	--	--		--	0.0
	Sn 3d5/2	34.04	Sn(II)	486.5	19936	1.7	0.6
			Sn(IV)	487.0	1152286	98.3	33.5

	O 1s	65.09	O-Sn(II)	530.1	2256	0.79	0.5
			O-Sn(IV)	530.7	262011	91.32	59.4
			Defect oxide	531.8	21131	7.37	4.8
			Organic, H_2O	532.4	1505	0.52	0.3
						Total %	100
SnO_x_N_2O-1	C 1s	3.47	--	--	--	--	3.5
	N 1s	2.32	N-Sn(II)	396.9	235	4.02	0.1
			N-Sn(IV)	397.5	2662	45.45	1.1
			N:SnO_x	399.3	713	12.18	0.3
			NO_y:SnO_x	402.4	2243	38.36	0.9
	Sn3d5/2	30.75	Sn(II)	486.4	90496	7.62	2.3
			Sn(IV)	486.9	1097363	92.38	28.4
	O 1s	63.46	O-Sn(II)	530.1	11404	3.53	2.2
			O-Sn(IV)	530.6	275984	85.55	54.3
			Defect oxide	531.7	21843	6.77	4.3
			Organic, H_2O	532.3	13363	4.14	2.6
						Total %	100
SnO_x_N_2O-2	C 1s	3.62	--	--	--	--	3.6
	N 1s	1.76	N-Sn(II)	396.7	93	1.58	0.0
			N-Sn(IV)	397.5	2028	34.36	0.6
			N:SnO_x	399.3	238	4.03	0.1
			NO_y:SnO_x	402.4	3538	60.03	1.1
	Sn3d5/2	30.6	Sn(II)	486.4	156101	13.51	4.1
			Sn(IV)	486.9	999095	86.49	26.5
	O 1s	64.02	O-Sn(II)	530.1	21171	6.5	4.2
			O-Sn(IV)	530.6	270991	83.23	53.3
			Defect oxide	531.7	20390	6.26	4.0
			Organic, H_2O	532.3	13032	4	2.6
						Total %	100

Table 3: XPS survey and chemical states quantification for as-deposited and N_2O plasma treated SnO_x films.

c) Optical Properties

The N_2O-1 treated SnO_x film exhibits (see Figure 7a) an average optical transmittance of 75.6% which is slightly lower as compared to as-deposited SnO_x of 76.5%. Nevertheless, N_2O-2 treated SnO_x was a subject of a more decrease in average optical transmittance down to 72.6% compared to the as-deposited SnO_x. This lower optical transmittance is suggested to be related to the incorporation of nitrogen within SnO_x which led to the decrease in oxygen as shown in chemical state analysis of N_2O treated SnO_x (table 3).

N_2O treatments for SnO_x has resulted in lowering the optical bandgap as shown in Figure 7b. N_2O-1 treated SnO_x has an optical bandgap of 3.75 eV compared to 4.15 eV for as-deposited SnO_x film. On the other hand, the N_2O-2 treatment of SnO_x has an optical bandgap of 3.92 eV compared to 4.15 eV for as-deposited SnO_x as shown in Table 4. This can be originated from the high disorder within the SnO_x film due to nitrogen enrichment treatment. Furthermore, the high decrease in optical bandgap following N_2O-1 treatment at 100°C compared to N_2O-2 treatment at 300°C is likely due to the lower temperature of the treatment N_2O-1. These results are in agreement with previous reports in the literature which show that the bandgap energy can be affected by the disorder within the SnO_x host film due to the nitrogen incorporation that forms energy levels close to the conduction or valence bands and reduces the bandgap energy[22, 23, 29, 40, 41].

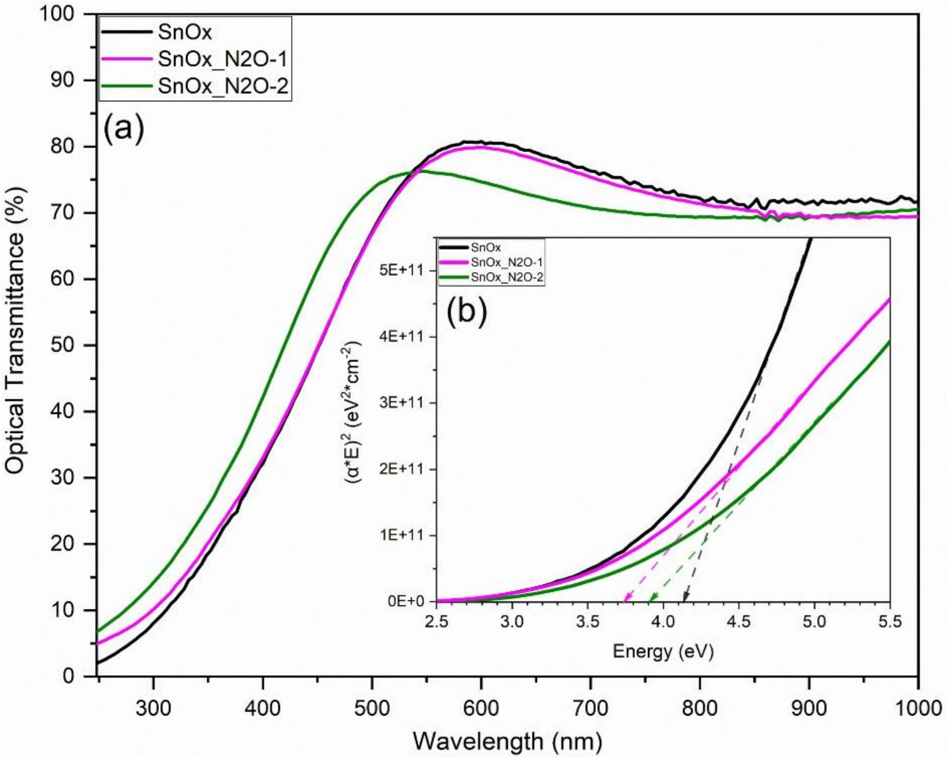

Figure 7: (a) Optical transmittance and (b) Tauc plot for as-deposited and N_2O treated SnO_x films.

Samples	Average optical transmittance (%)	Optical bandgap (eV)
SnO_x as deposited	76.5	4.15
N_2O-1 treated SnO_x	75.6	3.75
N_2O-2 treated SnO_x	72.6	3.92

Table 4: Average optical transmittance from 500 to 800 nm and optical bandgap energy for as-deposited and N_2O treated SnO_x films.

d) Electrical properties

The electrical properties of N_2O treated SnO_x films have been investigated using Hall effect measurements. All the results are summarized in table 5.

Upon the N_2O-1 treatment, the n-type conductivity of the SnO_x thin film has been enhanced. This improvement is related to the contribution of the mobility which has increased 7 times. The charge carrier concentration has slightly decreased compared to as-deposited SnO_x film. The behaviour is likely related to the decrease of oxygen vacancies due to the incorporation of oxygen, nitrogen and NO_y ions. The improved mobility can be attributed to the lower structural disorder due to the treatment temperature and the reduction of oxygen vacancies.

Regarding N_2O-2 treated SnO_x film, the conductivity has been also improved while keeping the conductivity of type-n. This improvement is related to the contribution of the mobility which has increased by 11-fold after the N_2O-2 treatment. The charge carrier concentration is relatively similar for both N_2O treatments and has slightly decreased compared to as-deposited SnO_x film. Similar to the previous N_2O-1, the improved mobility can be attributed to the lower structural disorder due to the treatment temperature and the reduction of oxygen vacancies.

Samples	Thickness (nm)	Resistivity (Ω·cm)	Mobility ($cm^2/V\cdot s$)	Charge carrier (cm^{-3})	Conductivity
SnO_x as deposited	120	2.52×10^{-1}	1.45	1.71×10^{19}	n-type
N_2O-1 treated SnO_x	122	7.52×10^{-2}	9.77	8.49×10^{18}	n-type
N_2O-2 treated SnO_x	119	4.58×10^{-2}	16.07	8.47×10^{18}	n-type

Table 5: Resistivity, mobility, and charge carrier concentration for as-deposited and N_2O treated SnO_x thin films.

e) Optoelectronic Performance

The optoelectronic performance for all SnO_x samples was evaluated using Haacke figure of merit (FoM) which was described in the previous Chapter[42] . The results are shown in Table 6. The N_2O plasma treated SnO_x films have a relatively higher figure of merit compared to the as-deposited undoped SnO_x. This is due to the lower resistivity of N_2O plasma treated SnO_x thin films. The highest FoM was recorded for N_2O-2 plasma treated SnO_x which is 1.06 x 10^{-5} Ω^{-1} for an average transmittance between 500 to 800 nm.

Samples	Figure of merit (10^{-3} Ω^{-1})		
	Average Transmittance 400 – 700 nm	Average Transmittance 500 – 800 nm	Transmittance at 550 nm
As-deposited SnO_x	1.04 x 10^{-03}	3.27 x 10^{-03}	4.28 x 10^{-03}
N_2O-1 plasma treated SnO_x	3.29 x 10^{-03}	9.89 x 10^{-03}	1.32 x 10^{-02}
N_2O-2 plasma treated SnO_x	6.60 x 10^{-03}	1.06 x 10^{-02}	1.70 x 10^{-02}

Table 6: Figure of Merit for as-deposited and N_2O plasma treated SnO_x thin films.

f) Summary

The above study has shown that both N_2O plasma treatments have enabled the incorporation of nitrogen with the SnO_x films while keeping the main chemical states of the host material. Furthermore, the host SnO_x films have kept their amorphous microstructure character and they highly smooth surface morphology. The N_2O plasma treatments have enabled an improvement in electrical properties of the SnO_x films via improving the electron mobility. The decrease in electrical resistivity has significantly improved the optoelectronic performance of N_2O plasma treated SnO_x films. Nevertheless, these treatments were not able to convert the conductivity from n-type to p-type.

4.3.4. Nitrogen (N_2) treatment for SnO_x thin films

N_2 treatments are likely to produce only nitrogen ions which are suggested to be incorporated within the SnO_x. The oxidation state change is expected due to the potential oxygen stoichiometry decrease following the nitrogen incorporation. N_2 plasma treatments were expected to break N-N bonds and deliver only nitrogen ions which are supposed to be incorporated within the SnO_x host material.

a) Structural Properties by GIXRD and surface morphology by AFM

GIXRD pattern for both N_2 plasma treated SnO_x did not show any peak which indicates that N_2 plasma treatments have resulted in conserving the amorphous microstructure of SnO_x host films as shown in Figure 8. Moreover, the structural properties by GIXRD did not show any sign of SnO_x film etching as the SiO_2 broad peak was not observed.

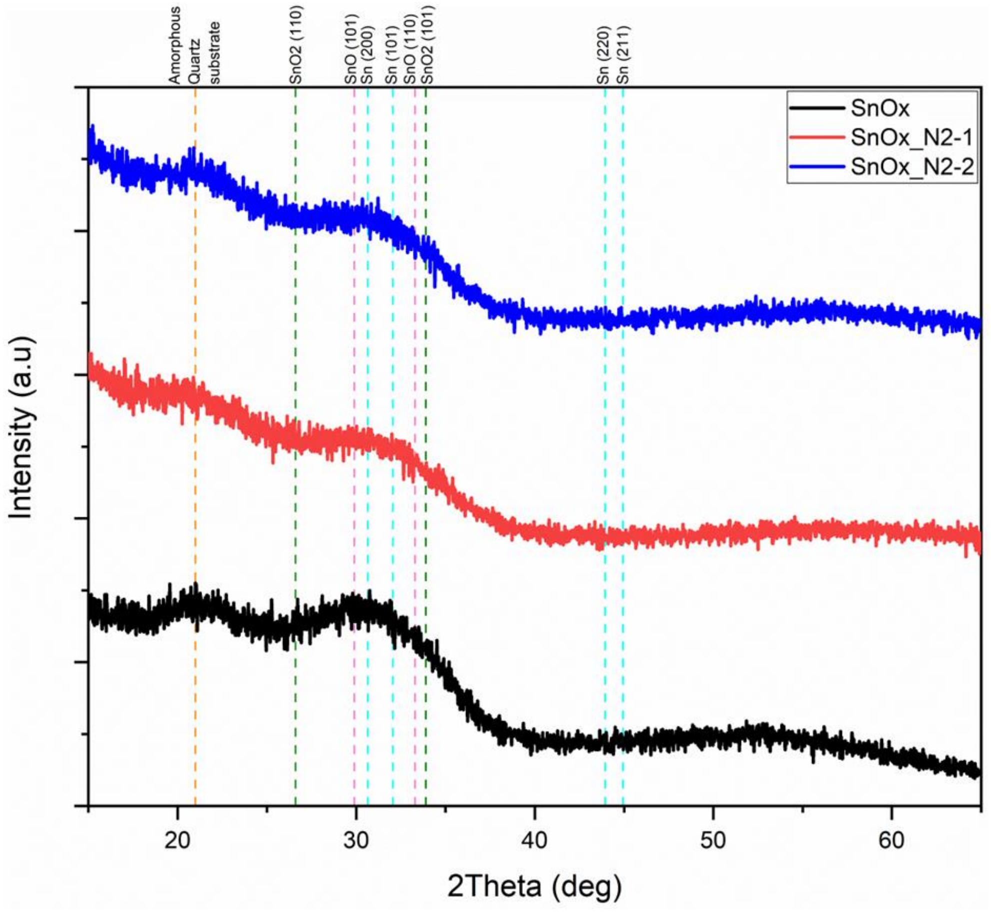

Figure 8: GIXRD patterns for as-deposited and N_2 plasma treated SnO_x films.

AFM analysis has further confirmed the results of the amorphous character related to N_2O plasma treated SnO_x films. Indeed, AFM image after N_2O-1 treatment has shown non-uniform surface morphology without any clear crystalline microstructure. On the other hand, AFM image after N_2O-2 plasma treatment has revealed a particle-like surface morphology without any clear crystalline microstructure formation as shown in Figure 9. The RMS roughness has increased to 1.8 nm after the N_2O-1 plasma treatment as compared to 0.5 nm for the reference SnO_x film, while the RMS roughness has increased to 2.1 nm after the N_2O-2 plasma treatment.

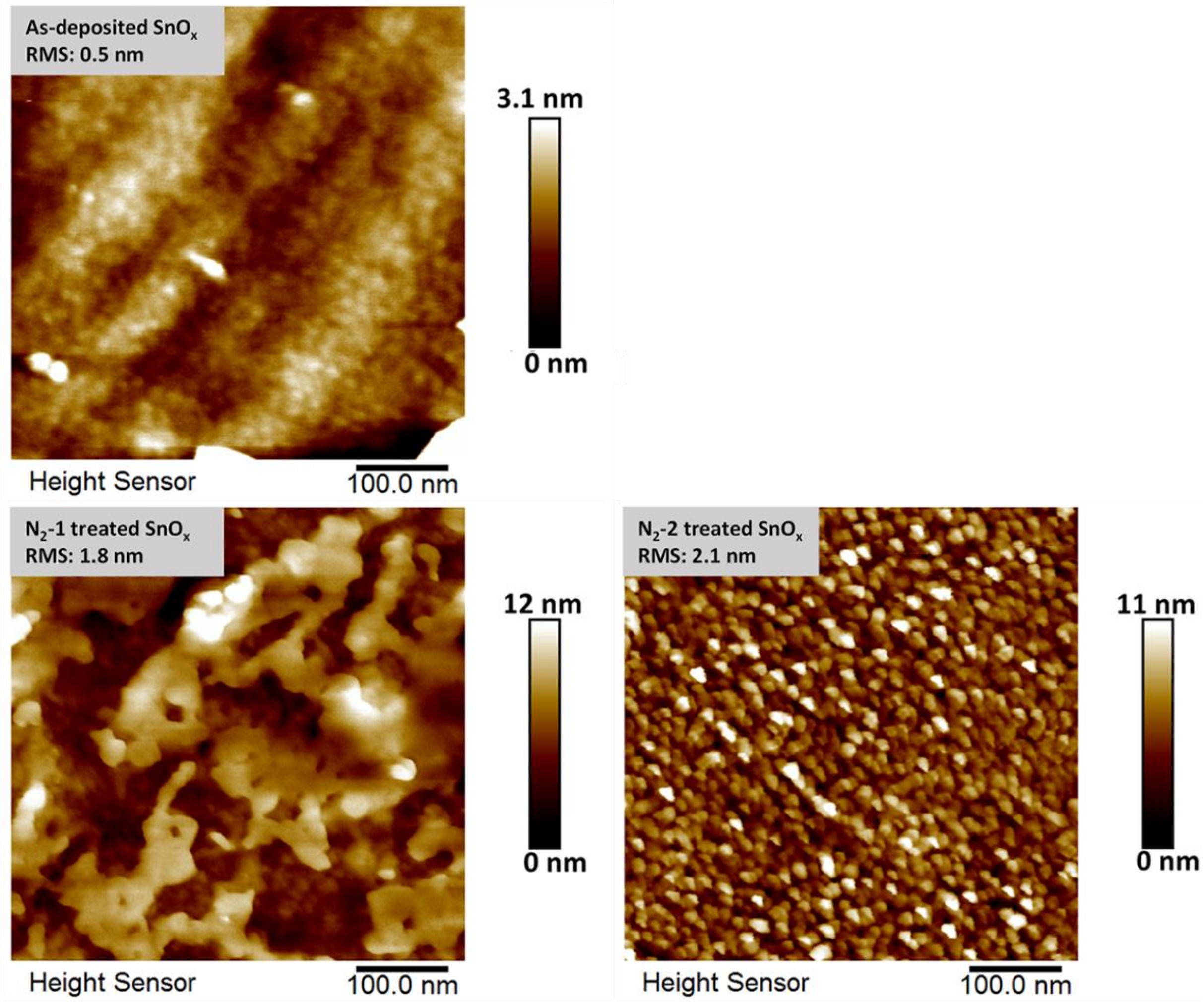

Figure 9: AFM images for as-deposited and N_2 plasma treated SnO_x films.

b) Surface chemical state analysis by XPS

Figure 10 plots the XPS spectra for the N_2 plasma exposed SnO_x films. The presence of O, Sn, N, C and Si is clearly seen. For N_2-1 treatment, Sn $3d_{5/2}$ spectrum has revealed that the main chemical state is Sn(II). However, Sn(IV) was found to be a minor chemical state. Nitrogen incorporation has mainly formed N-Sn(II) as well as N-Sn(IV) bonds. N:SnO_x and NO_y:SnO_x are relatively smaller. As per O 1s spectrum, 62% of oxygen formed bonds with Sn(II) and 28% of oxygen have formed bonds with Sn(IV). Oxygen-related SnO_x defect oxide was found to be 6.5 at. %. For N_2-2 sample, Sn $3d_{5/2}$ spectra reveal that the main chemical state is Sn(IV) with a smaller fraction of Sn(II). Nitrogen incorporation has mainly formed N-Sn(IV) bonds and partially N:SnO_x. N-Sn(II) related bonds are minor and there is a small-to-absent fraction of NO_y:SnO_x. N_2-2 treatment has produced the smallest content of molecular NO_y incorporation and the highest fraction of nitrogen atoms within the SnO_2 and N-Sn(IV) compared to all other treated SnO_x films. These chemical states are expected to potentially form acceptor sites within the SnO_x thin film compared to the other samples. On the other hand, the majority of oxygen (around 76%) is bound to Sn(IV) forming the SnO_2 and only a minor fraction of 2% have formed bonds with Sn(II). There is a relatively small part of oxygen (about 17%) related to SnO_x defect oxide. The small presence of Si is likely to be a surface contamination which will be discussed in the ToF-SIMS section. The chemical state analysis results are summarized in table 7.

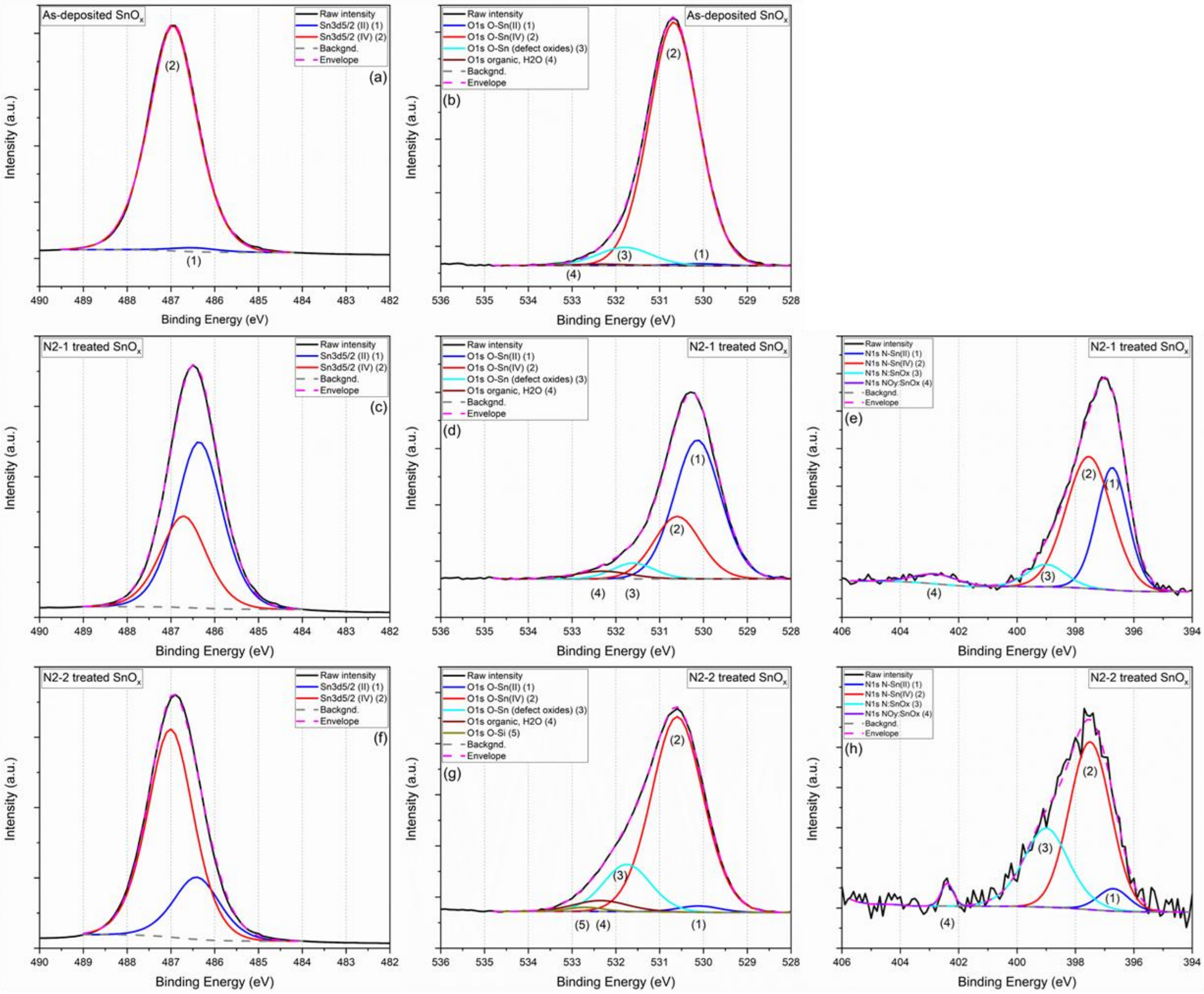

Figure 10: XPS Sn3d$_{5/2}$, O1s, and N1s spectra fitting for as-deposited and N_2 plasma treated SnO_x films.

The summary of all XPS survey and chemical states quantification, shown in Table 7, reveals that N_2-1 has drastically reduced oxygen atomic concentration and substantially increased nitrogen atomic concentration to 10 at. %. On the other hand, N_2-2 treatment has reduced the oxygen atomic concentration and favoured the incorporation of nitrogen with similar atomic concentration compared to N_2O treatments around 2 at. %.

Sample	Survey spectra		High resolution spectra deconvolution				Total Atomic (%)
	Element	Atomic (%)	Chemical state	Binding Energy (eV)	Area (CPS.eV)	Area (%)	
SnO$_x$ (as-deposited)	C 1s	0.87	--	--	--	--	0.9
	N 1s	0	--	--	--	--	0.0
	Sn3d5/2	34.04	Sn(II)	486.5	19936	1.7	0.6
			Sn(IV)	487.0	1152286	98.3	33.5
	O 1s	65.09	O-Sn(II)	530.1	2256	0.79	0.5
			O-Sn(IV)	530.7	262011	91.32	59.4
			Defect oxide	531.8	21131	7.37	4.8
			Organic, H$_2$O	532.4	1505	0.52	0.3
						Total %	100
SnO$_x$_N$_2$-1	Si 2p	1.11	--	--	--	--	1.1
	C 1s	8.08	--	--	--	--	8.1
	N 1s	10.06	N-Sn(II)	396.7	9048	34.83	3.5
			N-Sn(IV)	397.5	13915	53.58	5.4
			N:SnOx	399.0	2012	7.75	0.8
			NO$_y$:SnO$_x$	402.8	995	3.84	0.4
	Sn3d5/2	31.78	Sn(II)	486.4	841168	84.5	26.9
			Sn(IV)	486.9	154227	15.5	4.9
	O 1s	48.97	O-Sn(II)	530.1	133793	61.79	30.3
			O-Sn(IV)	530.6	60207	27.81	13.6
			Defect oxide	531.6	13723	6.34	3.1
			Organic, H$_2$O	532.3	8711	4.03	2.0
			SiO$_2$	532.8	78	0.04	0.0

						Total %	100
SnO_x_N_2-2	Si 2p	5.16	--	--	--	--	5.2
	C 1s	0.62	--	--	--	--	0.6
	N 1s	2.27	N-Sn(II)	396.7	378	6.06	0.1
			N-Sn(IV)	397.5	3722	59.7	1.4
			N:SnOx	399.0	1984	31.83	0.7
			NO_y:SnO_x	402.4	150	2.41	0.1
	Sn 3d5/2	30.87	Sn(II)	486.4	53603	5	1.5
			Sn(IV)	486.9	1019189	95	29.3
	O 1s	61.08	O-Sn(II)	530.1	6087	2.01	1.2
			O-Sn(IV)	530.6	231310	76.26	46.6
			Defect oxide	531.7	46022	15.18	9.3
			Organic, H_2O	532.2	391	0.13	0.1
			SiO_2	532.6	19485	6.43	3.9
						Total %	100

Table 7: XPS survey and chemical states quantification for as-deposited SnO_x and N_2 plasma treated SnO_x films.

c) Optical Properties

The N_2-1 treated SnO_x film reveals an average optical transmittance of 73.8% which is lower compared to as-deposited SnO_x of 76.5%. Nevertheless, N_2-2 treated SnO_x was a subject of a more decrease in average optical transmittance down to 71.8% compared to the as-deposited SnO_x. These results are similar to the ones of N_2O treatments. This lower optical transmittance is suggested to be related to the incorporation of nitrogen within SnO_x which led to the decrease in oxygen stoichiometry as shown in chemical state analysis of N_2 treated SnO_x (table 7).

Both N_2 treatments for SnO_x has led to decrease the optical bandgap as shown in Figure 11. N_2-1 treated SnO_x has an optical bandgap of 3.75 eV compared to 4.15 eV for as-deposited SnO_x film. On the other hand, the N_2O-2 treatment has led to an optical bandgap of 4.12 eV compared to the optical bandgap of as-deposited SnO_x as shown in Table 8. As stated previously, this decrease can be originated from the high disorder within the SnO_x film due to nitrogen enrichment treatment. However, the high decrease in optical bandgap following N_2-1 treatment at 100°C compared to slight decrease in N_2-2 treatment at 300°C is likely due to the lower temperature of the treatment N_2-1 which did not enable the material restructuring and lowering the disorder within the SnO_x host film. These results are also in agreement with previous reports in the literature [22, 23, 29, 40, 41].

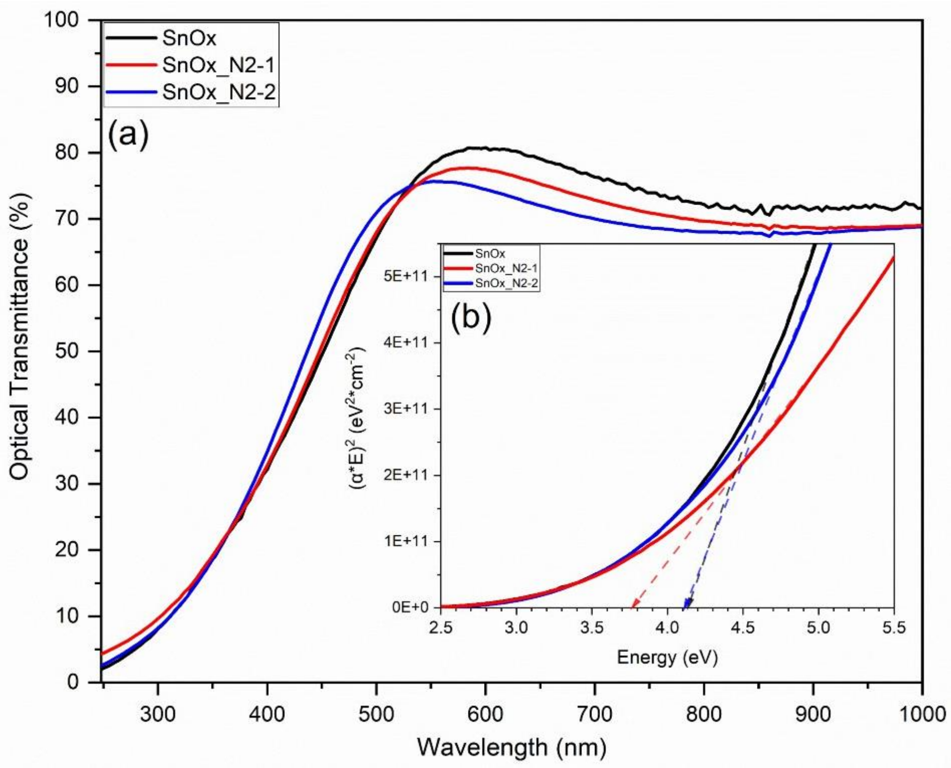

Figure 11: (a) Optical transmittance and (b) Tauc plot for as-deposited and N_2 treated SnO_x films.

Samples	Average optical transmittance (%)	Optical bandgap (eV)
SnO_x as deposited	76.5	4.15
N_2-1 treated SnO_x	73.8	3.86
N_2-2 treated SnO_x	71.8	4.12

Table 8: Average optical transmittance from 500 to 800 nm and optical bandgap energy for as-deposited and N_2 treated SnO_x films.

d) Electrical Properties

As for the N_2 plasma treatment, N_2-1 sample has shown a higher resistivity which might be due to a very high incorporation of nitrogen within the layer. In fact, this treatment has drastically reduced the Sn chemical state from major Sn(IV) to major Sn(II) as revealed by XPS data analysis. This is in agreement with a previous work which reported that N doping for SnO thin films can increase the resistivity[41].

On the other hand, N_2-2 sample has shown a moderate resistivity of 4.73 Ω·cm but more importantly it has a p-type character with a hole carrier concentration of about 6.7×10^{17} cm^{-3} (p-type). These results are presented in table 9. As per the literature, this p-type conductivity is related to nitrogen incorporation within the SnO_x, namely $N:SnO_2$ and N-Sn(IV). These chemical states of nitrogen form acceptor sites[27-29]. The minimal-to-absence of NO_y formation, which acts as a double donor, has enabled the p-type conductivity. The reduced charge carrier concentration is likely due to the donor compensation[43]. This treatment has increased slightly the mobility which can be attributed to the higher treatment temperature at 300 °C compared to the deposition temperature at 100 °C. This p-type conductivity was not permanent and stable over time as the Hall effect measurements have shown a mixture of p-type and n-type after the first measurement. This might be related to the presence of mixed phases as shown previously by surface characterization (XPS) and/or it is related to presence of deep energy level related to nitrogen doping as reported previously[44].

Samples	Thickness (nm)	Resistivity (Ω·cm)	Mobility ($cm^2/V \cdot s$)	Charge carrier (cm^{-3})	Conductivity
SnO_x as deposited	120	2.52×10^{-1}	1.45	1.71×10^{19}	n-type
N_2-1 treated SnO_x	121	N/A*	N/A	N/A	N/A
N_2-2 treated SnO_x	113	4.73	1.96	6.71×10^{17}	p-type

Table 9: Resistivity, mobility, and charge carrier concentration for as-deposited and N_2 plasma treated SnO_x films.

N/A* represents a SnO_x with a very high resistivity.

e) Optoelectronic Performance

The optoelectronic performance for all SnO_x samples was evaluated using Haacke figure of merit (FoM)[42] . The results are shown in Table 10. The FoM of N_2-2 plasma treated SnO_x film could not be determined due to the very high electrical resistivity. The N_2-2 plasma treated SnO_x film has resulted in a lower figure of merit around 10^{-7} Ω^{-1} for an average transmittance between 500 to 800 nm compared to the as-deposited SnO_x. This is due to the higher resistivity of the N_2-2 plasma treated SnO_x film.

Samples	Figure of merit (10^{-3} Ω^{-1})		
	Average Transmittance 400 – 700 nm	Average Transmittance 500 – 800 nm	Transmittance at 550 nm
As-deposited SnO_x	1.04 x 10^{-03}	3.27 x 10^{-03}	4.28 x 10^{-03}
N_2-1 plasma treated SnO_x	N/A	N/A	N/A
N_2-2 plasma treated SnO_x	6.06 x 10^{-05}	9.72 x 10^{-05}	1.56 x 10^{-04}

Table 10: Figure of Merit for as-deposited and N_2O plasma treated SnO_x thin films.

f) Depth Profiling for p-type conductive N doped SnO_x

To get more insight on the incorporation of nitrogen into the SnO_x host matrix, ToF-SIMS analysis were carried out on the N_2-2 sample which revealed a p-type conductivity character. In fact, atomic nitrogen detection can be challenging due to its low sputter yield. On the other hand, Cs_xN molecular ions, which are generated during the depth profile sputtering at high energy Cs ion beam, are reported to have a higher yield which can be used to probe nitrogen in both positive and negative polarity[45, 46]. Among the Cs based ions for this depth profiling, Cs_2N^- ions have revealed a much better sensitivity (sputter yield) and provided a stronger intensity. The depth profiles for several elements in the N_2-2 treated SnO_x are shown in Figure 12. This nitrogen doped SnO_x thin film seems to have a good chemical uniformity throughout the whole layer as shown by the flat intensities of O^- and Sn^-. The presence of silicon as a surface contaminant is found which confirms the XPS data reported above. The presence of carbon is also confirmed to be a surface contamination related the adventitious carbon. More interestingly, the Cs_2N^- distribution is uniform within the N:SnO_x region. This indirectly confirms that nitrogen atoms have been successfully incorporated uniformly in the host SnO_x matrix.

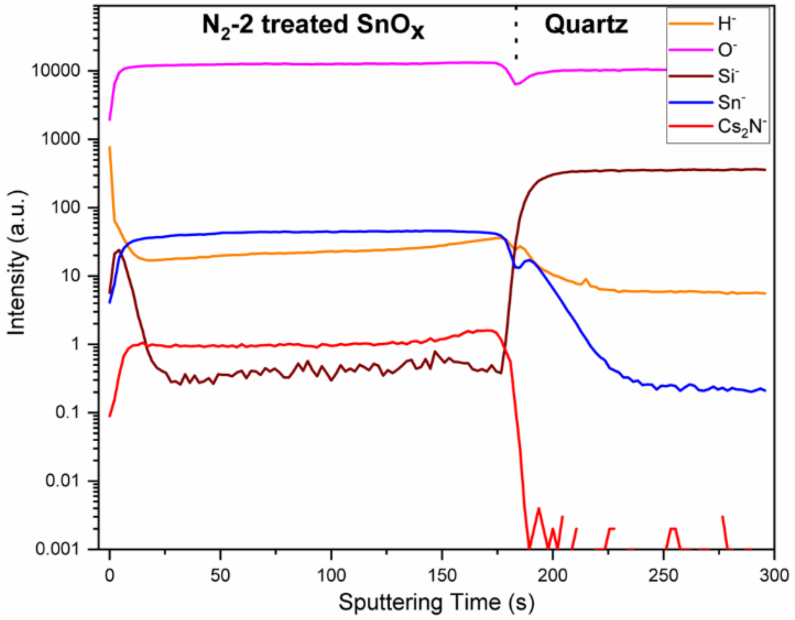

Figure 12: ToF-SIMS depth profiles for N_2-2 treated SnO_x film.

g) Summary

For N_2 plasma treatment, the moderate N_2-1 treatment resulted in a high incorporation of nitrogen as well as a substantial reduction of Sn(IV) to Sn(II). This has led to a large increase in electrical resistivity. The intense N_2-2 treatment instead resulted in a much smaller incorporation of nitrogen within SnO_x host film which has led to a relatively smaller increase in electrical resistivity but with a conductivity change from n-type towards p-type. The increase in electrical resistivity has significantly reduced the optoelectronic performance of N_2 plasma treated SnO_x films compared to as-deposited SnO_x. XPS studies for the case of intense N_2-2 plasma treatment revealed the presence mainly of the SnO_2 phase with a minor presence of the SnO phase, and especially the presence of nitrogen in different chemical states (see Figure 10f, g, h). The effective incorporation of elemental nitrogen into the SnO_x layer was confirmed by ToF-SIMS measurements (Figure 12) which showed that the nitrogen distribution profile is uniform over the entire depth.

4.4. Combined post-annealing and N doping effect

As discussed in our previous studies, both processes of thermal annealing under inert atmosphere namely, Ar and the N incorporation within the SnO_x have led to a potential ability to convert the conductivity of the SnO_x thin film from n-type to p-type. Therefore, the aim of this study is to explore the effect of synergy between two potential processes in order to improve the p-type conductivity of the SnO_x thin films. The applied two step processes are: annealing process which is thermal treatment in Ar atmosphere at 600 °C for 35 minutes and N_2 plasma treatment using ECR-PECVD reactor, which was described previously in this Chapter, whose temperature is 300 °C. For plasma treatment, Microwave power is 500 W, N_2 flow is set at 20 sccm, acceleration voltage at 150 V and treatment time of 30 minutes. The first set of samples were prepared starting by the N_2 plasma treatment and finishing by the annealing (named N-T) while the second set of samples was prepared starting with the annealing and finishing with the N_2 plasma treatment (named T-N).

4.4.1. N_2 intense treatment for SnO_x followed by thermal annealing under Ar (N-T case)

The SnO_x film deposited at O_2/Ar ratio of 0.015 and treated by an intense N_2 plasma, followed by thermal annealing under Ar, has shown a mixture of conductivity type measurements. On the other hand, The SnO_x film deposited at O_2/Ar ratio of of 0.035, 0.055 and 0.065, and treated by an intense N_2 plasma, followed by thermal annealing under Ar, have all shown a p-type conductivity while the one deposited at O_2/Ar of 0.075, has shown a n-type conductivity. There is no clear trend for the N_2 plasma treatment followed by thermal annealing compared to thermal annealing alone. However, the SnO_x deposited at O_2/Ar of 0.055 has shown a p-type conductivity in both sets of samples. The electrical resistivity for all samples had no significant change compared to the SnO_x samples which were thermally annealed only without N_2 plasma treatment.

It is worth noting that SnO_x deposited at O_2/Ar of 0.055 exhibit the highest charge carrier concentration of 9.24 x 10^{17} cm^{-3} compared to the other samples which have concentrations in the range of 10^{16} cm^{-3}. However, its mobility of 0.18 $cm^2/V{\cdot}s$ is low compared to the mobility values of the other samples that range between 1.1 to 3.9 $cm^2/V{\cdot}s$. All the results are presented in Table 11. The step of N_2 plasma treatment prior to the thermal annealing did not significantly improve the p-type conductivity character.

4.4.2. Thermal annealing under Ar for SnO_x followed by N_2 intense treatment (T-N case)

The SnO_x film deposited at O_2/Ar ratio of 0.015 and treated by thermal annealing under Ar, followed by an intense N_2 plasma, has shown a mixture of conductivity type measurements. This result is similar for SnO_x film deposited at O_2/Ar ratio of 0.015 with N_2 plasma treatment prior to the thermal annealing. Furthermore, all the other SnO_x samples have all shown a n-type conductivity. There is a clear trend for the thermal annealing followed by N_2 plasma treatment of converting the p-type conductive SnO_x samples to n-type conductivity as well as of improving the n-type conductivity for n-type SnO_x samples.

The n-type charge carrier concentration has significantly improved after the N_2 plasma treatment compared to the SnO_x samples deposited at O_2/Ar of 0.045, 0.055 and 0.065 followed only by annealing, their charge carrier concentration increased from 2.1 x 10^{16}, 5.5 x 10^{15} and 1.4 x 10^{17} cm^{-3} to 4.1 x 10^{18}, 3.4 x 10^{18} and 3.4 x 10^{18} cm^{-3}, respectively. For the p-type conductive SnO_x samples, the additional step of N_2 plasma treatment has changed the charge carrier concentration from relatively low hole (p-type) carrier concentration to high electron (n-type) carrier concentration in the range of 10^{18} cm^{-3}. This is due to the charge compensation which was discussed previously in this Chapter.

As the annealing is expected to form SnO phase and form hole charge carriers[43, 44, 47-51], the N_2 plasma treatment for the SnO phase is expected to form n-type charge carriers[52]. The electrical resistivity for all samples had a substantial decrease with an n-type conductivity. This is in comparison to the SnO_x samples which were thermally annealed only, without N_2 plasma treatment, and which have mixed conductivity type. All the electrical measurements' results by Hall effect are summarized in table 11.

Charge carrier concentration (cm^{-3})

O_2/Ar ratio	As deposited	Annealed at 600°C only - 35 minutes	Treatment → Annealing	Annealing → Treatment
0.015	-1.34E+15	1.51E+16	N/A**	N/A**
0.035	N/A**	-2.13E+16	4.02E+16	-4.10E+18
0.055	N/A*	8.24E+17	9.24E+17	-4.46E+18
0.065	N/A*	-1.37E+17	1.63E+16	-3.35E+18
0.075	N/A*	1.01E+16	-8.21E+16	-3.46E+18

Resistivity (Ω·cm)

O_2/Ar ratio	As deposited	Annealed at 600°C - 35 minutes	Treatment → Annealing	Annealing → Treatment
0.015	2.00E+02	1.68E+02	1.45E+02**	2.06E+00**
0.035	2.39E+02**	1.91E+02	1.73E+02	3.44E+00
0.055	N/A*	1.66E+02	1.67E+02	3.16E+00
0.065	N/A*	1.31E+02	1.13E+02	3.71E+00
0.075	N/A*	1.86E+02	1.28E+02	4.43E+00

Mobility (cm^2/V·s)

O_2/Ar ratio	As deposited	Annealed at 600°C - 35 minutes	Treatment → Annealing	Annealing → Treatment
0.015	2.38E+01	3.27E+00	1.05E+00**	6.07E-01**
0.035	4.48E+00**	1.67E+00	1.18E+00	4.48E-01
0.055	N/A*	6.90E-02	1.76E-01	4.46E-01
0.065	N/A*	3.53E-01	3.91E+00	5.09E-01
0.075	N/A*	3.40E+00	1.07E+00	4.14E-01

Table 11: Hall effect measurement for as deposited SnO$_x$ followed by thermal annealing then nitrogen plasma treatment and as deposited SnO$_x$ followed by nitrogen plasma treatment then thermal annealing.

* Values with orange background represent n-type conductive samples and blue represent p-type conductive samples. Values with white background represent the samples where the conductivity type could not be determined. The samples with the mark. N/A*: high resistivity SnO$_x$. **: conductivity type could not be determined

4.4.3. Summary

We have demonstrated that carrying out an intense N_2 plasma treatment followed by a thermal annealing under Ar might lead to an improvement of the p-type conductivity. However, reversing the order of these two processes (annealing under Ar followed by intense N_2 plasma treatment) can lead to the opposite effect that the films retain their n-type conductivity or change from p-type to n-type.

4.5. General Summary

P-type N:SnO_x has been achieved using a two-step method using magnetron sputtering for SnO_x deposition and N_2 plasma post treatment for SnO_x related nitrogen doping. To the best of our knowledge, this is the first detailed material characterization, particularly XPS analysis, for nitrogen-doped Sn oxide using three different nitrogen gas precursors (NH_3, N_2O and N_2) with two levels of treatments for each precursor. Unexpectedly, NH_3 treatments have etched and reduced the SnO_x. N_2O treatment has improved the n-type conductivity of SnO_x as well as the optoelectronic performance. N_2 plasma post-treatment has shown a potential ability to switch the conductivity from n-type to p-type. This conductivity conversion from p-type to n-type is associated with a reduction in optoelectronic performance. XPS N 1s spectra analysis for N_2-2 plasma treated SnO_x sample showed that the p-type conductivity was favoured by the atomic doping within the SnO_x as well as the Sn(IV)-N chemical states. The uniformity of the N:SnO_x throughout the depth was confirmed by ToF-SIMS analysis.

In other study to assess the synergy between two processes which provides p-type conductivity, we have demonstrated that performing N_2 plasma treatment followed by thermal annealing under Ar has the potential to improve the p-type conductivity. However, reversing the order of these two processes can lead to the opposite effect where all samples kept their n-type conductivity or have been converted from p-type back to n-type. Therefore, it is suggested that the thermal annealing process followed by N_2 plasma treatment has formed nitrogen doping for tin monoxide (N-doped SnO) which was reported in the first chapter to form donor charges.

Reference:

1. Levy, D. and E. Castellón, *Transparent Conductive Materials*. 2019, Newark: John Wiley & Sons, Incorporated.

2. Fujiwara, H. and S. Fujimoto, *Transparent Conductive Oxide Materials*, in *Spectroscopic Ellipsometry for Photovoltaics: Volume 1: Fundamental Principles and Solar Cell Characterization*, H. Fujiwara and R.W. Collins, Editors. 2018, Springer International Publishing: Cham. p. 523-563.

3. Nathan, A., et al., *Amorphous Oxide Semiconductor TFTs for Displays and Imaging.* Journal of Display Technology, 2014. **10**(11): p. 917-927.

4. Nomura, K., et al., *Room-temperature fabrication of transparent flexible thin-film transistors using amorphous oxide semiconductors.* Nature, 2004. **432**(7016): p. 488-492.

5. Kamiya, T. and H. Hosono, *Material characteristics and applications of transparent amorphous oxide semiconductors.* NPG Asia Materials, 2010. **2**(1): p. 15-22.

6. Hosono, H., *68.3: Invited Paper: Transparent Amorphous Oxide Semiconductors for High Performance TFT.* SID Symposium Digest of Technical Papers, 2007. **38**(1): p. 1830-1833.

7. Park, J.S., et al., *Review of recent developments in amorphous oxide semiconductor thin-film transistor devices.* Thin Solid Films, 2012. **520**(6): p. 1679-1693.

8. Jang, J., et al., *Thin-Film Optical Devices Based on Transparent Conducting Oxides: Physical Mechanisms and Applications.* Crystals, 2019. **9**(4): p. 192.

9. Zhang, T., et al. *Atomic Layer Deposited AlxNiyO as Hole Selective Contact for Silicon Solar Cells*.

10. Nakata, M., C. Zhao, and J. Kanicki, *DC sputtered amorphous In–Sn–Zn–O thin-film transistors: Electrical properties and stability.* Solid-State Electronics, 2016. **116**: p. 22-29.

11. Park, C., et al., *Nd-doped SnO2 and ZnO for application in Cu(InGa)Se2 solar cells.* Science of Advanced Materials, 2017. **9**.

12. Cui, X., et al., *Enhanced Heterojunction Interface Quality To Achieve 9.3% Efficient Cd-Free Cu2ZnSnS4 Solar Cells Using Atomic Layer Deposition ZnSnO Buffer Layer.* Chemistry of Materials, 2018. **30**(21): p. 7860-7871.

13. Zhang, T., et al., *Atomic layer deposited ZnxNi1−xO: A thermally stable hole selective contact for silicon solar cells.* Applied Physics Letters, 2018. **113**(26): p. 262102.

14. Aïssa, B., et al., *Impact of the oxygen content on the optoelectronic properties of the indium-tin-oxide based transparent electrodes for silicon heterojunction solar cells.* AIP Conference Proceedings, 2019. **2147**(1): p. 030001.

15. Rastei, M., et al., *Growth and Characterization of (Tb,Yb) Co-Doping Sprayed ZnO Thin Films.* 2020.

16. Nathan, A., et al., *Transparent Oxide Semiconductors for Advanced Display Applications.* Information Display, 2013. **29**(1): p. 6-11.

17. Lee, S., et al., *Transparent Semiconducting Oxide Technology for Touch Free Interactive Flexible Displays.* Proceedings of the IEEE, 2015. **103**(4): p. 644-664.

18. Barnes, T.M., K. Olson, and C.A. Wolden, *On the formation and stability of p-type conductivity in nitrogen-doped zinc oxide.* Applied Physics Letters, 2005. **86**(11): p. 112112.

19. Mao, Q., Z. Ji, and L. Zhao, *Mobility enhancement of p-type SnO2 by In–Ga co-doping.* physica status solidi (b), 2010. **247**(2): p. 299-302.

20. Wu, Y.J., et al., *Study of p-type AlN-doped SnO2 thin films and its transparent devices.* Applied Surface Science, 2015. **328**: p. 262-268.

21. Ng, Z.-N., et al., *P-Type Characteristic of Nitrogen-Doped ZnO Films.* Journal of Electronic Materials, 2018. **47**(9): p. 5607-5613.

22. Pan, S.S., et al., *Preparation and characterization of nitrogen-incorporated SnO2 films.* Applied Physics A, 2006. **85**(1): p. 21-24.

23. Fang, F., et al., *Electrical and optical properties of nitrogen doped SnO2 thin films deposited on flexible substrates by magnetron sputtering.* Materials Research Bulletin, 2015. **68**: p. 240-244.

24. Ji, Z., et al., *Fabrication and characterization of indium-doped p-type SnO2 thin films.* Journal of Crystal Growth, 2003. **259**(3): p. 282-285.

25. Ni, J., et al., *Electrical, structural, photoluminescence and optical properties of p-type conducting, antimony-doped SnO2 thin films.* Acta Materialia, 2009. **57**(1): p. 278-285.

26. Pan, S.S., et al., *Substitutional nitrogen-doped tin oxide single crystalline submicrorod arrays: Vertical growth, band gap tuning and visible light-driven photocatalysis.* Materials Research Bulletin, 2009. **44**(11): p. 2092-2098.

27. Pan, S.S., et al., *p-type conduction in nitrogen-doped SnO2 films grown by thermal processing of tin nitride films.* Applied Physics A, 2012. **109**(2): p. 267-271.

28. Pan, S.S., et al., *Atomic nitrogen doping and p-type conduction in SnO2.* Applied physics letters, 2009. **95**(22): p. 222112.

29. Kim, Y., et al., *Nitrogen-doped transparent tin oxide thin films deposited by sputtering.* Current Applied Physics; International Conference on Electronic Materials and Nanotechnology for Green Environment, 2011. **11**(4): p. S139-S142.

30. Ding, X., F. Fang, and J. Jiang, *Electrical and optical properties of N-doped SnO2 thin films prepared by magnetron sputtering.* Surface and Coatings Technology; Taiwan Association for Coating and Thin Film Technology (TACT 2011), 2013. **231**: p. 67-70.

31. Jiang, J., et al., *Transport mechanisms in SnO2:N,H thin film grown by chemical vapor deposition.* physica status solidi (b), 2017. **254**(7): p. 1700003.

32. Nguyen, T.T., et al., *Studying the influence of deposition temperature and nitrogen contents on the structural, optical, and electrical properties of N-doped SnO2 films prepared by direct current magnetron sputtering.* Ceramics International, 2019. **45**(7): p. 9147-9156.

33. Bhawna, et al., *Facile Synthesis of N-Doped SnO2 Nanoparticles: A Cocatalyst-Free Promising Photocatalyst for Hydrogen Generation.* ChemistrySelect, 2020. **5**(26): p. 7775-7782.

34. Wang, L.P., et al., *Novel Preparation of N-Doped SnO2 Nanoparticles via Laser-Assisted Pyrolysis: Demonstration of Exceptional Lithium Storage Properties.* Advanced Materials, 2017. **29**(6): p. 1603286.

35. Cao, P., et al., *Optical and electrical properties of p-type ZnO fabricated by NH3 plasma post-treated ZnO thin films.* Applied Surface Science, 2008. **254**(9): p. 2900-2904.

36. Taylor, J.A., G.M. Lancaster, and J.W. Rabalais, *Chemical reactions of N 2+ ion beams with group IV elements and their oxides.* Journal of Electron Spectroscopy and Related Phenomena, 1978. **13**(3): p. 435-444.

37. Inoue, Y., M. Nomiya, and O. Takai, *Physical properties of reactive sputtered tin-nitride thin films.* Vacuum, 1998. **51**(4): p. 673-676.

38. Soto, G., W. de la Cruz, and M.H. Farías, *XPS, AES, and EELS characterization of nitrogen-containing thin films.* Journal of Electron Spectroscopy and Related Phenomena, 2004. **135**(1): p. 27-39.

39. Lützenkirchen-Hecht, D. and R. Frahm, *Structure of reactively sputter deposited tin-nitride thin films: A combined X-ray photoelectron spectroscopy, in situ X-ray reflectivity and X-ray absorption spectroscopy study.* Thin Solid Films, 2005. **493**(1): p. 67-76.

40. Niwa, K., et al., *Crystal structures and electronic properties of Sn3N4 polymorphs synthesized via high-pressure nitridation of tin.* CrystEngComm, 2020. **22**(20): p. 3531-3538.

41. Kim, Y., et al., *Nitrogen doped p-type SnO thin films deposited via sputtering.* Materials science & engineering. B, Solid-state materials for advanced technology, 2012. **177**(16): p. 1470-1475.

42. Haacke, G., *New figure of merit for transparent conductors.* Journal of Applied Physics, 1976. **47**(9): p. 4086-4089.

43. Dang, H.P., et al., *Eliminating the charge compensation effect in Ga-doped SnO2 films by N doping.* Journal of Alloys and Compounds, 2019. **776**: p. 276-286.

44. Scanlon, D.O. and G.W. Watson, *On the possibility of p-type SnO2.* Journal of Materials Chemistry, 2012. **22**(48): p. 25236-25245.

45. Zhu, L., et al., *Time-of-flight secondary ion mass spectroscopic characterization of the nitrogen profile of shallow gate oxynitride thermally grown on a silicon substrate.* Surface and Interface Analysis, 2012. **44**(13): p. 1558-1564.

46. Saha, B. and P. Chakraborty, *MCsn+-SIMS: An Innovative Approach for Direct Compositional Analysis of Materials without Standards.* Energy Procedia; International workshop Energy 2012, 2013. **41**: p. 80-109.

47. Barros, R., et al., *Role of Structure and Composition on the Performances of P-Type Tin Oxide Thin-Film Transistors Processed at Low-Temperatures.* Nanomaterials, 2019. **9**(3): p. 320.

48. Guo, W., et al., *Microstructure, optical, and electrical properties of p-type SnO thin films.* Applied Physics Letters, 2010. **96**(4): p. 042113.

49. Liang, L.Y., et al., *Phase and Optical Characterizations of Annealed SnO Thin Films and Their p-Type TFT Application.* Journal of The Electrochemical Society, 2010. **157**(6): p. H598.

50. Liu, X., et al., *Preparation and characterization of p-type semiconducting tin oxide thin film gas sensors.* Journal of Applied Physics, 2010. **107**(6): p. 064309.

51. Ogo, Y., et al., *p-channel thin-film transistor using p-type oxide semiconductor, SnO.* Applied Physics Letters, 2008. **93**(3): p. 032113.

52. Kim, Y., et al., *Nitrogen doped p-type SnO thin films deposited via sputtering.* Materials Science and Engineering: B, 2012. **177**(16): p. 1470-1475.

General Conclusion

The aim of this thesis was to conduct a detailed study of undoped tin oxide and nitrogen doped tin oxide as a transparent conducting oxide (TCO) using different growth conditions and exploring the material properties thanks to different characterisation techniques, as well as assessing the performance of tin oxide as electron transport layer (ETL) for perovskite solar cells.

The first chapter of this work has focused on discussing the literature review of transparent conducting oxides (TCOs) in general and their respective applications. In particular, the material synthesis and properties, and the applications of In_2O_3 and ZnO thin films as TCOs have been discussed thoroughly in this chapter. The state-of-the-art of tin oxide (SnO_x), in both chemical states SnO_2 and SnO, has been addressed in depth in terms of material synthesis and properties as well as their applications.

The work in the second chapter presented different tin oxide thin films synthesised by magnetron sputtering using different conditions namely, sputtering target material, substrate temperature, O_2/Ar flow rate ratio, and post-deposition thermal annealing. The results related to oxidized tin as a target have shown that the temperature substrate plays a major role in the structural properties of the grown tin oxide thin films. Thus, as-deposited samples grown at 250°C exhibited better crystallinity than the ones deposited at 100°C. On the other hand, the post-thermal annealing at 400°C under vacuum has improved the structural properties by improving the crystallinity. Nevertheless, after the annealing, the tin oxide grown at 250°C have kept a better crystalline structure compared the ones grown at 100°C. Furthermore, annealing under air has improved the crystalline structure for all samples compared to vacuum annealing. Both SnO_x deposited films without adding O_2 but annealed in air have revealed the presence of both phases SnO and SnO_2. Vacuum annealing has substantially improved the electrical properties of tin oxide samples compared to the air annealing. On the other hand, air annealing has provided slightly better optical transmittance compared to vacuum annealing. The best conductive sample was deposited at 250°C, at 0.015 O_2/Ar flow rate ratio and annealing under vacuum while the best crystalline sample with highest crystallite size, was deposited at 250°C without O_2 flow and annealed in air. It is worth noting that the best conductive sample has also the highest optoelectronic performance as assessed by figure of merit (FoM) of $5.14 \times 10^{-5}\ \Omega^{-1}$. As a result of these investigations, the best operational conditions are deposition at 250°C, at O_2/Ar flow rate ratio of 0.015 and annealing under vacuum.

The results related to SnO_x films produced using a metallic tin as a target have shown that the O_2/Ar flow rate ratio plays a major role in the structural properties of the grown films at relatively lower temperature of 100°C. At lower O_2/Ar flow rate ratios, the deposited tin oxide thin films have an amorphous structure. At higher O_2/Ar flow rate ratios, the deposited tin oxide thin films have a crystalline structure. The structural properties have influenced the optoelectronic properties of SnO_x thin films. SnO_x thin films have a lower optical bandgap at lower O_2/Ar flow rate ratios indicating the presence of mainly SnO phase, and the optical bandgap increase at higher O_2:Ar flow rate ratios indicating the presence of SnO_2. Tin oxide thin films deposited at lower O_2/Ar flow rate ratios have a high resistivity, and the resistivity decreases at higher O_2/Ar flow rate ratios. Substrate temperature did not significantly influence the structural properties of SnO_x at a low O_2/Ar flow rate ratio as grazing incident X-ray diffraction shows a typical SnO phase broad peak around 30° for temperatures between room temperature to 300°C. However, there is small minor peak related to SnO_2 for deposition at 400°C. Optical bandgap was lower for all samples indicating the presence of mainly SnO phase which is due to the poor oxygen condition at the growth. The amorphous structure related to SnO phase have resulted in high resistivity for all samples. **As a result of these investigations, the best operational set of conditions which provided the best conductive n-type SnO_x film as well as the best optoelectronic performance, is deposition at 100°C using metallic Sn target, at 0.33 O_2/Ar flow rate ratio without any post-deposition annealing**.

In the previous chapter, the annealing under air has shown a better crystallinity of the SnO_x films grown by reactive magnetron sputtering with SnO target , with potential ability to form SnO phase. It was also observed that the degree of crystallinity is related mainly due to the pressure of the ambient during the annealing. Using different annealing series, p-type conductivity could be achieved. The first series of annealing under Ar ambient have shown that the higher temperature of 600°C has enabled the formation of more p-type conductive samples, annealing at 500°C have enabled less p-type conductive samples while no p-type conductive samples were produced at 400°C. This has confirmed the importance of high temperature during the annealing to achieve p-type conductivity. Moreover, it is also confirmed that the p-type resistivity is related to SnO phase thanks to the transmission electron microscopy diffraction analysis which revealed the presence of SnO and confirmed by the reduction in the bandgap. On the other hand, it is worth noting the SnO_x is very sensitive to air, and it oxidises easily in presence of O_2. The experiments investigating the annealing time under Ar ambient has shown that extending the annealing duration to two hours has conducted to the conversion the conductivity from p to n-type while it provides p-type conductivity for shorter time of annealing. **As a result of these investigations, the best operational set of conditions which provided the best conductive p-type SnO_x film is deposition at 250°C using SnO target, at 0.065 O_2/Ar flow rate ratio with post-deposition annealing under Ar at 600°C for 50 minutes**.

The ageing effect in air was assessed after seven days, and as a result tin oxide thin films have been converted from p-type to n-type conductivity and the resistivity has decreased. This could be explained by the further oxidation of SnO_x from SnO towards SnO_2 and the increasing formation of the intrinsic n-type charge carriers which compensated the p-type charge carriers and increased the n-type carriers reducing consequently the resistivity. On the other hand, the effect of presence of moisture on tin oxide after seven days of the ageing has been assessed using heating process at 150°C in the presence of air. This process did not recover the p-type conductivity and instead it has led to further oxidation of SnO_x film and further decrease in resistivity by forming more n-type charge carriers.

In the third, the performance of SnO_2 material, as electron transport layer (ETL) in perovskite solar cells (PSCs) without mesoporous scaffold structure, was assessed using radio frequency magnetron sputtered SnO_2. Power conversion efficiency (PCE) of PSC using as-deposited SnO_2 thin film applied as ETL, is 15.07% while the use of **annealed SnO_2 thin film increases the PCE up to 17.1%**. It can be concluded that a deposition of SnO_2 ETL and its subsequent air annealing process have enabled a better solar cell performance by improving the optoelectronic properties, particularly the electron mobility.

In the last chapter, the nitrogen doping for SnO_x was studied using three nitrogen gas precursors (NH_3, N_2O and N_2) with two levels of treatments for each precursor. HN_3 treatments have resulted in etching and damaged the SnO_x thin films. N_2O treatments have rather improved the n-type conductivity. One treatment under N_2 plasma has increased the nitrogen atoms' incorporation and enhanced the electrical resistivity of the film while the other **N_2 treatment has moderately increased the electrical resistivity while converting the n-type conductivity to p-type**. Applying thermal treatment to the last N_2 treatment condition has been assessed in this chapter, and it was found that such double processes have a potential to improve the p-type conductivity. However, reversing the order of these two steps lead to the opposite effect where all samples kept their n-type conductivity or have been converted from p-type back to n-type. Therefore, the thermal annealing process followed by N_2 treatment has formed nitrogen doped tin monoxide (N-doped SnO) films.

Perspectives

This thesis work has enabled us to explore SnO_x thin films as transparent conducting oxide which can be employed in different applications, particularly in the optoelectronic field. We have demonstrated the possibility to customise the SnO_x material properties by tuning the growth condition and the post-deposition treatments. Yet, there is a room for further investigation such as, the ageing effect which has shown that can alter seriously the material properties of SnO_x. This is crucial for the grown thin film reliability particularly for the performance of the device where this film will be implemented. Such study is already planned to be conducted in the near future with real world conditions, accelerated conditions using weathering chamber which is available in the laboratory as well as the effect of radiation on SnO_x thin films which can simulate the space conditions. Another study which was not possible to be included in this thesis due to time limitation and infrastructure availability, is to develop potential sensing and actuator applications beyond the present state-of-the-art SnO_x.

SnO_x has shown the ability to achieve p-type conductivity particularly by forming mainly SnO phase thin film. However, there is still a room for improvement regarding the performance and the stability of this p-type conductivity. One rational way to tackle this issue is to stabilise the SnO phase and enhance the p-type conductivity by introducing doping elements which inhibit the further oxidation of SnO to SnO_2. The selection of the doping element and its concentration is another study that can further investigate the possibility to achieve a high performance and stabile SnO thin film.

Appendix

1.1. Literature review of SnOx thin film as Transparent Conducting Oxide

FoM Ref.	Material	Synthesis method	Doping	Eg (eV)	resistivity (Ω.cm)	Sheet resistivity (Ω/□)	T (%)	FoM (10^{-3} Ω^{-1})
1[53]	SnO_2:Sb	Spray Pyrolysis	Yes	3.82	5.8 x 10^{-5}	0.61	88	47.2
2[54]	SnO_2:Ba	Spray Pyrolysis	Yes	3.85	6.95 × 10^{-4}	69 (calculated)	90	5.02
3[55]	SnO_2:Sb	Spray Pyrolysis	Yes	3.77	1.16 x 10^{-3}	141 (calculated)	85	1.39
4[56]	SnO_2:Sb	Spray Pyrolysis	Yes	3.81	7.89 x 10^{-4}	24.9	89	12.5
5[57]	SnO_2:Ta	Spray Pyrolysis	Yes	3.77	4.55 x 10^{-4}	25.1	81	6.15
6[58]	SnO_2	Spin Coating	No	3.92	2.63 x 10^{-3}	63	85	3.3
7[59]	SnO_2:Ti	Sol Gel Spin Coating	Yes	3.83	1.77 x 10^{-3}	42.3	83	3.66
8[60]	SnO_2:F	Spray Pyrolysis	Yes	NA	8 x 10^{-4}	40	89	2
9[61]	SnO_2:F	Sol Gel Dip Coating	Yes	3.91	7 x 10^{-4}	14.5	90	24.3
10[62]	SnO_2:F	Chemical Vapour Deposition / Pulsed Laser Annealed	Yes	NA	NA	8.8	85	23.2
11[63]	SnO_2:Te	Pulsed Laser Deposition	Yes	3.5	0.2	2.22 x 10^{4}	87	0.012
12[64]	SnO_2:La	Spray Pyrolysis	Yes	3.86	NA	2.1	80	20
13[65]	SnO_2:Li	Spray Pyrolysis	Yes	3.89	1.19	2.05	80	0.02
14[66]	SnO_2:F	Atmospheric Pressure Chemical Vapour Deposition	Yes	4.15	8.4 x 10^{-4}	10.5	84	16.7
15[67]	SnO_2:F	Spray Pyrolysis	Yes	NA	4 x 10^{-4}	3.71	87	61.8
16[68]	SnO_2:Ta	Spray Pyrolysis	Yes	4.01	4.36 x 10^{-4}	17.96	85	47.3

17[69]	SnO_2:F	Spray Pyrolysis	Yes	NA	1.14 x 10^{-3} (calculated)	7.48	65	1.93
18[70]	SnO_2:GO	Spray Pyrolysis	Yes	3.69	NA	26	77	2.83
19[71]	SnO_2:Gd	Spray Pyrolysis	Yes	3.63	1.02 x 10^{-3}	27	86	8.2
20[72]	SnO_2	Sputtering	No	3.86	4.45 x 10^{-3}	287 (calculated)	84	0.57
21[73]	SnO_2:Sb	Spray Pyrolysis	Yes	NA	1.22 x 10^{-3}	15.42	71	2.11
22[74]	SnO_2:As	Chemical Vapour Deposition	Yes	3.87	1.5 x 10^{-4}	15	85	13.1
23[75]	SnO_2:Sb	Spray Pyrolysis	Yes	3.88	8 x 10^{-4} (calculated)	40	88	6.9
24[75]	SnO_2:F	Spray Pyrolysis	Yes	4.07	3.8 x 10^{-4} (calculated)	20	93	24.19
Present Work	SnO_2	Sputtering	No	4.4	7.2 x 10^{-2}	4.8 x 10^{4}	87	0.05

Table 1: Summary of the FoM values and SnO_x electrical and optical properties selected from relevant literature [53-75].

1.2. Perovskite Solar Cell and SnO_2 as Electron Transport Layer

a) Solar Cells overview

Nowadays, the world is constantly seeking renewable sources of energy due to the increasing energy demand. Predictions are already projecting that the global energy demand will exceed 30 TW by 2050 as shown in Figure 1 and while this demand is quite immense, a major part of it must be renewable to sustain the energy supply for the long term. As the sun is one of the most sustainable sources of energy, solar cells are playing an essential role in supporting the current and future energy demand. The spectral irradiance and contained power of various solar spectra are shown in Figure 2. There is still a lot of effort to employ more solar cells and solar energy in general at regional, national, and international levels. To tackle this issue, scientists, engineers, experts, and policy makers have to work on different aspects particularly, science and technology, economics, and policies. In terms of science and technology, solar cells need to be more efficient and reliable to compete with other sources of energy. However, the most important factor is to be more cost-effective in order to reach the grid parity.

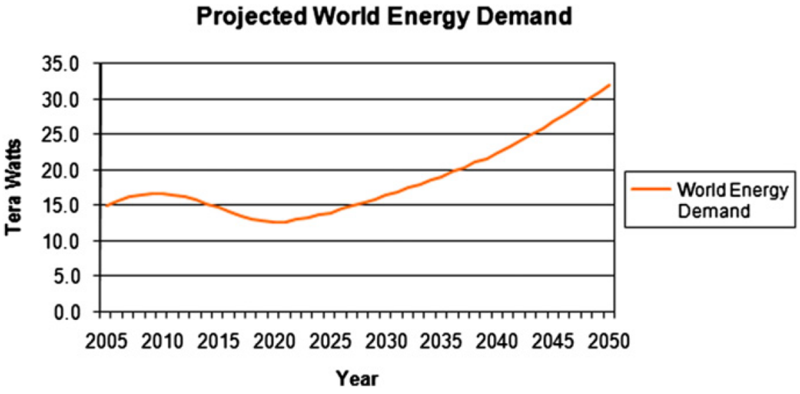

Figure 1: World energy demand projection[24].

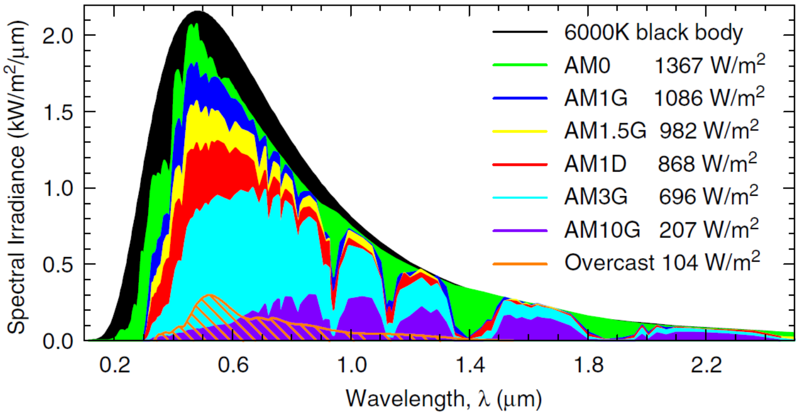

Figure 2: Spectral irradiance and contained power of various solar spectra[25].

b) Introduction to Solar Cells

It is important to highlight the properties of the solar spectral irradiance and its related power as it is the source of an enormous energy provided by the sun. The spectral irradiance has a behaviour of black body at 5800 K and its maximum irradiance is at 500 nm. Air mass (AM) coefficient which defines the length of the optical path across the atmosphere. AM0 is the solar spectrum outside the atmosphere with an average solar irradiance power of 1367 W/m^2 and AM1.5 is related to 1.5 times atmosphere thickness where the solar zenith angle is z = 48.2° with an average solar irradiance power of 982 W/m^2 (nearly 1 kW/m^2). In solar related technologies, AM1.5 is used a standard for solar irradiance on earth for solar cells and panels.

Solar cells, which are also technically known as photovoltaic cells, are solar light harvesting electronic devices based on semiconducting materials where they convert light from solar spectral irradiance into electricity directly and without any intermediate form of energy. The very basic principle of photovoltaic energy conversion, which is the main principle of solar cells, consists of three stages. The first is to absorb a photon which has a sufficient energy hv by a semiconducting material (absorber) to generate a pair of hole/electron. The energy of the photon must be equal or higher than the bandgap of the absorber. The second phase is to separate these charge carriers towards the two different contacts, electrons towards the negative contact and holes towards the positive contact. The third is to extract these charges to an external electrical circuit. This whole process enables the generation of electrical current. The basic structure of the solar cell device is based on a p-n junction diode made of two semiconducting materials one is p-type and the other is n-type. There are many technological-based types of solar cells such as silicon solar cells, thin film solar cells and perovskite solar cells as shown in Figure 3 and their performance (power conversion efficiency) progress is illustrated in NREL chart in Figure 4[24, 26].

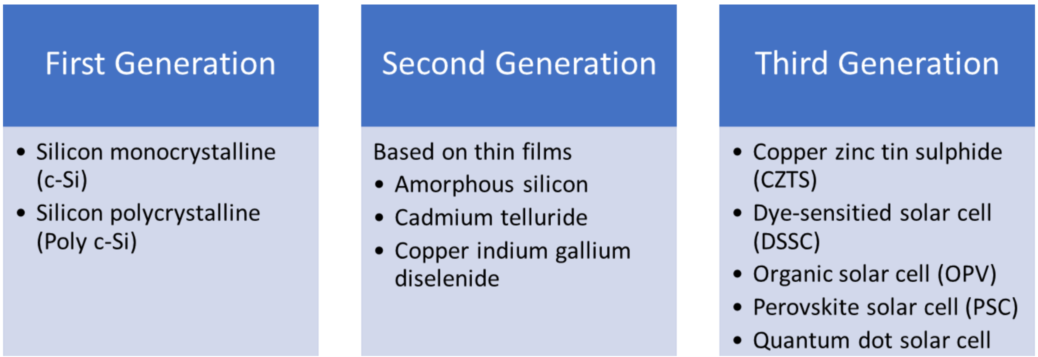

First Generation

- Silicon monocrystalline (c-Si)
- Silicon polycrystalline (Poly c-Si)

Second Generation

Based on thin films

- Amorphous silicon
- Cadmium telluride
- Copper indium gallium diselenide

Third Generation

- Copper zinc tin sulphide (CZTS)
- Dye-sensitied solar cell (DSSC)
- Organic solar cell (OPV)
- Perovskite solar cell (PSC)
- Quantum dot solar cell

Figure 3: Solar cells classification.

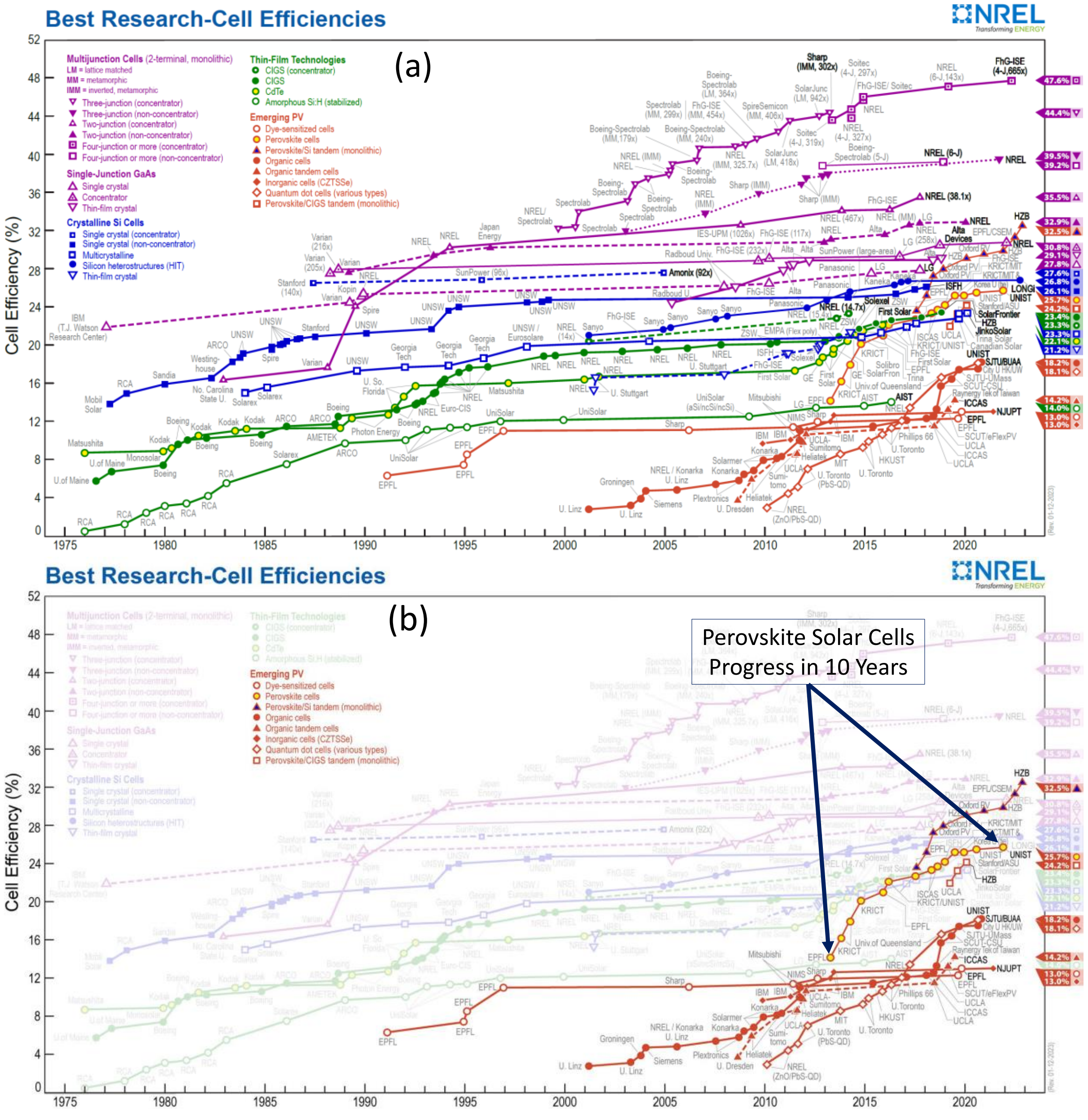

Figure 4: (a) NREL chart for best research-cell efficiencies, (b) NREL chart highlighting Perovskite Solar Cells progress in 10 years[27].

c) Perovskite Solar Cell

There is a remarkable improvement in various technologies of solar cells in the last decades as shown in NREL chart in Figure 4(a). However, the improvement in performance of hybrid organic-inorganic Perovskite Solar Cells (PSCs) is substantial in the last 15 years. The power conversion efficiency (PCE) has improved from 3.8% in 2009 achieved by researchers from The University of Tokyo to PCE of 25.6% in 2021 achieved by researchers from Ulsan National Institute of Science and Technology (UNIST) as shown in NREL chart in Figure 4(b). Organic-inorganic perovskite is very attractive material as an absorber layer due to its appealing physical properties such as high light absorption coefficient, the ability to tolerate high concentration of defect, long carrier diffusion. Perovskite materials have the structure of ABX_3 and the first perovskite material, which was discover a long time back in 1839, was calcium titanium oxide $CaTiO_3$. Organic-inorganic perovskite also follow the same structure of ABX_3 where A can be an organic, inorganic, or mixed cation such as $CH_3NH_3^+$, $CH_3CH_2NH_3^+$, Cs^+. B is a metallic cation namely, Pb^{2+}, Sn^{2+}, Ge^{2+}, and X is related to halogen anion namely, I^-, Br^-, Cl^-, F^-. It is worth noting that the cation A is surrounded by BX_6 octahedra as shown in Figure 5.

There are various types of architecture for perovskite solar cells. However, there are some layers which are essential for all PSC devices. These layers are the perovskite absorber layer, the electron transport layer (ETL), the hole transport layer (HTL), the transparent conducting oxide layer (anode), the metal contact (cathode), and a transparent substrate which is usually glass. There are two basic architectures of perovskite solar cells, the first is called conventional PSC n-i-p structure which is illustrated in Figure 6(a) and the second is called inverted and has p-i-n structure which is in Figure 6(b). The notation n-i-p is referring to ETL(n)-Absorber(i)-HTL(p) which means ETL on the TCO/Substrate first. The notation p-i-n means the HTL on TCO/Substrate first. The mechanism of PSC is that the perovskite absorber layer with a defined bandgap would absorb a photon, of equal or higher energy than the bandgap, and convert it into a pair of electron and hole. The electrons are transported through ETL while the holes are transported through HTL. These charges (holes and electrons) are collected via contacts anode and cathode and utilised by an external circuit. ETL, HTL and perovskite layer must be selected by their bandgaps and the position of highest occupied molecular orbital (HOMO) and lowest unoccupied molecular orbital (LUMO) to assure a proper band alignment to allow the electrons to move spontaneously towards and through the ETL and vise versa for the holes towards and through the HTL as shown in Figure 7, where FTO ($F:SnO_2$) is TCO, TiO_2 is the ETL, Spiro is HTL and Au is the metallic contact [27-32].

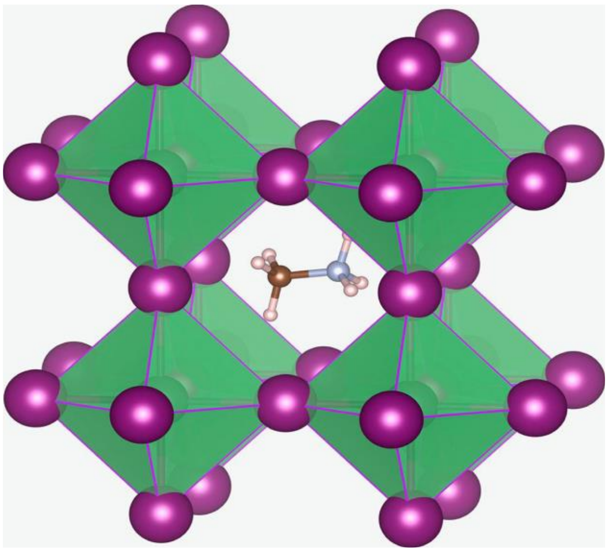

Figure 5: Cubic crystal structure (ABX_3) of perovskite: A is methylammonium (CH3NH3+) surrounded by PbX_6 octahedra [30].

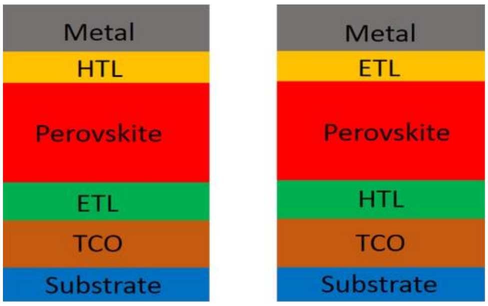

Figure 6: Perovskite solar cell device: (a) conventional architecture, (b) invested architecture[30].

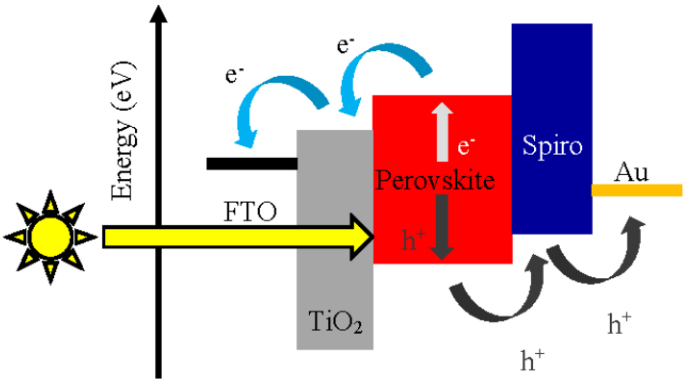

Figure 7: Operating mechanism of perovskite solar cell in a conventional architecture[32].

d) ETL in Perovskite Solar Cell

Electron Transport Layer (ETL) is one of the essential layers in perovskite solar cells. An efficient ETL must be aligned successfully with the perovskite absorber layer as described in the previous section. Therefore, both ETL LUMO and HOMO should be higher than the ones of perovskite layer. ETL layer should be a wide bandgap with high optical transmittance in the UV spectra. The generated excitons through the absorption of light within the perovskite layer have to be dissociated prior the collection by ETL or HTL. This dissociation can take place at the interfaces of the absorber perovskite layer. Several metal oxides have been heavily explored at ETL or as a scaffold material such as, TiO_2, ZnO and SnO_2. Each of these materials have certain advantages to improve the overall performance of PSC. Figure 8 shows that Energy levels, bulk electron mobility (BEM) and the preferable temperature processing (PTP) of electron transport material in perovskite solar cells. Therefore, there are several metal oxides than can be aligned with perovskite in PSC. Among all these metal oxides, the most appealing ones which have a suitable band alignment with perovskite, requires low temperature processing, and can potentially achieve a high mobility are ZnO, SnO_2 and CdSe. It is worth to note that low processing temperature is an important advantage for industrial applications. Although, ETL made of CdSe can achieve a very high mobility which is the highest among all these materials, the presence of Cd is highly undesirable particularly in industrial applications due to its high toxicity. On the other hand, SnO_2 is the most appealing material as ETL as it has a high mobility and can be process even at room temperature[33-35].

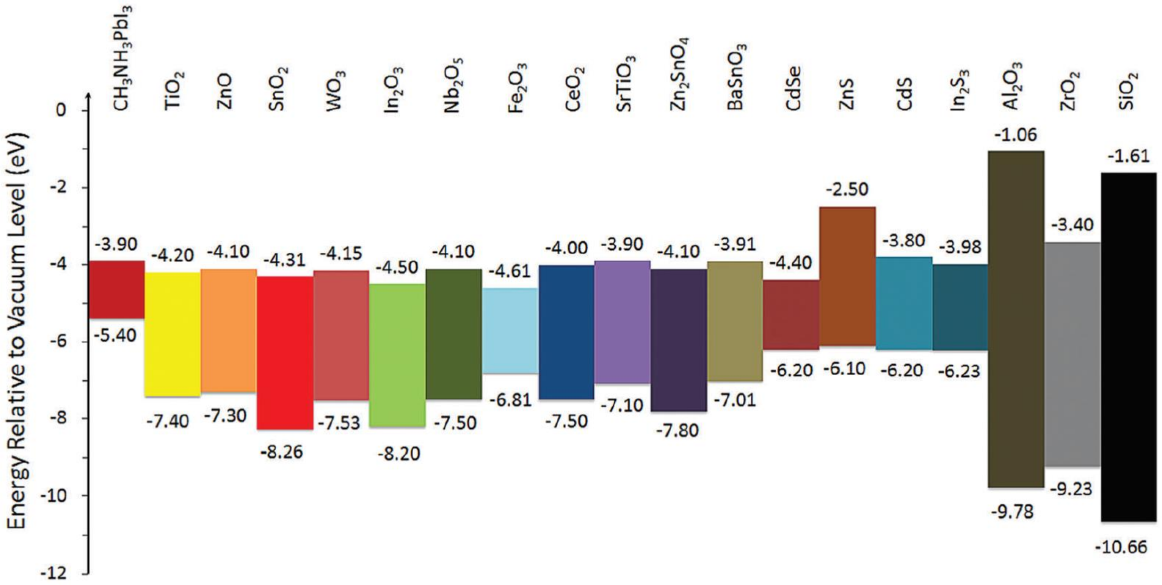

BEM (cm^2/Vs)	-	1	200	250	10-20	20	0.07	0.06	10^{-7}	5-8	10-15	320	450-900	250	440	18	-	-	-
PTP	-	HT	LT	LT	LT	LT	LT	HT	LT	HT	HT	HT	LT	LT	LT	LT	LT	HT	HT

Figure 8: Energy levels, bulk electron mobility (BEM) and the preferable temperature processing (PTP) of electron transport material in perovskite solar cells[35].

The survey of PSC performance in terms of Power Conversion Efficiency (PCE) for atomic layer deposition (ALD) grown layers under perovskite absorber has been summarised in the Table 2. There are many inorganic ETL materials that can fulfil the solar cell structure requirement and provide a high performance in PSC. As also reported previously, this survey shows that SnO_2 processing temperature is relatively lower compared to other materials and the use of it as ETL can enable a very high performance in different device configuration compared to other ETL materials.

Material	Precursors	Temp. (°C)	Application/ Structure	Device Stack	*Jsc* (mA/cm^2)	*Voc* (V)	*FF* (%)	η (%)
SnO_2	TDMASn + O_3	118	ETL/ *n-i-p*	FTO/SnO_2 (15 nm)/$FA_{0.85}MA_{0.15}Pb(I_{0.85}Br_{0.15})_3$/ spiro-OMeTAD/Au	21.3	1.14	74.0	18.4
SnO_2	TDMASn + O_3	100–120	ETL/ *n-i-p*	FTO/*d*-TiO_2/SnO_2/$FA_{0.85}MA_{0.15}Pb(I_{0.85}Br_{0.15})_3$/ PTAA/Au	22.7	1.13	78.0	20.0
SnO_2	TDMASn + O_3	118	ETL/ *n-i-p*	FTO/SnO_2 (15 nm)/ Rb1$(FA_{0.83}MA_{0.17})$99$Pb(I_{0.83}Br_{0.17})_3$/ spiro-OMeTAD/Au	23.0	1.17	71.0	20.0
SnO_2	TDMASn + O_2 Plasma	100	ETL/ *n-i-p*	FTO/SnO_2/100 °C/C_{60}-SAM/$FA_{0.30}MA_{0.70}PbI_3$/ spiro-OMeTAD/Au	22.6	1.13	80.0	20.4
SnO_2	TDMASn + O_2 Plasma	100	ETL/ *n-i-p*	PET/ITO/SnO_2/C_{60}-SAM/$FA_{0.30}MA_{0.70}PbI_3$/ spiro-OMeTAD/Au	22.1	1.10	75.4	18.4
SnO_2	TDMASn + O_2 Plasma	100	ETL/ *n-i-p*	FTO/SnO_2/C_{60}-SAM/$FA_{0.30}MA_{0.70}PbI_3$/ spiro-OMeTAD/Au	21.6	1.13	78.1	19.0
TiO_2	$TiCl_4$ + H_2O	150	ETL/ *n-i-p*	FTO/TiO_2 (17 nm)/*mp*-TiO_2/$MAPbI_3$/ Graphene Oxide/spiro-OMeTAD/Au	20.2	1.04	73.0	15.1
TiO_2	TDMAT + H_2O	120	ETL/ *n-i-p*	FTO/TiO_2 (4 nm)/*mp*-TiO_2/$MAPbI_3$/ spiro-OMeTAD/Au	23.1	1.08	73.4	18.3
TiO_2	TDMAT + H_2O	150	ETL/ *n-i-p*	ITO/TiO_2 (10 nm)/*np*-SnO_2/$PC_{61}BM$/ $FA_{0.30}MA_{0.70}Pb(I_{1-x}Cl_x)_3$/spiro-OMeTAD/Au	23.0	1.08	78.2	19.5
TiO_2	TDMAT + H_2O	225	ETL/ *n-i-p*	FTO/TiO_2 (11 nm)/*mp*-TiO_2/$MAPbI_3$	22.3	1.11	74.0	18.4
TiO_2	TDMAT + H_2O		ETL/ *n-i-p*	FTO/*mp*-Sb:SnO_2/TiO_2 (10 nm)/$MAPbI_3$/PTAA/Au	23.8	1.10	77.0	20.1
TiO_2	TDMAT + H_2O	120	ETL, Passivation/ *n-i-p*	FTO/*np*-TiO_2/TiO_2 (2 nm)/$MAPbI_3$/ spiro-OMeTAD/Au	17.6	0.97	67.0	11.5
TiO_2	TTIP + O_2 Plasma	130	ETL/ *n-i-p*	ITO/CF_4 plasma TiO_2 (20 nm)/$MAPbI_3$/ spiro-OMeTAD/Au	20.3	1.03	75.5	15.8
TiO_2	$Ti(CpMe)(NMe_2)_3$ + H_2O	150	ETL Passivation/ *n-i-p*	ITO/ZnO (80 nm)/TiO_2 (<3 nm)/ $Cs_{0.15}FA_{0.75}MA_{0.10}PbI_{2.9}Br_{0.1}$/ spiro-OMeTAD/$MoO_3$/Au	22.5	1.03	74.0	17.1
TiO_2	TTIP + H_2O	250	Passivation/ *n-i-p*	FTO/*c*-TiO_2/*NR*-TiO_2/TiO_2 (4 nm)/ $MAPbI_3$/spiro-OMeTAD/Au	19.8	0.95	72.0	13.5
TiN	$TiCl_4$ + NH_3	350	ETL Passivation/ *n-i-p*	FTO/*c*-TiO_2/*mp*-TiO_2/TiN (<2 nm)/ $FA_{0.83}MA_{0.17}Pb(I_{0.83}Br_{0.17})_3$/PTAA/Au	22.5	1.14	75.0	19.0
TiO_2-IrO_x	TDMAT + H_2O (EtCp)Ir(CHD) + O_3	175	HTL/ *p-i-n*	ITO/TiO_2-IrO_x(10 nm)/$Cs_{0.17}FA_{0.83}Pb(I_{0.83}Br_{0.17})_3$/ C_{60}/BCP/Ag	19.6	1.01	80.0	15.8
GaN	TEG + Ar/N_2/H_2 plasma	280	ETL/ *n-i-p*	FTO/GaN (5 nm)/$FA_{0.85}MA_{0.15}Pb(I_{0.85}Br_{0.15})_3$/ spiro-OMeTAD/Au	22.6	0.98	68.9	15.2
HfO_2	TEMAHf + H_2O	90	Passivation/ *n-i-p*	PEN/ITO/HfO_2 (<1 nm)/SnO_2/ $Cs_{0.05}(FA_{0.83}MA_{0.17})_{0.95}Pb(I_{0.83}Br_{0.17})_3$ + RbI + KI/spiro-OMeTAD/Au	21.2	1.14	79.2	19.1
Nb_2O_5	(tert-butylimido) bis(diethylamino) niobium + O_3	170	ETL/ *n-i-p*	FTO/Nb_2O_5 (15 nm)/$FA_{0.85}MA_{0.15}Pb(I_{0.85}Br_{0.15})_3$/ spiro-OMeTAD/Au				Very low
NiO	$Ni(MeCp)_2$ + O_2	350	HTL/ *p-i-n*	ITO/s-ALD NiO_x/$FA_{0.2}MA_{0.8}PbI_3$/$PC_{61}BM$/Al	23.0	1.08	81.0	17.1
NiO	$Ni(MeCp)_2$ + O_2 plasma	150	HTL/ *p-i-n*	ITO/NiO (10 nm)/ $Cs_{0.05}(FA_{0.83}MA_{0.17})Pb(I_{0.83}Br_{0.17})_3$/$C_{60}$/BCP/Cu	21.8	1.07	73.4	17.1
NiO, AZO, Al_2O_3	$Ni(dmamb)_2$ + O_3, TMA/DEZ + H_2O	200, 100, 100	ETL/ *p-i-n*	FTO/NiO (6 nm)/$Cs_{0.05}MA_{0.95}PbI_3$/PCBM/ BCP/AZO (40 nm)/Ag/Al_2O_3 (50 nm)	22.5	1.03	80.8	18.8
VO_x	$V(dma)_4$ + H_2O	50	HTL/ *p-i-n*	ITO/VO_x (1 nm)/$MAPbI_3$/$PC_{61}BM$/BCP/Ag	17.9	0.90	71.2	11.5
ZnO/Al_2O_3	DEZ + H_2O	150	ETL/ *n-i-p*	FTO/ZnO (50 nm)/Al_2O_3 (<1 nm)/*mp*-TiO_2/ $MAPbI_3$/spiro-OMeTAD/Au	18.9	1.01	62.0	15.6
ZnS	DEZ + H_2S	150	Passivation/ *n-i-p*	FTO/*c*-TiO_2/*mp*-TiO_2/ZnS (<2 nm)/ $FA_{0.85}MA_{0.15}Pb(I_{0.85}Br_{0.15})_3$/PTAA/Au	22.5	1.13	75.0	18.8

Table 2: PSC performance in terms of Power Conversion Efficiency (PCE) for atomic layer deposition (ALD) grown layers under perovskite absorber[34].

1.3. Material synthesis and characterization

a) Magnetron Sputtering (MS)

Magnetron sputtering technique is one of the most employed Physical Vapour Deposition (PVD) techniques. The vacuum based growth and the high purity material sources assure the high quality of the deposited films. One of the advantages of sputtering is the use of inorganic sources without the need of organic precursors. Thin film sputtering is a mature technology, and it can be used whether at a lab scale or for industrial thin film application. Sputtering has the scalable capability which allows thin films deposition on large areas. In general, the basic principle of sputtering in physics is the bombardment of a solid material surface by high energy plasma or gas which results the ejection of microscopic particles. In magnetron sputtering, the magnetic field, generated by the presence of magnets, is used to restrict the movement of secondary electrons close to surface of the target as shown in Figure 1. The design and strength of the magnetic field can improve the ionisation efficiency and the sputtering deposition rate. Reactive magnetron sputtering refers to the process of magnetron sputtering growth in the presence of reactive gas such as O_2 or N_2.

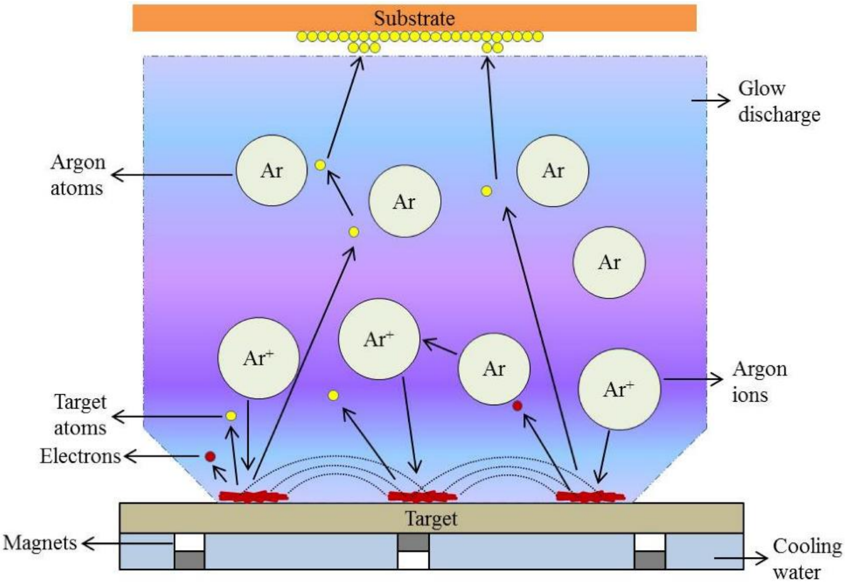

Figure 9: Basic principle of magnetron sputtering. (Maurya, D.K.; Sardarinejad, A.; Alameh, K. Recent Developments in R.F. Magnetron Sputtered Thin Films for pH Sensing Applications—An Overview. Coatings 2014, 4, 756-771 https://doi.org/10.3390/coatings4040756)

i. Equipment 1 - Torr International

The first equipment, which was used for this thesis, is MagSput^{TM} from Toor International. It has four sputtering 2” diameter target sources where two can be used for radiofrequency (RF) magnetron sputtering and two for direct current (DC) magnetron sputtering. It has a 4” diameter view port with a manual shutter to monitor the growth. This system is equipped with Turbo Molecular vacuum pumping supported by primary roughing pumping system to assure high vacuum in the deposition chamber while the growth. The magnetron sputtering is not equipped with an entry chamber (load-lock), so the deposition chamber, which is relatively large, is always vented to the atmosphere. The sputtering target to growth SnO_x using this equipment is the oxidised SnO (2” diameter) target.

Figure 10: Photo of magnetron sputtering made by Torr International.

ii. Equipment 2 - AJA International

The second equipment, which was also used for this thesis, is Orion 5 from AJA International. It has the ability to fit up to (5) 3" or (8) 2" diameter target sources to be used for radiofrequency (RF) magnetron sputtering or for direct current (DC) magnetron sputtering. This system is equipped with Turbo Molecular vacuum pumping supported by primary roughing pumping system to assure high vacuum in the deposition chamber while the growth. The magnetron sputtering is equipped with a high vacuum entry chamber (load-lock), so the deposition chamber, which is relatively smaller compared to the Torr International one, is always kept under high vacuum. The sputtering target to growth SnO_x using this equipment is the metallic Sn (2” diameter) target.

Figure 11: Photo of magnetron sputtering made by AJA International.

b) Electron Cyclotron Resonance - Plasma-Enhanced Chemical Vapor Deposition (ECR-PECVD)

Plasma-Enhanced Chemical Vapor Deposition is a thin film deposition technique through gaseous phase. The gas precursors are injected and decomposed inside the growth chamber where the deposition takes place through chemical reaction in presence of a plasma of reacting gases. Electron Cyclotron Resonance (ECR) system, which is also known as a High Density Plasma (HDP) system, is the capability related to microwave source of 2.45 GHz incorporated within the reaction chamber and provides higher plasma ionization and dissociation.

The equipment used for this thesis is made by Roth & Rau and the model is MycroSys 400 PECVD system, which has the capability to deposit thin films from a few nanometres to a few micrometres for areas up to four inches. The temperature range is from room temperature to 500°C and the possible precursor/process gases are SiH_4, Ar, H_2, N_2O, N_2 and NH_3. In this thesis, this equipment was used only for post deposition treatment where the treatment gases were N_2O, N_2 and NH_3.

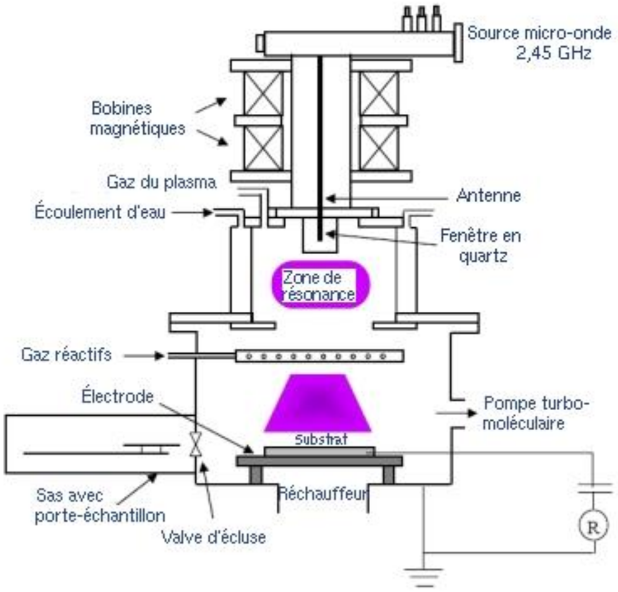

Figure 12: Schematics of Electron Cyclotron Resonance - Plasma-Enhanced Chemical Vapor Deposition

Figure 13: Photo of Electron Cyclotron Resonance - Plasma-Enhanced Chemical Vapor Deposition

c) X-ray Diffraction

X-Ray diffraction (XRD) is widely considered as one of the most important and useful materials characterization techniques. It has the advantage of giving detailed information about material crystalline properties particularly the crystalline structure, lattice constant, dislocation density and lattice strain. There are many techniques/configurations based on XRD such as Theta/2Theta or Theta/Theta Bragg Brentano measurements for bulk materials, four circles configuration which is mainly related to single crystals, and grazing incidence XRD (GIXRD) for surface sensitive measurements mainly for thin films where the incident X-ray beam is kept fixed at a very low angle (mainly below 1°)

and the scan is only by varying the detector angle. One of the other advantages of XRD is the non-destructive aspect of this technique. XRD is mainly consisting of X-ray source, sample manipulator, goniometer (which controls the angles) and detector as shown in Figure 14. The physical principle of XRD is based on Bragg's law which relates the x-rays wavelength, the lattice spacing of the crystal and the diffraction angle; so, at Bragg conditions when x-rays scattered through the crystalline material, they interfere out of certain crystalline planes in a certain direction which is the diffraction angle (angle between the incident x-rays and the scattered ones) as shown in Figure 15. In this thesis, only GIXRD configuration was employed.

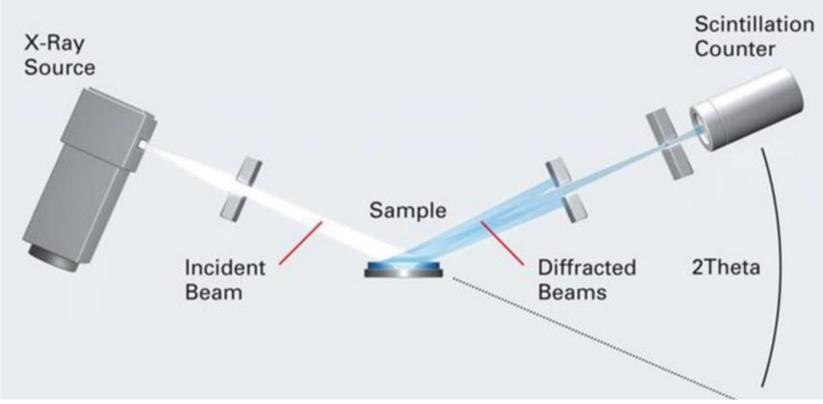

Figure 14: X-ray diffraction schematics (Bruker Corporation).

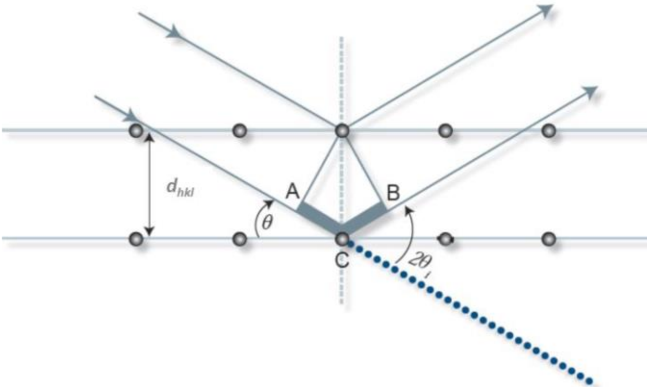

Figure 15: X-ray diffraction principle (Bruker Corporation).

d) Surface Analysis

Surface science is a branch of science that focuses on the physical and chemical phenomena that takes place at the surface of materials and the interfaces between two layers. It is involved in many aspects of our lives namely battery electrodes, airplane engine blade, microchips, hetero-junction solar cells, fuel cells, super-hydrophobic, self-cleaning coatings, etc. However, it is still a debate to how define the "Surface" thickness used in surface science. Generally, a bulk material has all dimensions above 1 µm, Thin film is a material that has a thickness between 10 and 1000 nm, while materials with a thickness above 1000 nm are generally called films. The ultra-thin film is between 1 and 10 nm and the “surface” is few atomic layers thickness which is up to 1nm. Surface analysis and characterization play a major role in surface science and most of them require sophisticated sources, ultra-high vacuum (UHV) and specialized and sensitive spectrometers, which make them very expensive equipment that are available only in central laboratories. There are many surface analysis techniques, few of them are relatively common, such as X-ray Photoelectron Spectroscopy (XPS) or sometimes called Electron Spectroscopy for Chemical Analysis (ESCA), Time of Flight Secondary Ion Mass Spectroscopy (TOF-SIMS), Auger Electron Spectroscopy (AES). All these techniques are involved in the surface science and provide complementary information. The diagram in Figure 16 (from Evans group) shows different characteristic of these techniques such as the detection range, the analytical spot for many techniques including XPS, SEM, AFM and TOF-SIMS.

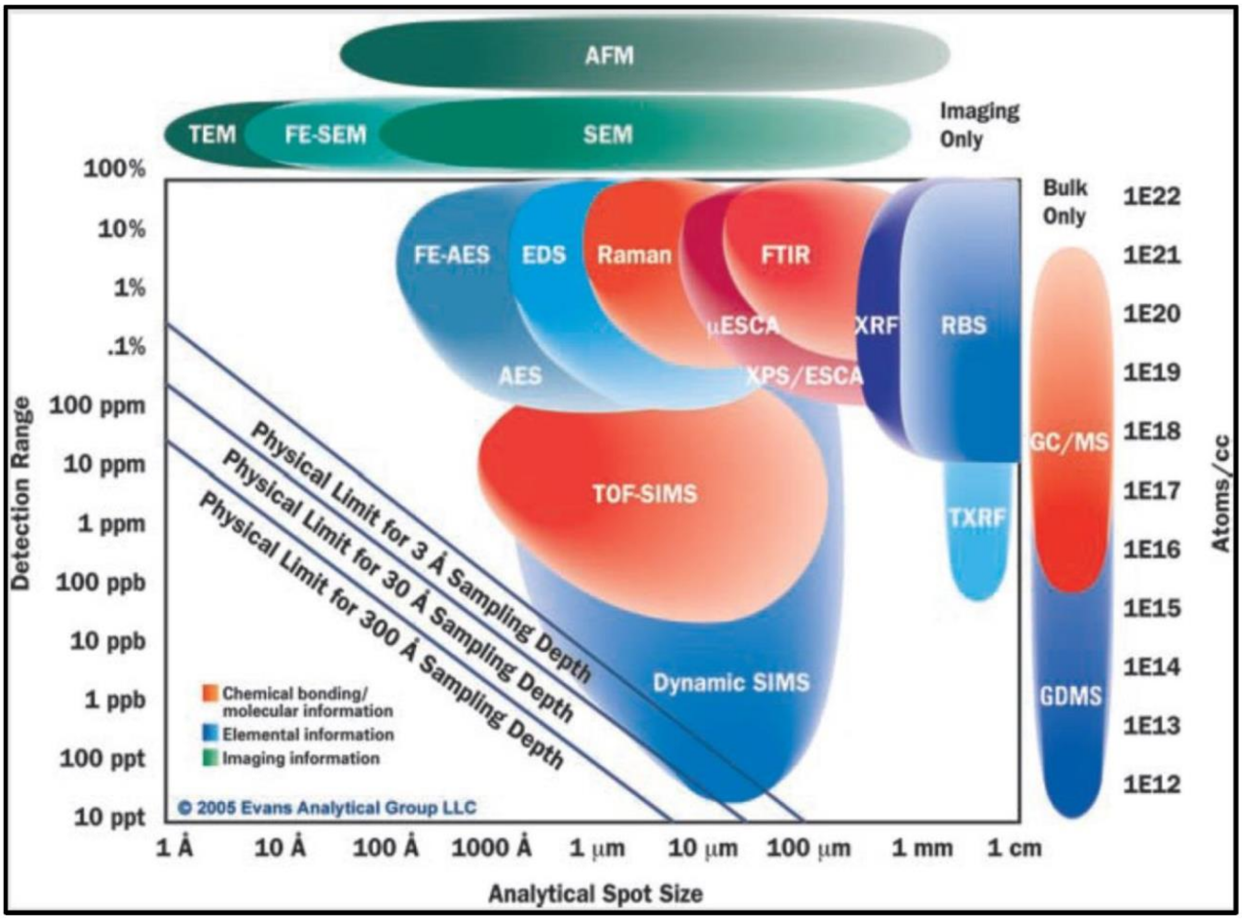

Figure 16: Analytical resolution & detection limit for the most common characterization tools (Evans Analytical Group LLC website).

i. X-ray Photoelectron Spectroscopy

XPS is a non-destructive analysis technique and gives information about the existing elements on the surface as well as their chemical state. It also provides the quantitative analysis and other information about the material surface combined with different sources or techniques such as UV Photoelectron Spectroscopy (UPS). XPS is surface sensitive technique which can detect effectively signals only up to approximately 5 nm depending mostly on photoelectron energy. Depth profiling technique using Argon source for surface etching allows performing XPS measurement through depth, this technique is highly important for characterization of hetero junction thin films and interfaces.

As per Evans diagram in figure 16, XPS detection range for a reliable quantitative analysis is between 0.5 to 100% with an analysis area (spot size) from 3 µm up to hundreds of micrometers in diameter using monochromated x-ray source and up to millimeters using a direct source. The basic principle of XPS relies on the Photoelectric effect as shown in figure 17. The incident x-ray interacts with a core level electron; the energy of the x-ray photon is transferred to the electron. Part of this energy will be used to move the electron from it energy level to the fermi level, in other words to leave the atom, this required energy is known as the binding energy. The second part of the energy is used to carry the electron from the Fermi level to the vacuum level; this energy is required for the electron to leave the material surface which is known as the work function. The rest of the energy will be converted into kinetic energy for the electron as illustrated in figure 18.

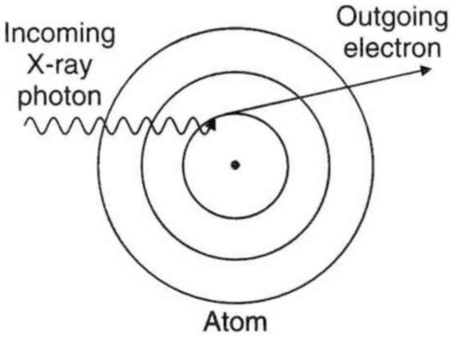

Figure 17: Schematic of photoelectric effect (University of Hang Kong 2011).

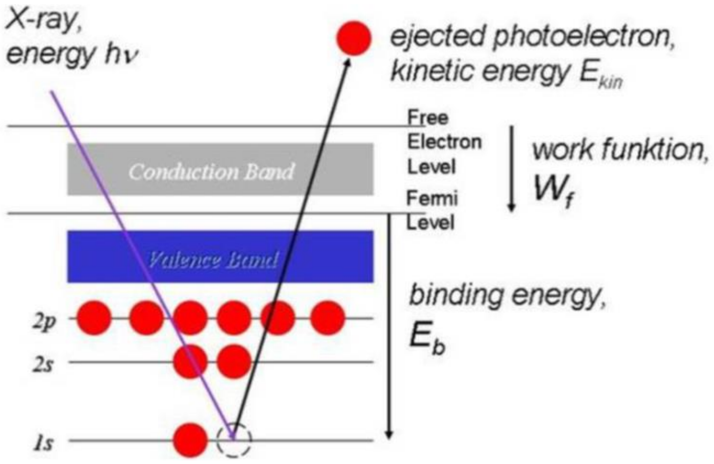

Figure 18: Schematic of electrons energy levels in photoelectric process (Leibniz Institute for Solid State and Materials Research Dresden).

ii. Time of Flight – Secondary Ion Mass Spectroscopy (TOF-SIMS)

The TOF-SIMS provides the mass spectroscopy of the existing elements and compounds (atoms and molecules) on the surface, it has high sensitivity suitable for surface traces analysis. It has the capability of detecting the majority of elements and compounds from ppm to ppb range. It has also a very high mass resolution that can easily give information about the isotopes and its mass range is from 0 to 10000 amu (atomic mass unit) including hydrogen. It is extremely surface sensitive because the analysed ions are released from the first two atomic layers. To probe through the material depth, TOFSIMS is usually combined with a sputtering source to enable the depth profiling capability to investigate elements and compounds concentration as a function of depth. This capability is highly required in semiconductor research and development to track the doping and defects as well as secondary phases at the interfaces. Although the TOFSIMS is highly sensitive, the quantification is quite challenging and requires specialized standard samples.

As per Evans diagram, TOF-SIMS analytical spot size (primary beam sport size) varies from 100 nm to 100 µm and the detection limit which is related to the sensitivity is approximately from 100 ppb to 0.1 %. Its basic principle relies on the bombardment of the material surface by a primary ion beam source of high energy up to 50 keV, these ions collide with the surface of material to generate secondary ions as illustrated in figure 19, the primary ions are energetic enough to generate these secondary ions. However, their energy should not exceed certain level to avoid the fragmentation of large molecules.

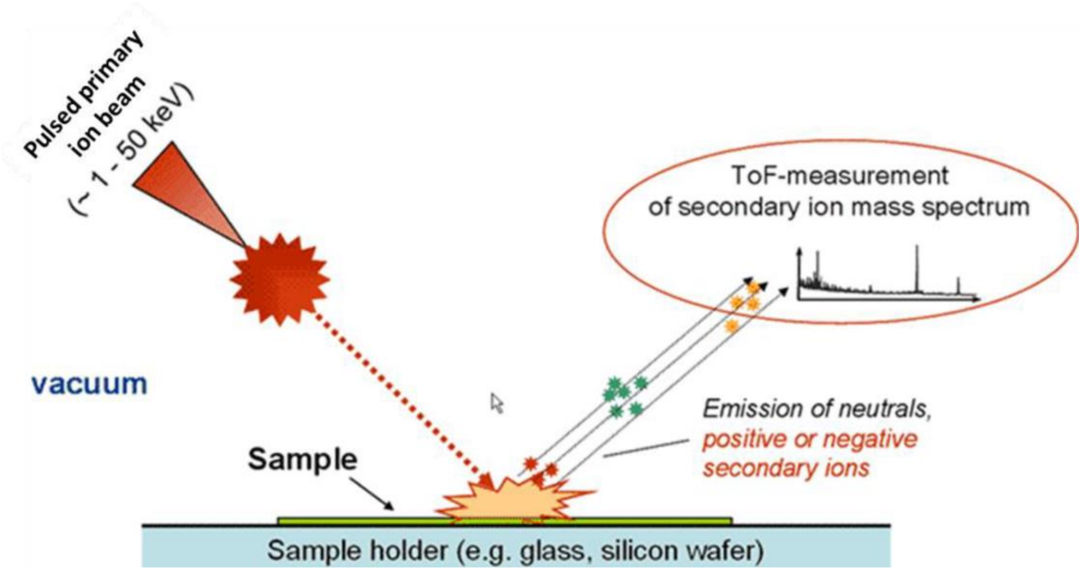

Figure 19: TOF-SIMS basic principle (University of Göttingen).

e) Surface Imaging

i. Scanning Electron Microscopy (SEM)

The SEM technique gives a variety of information about the material surface. It provides mainly imaging and surface topography using a focused electron beam which interacts with the surface and generates a magnified image with resolution in the nanometre range. Other information such as the elemental composition and crystal orientation can be obtained when SEM is combined with certain accessories. The spot size is in the range of a few nanometres (sometimes in sub-nanometre range) which provides a high lateral resolution.

As per duality wave-particle concept, the particles such as electrons can be described as waves and particles. Thus, electrons behave as waves just like photons (light), however, their associated wavelength is extremely small (approximately 100,000 time shorter than light) as shown in Figure 20. This very short wavelength of high energy electrons makes them a very good source of “illumination” to “see” very small features.

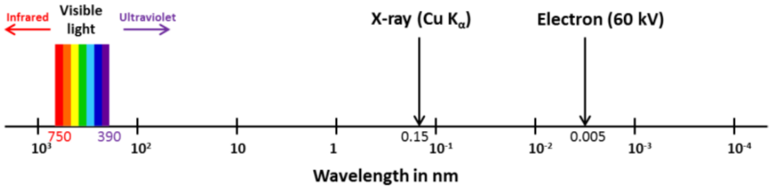

Figure 20: Comparison between the wavelength of a 60 kV electron and visible light.

The electron beam is produced at the electron gun and then through the column it is focused and directed toward the sample surface. The electromagnetic lenses and the electronics control the beam focus and raster to scan the selected area as shown in the schematics in Figure 21.

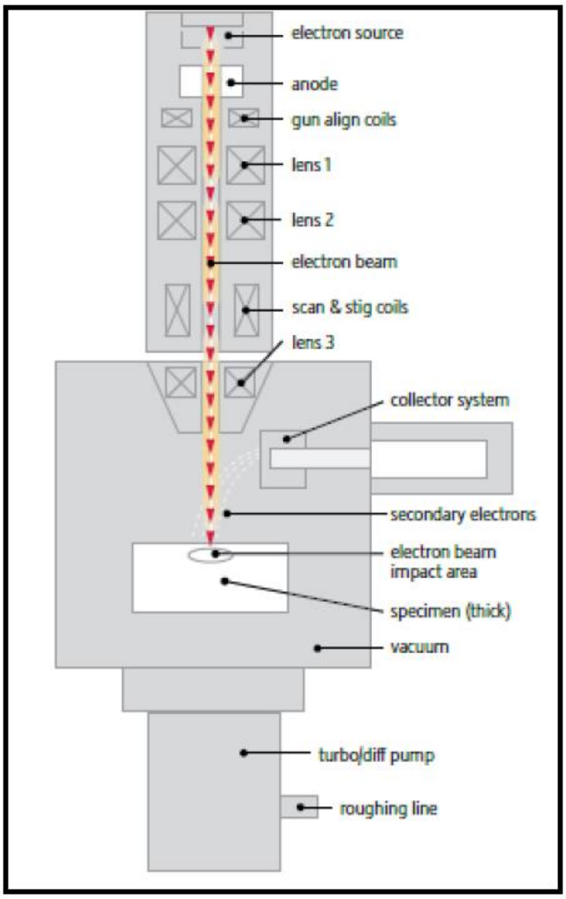

Figure 21: Basic components of Scanning Electron Microscope (FEI part of Thermo Fisher Scientific).

The electrons will interact differently with the surface due mainly to chemical composition and morphology. The electron beam interactions with the surface will produce emissions as shown in Figure 22. Measuring these emissions, namely, secondary electrons provide the imaging capability.

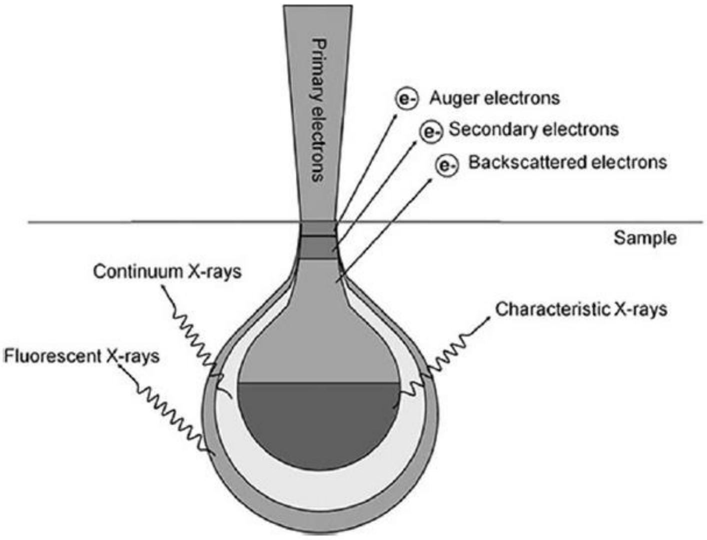

Figure 22: Scanning electron microscopy interaction zones and related emissions (Nanotechnologies for the Life Sciences 2007).

ii. Atomic Force Microscopy (AFM)

AFM is one of the most multipurpose imaging microscopes at the nanometer scale, it has three main capabilities which are imaging, measuring, and manipulating.

Firstly, imaging is used to provide three-dimensional images to give idea about the surface morphology. Also the scanning probes collect different localized measured information such as electrical properties, mechanical properties within a small area of the sample surface. Finally, AFM has some manipulation applications such as nanolithography using anodic oxidation by a special tip, this technique can provide a small oxide layers for nanofabrication with high precision.

AFM has very high resolution and can provide imaging with atomic lateral resolution and sub-nanometer height resolution. AFM probe consists of an extremely sharp tip (less than 10 nm tip radius) on the edge of the cantilever as shown in Figure 23.

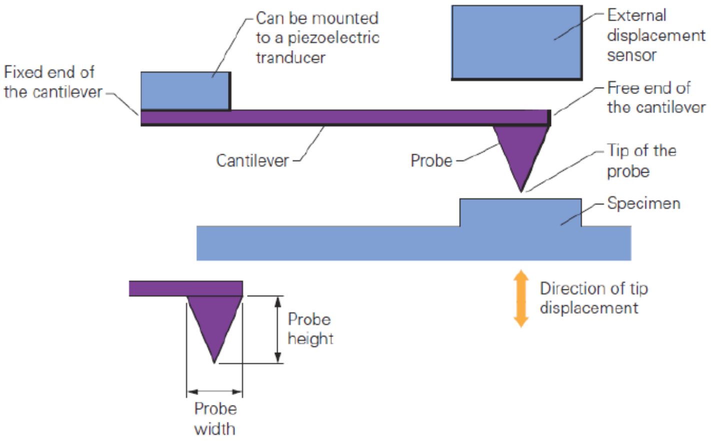

Figure 23: AFM cantilever and tip schematic (Bruker Corporation).

AFM basic principle relies on approaching the tip to the sample surface and the interactions with the surface are quantified by sensing the small deflection of the cantilever using a laser source and detector as shown in the Figure 24. In the scanning operation, when the probe is deflected, the laser light spot is deviated from the photo-detector center to a (x,y) position. This change in the signal is monitored and processed to provide a three-dimensional (3D) image.

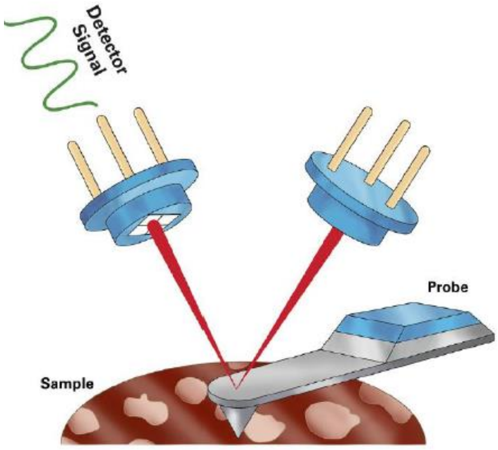

Figure 24: Probe deflection sensing schematic (Bruker Corporation).

There are different modes used in AFM, the main modes are Contact Mode and Taping Mode. In Contact Mode, the sharp tip is continuously in contact with the surface and the deflection of the laser spot is directly related to change in height. In Tapping Mode, the probe is in continuous mechanical oscillation and its frequency is close or at its resonance frequency. In this case, the detector measures the cantilever oscillation amplitude and with a feedback mode it adjusts the probe height based on the amplitude signal to maintain the same amplitude set-point. The change in height is measured and processed into a 3D image.

Reference

1. Fauzia, V., et al., High figure of merit transparent conducting Sb-doped SnO2 thin films prepared via ultrasonic spray pyrolysis. Journal of Alloys and Compounds, 2017. **720**: p. 79-85.

2. Islam, M.A., et al., Highly transparent conducting and enhanced near-band edge emission of SnO2:Ba thin films and its structural, linear and nonlinear optical properties. Optical Materials, 2020. **106**: p. 109996.

3. Hossain, M.F., et al., Transparent conducting SnO2 thin films synthesized by nebulized spray pyrolysis technique: Impact of Sb doping on the different physical properties. Materials Science in Semiconductor Processing, 2021. **121**: p. 105346.

4. Ramarajan, R., et al., Substrate Temperature Dependent Physical Properties of Spray Deposited Antimony-Doped SnO2 Thin Films. Thin Solid Films, 2020. **704**: p. 137988.

5. Ramarajan, R., et al., Large-area spray deposited Ta-doped SnO2 thin film electrode for DSSC application. Solar Energy, 2020. **211**: p. 547-559.

6. Sivakumar, P., et al., Influence of Ga doping on structural, optical and electrical properties of transparent conducting SnO2 thin films. Optik, 2021. **226**: p. 165859.

7. Sivakumar, P., et al., Effect of Ti doping on structural, optical and electrical properties of SnO2 transparent conducting thin films deposited by sol-gel spin coating. Optical Materials, 2021. **113**: p. 110845.

8. Tarighi, A. and A. Mashreghi, Dependence of Photovoltaic Properties of Spray-Pyrolyzed F-Doped SnO2 Thin Film on Spray Solution Preparation Method. Journal of Electronic Materials, 2019. **48**(12): p. 7827-7835.

9. Tran, Q.-P., J.-S. Fang, and T.-S. Chin, Properties of fluorine-doped SnO2 thin films by a green sol–gel method. Materials Science in Semiconductor Processing, 2015. **40**: p. 664-669.

10. Li, B.-j., et al., Influences of ultrasonic vibration on morphology and photoelectric properties of F-doped SnO2 thin films during laser annealing. Applied Surface Science, 2018. **458**: p. 940-948.

11. Chan y Díaz, E., et al., Influence of the oxygen pressure on the physical properties of the pulsed-laser deposited Te doped SnO2 thin films. Journal of Alloys and Compounds, 2010. **508**(2): p. 342-347.

12. Mrabet, C., et al., Improvement of the optoelectronic properties of tin oxide transparent conductive thin films through lanthanum doping. Journal of Alloys and Compounds, 2016. **666**: p. 392-405.

13. Joseph, D.P., et al., Effect of Li doping on the structural, optical and electrical properties of spray deposited SnO2 thin films. Thin Solid Films, 2009. **517**(21): p. 6129-6136.

14. Talaty, N.N., et al., Characterization of Tin(IV) Oxide Thin Films Prepared by Atmospheric Pressure Chemical Vapor Deposition of cis-[SnCl4{OC(H)OC2H5}2]. Zeitschrift für anorganische und allgemeine Chemie, 2009. **635**(1): p. 53-63.

15. Moholkar, A.V., et al., Effect of concentration of SnCl4 on sprayed fluorine doped tin oxide thin films. Journal of Alloys and Compounds, 2008. **455**(1): p. 440-446.

16. Ramarajan, R., et al., Boltzmann conductivity approach for charge transport in spray-deposited transparent Ta-doped SnO2 thin films. Journal of Alloys and Compounds, 2022. **897**: p. 163159.

17. Moholkar, A.V., et al., Properties of highly oriented spray-deposited fluorine-doped tin oxide thin films on glass substrates of different thickness. Journal of Physics and Chemistry of Solids, 2007. **68**(10): p. 1981-1988.

18. El Radaf, I.M. and R.M. Abdelhameed, Surprising performance of graphene oxide/tin dioxide composite thin films. Journal of Alloys and Compounds, 2018. **765**: p. 1174-1183.

19. Adjimi, A., et al., Gadolinium doping effect on SnO2 thin films optical and electrical properties. Materials Research Express, 2019. **6**(9): p. 096405.

20. Belayachi, W., et al., SnO2 Films Elaborated by Radio Frequency Magnetron Sputtering as Potential Transparent Conducting Oxides Alternative for Organic Solar Cells. ACS Applied Energy Materials, 2022. **5**(1): p. 170-177.

21. Babar, A.R., et al., Physical properties of sprayed antimony doped tin oxide thin films: The role of thickness. Journal of Semiconductors, 2011. **32**(5): p. 053001.

22. Vishwakarma, S.R., J.P. Upadhyay, and H.C. Prasad, Physical properties of arsenic-doped tin oxide thin films. Thin Solid Films, 1989. **176**(1): p. 99-110.

23. Singh, S.K. and S. Basu, Characterisation of conducting SnO2layers deposited by modified spray pyrolysis technique. Materials Chemistry and Physics, 1988. **20**(4): p. 381-396.

24. Asim, N., et al., A review on the role of materials science in solar cells. Renewable and Sustainable Energy Reviews, 2012. **16**(8): p. 5834-5847.

25. Richards, B.S., Enhancing the performance of silicon solar cells via the application of passive luminescence conversion layers. Solar Energy Materials and Solar Cells, 2006. **90**(15): p. 2329-2337.

26. Green, M.A., Solar cells—Operating principles, technology and system applications. Solar Energy, 1982. **28**(5): p. 447.

27. NREL, NREL Chart. https://www.nrel.gov/pv/cell-efficiency.html.

28. Kojima, A., et al., Organometal Halide Perovskites as Visible-Light Sensitizers for Photovoltaic Cells. Journal of the American Chemical Society, 2009. **131**(17): p. 6050-6051.

29. Chen, Y., et al., SnO2-based electron transporting layer materials for perovskite solar cells: A review of recent progress. Journal of Energy Chemistry, 2019. **35**: p. 144-167.

30. Ansari, M.I.H., A. Qurashi, and M.K. Nazeeruddin, Frontiers, opportunities, and challenges in perovskite solar cells: A critical review. Journal of Photochemistry and Photobiology C: Photochemistry Reviews, 2018. **35**: p. 1-24.

31. Roy, P., et al., Perovskite Solar Cells: A Review of the Recent Advances. Coatings, 2022. **12**(8): p. 1089.

32. Gheno, A., et al., π-Conjugated Materials as the Hole-Transporting Layer in Perovskite Solar Cells. Metals, 2016. **6**(1): p. 21.

33. Mahmood, K., S. Sarwar, and M.T. Mehran, Current status of electron transport layers in perovskite solar cells: materials and properties. RSC Advances, 2017. **7**(28): p. 17044-17062.

34. Park, H.H., Inorganic Materials by Atomic Layer Deposition for Perovskite Solar Cells. Nanomaterials, 2021. **11**(1): p. 88.

35. Mohamad Noh, M.F., et al., The architecture of the electron transport layer for a perovskite solar cell. Journal of Materials Chemistry C, 2018. **6**(4): p. 682-712.

Extended Abstract in French (Résumé étendu)

Titre de la thèse : **Etude des couches minces d'oxyde d'étain en vue de leurs applications dans les cellules photovoltaïques.**

La mise en œuvre de matériaux à base d'éléments abondants et peu couteux pour des applications dans les cellules solaires photovoltaïques est l'un des aspects clés pour réduire le coût de fabrication et respecter l'environnement. Pour répondre à cet objectif, il y a un effort constant de recherche depuis des décennies pour mettre en œuvre des oxydes conducteurs transparents (OCT) performants très utilisés dans cette technologie. En particulier, l'oxyde d'indium et d'étain, InSnO (ITO), qui est l'un des OCT les plus utilisés dans plusieurs applications liées à l'optoélectronique, est déjà confronté à des problèmes de ressources en raison du coût élevé de l'indium ainsi que de son abondance limitée sur la croûte terrestre par rapport à la plupart des éléments métalliques de transition. D'autre part, l'étain (Sn) est un élément plus accessible et plus abondant que l'indium. Les couches minces d’oxyde d’étain (SnO_x), basées sur l'élément métallique Sn, peuvent atteindre une conductivité et une mobilité électrique élevées en optimisant les conditions de croissance du film SnO_x. L'objectif de cette thèse était de mener une étude détaillée de l'oxyde d'étain non dopé et de l'oxyde d'étain enrichi en azote (N-SnO_x) en tant qu'oxyde conducteur transparent (OCT) en utilisant différentes conditions de croissance et d'explorer les propriétés de ces matériaux à l'aide de différentes techniques de caractérisation. Il a été également question d'évaluer les performances de l'oxyde d'étain comme couche de transport d'électrons (CTE) pour les cellules solaires de type pérovskite.

Le **premier chapitre** présente une revue non-exhaustive de littérature sur les oxydes transparents conducteurs (OTC) et leurs applications respectives. En particulier, la synthèse et les propriétés des matériaux, ainsi que les applications des couches minces In_2O_3 et ZnO en tant que OTC sont abordées dans ce chapitre. Plus particulièrement, l'état de l'art de l'oxyde d'étain (SnO_x), dans les deux états chimiques SnO_2 et SnO, est discuté en termes de synthèse et de propriétés de ces matériaux ainsi que de leurs applications potentielles.

Le **deuxième chapitre** est consacré à la synthèse et à la caractérisation complète de couches minces d'oxyde d'étain élaborées par deux méthodes de pulvérisation magnétron qui diffèrent principalement par le matériau cible lors de la pulvérisation et en faisant varier plusieurs conditions expérimentales, notamment la température du substrat lors du dépôt, le rapport de débit des gaz O_2 et Ar, et le recuit thermique post-dépôt.

La première voie de recherche a consisté à préparer les films de SnO_x à partir d'une cible d'étain oxydé. Nous avons montré que la température du substrat joue un rôle majeur dans les propriétés structurales des couches minces d'oxyde d'étain élaborées. Ainsi, les films déposés à 250°C présentent une meilleure cristallinité que ceux déposés à 100°C. D'autre part, le post-recuit sous vide à 400°C a amélioré les propriétés structurales en rehaussant la cristallinité. Néanmoins, après le recuit, l'oxyde d'étain développé à 250°C a conservé une meilleure structure cristalline par rapport à celui fabriqué à 100°C. Le recuit sous ambiance air a amélioré la structure cristalline de tous les films par rapport au recuit sous vide. Les deux couches SnO_x déposées sans O_2 et recuits à l'air ont révélé la présence de deux phases SnO et SnO_2. Le recuit sous vide a considérablement amélioré les propriétés électriques des échantillons d'oxyde d'étain par rapport au recuit à l'air. Pourtant, le recuit sous air ambiant a permis d’atteindre une transmission optique légèrement meilleure par rapport à la condition de recuit sous vide. Le meilleur film conducteur a été déposé à 250°C sous un rapport de débit O_2/Ar de 0.015 et suite à un recuit sous vide. Figure 1 montre l’image et la diffraction de microscopie électronique à transmission (MET) de ce film, où la distance interréticulaire et les cercles de diffraction confirment la présence de la phase SnO_2. Cependant, le film cristallin avec la taille de cristallite la plus élevée a été déposé à 100°C sans flux d'O_2 et avec recuit à l'air. Il est à noter que le meilleur film conducteur a les performances optoélectroniques les plus élevées, évaluées par le facteur de mérite (FdM).

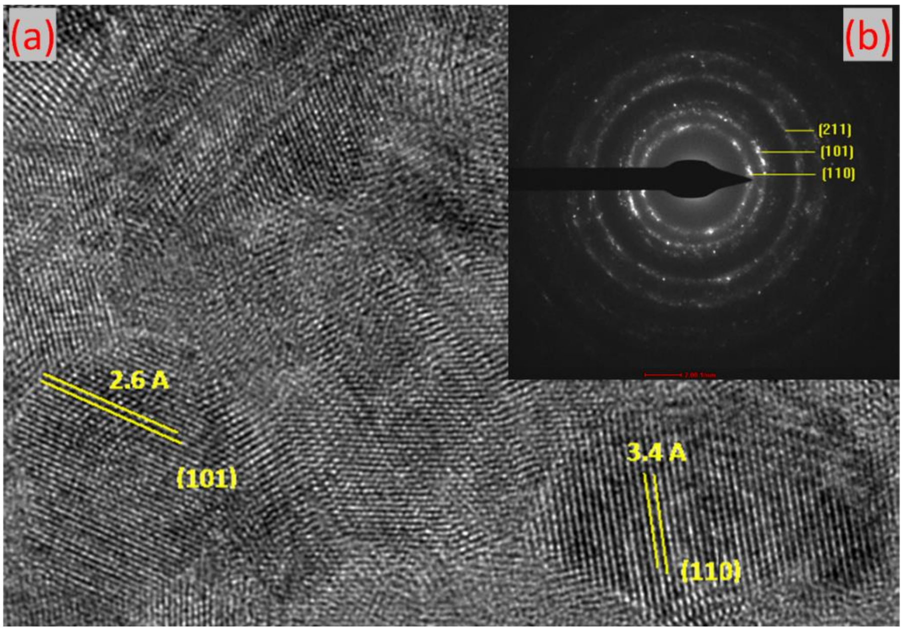

Figure 1: Image MET de coupe transversale de lamelle pour le meilleur film conducteur (a) image MET à haute résolution, (b) diagramme de diffraction MET . Ce film SnO_x a été déposé à 250°C, sous un rapport de débit O_2:Ar de 0.015 puis recuit sous vide.

La deuxième voie étudiée dans cette thèse est la croissance PVD de SnO_x utilisant une cible d'étain métallique. Nous avons montré que le rapport de débit de gaz O_2/Ar joue un rôle majeur dans les propriétés structurelles des couches minces d'oxyde d'étain déposées à une température inférieure de 100°C. Pour des rapports de débit O_2/Ar faibles, les couches de SnO_x déposés ont une structure amorphe. Par contre, pour les rapports de débit O_2/Ar plus élevés, les films ont une structure cristalline. Comme attendu, les propriétés structurelles ont un effet important sur les propriétés optoélectroniques des couches minces de SnO_x où la bande interdite optique est plus faible pour des rapports de débit O_2/Ar faibles. Cela indique la présence principale de la phase SnO. En revanche, pour des rapports de débit O_2/Ar plus élevés, la bande interdite optique augmente, indiquant la présence de SnO_2. Nous avons aussi démontré que la résistivité de ces derniers est bien plus faible.

Dans les films SnO_x obtenus en utilisant une cible d'étain métallique, nous avons constaté que la température du substrat n'influençait pas de manière significative les propriétés structurelles de SnO_x produits avec un faible rapport de débit O_2/Ar. Ceci a été confirmé par la diffraction des rayons X - incidente rasante en montrant la présence d'une large bande autour de 30° typique de la phase SnO pour des températures du substrat comprises entre la température ambiante et 400°C. Cependant, nous avons constaté une singularité mineure lié à la présence de SnO_2 pour le dépôt à 400°C. La bande interdite optique a légèrement augmenté de 3.5 à 3.7 eV en augmentant la température du substrat á 400°C, indiquant la présence principalement de la phase SnO. Ceci est due à l'appauvrissement de l'atmosphère en oxygène pendant la croissance. On note aussi que la structure amorphe liée à la phase SnO a engendrée une résistivité élevée.

Les couches SnO_x de type p étant fortement recherchées pour plusieurs applications, certains paramètres expérimentaux ont été variées pour atteindre cet objectif en utilisant des films SnO_x obtenus par cible oxydé et soumis à un traitement thermique de recuit. Ainsi, une conductivité de type p a été démontrée dans certains cas spécifiques. La première série d'essais de recuit postérieur au dépôt en variant la température de recuit sous atmosphère d'Argon, a montré que la température de recuit de 600°C a permis d'obtenir plus de films conducteurs de type p tandis que le recuit à 500°C a permis de réaliser moins de films conducteurs de type p. Par contre, le recuit à 400°C n'a pas permis de convertir la conductivité des films SnO_x de type n vers type p. Ceci a confirmé l'importance de la température du recuit. Il est également montré que la conductivité de type p est liée à la présence de la phase SnO, grâce à la diffraction par microscopie électronique à transmission in-situ et aux mesures de valeurs faibles de la bande interdite. La durée de recuit sous Ar a montré que l'extension du temps de recuit à deux heures a fourni l'effet inverse où tous les films deviennent conducteurs de type n alors qu'ils présentaient une conductivité de type p pour des temps de recuit court.

Il convient de noter que les couches SnO_x sont très sensible à l'air et qu'ils s'oxydent facilement en présence d'O_2. L'effet de vieillissement sous air a également été évalué après sept jours d'exposition, et il s'avère que la conductivité des couches SnO_x a évolué du type p au type n et que la résistivité a diminué. Cela pourrait s'expliquer par la continuation de l'oxydation de SnO_x par l'air ambiant vers SnO_2 et en conséquence la formation croissante de porteurs de charge intrinsèques de type n qui compensent les porteurs de charge de type p. L'effet de la présence d'humidité sur l'oxyde d'étain après sept jours de vieillissement a été étudié en utilisant un procédé de chauffage à 150°C en présence d'air. Ce processus n'a montré aucune influence de l'humidité et a conduit à une oxydation additionnelle de SnO_x et à une diminution de la résistivité en formant davantage de porteurs de charge de type n.

Dans le **troisième chapiter**, les performances du matériau SnO_2 en tant que semiconducteur de type n, obtenu par pulvérisation, ont été évaluées comme couche de transport d'électrons (CTE) et implémenté dans les cellules solaires pérovskite (CSP) sans structure mésoporeuse. Le rendement de conversion de puissance (RCP) de la cellule CSP, utilisant une couche mince de SnO_2 (telle que déposée) comme CTE, a révélé un rendement de 15,07 %. En revanche, le RCP du CSP avec une couche mince de SnO_2 recuite est augmenté de 2 points, à 17,1 %. La Figure 2 montre la caractéristique J-V des deux cellules avec du SnO_2 tel que déposé et du SnO_2 recuit en tant que CTE. Le procédé de recuit post-dépôt sous air pour SnO_2 en tant que CTE a donc permis une meilleure performance des cellules solaires pérovskite en améliorant les propriétés optoélectroniques du SnO_2.

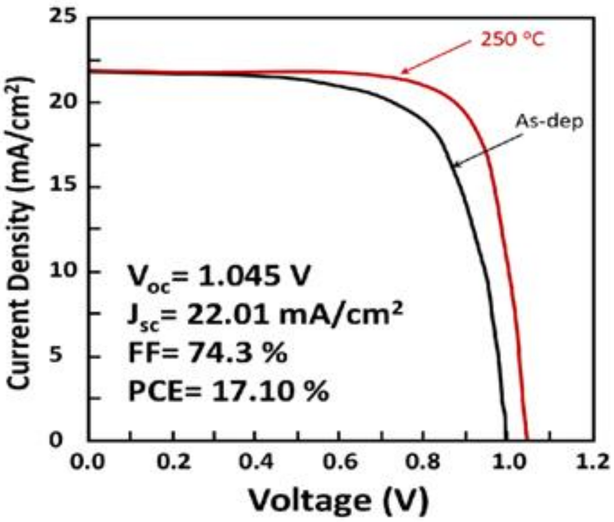

Figure 2: Caractéristiques densité de courant-tension sous illumination de cellules solaires en pérovskite basées sur les couches minces de SnO_2 (telle que déposé et recuite à 250°C) utilisés comme couche de transport d'électrons.

Dans le **quatrième et dernier chapitre**, le dopage à l'azote de films SnO_x a été étudié en utilisant trois précurseurs d'azote, à savoir des plasmas de NH_3, N_2O et N_2, avec deux niveaux de traitements modéré et intense pour chaque précurseur. L'objectif encore une fois est de tenter de former des films SnO_x de type p. Les traitements sous plasma HN_3 ont gravé et endommagé les couches minces de SnO_x tandis que les traitements sous plasma N_2O ont augmenté la conductivité de type n. Pour le dopage sous plasma d'azote (N_2), le traitement modéré a abouti à une augmentation importante de la résistivité et le traitement intense a plutôt abouti à une augmentation relativement plus faible de la résistivité mais avec un changement de conductivité du type n vers le type p. Les études par XPS pour le cas de traitement plasma N_2 intense ont révélé la présence principalement de la phase SnO_2 avec une présence mineure de la phase SnO , et surtout la présence de l'azote sous différents états chimiques (voir Figures 3a,b,c). L'incorporation effective d'azote élémentaire dans la couche SnO_x, a été confirmée par des mesures de ToF-SIMS (Figure 2d) qui ont montré que le profil de distribution de l'azote est uniforme sur toute la profondeur.

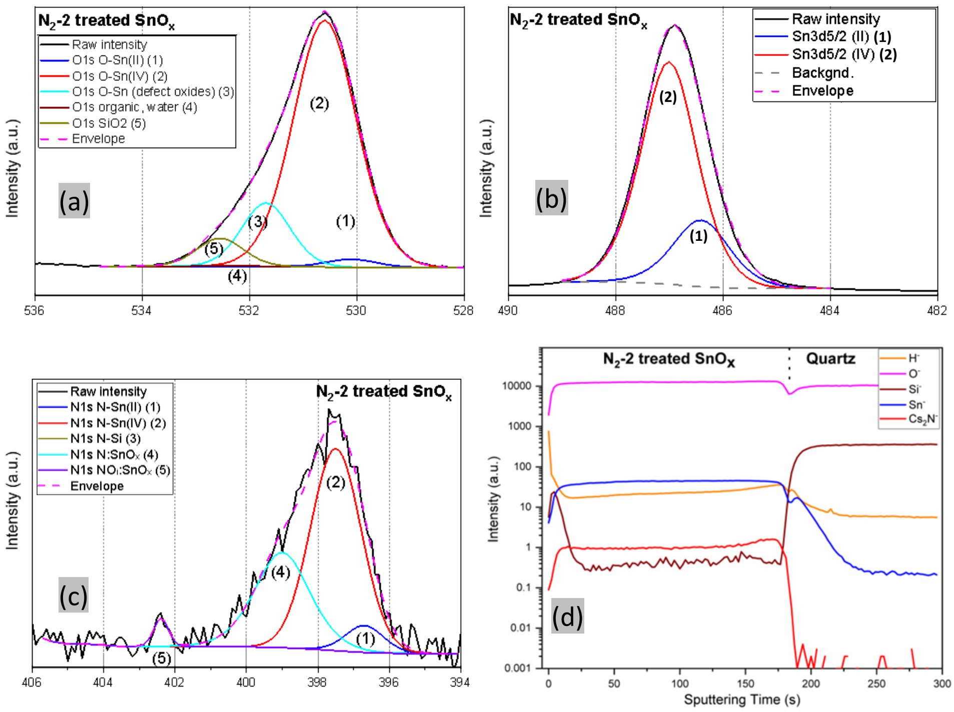

Figure 3: Analyse de surface pour la couche SnO_x traités au plasma N_2 intense à l'aide de spectres XPS déconvolués pour (a) O 1s (b) Sn 3d5/2 (c) N 1s et (d) profils de profondeur ToF-SIMS.

Par ailleurs, nous avons également démontré que la réalisation d'un traitement plasma N_2 intense suivi d'un recuit thermique sous Ar conduit à l'amélioration de la conductivité de type p. Cependant, l'inversion de l'ordre de ces deux procédés (recuit sous Ar suivi par traitement plasma N_2 intense) peut conduire à l'effet opposé à savoir que les films conservent leur conductivité de type n ou changent du type p au type n.

Pour résumer les principaux résultats, ce travail de thèse a permis d'ajuster les propriétés structurelles, optiques et électriques des couches de SnO_x , déposées à l'aide de deux configurations différentes de pulvérisation magnétron, en optimisant les conditions de croissance. Pour les couches minces de SnO_x déposées en utilisant SnO comme cible de pulvérisation, le recuit thermique sous Ar et à une température relativement élevée (autour de 600°C) a montré la possibilité de convertir la conductivité de type n en type p. Les propriétés du matériau SnO_x avant et après le recuit ont montré que cette conductivité de type p est liée à la formation de la phase de monoxyde d'étain (SnO). D'autre part, nous avons aussi testé l'emploi des couches minces de SnO_2 comme couche de transport d'électrons dans des cellules solaires à pérovskite. Le recuit thermique de SnO_2 post- dépôt a permis une amélioration nette du rendement de conversion photovoltaïque des cellules testées. L’ensemble de ces résultats montre l’importance des films SnO_x à utiliser pour la prochaine génération de cellules photovoltaïques (perovskite, tandem perovskite/perovskite, tandem pervoskite/Si ou CIGS).

Dans la dernière partie de ce travail, nous avons exploré l'incorporation d'azote, par traitement sous plasma N_2 intense, dans les couches minces de SnO_x, cette incorporation a indiqué la capacité de convertir la conductivité de type n en type p. Cette conversion est suggérée comme étant le résultat d'éléments azotés occupant les lacunes d'oxygène.

Publications

1. Y. Zakaria, B. Aïssa, T. Fix, S. Ahzi, A. Samara, S. Mansour, A. Slaoui - Study of wide bandgap SnO_x thin films grown by a reactive magnetron sputtering via a two-step method. Scientific Reports 12, 15294 (2022). https://doi.org/10.1038/s41598-022-19270-w

2. Y. Zakaria, B. Aïssa, T. Fix, S. Ahzi, S. Mansour, A. Slaoui - Moderate temperature deposition of RF magnetron sputtered SnO_2-based electron transporting layer for triple cation perovskite solar cells – Scientific Reports 13, 9100 (2023). https://doi.org/10.1038/s41598-023-35651-1

3. Y. Zakaria, B. Aïssa, T. Fix, S. Roques, G. Ferblantier, S. Ahzi, S. Mansour, A. Slaoui - P-type nitrogen doped SnO_x synthesis and characterization using magnetron sputtering and plasma post-treatment (In preparation)

4. Y. Zakaria, B. Aïssa, S. Ahzi, A. Slaoui - SnO_x based thin films as transparent conductive oxides: review (In preparation)

Communications

1. Y. Zakaria, S. Ahzi, S. Mansour, A. Samara, A. Slaoui - SnO_x Thin Film RF Sputtering Deposition and Post Annealing (Poster Presentation) - 5th Ed. Smart Materials and Surfaces (2019)

2. Y. Zakaria, A. Slaoui, S. Ahzi, B. Aissa, T. Fix, G. Ferblantier, A. Samara, S. Mansour- P-type N doped SnO_x using Magnetron Sputtering and Post Plasma Treatment (Poster Presentation) - European Materials Research Society (Spring 2021)

3. Y. Zakaria, B. Aïssa, T. Fix, S. Ahzi, S. Mansour, A. Slaoui - Synthesis and Characterization of Magnetron Sputtered SnO_2 and its application as Electron Transport Layer (Poster Presentation) - European Materials Research Society (Spring 2023)

4. Y. Zakaria, B. Aïssa, T. Fix, S. Ahzi, S. Mansour, A. Slaoui - Magnetron Sputtered SnO_2 as Electron Transport Layer for Perovskite Solar Cells (Poster Presentation) - European Materials Research Society (Spring 2023)

Université de Strasbourg

Yahya ZAKARIA

Study of Thin Layers of Tin Oxide for Applications in Photovoltaic Solar Cells

École doctorale
Mathématiques, sciences de l'information et de l'ingénieur | ED 269
Université de Strasbourg

Résumé

L'oxyde d'étain est un oxyde conducteur transparent prometteur qui peut être utilisé dans diverses applications, notamment dans le photovoltaïque. Dans ce travail, nous avons étudié l'effet des conditions de croissance de SnO_x en utilisant la pulvérisation magnétron, à savoir le rapport de débit O_2/Ar et la température de croissance, sur les propriétés structurales, optiques et électriques. Nous avons également exploré l'effet du recuit thermique post-dépôt sous vide, air et argon sur les propriétés structurales et optoélectroniques des couches minces de SnO_x. De plus, nous avons évalué le film mince SnO_x en tant que couche de transport d'électrons pour les cellules solaires à pérovskite et nous avons constaté que l'efficacité de conversion de puissance était passée de 15,07 % à 17,10 % après recuit thermique sous air. Enfin, nous avons étudié la possibilité de doper SnO_x avec de l'azote en utilisant trois gaz précurseurs d'azote, à savoir NH_3, N_2O et N_2. Nous avons constaté que les traitements NH_3 ont gravé et endommagé les couches SnO_x, les traitements N_2O ont amélioré la conductivité de type n et les traitements N_2 ont montré la capacité de convertir la conductivité de type n en type p.

Mots clés : Oxides, Pulvérisation Magnétron, Recuit Thermique, Cellule Solaire, SnO_x

Résumé en anglais

Tin oxide is a promising transparent conducting oxide which can be employed in various application, particularly in photovoltaic. In this work, we studied the effect of the growth conditions of SnO_x using magnetron sputtering namely, O_2/Ar flow rate ratio and growth temperature, on the structural, optical and electrical properties. We also explored the effect of post-deposition thermal annealing under vacuum, air and argon on the structural and optoelectronic properties of SnO_x thin films. Furthermore, we assessed the SnO_x thin film as electron transport layer for perovskite solar cells and we found that power conversion efficiency has been increased from 15.07% to 17.10% after thermal annealing in air. Finally, we investigated the possibility to dope SnO_x with nitrogen using three nitrogen precursor gases namely, NH_3, N_2O and N_2. We found that NH_3 treatments have etched and damaged the SnO_x films, N_2O treatments have enhanced the n-type conductivity and N_2 treatments have shown the ability to convert the conductivity from n-type to p-type.

Keywords: Oxides, Magnetron Sputtering, Thermal Annealing, Solar Cell, SnO_x